

# **Dynamic Operation of Power-to-X Processes Demonstrated by Methanol Synthesis**

zur Erlangung des akademischen Grades eines  
DOKTORS DER INGENIEURWISSENSCHAFTEN

von der KIT-Fakultät für Chemieingenieurwesen und Verfahrenstechnik des  
Karlsruher Instituts für Technologie (KIT)  
genehmigte

DISSERTATION

von

Florian Nestler

---

Tag der mündlichen Prüfung: 20.05.2022

Erstgutachter: Prof. Dr.-Ing. Thomas Kolb

Zweitgutachter: Prof. Dr.-Ing. Jürgen Karl



Beharrlichkeit  
– Perseverance



# Abstract

Chemical energy storage in the context of so-called Power-to-X (PtX) processes will play a key-role in the future energy system due to the increasing power production from renewable energy and the urging defossilization of industry and transport sector. Among possible PtX products, methanol produced from carbon dioxide ( $\text{CO}_2$ ) and sustainably produced hydrogen ( $\text{H}_2$ ) is going to play a key-role due to its high relevance in the global fuel and chemical market. Compared to conventional methanol synthesis based on fossil feedstocks, methanol synthesis based on  $\text{CO}_2$ -rich gas streams captured from industrial processes, biomass processing or ultimately captured from air is subjected to decreased equilibrium conversions, inhibited reaction kinetics and an accelerated catalyst aging. Moreover, the production of  $\text{H}_2$  from water electrolysis operated with renewable power and the coupled  $\text{CO}_2$ -supplying industrial process can impose dynamic fluctuations to syngas supply unknown to the current-state-of-the-art. For these new boundary conditions, design of the synthesis reactor and operation of the process become more challenging and do demand for detailed models for each unit operation in the synthesis process. However, for the kinetic simulation of the synthesis reactor under these conditions only scarce knowledge exists in the scientific community. Thus, a detailed kinetic description of the reaction network in industrial reactors is required to enable methanol synthesis from sustainable resources in the future.

To tackle that deficit, this work used a scale-flexible simulation platform to design a miniplant facility with the reactor reproducing the thermochemical behavior of an industrial steam cooled tube bundle reactor with a high agreement. An innovative analytical concept using the highly resolved fiber optic temperature measurement to analyze the axial temperature profile in the reactor combined with an FTIR product composition measurement was implemented to derive a kinetic model for reactor- and process design validated over the complete range of relevant load conditions for Power-to-Methanol (PtM) processes. Comparison to kinetic models obtained from literature highlighted both the scientific value of methodical approach implemented in this work and the high relevance of the herein proposed kinetic model for the practical implementation of PtM processes. Furthermore, the validation of the dynamic reactor model implemented in this work by a exemplary load change performed with the miniplant showed a high level of agreement between the experimental data and the simulation results. Thus, the scientific potential of the herein proposed miniplant validation approach for the investigation of stationary and dynamically operated PtX processes could be demonstrated.

# Kurzfassung

Chemische Energiespeicher hergestellt im Rahmen von sogenannten Power-to-X (PtX) Prozessen werden in Zukunft aufgrund des fortschreitenden Ausbaus der Stromproduktion aus regenerativen Energiequellen und der notwendigen Defossilisierung von Industrie- und Verkehrssektor eine zunehmend wichtige Rolle spielen. Hierbei wird der Methanolsynthese aus Kohlendioxid ( $\text{CO}_2$ ) und nachhaltig produziertem Wasserstoff ( $\text{H}_2$ ) im Energiesystem eine Schlüsselposition zugeschrieben, da Methanol bereits heute ein wichtiger Baustein im globalen Treibstoff- und Chemiemarkt ist. Im Vergleich zur konventionellen Methanolsynthese basierend auf fossilen Energieträgern birgt die Methanolsynthese aus  $\text{CO}_2$ -reichen Gasen, welche aus industriellen Prozessen, der Biomasseverwertung oder der Luft gewonnen werden, die Problematik schlechterer Gleichgewichtsumsätze, einer veränderten Reaktionskinetik und der beschleunigten Katalysatordeaktivierung. Zudem unterliegen die Herstellung von  $\text{H}_2$  aus der Wasserelektrolyse mit erneuerbarem Strom und ggf. die  $\text{CO}_2$ -Versorgung aus dem gekoppelten Industrieprozess einer Dynamik, die für die Methanolsynthese eine große Abweichung vom aktuellen Stand der Technik darstellt. Für diese geänderten Rahmenbedingungen existieren in der wissenschaftlichen Gemeinschaft insbesondere zur Simulation des Synthesereaktors keine validierten Modelle. Eine detaillierte reaktionskinetische Beschreibung des Reaktionsnetzwerkes in technischen Reaktoren ist daher notwendig, um die Methanolsynthese aus nachhaltigen Rohstoffen in Zukunft zu ermöglichen.

Um dieses Defizit zu adressieren, wurde in dieser Arbeit mithilfe einer skalenübertragbaren Simulationsplattform eine Miniplantanlage dimensioniert, deren Reaktor das thermochemische Verhalten eines industriellen dampfgekühlten Rohrbündelreaktors mit hoher Übereinstimmung abbildet. Ein neuartiges Messkonzept bestehend aus einer hochaufgelösten faseroptischen Temperaturmessung zur Erfassung des axialen Temperaturprofils im Reaktor sowie einer FTIR-Produktanalyse wurde implementiert, um ein Kinetikmodell für das Reaktor- und Prozessdesign abzuleiten, welches über den gesamten für Power-to-Methanol (PtM) Prozesse relevanten Parameterbereich validiert wurde. Der Vergleich zu Kinetikmodellen aus der Literatur demonstrierte deren Limitierungen und zeigte den Mehrwert des in dieser Arbeit implementierten methodischen Ansatzes sowie die Relevanz des neuen Kinetikmodells zur praktischen Umsetzung von PtM Verfahren. Darüber hinaus zeigte die Validierung des im Rahmen dieser Arbeit aufgestellten dynamischen Modells anhand eines exemplarischen Lastwechsels an der Miniplant eine hohe Übereinstimmung zwischen experimentellen Daten und Simulationsergebnissen. Somit konnte die hohe wissenschaftliche Relevanz des vorgestellten Miniplant-Validierungsansatzes für die Untersuchung des stationären und dynamischen Reaktorverhaltens von PtX Synthesen gezeigt werden.

# Contents

<b>Abstract</b> . . . . .	<b>iv</b>
<b>Kurzfassung</b> . . . . .	<b>v</b>
<b>Notation</b> . . . . .	<b>ix</b>
<b>List of Figures</b> . . . . .	<b>xv</b>
<b>List of Tables</b> . . . . .	<b>xix</b>
<b>1 Introduction</b> . . . . .	<b>1</b>
<b>2 Literature Review and Scientific Approach</b> . . . . .	<b>4</b>
2.1 Significance of methanol as a commodity chemical . . . . .	4
2.2 Properties of the synthesis gas for methanol synthesis . . . . .	5
2.2.1 Carbon oxide ratio . . . . .	6
2.2.2 Stoichiometric number . . . . .	6
2.2.3 Inert gas fraction . . . . .	7
2.2.4 Impurities . . . . .	7
2.3 Feedstocks used for methanol synthesis . . . . .	7
2.3.1 Coal, biomass and refinery residues . . . . .	7
2.3.2 Natural gas . . . . .	8
2.3.3 Alternative feedstocks . . . . .	9
2.3.4 Classification of make-up-gases . . . . .	11
2.4 Technological overview on methanol synthesis . . . . .	12
2.4.1 Reaction conditions and equilibrium . . . . .	12
2.4.2 Synthesis process . . . . .	15
2.4.3 Reactor concepts . . . . .	18
2.4.4 Dynamic operation . . . . .	20
2.4.5 Capability of reactor types for dynamic operation . . . . .	22
2.5 Kinetic validation in methanol synthesis . . . . .	24
2.6 Problem definition and scientific approach . . . . .	26
<b>3 Materials and Methods</b> . . . . .	<b>29</b>
3.1 Simulation platform . . . . .	29
3.1.1 Heat transfer model . . . . .	30
3.1.2 Kinetic models . . . . .	37
3.1.3 Diffusion model . . . . .	41
3.1.4 Steady state reactor model . . . . .	42
3.1.5 Dynamic reactor model . . . . .	42
3.1.6 Process simulation model . . . . .	43

3.2	Numerical methods . . . . .	44
3.2.1	Optimization methodology . . . . .	45
3.3	Scale-down of the industrial reactor . . . . .	46
3.4	Miniplant setup . . . . .	49
3.4.1	Fiber optic temperature measurement . . . . .	51
3.5	Experimental validation . . . . .	54
3.5.1	Integral literature data . . . . .	54
3.5.2	Differential miniplant data . . . . .	55
<b>4</b>	<b>Results and Discussion . . . . .</b>	<b>60</b>
4.1	Kinetic model derived from integral literature data . . . . .	60
4.1.1	Analysis of the reaction rates . . . . .	63
4.1.2	Comparison of reactor simulations . . . . .	65
4.1.3	Concluding remarks on the integral kinetic model . . . . .	69
4.2	Kinetic model derived from differential miniplant data . . . . .	70
4.2.1	Experimental results . . . . .	70
4.2.2	Validation of literature kinetics . . . . .	73
4.2.3	Fitted kinetic model . . . . .	76
4.2.4	Impact on industrial scale . . . . .	77
4.2.5	Co-verification of the kinetic model Nestler <sub>diff</sub> . . . . .	80
4.2.6	Optimal design for the miniplant setup . . . . .	81
4.2.7	Concluding remarks on the differential kinetic model . . . . .	82
4.3	Validation of the dynamic reactor model . . . . .	84
4.4	Application on process scale . . . . .	89
<b>5</b>	<b>Conclusion and Outlook . . . . .</b>	<b>94</b>
	<b>Bibliography . . . . .</b>	<b>98</b>
	<b>Acknowledgements . . . . .</b>	<b>120</b>
	<b>Verification of the contribution of co-authors . . . . .</b>	<b>121</b>
	<b>Publication list . . . . .</b>	<b>125</b>
	<b>Appendix . . . . .</b>	<b>A</b>
A.1	Derivation of the equilibrium constant . . . . .	A
A.2	Literature use of kinetic models . . . . .	C
A.3	Industrial reactor data available in scientific literature . . . . .	C
A.4	Cell model for heat transfer inside the packed bed . . . . .	D
A.5	Sensitivity of Thiele modulus . . . . .	E
A.6	Experimental data used for integral kinetic model . . . . .	G
A.7	CAD drawing of the miniplant setup . . . . .	L
A.8	Measurement of thermal oil flow rate . . . . .	M

A.9 Thermophysical properties of the thermal oil . . . . .	N
A.10 Analysis of the catalyst particle size distribution . . . . .	O
A.11 Purity of the gases used within the miniplant experiments . . . . .	O
A.12 Overview on the experimental campaign executed on the scale down miniplant . . . . .	P
A.13 Experimental data obtained from the miniplant experiments . . . . .	S
A.14 Mass balances of the miniplant experiments . . . . .	AB
A.15 Axial deactivation . . . . .	AC
A.16 NMR liquid phase measurement . . . . .	AD
A.17 Kinetic model by Graaf . . . . .	AE
A.18 Kinetic model by Bussche . . . . .	AH
A.19 Kinetic model by Park . . . . .	AJ
A.20 Kinetic model by Henkel . . . . .	AL
A.21 Alternative kinetic approaches . . . . .	AN
A.22 Single versus global data fitting . . . . .	AP
A.23 Comparison of experimental and simulated gas phase composition data . . . . .	AR
A.24 Dynamic simulation study . . . . .	AS

# Notation

## Abbreviations

ATR	Autothermal reforming
BFG	Blast furnace gas
BOFG	Basic oxygen furnace gas
CAGR	Compound annual growth rate
COG	Coke oven gas
CCU	Carbon capture and utilization
CRI	Carbon Recycling International
DAC	Direct air capture
DIPPR	Design Institute for Physical Properties
DME	Dimethyl ether
EoS	Equation of state
FTIR	Fourier-transform infrared spectrometer
GHG	Greenhouse gas
ICI	Imperial Chemical Industries
LCA	Life cycle assessment
LPG	Liquefied petroleum gas
MTBE	Methyl tert-butyl ether
MTO	Methanol-to-olefin
MTP	Methanol-to-propylene
MUG	Make-up gas
NIST	National Institute of Standards and Technology
NMR	Nuclear magnetic resonance spectroscopy
NG	Natural gas
ODE	Ordinary differential equation
PDE	Partial differential equation
PO <sub>x</sub>	Partial oxidation
PtM	Power-to-Methanol
PtX	Power-to-X
RDS	Rate determining step
RMSE	Root mean square error
rWGS	Reverse water-gas-shift
SMR	Steam methane reforming
SRK	Soave-Redlich-Kwong
ToS	Time on stream
VDI	Verein Deutscher Ingenieure
WGS	Water-gas-shift

## Symbols (Latin)

Symbol	Designation	Unit
$a_i$	Parameter	variable unit
$A_R$	Cross sectional area	$m^2$
$B$	Deformation parameter	-
$Bo$	Bodenstein number	-
$C_f$	Shape factor	-
$COR$	Carbon oxide ratio	-
$c_p$	Specific heat capacity	$J kg^{-1} K^{-1}$
$\tilde{c}_p$	Specific molar heat capacity	$J mol^{-1} K^{-1}$
$d$	Diameter	m
$D_{ax}$	Axial diffusion coefficient	$m^2 s^{-1}$
$D_{j,k}$	Binary diffusion coefficient between component j and k	$m^2 s^{-1}$
$D_{K,j}$	Knudsen diffusion coefficient of component j	$m^2 s^{-1}$
$D_{m,j}^e$	Effective diffusion coefficient of component j	$m^2 s^{-1}$
$EQ_i$	Equilibrium term of reaction i	-
$f_j$	Fugacity of component j	Pa
$f(x)$	Objective function	variable unit
$G$	Gibbs free energy	$J mol^{-1}$
$GHSV$	Gas hourly space velocity	$h^{-1}$
$h$	Height	m
$\Delta H_R^0$	Enthalpy of formation under standard conditions	$kJ mol^{-1}$
$k_{bed}$	Reduced thermal conductivity of the catalyst bed	-
$k_c$	Reduced thermal conductivity of the core of the unit cell (see Appendix A.4)	-
$K_{eq}$	Equilibrium constant	variable unit
$K'_{eq}$	Pseudo equilibrium constant	-
$k_i$	Reaction rate constant of reaction i	variable unit
$k'_i$	Pseudo-first-order rate constant of reaction i	$mol s^{-1} m^{-3} Pa^{-1}$
$K_j$	Adsorption constant of component j	variable unit
$k_p$	Reduced thermal conductivity of the catalyst particle	-
$K_r$	Reciprocal of the slope parameter	-
$LCE$	Loop carbon efficiency	%
$LCE_{ext}$	External hydrogen efficiency	%
$LCE_{int}$	Internal hydrogen efficiency	%
$M_j$	Molar mass of component j	$kg mol^{-1}$
$N$	Number	-

Symbol	Designation	Unit
$\dot{n}_j$	Molar flow of component or stream j	$\text{mols}^{-1}$
$Nu$	Nusselt number	-
$p$	Pressure	Pa
$p_r$	Relative pressure	-
$Pe_0$	Molecular Péclet number	-
$Pr$	Prandtl number	-
$\dot{q}$	Heat flow density	$\text{W m}^{-2}$
$R$	Universal gas constant	$\text{J mol}^{-1} \text{K}^{-1}$
$Re$	Reynolds number	-
$Re_p$	Reynolds particle number	-
$r_i$	Reaction velocity of reaction i	$\text{mol s}^{-1} \text{kg}_{\text{cat}}^{-1}$
$RMSE$	Root mean square error	variable unit
$RR$	Recycle ratio	-
$s_i$	Active site number i	-
$S_{MeOH}$	Selectivity towards methanol	-
$SN$	Stoichiometric number	-
$STY$	Space time yield	$\text{kg}_{\text{MeOH}} \text{l}_{\text{cat}}^{-1} \text{s}^{-1}$
$t$	Time	s
$T$	Temperature	K
$U$	Overall heat transfer coefficient	$\text{W m}^{-2} \text{K}^{-1}$
$u$	Velocity	$\text{m s}^{-1}$
$u_0$	Empty tube velocity	$\text{m s}^{-1}$
$V$	Volume	$\text{m}^3$
$\dot{V}_j$	Volumetric flow rate of component j	$\text{m}^3 \text{s}^{-1}$
$x_j$	Mass fraction of component j	-
$X_C$	Carbon conversion	-
$Y_C$	Carbon yield	-
$y_j$	Molar fraction of component j	-
$z$	Axial length	m

## Symbols (Greek)

Symbol	Designation	Unit
$\alpha$	Convective heat transfer coefficient	$\text{W m}^{-2} \text{K}^{-1}$
$\Delta$	Difference	-

Symbol	Designation	Unit
$\varepsilon$	Porosity	-
$\zeta_i$	Reaction progress coefficient of reaction i	$\text{mol s}^{-1}$
$\eta_{eff,j}$	Efficiency factor of component j	-
$\lambda_{bed}$	Radial heat conductivity of catalyst bed without fluid flow	$\text{W m}^{-1} \text{K}^{-1}$
$\lambda_c$	Radial heat conductivity of the core of the unit cell (see Appendix A.4)	$\text{W m}^{-1} \text{K}^{-1}$
$\lambda_{rad}$	Radial heat conductivity of flowed-through catalyst bed	$\text{W m}^{-1} \text{K}^{-1}$
$\lambda_{wall}$	Heat conductivity of reactor wall	$\text{W m}^{-1} \text{K}^{-1}$
$\nu_f$	Kinematic viscosity of fluid	$\text{m}^2 \text{s}^{-1}$
$\nu_j$	Stoichiometric factor of component j	-
$\rho$	Density	$\text{kg m}^{-3}$
$\tau$	Tortuosity	-
$\varphi$	Reactor-particle diameter ratio	-
$\phi_{M,j}$	Thiele modulus of component j	-

## Indices

Symbol	Designation
$\infty$	Infinite
<i>ann</i>	Annular
<i>b</i>	Boiling
<i>bulk</i>	Bulk
<i>cat</i>	Catalyst
<i>calib</i>	Calibrated
<i>CO</i>	Carbon monoxide (-hydrogenation)
<i>CO2</i>	Carbon dioxide (-hydrogenation)
<i>CO2, eq</i>	CO <sub>2</sub> -equivalent
<i>comp</i>	Components
<i>cool</i>	Coolant
<i>crit</i>	Critical
<i>data pt</i>	Experimental data points
<i>diff</i>	Differential
<i>eff</i>	Efficient
<i>eq</i>	Equilibrium
<i>exp</i>	Experimental

Symbol	Designation
<i>ext</i>	External
<i>f</i>	Fluid phase
<i>feed</i>	Reactor feed
<i>flash</i>	At flash separator
<i>g</i>	Gas phase
<i>H<sub>2</sub></i>	Hydrogen
<i>H<sub>2</sub>O</i>	Water
<i>hs</i>	Hot spot
<i>hydr</i>	Hydraulic
<i>i</i>	Counting index (reaction, data point)
<i>in</i>	At inlet
<i>inc</i>	Increment
<i>ind</i>	Industrial scale
<i>inert</i>	Inert gas
<i>int</i>	Internal
<i>integ</i>	Integral
<i>j</i>	Counting index (component, axial increment)
<i>k</i>	Counting index (component)
<i>l</i>	Liquid phase
<i>min</i>	Minimal
<i>miniplant</i>	Miniplant scale
<i>max</i>	Maximal
<i>MeOH</i>	Methanol
<i>MUG</i>	Make-up gas
<i>norm</i>	Norm conditions
<i>oil</i>	Thermal oil
<i>original</i>	Original
<i>out</i>	At outlet
<i>p</i>	Particle
<i>profil</i>	Profile
<i>purge</i>	Purge gas
<i>R</i>	Reactor
<i>recycle</i>	Recycle gas
<i>ref</i>	Reference condition
<i>rWGS</i>	Reverse water-gas-shift-reaction
<i>shell</i>	Shell
<i>sim</i>	Simulated
<i>T</i>	Temperature
<i>tubes</i>	Reactor tubes

---

Symbol	Designation
<i>wall</i>	Reactor wall
<i>y</i>	Molar composition

---

# List of Figures

1.1	Schematic flow diagram of the Power-to-Methanol process chain. . . . .	1
2.1	Worldwide consumption of methanol divided by the sectors fuel, methanol-to-olefin/methanol-to-propylene and traditional derivatives. . . . .	5
2.2	Gas composition of steel mill gas streams. . . . .	10
2.3	Comparison of the estimated inert gas content and COR of syngas obtained from conventional and alternative feedstocks conditioned for methanol synthesis. . . . .	11
2.4	Carbon yield of methanol at equilibrium over temperature. . . . .	14
2.5	Basic scheme of a methanol synthesis process. . . . .	16
2.6	Comparison of LCE, $LHE_{ext}$ , and $LHE_{int}$ computed with varied COR in the MUG at constant loop conditions. . . . .	18
2.7	Main types of industrially applied methanol synthesis reactors. . . . .	19
2.8	Number of publications in the literature data base generated in this work over decades for experimental work as well as simulation work. . . . .	21
2.9	Exemplary simulation of a multi-bed adiabatic quench bed reactor. . . . .	23
2.10	Range of experimental validation conditions applied by Graaf, Bussche, Henkel and Park. . . . .	25
3.1	Simulation platform applied in this work. . . . .	29
3.2	External heat transfer coefficient calculated using the correlations by Fritz, Holman and VDI Heat Atlas over the temperature difference between wall and cooling fluid. . . . .	35
3.3	Sensitivity of the parameters of the heat transfer model towards the overall heat transfer coefficient. . . . .	37
3.4	Speed-up of the simulation platform exemplified by a sensitivity analysis. . . . .	44
3.5	Simplified flow sheet of the experimental miniplant setup. . . . .	50
3.6	Calibration offset over the calibrated temperature between 50 °C and 265 °C together with the fitted 3rd-order polynomial extrapolated to 25 °C and 300 °C. . . . .	52
3.7	Calibrated and Savitky-Golay smoothed temperature profile measured by the fiber optic processing unit. . . . .	53
3.8	Illustration of the parameter fitting methodology applied in this work. . . . .	58
4.1	Parity plot of the kinetic model fitted to the measured data published by Park et al. [203]. . . . .	60
4.2	Arrhenius plot of the kinetic constants $k_1$ , $k_2$ , $K_1$ , $K_2$ , and $K_3$ for the Nestler <sub>integ</sub> model in comparison to those calculated with the model by Henkel. . . . .	62
4.3	Reaction rates of the kinetic models considered within this study. . . . .	63
4.4	Carbon conversion over COR in the reactor feed for the kinetic models by Graaf, Bussche, Henkel and the Nestler <sub>integ</sub> model at a reaction pressure of 50 bar. . . . .	64

4.5	Comparison of the one-dimensional temperature and product molar fraction profiles obtained by a reactor simulation at $COR = 0.75$ , $SN = 3.0$ , $GHSV = 10,000 \text{ h}^{-1}$ at a pressure of 65 bar utilizing the kinetic model by Bussche and the $Nestler_{integ}$ kinetic model. . . . .	66
4.6	Sensitivity study discussing the hot spot temperatures and positions obtained from the simulation of an industrial scale tubular reactor with the kinetic models by Graaf, Bussche and Henkel (Berty) as well as with the $Nestler_{integ}$ kinetic model. . . . .	67
4.7	Trend of the space time yield over time-on-stream at benchmark conditions. . . . .	71
4.8	Equilibrium and measured molar fraction of methanol and water at $COR = 0.7$ and $COR = 0.95$ . . . . .	72
4.9	Hot spot temperature measured at $COR = 0.7$ and $COR = 0.95$ and $GHSV = 12,000 \text{ h}^{-1}$ . . . . .	73
4.10	Parity plots for the outlet molar fractions of methanol and water as well as hot spot temperature and axial hot spot position; Experiments were carried out with the miniplant setup; Simulation was performed using the kinetic models by Graaf and Bussche as published as well as the $Nestler_{integ}$ kinetic model. . . . .	74
4.11	Parity plots of the refitted kinetic model $Nestler_{diff}$ for outlet molar fractions of methanol and water as well as hot spot temperature and axial hot spot position; Experiments were carried out with the miniplant setup. . . . .	78
4.12	Sensitivity study discussing the behavior of the kinetic models $Nestler_{integ}$ and $Nestler_{diff}$ by means of hot spot temperature and position as well as product molar fraction of methanol and water at a synthesis pressure of 50 bar and 80 bar in the range $0.7 \leq COR \leq 0.98$ , $2.0 \leq SN \leq 8.0$ at $GHSV = 6,000 \text{ h}^{-1}$ . . . . .	79
4.13	Parity plot comparing the kinetic model $Nestler_{diff}$ fitted to the miniplant experimental data to the integral experimental data published by Park et al. [203]. . . . .	81
4.14	Optimized inner reactor diameter of the miniplant over $COR$ and $SN$ at $GHSV = 9,000 \text{ h}^{-1}$ and $T_{cool} = 240 \text{ }^\circ\text{C}$ for maximized comparability towards the industrial reactor at 50 bar and 80 bar. . . . .	82
4.15	Smoothened temperature profiles obtained from the miniplant experiments and simulated temperature profiles using the kinetic models by Graaf [192], Bussche [145] as well as the kinetic model $Nestler_{integ}$ and $Nestler_{diff}$ . . . . .	83
4.16	Shift of the temperature profile during a load change from $COR = 0.8$ ; $SN = 2.0$ ; $GHSV = 6,000 \text{ h}^{-1}$ to $COR = 0.9$ ; $SN = 4.0$ ; $GHSV = 12,000 \text{ h}^{-1}$ at 80 bar and a cooling temperature of $240 \text{ }^\circ\text{C}$ . . . . .	85
4.17	Comparison of experimental and simulation data obtained during a load change using different heat capacities for the catalyst particle. . . . .	88
4.18	Sensitivity of $SN_{MUG}$ and $RR$ on the operating condition of the process. . . . .	90
4.19	Sensitivity of $SN_{MUG}$ and $RR$ on the operating condition of the process. . . . .	92
A.1	Literature use of the kinetic models by Bussche [145] and Graaf [192] over decades since 1980. . . . .	C
A.2	Schematic of the unit cell model as defined by Zehner and Schlünder [213]. . . . .	D

A.3	Intrinsic reaction rate of CO <sub>2</sub> -hydrogenation ( $r_{\text{CO}_2}$ ) and rWGs ( $r_{\text{rWGs}}$ ) simulated with the kinetic model Nestler <sub>diff</sub> as well as the efficiency factor calculated by Thiele modulus for an ideal isothermal reactor. . . . .	E
A.4	Sensitivity analysis of efficiency factor calculated using Thiele modulus . . . . .	F
A.5	Experimental data published by Park et al. [203] classified with regard to synthesis pressure, reactor temperature, GHSV COR <sub>feed</sub> and SN <sub>feed</sub> . . . . .	K
A.6	CAD drawing of the miniplant setup with its most important components [250]. . . . .	L
A.7	Measurement and simulation of the system characteristic curve of the miniplant setup at 130 °C, 200 °C and 250 °C. . . . .	M
A.8	Temperature-compensated volumetric flow rate obtained in the thermal oil cycle at constant rotational speed of the thermostat pump shaft between 130 °C and 250 °C thermal oil temperature [260]. . . . .	M
A.9	Thermophysical properties of the thermal oil used in the miniplant setup. . . . .	N
A.10	Particle size distribution of the catalyst obtained by a flotation measurement using the Laser Diffraction Particle Size Analyzer LS 13 320 by Beckman Coulter. . . . .	O
A.11	C-/H-/O- balance of the miniplant experimental points used within this study. . . . .	AB
A.12	Temperature profile at benchmark point at beginning of the experimental campaign, after 25 h, 50 h, 75 h as well as 100 h. . . . .	AC
A.13	NMR measurement of a liquid product sample. . . . .	AD
A.14	Parity plots of the refitted model "Graaf <sub>fit</sub> " for outlet molar fractions of methanol and water as well as hot spot temperature and axial hot spot position; Experiments were carried out with the miniplant setup. . . . .	AG
A.15	Parity plots of the refitted model "Bussche <sub>fit</sub> " for outlet molar fractions of methanol and water as well as hot spot temperature and axial hot spot position; Experiments were carried out with the miniplant setup. . . . .	AI
A.16	Remaining objective function with respect to Eq. 3.79 obtained for the kinetic models Bussche <sub>fit</sub> , Graaf <sub>fit</sub> and Nestler <sub>diff</sub> as well as for all possible combinations of Eq. A.89 until Eq. A.96. . . . .	AO
A.17	Sensitivity analysis of the objective function defined in Eq. 3.79 on the kinetic parameters $A_{k1}$ and $B_{k1}$ as well as $A_{k2}$ and $B_{k2}$ simulated for all experimental data points with the kinetic model Nestler <sub>fit</sub> . . . . .	AP
A.18	Sensitivity analysis of the objective function defined in Eq. 3.79 on the adsorption parameters $A_{K1}$ and $B_{K1}$ , $A_{K2}$ and $B_{K2}$ as well as $A_{K3}$ and $B_{K3}$ simulated for all experimental data points with the kinetic model Nestler <sub>fit</sub> . . . . .	AQ
A.19	Gas phase compositions obtained from the miniplant experiments and simulated using the kinetic models by Graaf [192], Bussche [145] as well as the kinetic model Nestler <sub>integ</sub> and Nestler <sub>diff</sub> . . . . .	AR
A.20	Development of the reactor's space time yield and hot spot temperature during a load reduction from GHSV = 10,000 h <sup>-1</sup> to GHSV = 4,000 h <sup>-1</sup> . . . . .	AT
A.21	Development of the reactor's temperature profile during a load reduction from GHSV = 10,000 h <sup>-1</sup> to GHSV = 4,000 h <sup>-1</sup> . . . . .	AU

A.22 Dynamic simulation campaign applying load changes as a step as well as a ramp  
within 1 s, 2 s and 5 s. . . . . AV

# List of Tables

3.1	Kinetic parameters proposed by Graaf et al. [193]. . . . .	39
3.2	Kinetic parameters proposed by Bussche et al. [145]. . . . .	40
3.3	Kinetic parameters fitted by Henkel for the Berty reactor and the micro fixed bed reactor [202]. . . . .	40
3.4	Characteristic catalyst properties for the calculation of Thiele modulus determined by Henkel [202]. . . . .	41
3.5	Design parameters of the Shiraz methanol synthesis reactor based on scientific literature [74]. . . . .	47
3.6	Design parameters determined for the miniplant setup determined by the simulation-based scale-down and experiments. . . . .	48
3.7	Dimensionless index numbers for the industrial and the miniplant reactor. . . . .	48
3.8	Parameters applied for the experimental campaign at the miniplant setup. . . . .	55
4.1	Parameters for the $Nestler_{integ}$ kinetic model proposed within this work. . . . .	61
4.2	Comparison of the RMSE for the molar fractions measured by Park and simulated using the kinetic models by Graaf, Bussche and Henkel as well as the kinetic model $Nestler_{integ}$ . . . . .	61
4.3	Parameter set varied within the sensitivity study in this section. . . . .	65
4.4	Objective function and RMSEs calculated between the experimental data and the reactor simulations using the original kinetic models by Graaf and Bussche as well as the $Nestler_{integ}$ kinetic model. . . . .	75
4.5	Objective function and RMSEs calculated between the experimental data and the reactor simulations using the fitted kinetic models. . . . .	76
4.6	Parameters for the kinetic model $Nestler_{diff}$ . . . . .	77
4.7	Comparison of the RMSE for the measured molar fractions published by Park [203] and the simulated molar fractions utilizing the kinetic models $Nestler_{integ}$ and $Nestler_{diff}$ . . . . .	80
A.1	Design parameters for steam cooled tube bundle reactors available in scientific literature. . . . .	C
A.2	Experimental data taken from Park et al. [203] that was used for the integral kinetic model $Nestler_{integ}$ . . . . .	G
A.3	Supplier and purity of the technical gases used for the miniplant experiments. . . . .	O
A.4	Chronological progress of the experimental campaign. . . . .	P
A.5	Experimental data obtained during the steady state experiments at the miniplant setup. . . . .	S
A.6	Original kinetic parameters proposed by Graaf et al. [193]. . . . .	AF
A.7	Kinetic parameters for the $Graaf_{fit}$ model obtained with the miniplant setup. . . . .	AF
A.8	Original kinetic parameters proposed by Bussche et al. [145]. . . . .	AH

A.9	Kinetic parameters for the Bussche <sub>fit</sub> model obtained with the miniplant setup. . .	AI
A.10	Kinetic parameters proposed by Park et al. [203, 261]. . . . .	AK
A.11	Kinetic parameters fitted by Henkel for the Berty reactor and the micro fixed bed reactor [202]. . . . .	AL
A.12	Fitted parameters for the Nestler <sub>integ</sub> kinetic model obtained from the measured data by Park et al. [203]. . . . .	AM
A.13	Fitted parameters for the Nestler <sub>diff</sub> kinetic model obtained from the miniplant data.	AM

# 1 Introduction

The international commitment to mitigate greenhouse gas emissions with the aim of limiting anthropogenic global warming to less than 2K has triggered political efforts to implement zero CO<sub>2</sub> emission technologies in many countries [1, 2]. As the share of renewable power production in the electric grid increases, the need for a so-called defossilization of other sectors as transportation as well as heavy industries, e.g. steel production, and chemical industry arises to further reduce carbon dioxide (CO<sub>2</sub>) emissions. The avoidance of fossil fuels in these sectors will inevitably lead to their substitution by electric energy produced with a low greenhouse gas (GHG) footprint. Nuclear accidents as the disaster of Fukushima in 2011 have forced many governments to reconsider their view on nuclear power production, creating new perspectives for renewable energy sources as solar-, wind-, biomass-, or hydropower [3]. However, as renewable energy power plants rely on natural resources with fluctuations determined by weather, daytime, seasons and location, strategies for their storage and distribution need to be examined. Hydrogen (H<sub>2</sub>) produced by water electrolysis operated with renewable energies was recently politically identified as a promising molecular platform for large-scale energy storage [4, 5].

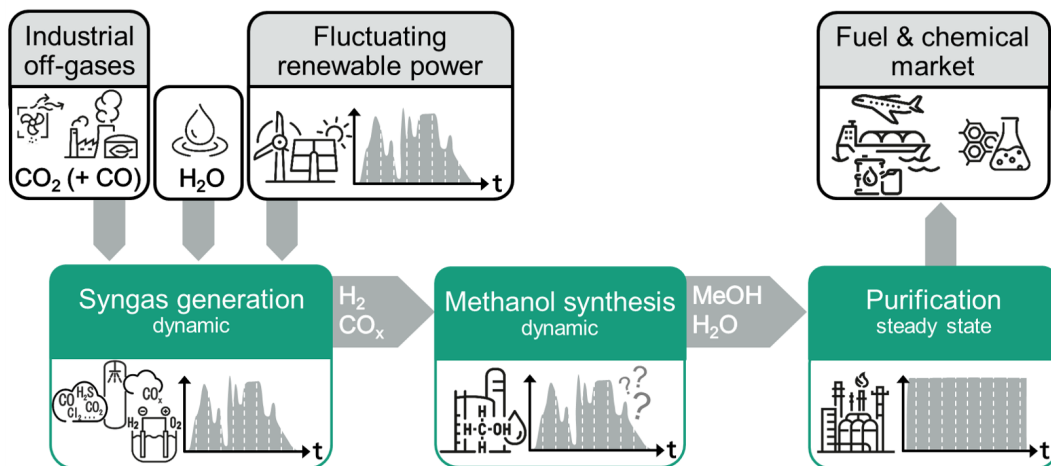


Figure 1.1: Schematic flow diagram of the Power-to-Methanol process chain.

Chemical conversion of H<sub>2</sub> to molecules with enhanced properties for handling and transportation, e.g. increased energy densities, opens manifold possibilities for H<sub>2</sub>-derived energy carriers and base chemicals. As these H<sub>2</sub> carriers vary in molecular nature, aggregate phase and physical properties, their synthesis processes are collectively referred to as "Power-to-X" (PtX) technologies [6]. Among the currently most discussed H<sub>2</sub> carrier molecules range ammonia (NH<sub>3</sub>) [7], methane (CH<sub>4</sub>) [8], light hydrocarbons, dimethyl ether (DME) as well as methanol (MeOH) [9]. Many of the chemical processes to produce these chemicals are among the oldest known to chemical industry, e.g. Sabatier (CH<sub>4</sub>), Haber-Bosch (NH<sub>3</sub>), methanol synthesis and Fischer-Tropsch (hydrocarbons) [10]. However, the transition of these processes currently operated with fossil energy carriers towards sustainable feedstocks supplied by renewable energy and off-gases from

industrial processes demands for manifold research activities.

Among possible PtX products, methanol is one of the most promising candidates for a technological application as the synthesis is operated at moderate process conditions, it is a liquid at ambient conditions and provides access to a worldwide trade infrastructure related to the fuel and chemical market [10, 11]. Besides economical barriers due to the comparably high production costs for electrolytic  $H_2$  [12, 13] and the low prices for fossil feedstocks, some technological challenges prevent so-called "Power-to-Methanol" (PtM) processes from their industrial implementation [14]. Today methanol is commercially produced from carbon monoxide (CO)-rich synthesis gas (syngas) derived from gasification of coal or heavy oil residues as well as reforming of natural gas. Opposed to that, sustainable methanol synthesis is based on electrolytic  $H_2$  and  $CO_2$  captured from industrial processes, biomass fermentation or from the air. High  $CO_2$  contents are known to negatively affect the reaction kinetics, the chemical equilibrium as well as catalyst lifetime in methanol synthesis. Moreover, fluctuations in syngas quality and/or quantity caused by intermittent availability of renewable power or load changes in the coupled  $CO_2$  supplying process are unknown to state-of-the-art methanol processes, conventionally operated at steady state (compare Fig. 1.1). The usage of gas buffer tanks would be an option to prevent dynamic load changes in the syngas generation from breaking through to the stationary operated methanol synthesis process. However, the extensive application of buffer tanks was shown to be economically detrimental [15]. Dynamic operation of the methanol synthesis process could be feasible, though, for this option a better understanding of the behavior of the synthesis reactor under transient load conditions is necessary.

This work aims to contribute to the technological implementation of PtM processes from  $CO_2$ -rich gas streams under steady state and dynamic load conditions. To obtain in-depth insights into the kinetic behavior of a dynamically operated synthesis reactor, an experimental miniplant setup featuring a highly resolved axial temperature measurement was designed, built and operated within this work with the aim to reflect the thermochemical conditions in an industrial scale reactor. Based on the comprehensive set of steady state experimental data obtained from this setup an enhanced differential kinetic model was derived. Comparison of this model to an integral kinetic model derived from an isothermal fixed bed reactor for a similar catalyst as well as towards important scientific literature standard kinetic models was executed to demonstrate the significance of this work. Finally, the differential kinetic model derived under steady state conditions was integrated into a dynamic simulation model and validated against data from a representative load change experiment on the miniplant setup.



## 2 Literature Review and Scientific Approach

Patented in 1923, methanol synthesis is one of the oldest thermochemical high pressure processes [14]. In order to maximize catalyst selectivity and productivity, methanol synthesis was subject of numerous scientific studies in the past century [10, 11, 16]. The long scientific and industrial history of the process shows the necessity of a comprehensive literature survey to identify the scientific potential and ensure the novelty of the herein conducted work.

The composition of the make-up gas (MUG) fed into the process emerges as one main difference between conventional and renewable methanol synthesis. Therefore, a technological overview presenting key indicators for the gas composition will be provided in Sec. 2.2. These key indicators are then applied to the most important feedstocks from conventional and renewable sources in Sec. 2.3.

As a strong feedback between research in methanol synthesis and the technological application exists, Sec. 2.4 will deal with the current state-of-the-art in methanol synthesis technology – practical limitations caused by chemical equilibrium and the narrow thermal operational window of methanol synthesis are related to process and reactor scale. This discussion finally leads to a discrimination of different reactor types for dynamic operation of methanol synthesis.

As the kinetic modeling was identified one key-challenge for the simulative description of methanol synthesis, state-of-science in reaction kinetics and the validation of kinetic models in methanol syntheses will be presented in Sec. 2.5. The overall scientific approach of this work is then summarized in Sec. 2.6.

### 2.1 Significance of methanol as a commodity chemical

With an annual consumption of 105 Mt estimated for 2019 [17], methanol is after ammonia (182 Mt a<sup>-1</sup> [18]) and ethylene (160 Mt a<sup>-1</sup> [19]) one of the most important base chemicals on the world market.

In Fig. 2.1 the development of world-wide methanol production is given divided by sectors according to a study published by IHS Markit [20]. In this graph, traditional derivatives are mainly considered formaldehyde and acetic acid, while fuels are regarded as dimethyl ether (DME), methyl tert-butyl ether (MTBE) as well as direct blend in gasoline [20]. The trends of both fuel market and traditional derivatives show a steady increase over time. From 2012 the application of so-called methanol-to-olefin (MTO) and methanol-to-propylene (MTP) processes started developing a significant share in methanol consumption [17]. These processes are operated with the goal of producing ethylene and propylene from coal-based methanol instead of mineral oil and natural gas. Similar to the application of methanol in the fuel sector, this development was mainly driven by China with the aim of substituting mineral oil by local coal and lignite reserves.

Independently of the utilization chain, methanol production was responsible for 7.2% of the green house gas (GHG) emission of the chemical industry in 2010, with an average cradle-to-gate GHG

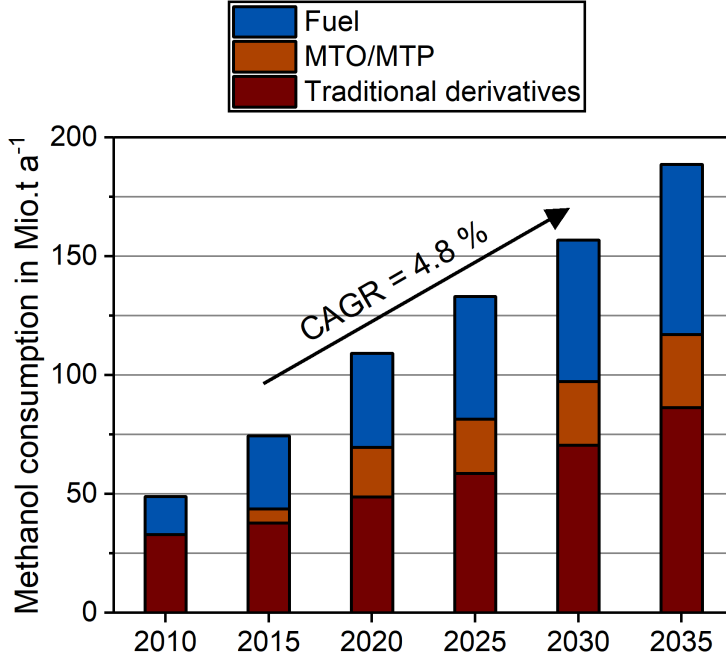
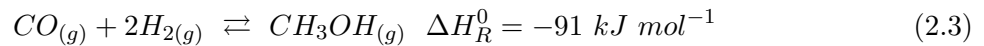
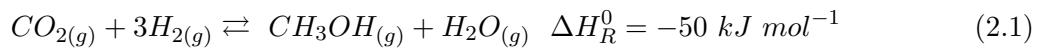


Figure 2.1: Worldwide consumption of methanol divided by the sectors fuel, methanol-to-olefin (MTO)/methanol-to-propylene (MTP) and traditional derivatives [17, 20].

footprint of  $1.55 \text{ t}_{\text{CO}_2, \text{eq}} \text{ t}_{\text{MeOH}}^{-1}$  [21]. Transfer of this footprint to the  $\text{CO}_2$  emissions and methanol production in 2019, makes methanol production responsible for approximately 0.4% of the global GHG emissions [22]. These numbers emphasize the necessity for carbon-neutral technologies for methanol production in the future. The use of  $\text{CO}_2$  captured from industry off-gases, e.g. the cement or steel industry as well as biomass processing or direct air capture (DAC) could deliver  $\text{CO}_2$ -neutral or even negative possibilities for methanol production.  $\text{H}_2$  production by water electrolysis operated with renewable energy or by methane pyrolysis were identified as sustainable pathways for  $\text{H}_2$  production [15, 23, 24]. The main differences in gas composition and supply of these sustainable feedstocks compared to their conventional counterpart will be elaborated in the following sections.

## 2.2 Properties of the synthesis gas for methanol synthesis

Methanol synthesis on commercial  $\text{Cu}/\text{ZnO}/\text{Al}_2\text{O}_3$  catalysts is macroscopically observed via the following equilibrium-limited exothermal reactions including  $\text{CO}_2$ -hydrogenation (Eq. 2.1), water-gas-shift (WGS) (Eq. 2.2) and  $\text{CO}$ -hydrogenation (Eq. 2.3) [25]:



Radiolabeling studies by several research groups proved that methanol mainly originates from CO<sub>2</sub>-hydrogenation, whereas the direct hydrogenation of CO does scarcely proceed [26, 27]. Hence, CO conversion towards methanol can be considered as WGS with subsequent CO<sub>2</sub>-hydrogenation [28, 29]. However, the interplay between CO and CO<sub>2</sub> in methanol synthesis is even today a controversial topic in the scientific community [14].

The quality of the synthesis gas (syngas) plays an important role in the design of both, methanol synthesis processes and reactors. The following four main factors can be considered concerning syngas composition.

### 2.2.1 Carbon oxide ratio

The methanol synthesis process can be designed for different ratios of the molar fractions of CO<sub>2</sub> ( $y_{CO_2}$ ) and CO ( $y_{CO}$ ) in the syngas. The carbon oxide ratio (COR) is defined as follows [30–33]:

$$COR = \frac{y_{CO_2}}{y_{CO_2} + y_{CO}} \quad (2.4)$$

Based on the reaction enthalpies of Eq. (1) and (3), the overall temperature rise in the reactor decreases with increasing COR. As an equimolar amount of H<sub>2</sub>O is produced during the conversion of CO<sub>2</sub>, H<sub>2</sub>-consumption of methanol synthesis increases with COR. Several research groups observed that an increased H<sub>2</sub>O content in the reactor enhances deactivation of the catalyst and decreases catalyst activity [32, 34–37]. For these reasons COR is kept as low as possible in conventional applications.

However, as the direct hydrogenation of CO does scarcely occur on commercial catalysts, a certain amount of CO<sub>2</sub> (or water) needs to be present in the reactor feed to enable the WGS reaction and, thus, CO conversion to methanol on Cu/ZnO/Al<sub>2</sub>O<sub>3</sub> catalysts [30, 31, 34, 38–41]. A maximum methanol formation rate was experimentally observed by various researchers at a CO<sub>2</sub> mole fraction of approximately 2 mol.-% in the reactor feed [28, 30, 31, 38, 42–48]. With a further increase in CO<sub>2</sub> content, the reaction rate of the methanol synthesis is known to decelerate and the equilibrium yield decreases [49, 50]. The distribution and amount of side-products is also known to depend on the COR - typically more carbonaceous side-products are formed with decreasing COR [35, 51, 52].

### 2.2.2 Stoichiometric number

As the conversion of CO and CO<sub>2</sub> to methanol demand for different molar ratios of H<sub>2</sub>, a measure of the stoichiometry, the stoichiometric number (SN), is defined by the molar fractions of H<sub>2</sub> ( $y_{H_2}$ ), CO and CO<sub>2</sub> in the syngas [53]:

$$SN = \frac{y_{H_2} - y_{CO_2}}{y_{CO} + y_{CO_2}} \quad (2.5)$$

For a stoichiometric conversion SN = 2 is necessary. Most methanol synthesis processes are known to operate at slightly increased H<sub>2</sub> content [11, 54]. Nevertheless some processes employ an excess of H<sub>2</sub> with SN ≤ 3 (see Sec. 2.3.2). A high stoichiometric number can be lowered via the addition

of CO or CO<sub>2</sub>, providing room for a capacity revamp.  $SN < 2$  should be avoided, as a H<sub>2</sub> shortage in the syngas is known to promote the formation of undesired byproducts [10, 55].

### 2.2.3 Inert gas fraction

Inert gases are components that do not contribute to the synthesis reactions. Thus, their effect on process design is limited to a dilution, in turn lowering the partial pressures of the reactants. On the other hand, the presence of inert gases can be useful to lower the temperature rise in the reactor. A high inert gas fraction in the syngas leads to an accumulation of inert components in the recycle loop of a methanol synthesis process (see Sec. 2.4.2), which has to be compensated by either increasing the recycle ratio or the purge fraction, in turn negatively influencing overall process economics [56, 57]. Therefore, the inert gas content in the syngas should be kept as low as possible in order to minimize methanol production costs [58]. Common inert gases in the methanol process are nitrogen (N<sub>2</sub>) and methane (CH<sub>4</sub>), but also argon (Ar) or helium (He).

### 2.2.4 Impurities

In contrast to inert components, impurities in this work are referred to as all species originating from the feedstock and influencing the synthesis reaction, i.e. without being a main reactant. Most impurities have an inhibiting or deactivating effect on the catalyst, e.g. sulfur or chlorine [34, 59–61]. Other than that, unwanted side-product formation can occur, for example the presence of NH<sub>3</sub> is known to result in the formation of trimethylamine, decreasing the product value due to its characteristic odor [62]. Specific countermeasures can be taken to cope with impurities, such as an enhanced upstream gas cleaning, a more complex downstream distillation unit or a higher catalyst volume in the reactor.

## 2.3 Feedstocks used for methanol synthesis

Methanol synthesis is today almost exclusively based on fossil feedstocks such as coal, crude oil and natural gas (NG). Despite growing coal-to-methanol capacities in China, 55 % of the total installed production capacity is based on NG [63]. Independently of source, fossil feedstocks must firstly be converted into syngas via a gas generation process. Carbon-containing compounds, such as elemental carbon, CH<sub>4</sub> and higher hydrocarbons, need to be converted to CO, CO<sub>2</sub> and H<sub>2</sub>. The two main technologies used for syngas generation are gasification and reforming, see references [11, 57, 58, 64–66] for further details. This section continues with an overview on feedstocks used for methanol synthesis, highlighting the respective properties of the generated syngas.

### 2.3.1 Coal, biomass and refinery residues

There are numerous solid and liquid feedstocks that are commonly used to prepare an appropriate syngas for the methanol synthesis [11, 66]. Among them are fossil products of natural coalification processes, including peat, lignite, bituminous coal through to anthracite - these are all typically gasified. Most residues from crude oil, like heavy oils, naphtha or liquefied petroleum gas (LPG)

can either be gasified or reformed. Due to limited local availability and chemical heterogeneity, gasification of (municipal) waste and biomass can only be seen as a minor source for the production of methanol. However, benefits of their utilization are the potential mitigation of greenhouse gases and, in the case of waste, reduction of hazards associated with emittance to the natural environment [67].

All feedstocks differ in their chemical composition and impurity content. Accordingly, numerous technologies for syngas generation are existing on current-state-of-the-art, also with respect to gasification schemes [52, 68, 69]. Through natural carbonization, the amount of fixed carbon increases, whereas volatile compounds, especially bound  $H_2$  and oxygen ( $O_2$ ), are decreased [52]. As a result, the produced syngas is sub-stoichiometric for methanol synthesis [66]. Hence, in order to adjust SN to the correct level,  $H_2$  can either be added or the carbon oxide content can be decreased by shifting CO (Eq. 2.2) and subsequently removing surplus  $CO_2$  [52]. Typical syngas from coal gasifiers has an inert gas fraction between 0.5 % and 6 %, predominantly of  $CH_4$  [52, 66, 69].

Most syngases originating from biomass or fossil carbonization products typically contain many organic and inorganic impurities, making a comprehensive gas cleaning necessary [11, 52]. The main advantage of coal gasification processes is the inexpensive feedstock price compared to NG. As it is well distributed in the world, it is also geopolitically more independent, but entails drawbacks like significantly higher  $CO_2$  emissions arising from gas conditioning and elevated investment costs compared to a NG-based synthesis process [10, 57, 70].

### 2.3.2 Natural gas

NG contains light hydrocarbons, mainly  $CH_4$ , inert components (e.g.  $N_2$ ) and impurities, such as sulfur-containing compounds or He. Besides ongoing efforts to develop methods for direct selective oxidation of  $CH_4$  to methanol [71, 72], in commercial processes hydrocarbons are (catalytically) reformed into syngas. Steam methane reforming (SMR) is the most established route for NG-based feedstocks [14]. However, there are also routes utilizing  $CO_2$  such as dry reforming and bi-reforming [73]. Syngas produced by SMR usually contains excess  $H_2$  ( $2.5 \leq SN \leq 3.0$ ) [57, 64, 74]. External  $CO_2$  can therefore be added to increase methanol capacity [58]. Steam reforming of higher hydrocarbons, however, can result in a  $H_2$ -shortage.

The inert gas content of the syngas is determined by the  $N_2$  content of NG and the  $CH_4$  slip of the SMR reaction, with a value of 3 % to 5 % considered typically. As NG contains fewer impurities and is easier to handle than solid feedstocks, the gas cleaning is simplified compared to gasification processes. With the development of new reforming technologies, such as partial oxidation (POx) [58], autothermal reforming (ATR) [75, 76] and combined reforming [64], the reaction conditions have been increasingly optimized for the reforming reaction, resulting in a significant decrease of the  $CH_4$  content in the syngas. These technologies also provide the possibility to adjust stoichiometry to the perfect level for methanol synthesis [58].

### 2.3.3 Alternative feedstocks

Qin et al. have calculated a CO<sub>2</sub>-equivalent of 2.97 t<sub>CO<sub>2</sub>,eq</sub> t<sub>MeOH</sub><sup>-1</sup> based on a cradle-to-gate life cycle assessment (LCA) of a coal-based methanol production plant in China [77]. For a NG-based process the according CO<sub>2</sub>-equivalent accounts to 0.85 t<sub>CO<sub>2</sub>,eq</sub> t<sub>MeOH</sub><sup>-1</sup> [6]. In comparison, the direct hydrogenation of captured CO<sub>2</sub> to produce methanol, i.e. based on renewable electricity driven H<sub>2</sub>O electrolysis - commonly referred to as "Power-to-Methanol" (PtM), has been reported to have a CO<sub>2</sub>-equivalent of -0.67 t<sub>CO<sub>2</sub>,eq</sub> t<sub>MeOH</sub><sup>-1</sup> [6]. This implicates possible carbon emission savings of 1.52 t<sub>CO<sub>2</sub>,eq</sub> t<sub>MeOH</sub><sup>-1</sup> of PtM-based methanol in comparison to NG-based methanol showing the sensitivity of methanol pricing towards political regulations such as CO<sub>2</sub> taxation and trading systems [6, 15, 78].

The debate regarding the use and implementation of sustainable feedstocks and CO<sub>2</sub>-neutral processes for methanol synthesis arrived in the scientific community in the early 90s via contributions from both academic and industrial research groups [79–84]. As a consequence, new feedstocks are under discussion in order to find methanol synthesis concepts with increasingly lower carbon footprints. The following two sections introduce two types of alternative feedstocks: CO<sub>2</sub> point sources as e.g. cement production, biogas plants or DAC, and carbon oxide (CO<sub>x</sub>)-rich industrial off-gases that may arise from existing industrial processes, e.g. steel industry.

#### 2.3.3.1 CO<sub>2</sub>-based feedstocks

CO<sub>2</sub>-rich gas streams can be captured from industrial processes such as the chemical, steel or cement industry as well as combustion-based power plants [6]. Demonstration facilities at the small and industrial scale have led to enhanced knowledge concerning the advantages and drawbacks of CO<sub>2</sub>-based methanol synthesis [81, 84–92].

A benefit of a CO<sub>2</sub>-rich syngas for methanol synthesis is the lower heat duty emerging from CO<sub>2</sub>-hydrogenation enabling less complex cooling concepts for the reactor. Another advantage compared to conventional processes is the lower catalyst selectivity towards hydrocarbon side-products, e.g. ketones, leading to lower costs in product purification [81, 84, 91, 93–95]. The main drawbacks of the CO<sub>2</sub>-based methanol synthesis arise from an increased H<sub>2</sub> consumption due to the formation of H<sub>2</sub>O leading to an increased catalyst deactivation and efficiency losses of the process chain [37, 81, 91, 96].

Besides catalyst research, industrial process solutions were developed allowing handling of CO<sub>2</sub>-rich syngas [28, 79, 84, 97, 98]. While some processes directly hydrogenate CO<sub>2</sub> to methanol [91], most of CO<sub>2</sub>-based process concepts condition the CO<sub>2</sub>-rich syngas by shifting CO<sub>2</sub> to CO via reverse WGS chemistry, e.g. the so-called CAMERE process [12, 83, 86, 99]. A process concept proposed and indeed realized at a near industrial scale by Carbon Recycling International (CRI), also considers the option of a reverse WGS reactor to increase the CO content in the syngas [100]. The inert gas fraction for CO<sub>2</sub>-based processes is almost zero if an appropriate CO<sub>2</sub> removal is used in CO<sub>2</sub> capture. However, even with optimized process solutions the disadvantage of an elevated H<sub>2</sub> consumption persists [11]. This reinforces concerns linked to a sustainable H<sub>2</sub> supply which is known to be one of the core issues regarding future methanol synthesis [10, 87, 101].

## 2.3.3.2 Steel Mill Gases

Compared to carbon capture and utilization (CCU) schemes based on CO<sub>2</sub>-rich syngases, gas sources with an elevated CO content decrease water content in the reaction product and therefore increase the overall process efficiency. Promising options in this context are gases emerging from steel mill processes [6]. The steelmaking industry has the potential to provide large volume gas streams containing H<sub>2</sub>, CO and CO<sub>2</sub> over the blast furnace route schematically depicted in Fig. 2.2. As such, a number of research initiatives aim to utilize steel mill gases for synthesis processes in order to decrease overall GHG emissions [102–105]. Other routes for steel production with H<sub>2</sub> as reducing agent and electric arc furnaces are proposed by industry, but will not be further discussed within this work [106–108]. As the steel industry accounts for approximately 6.7% of all global CO<sub>2</sub> emissions [109] (1.9 tCO<sub>2,eq</sub> tSteel<sup>-1</sup> are emitted on average through steel production [110]), it is reasonable to utilize "waste" process gases.

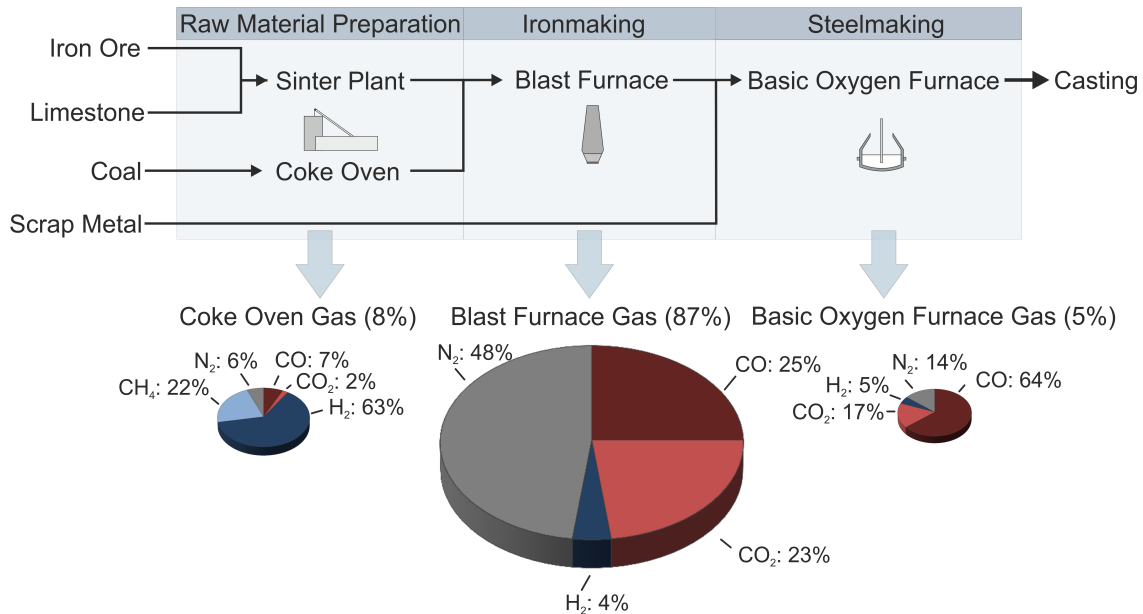


Figure 2.2: Gas composition of steel mill gas streams according to [111, 112]; Values in brackets show fraction of the total volumetric gas stream emitted from the steel mill.

The compositions of three main types of steel mill gases, i.e. blast furnace gas (BFG), coke oven gas (COG) and basic oxygen furnace gas (BOFG), are provided in Fig. 2.2 [111]. With a fraction of approximately 87% of the total volume of all gases, BFG is the predominant gas stream [112]. However, this gas stream has an inert gas fraction of approx. 50%, in this case N<sub>2</sub> [105, 113, 114]. BOFG and COG have smaller inert gas contents, but cover only a small percentage of the total volume of all gas streams. Due to a high H<sub>2</sub> content, COG can be considered as a H<sub>2</sub> source [115–117] that can also be transferred to commercial syngas by conventional reforming technologies [116, 118–122]. BOFG and BFG are both poor in H<sub>2</sub> (BFG: SN ≈ -0.40 and BOFG: SN ≈ -0.15) and therefore require additional H<sub>2</sub> to establish the correct SN. Another possibility of BFG utilization is the removal of CO<sub>2</sub>. In this case pure CO<sub>2</sub> is obtained and can therefore be processed with respect to Sec. 2.3.3.1.

Research projects concerning the utilization of steel mill gases are currently being funded in Europe, where reduction and recycling of CO<sub>2</sub> are major political goals, e.g. as supported by national initiatives [123], creating new challenges for energy-intensive industries. One project initiated in this context by the European Union through the FP8/Horizon2020 "SPIRE" program is FReSMe, which is the follow-on of the previously funded MefCO<sub>2</sub> and STEPWISE projects [102, 124, 125]. It focuses on CO<sub>2</sub> capture and methanol synthesis at a Swedish steel mill. A comparable project funded by the German ministry of research and education (BMBF) is Carbon2Chem<sup>®</sup> [105]. This initiative aims to utilize steel mill gases in order to produce methanol, but also higher hydrocarbons, ammonia, urea and polymers in a cross industrial or "sector coupling" network. The project collaborations Carbon2Value and Steeanol set a focus on Fisher-Tropsch synthesis and fermentation processes from steel mill gases [103, 104].

### 2.3.4 Classification of make-up-gases

Fig. 2.3 categorizes the estimated composition of conventional and alternative syngases conditioned for methanol synthesis by means of COR and inert gas fraction [66, 126, 127]. For the conventional

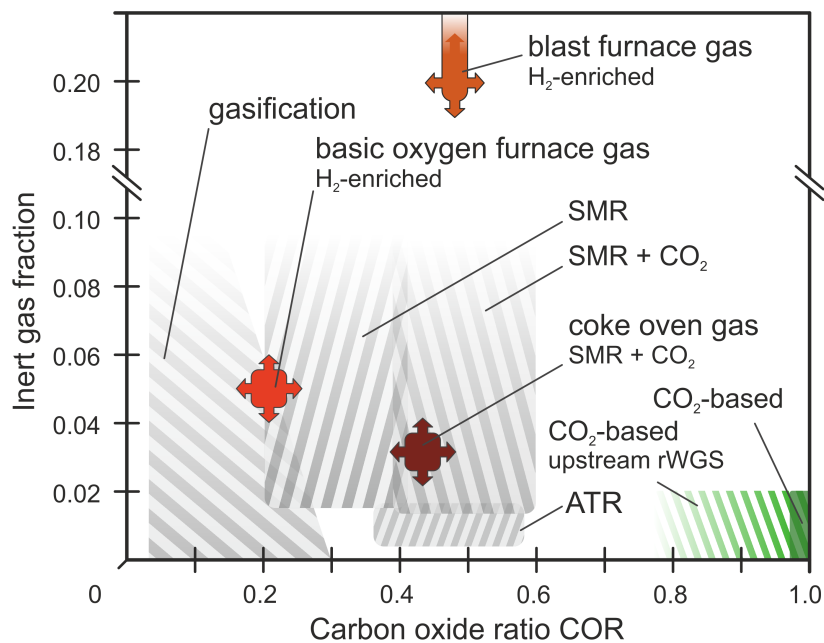


Figure 2.3: Comparison of the estimated inert gas content and COR of syngas obtained from conventional and alternative feedstocks conditioned for methanol synthesis [52, 66, 111, 112, 126, 127]; Arrows indicate fluctuations in gas composition.

syngas generation processes like gasification or reforming, wide ranges were defined in the diagram, as the inert gas fraction as well as COR strongly depend on the composition of the feedstock used. In case of the steel mill gases, SN was adapted to  $SN = 2.1$ . As the design of methanol synthesis process mainly depends on syngas composition, even different feedstocks can lead to the same design, if comparable syngas compositions are available. Therefore Fig. 2.3 is capable of showing whether new feedstocks either result in the elaboration of completely new synthesis processes or only in the slight adaptation of existing processes. This simplifies the selection of

synthesis loop parameters and helps to categorize different syngas compositions.

As mentioned in Sec. 2.3.3.2, the steel mill gases can be processed by a WGS unit with subsequent N<sub>2</sub>-removal in order to decrease the inert gas content. This option is especially promising for the blast furnace gas representing the biggest share of steel mill gases (87%). In this case, the processed synthesis gases from the steel mill would be assigned CO<sub>2</sub>-based in Fig. 2.3. However, with regard to CO<sub>2</sub>-rich synthesis gases in methanol synthesis many open questions arise at current-state-of-science with regard to reaction kinetics, catalyst deactivation and dynamic operation [14]. Therefore, this work will focus on gas compositions at high COR without inert gas.

## 2.4 Technological overview on methanol synthesis

As a measure to assess the quality of methanol synthesis in a technical process or reactor, some basic key indicators must be defined:

1. The carbon conversion  $X_C$  can be used as a measure of the molar quantity of CO<sub>x</sub> reacted towards methanol related to the molar quantity of CO<sub>x</sub> in the feed. In a continuous reactor it is defined via the molar flow entering  $\dot{n}_{j,in}$  and the molar flow leaving the reactor  $\dot{n}_{j,out}$  as follows:

$$X_C = \frac{(\dot{n}_{CO,in} + \dot{n}_{CO_2,in}) - (\dot{n}_{CO,out} + \dot{n}_{CO_2,out})}{\dot{n}_{CO,in} + \dot{n}_{CO_2,in}} \quad (2.6)$$

2. The carbon yield  $Y_C$  relates the amount of the desired product towards the maximum possible amount of product with regard to the stoichiometry of the educts. Related to CO and CO<sub>2</sub> present in the feed gas, the carbon yield can be defined as follows:

$$Y_C = \frac{\dot{n}_{MeOH,out}}{\dot{n}_{CO,in} + \dot{n}_{CO_2,in}} \quad (2.7)$$

3. Methanol selectivity  $S_{MeOH}$  represents the degree of the formation of the desired product among all products formed. In case of methanol synthesis, selectivity with regard to carbon is defined as follows:

$$S_{MeOH} = \frac{\dot{n}_{MeOH,out}}{(\dot{n}_{CO,in} + \dot{n}_{CO_2,in}) - (\dot{n}_{CO,out} + \dot{n}_{CO_2,out})} \quad (2.8)$$

4. The space-time-yield  $STY$  is defined as the mass flow of product formed over time related to the volume of the catalyst bed inside the reactor  $V_{cat}$ . Therefore it can be used as a measure of productivity influenced by reaction kinetics and operating conditions. For methanol synthesis is defined as follows [11]:

$$STY = \frac{\dot{n}_{MeOH,out} \cdot M_{MeOH}}{V_{cat}} \quad (2.9)$$

### 2.4.1 Reaction conditions and equilibrium

Due to the exothermic and mole-decreasing nature of methanol synthesis from CO and CO<sub>2</sub>, the equilibrium of these reactions is positively affected by low temperatures and high pressures

(compare Eq. 2.1 and Eq. 2.3). Equilibrium constant  $K_{eq}$  at a temperature  $T$  can be calculated using the following equation including the change of Gibbs free energy  $\Delta G^0$  caused by the reaction at the respective temperature [128]:

$$\ln(K_{eq}(T)) = -\frac{\Delta G^0(T)}{R \cdot T} \quad (2.10)$$

To obtain an accurate description of the equilibrium of methanol synthesis, many studies were conducted by the scientific community providing a set of equilibrium constants [128–132].

In Eq. 2.10,  $\Delta G^0(T)$  is calculated based on the change of Gibbs free energy at reference conditions  $\Delta G^0(T_{ref})$ . Given the exact value for  $\Delta G^0(T_{ref})$  and the temperature dependent change in heat capacity,  $\Delta G^0(T)$  can be calculated by the change in enthalpy  $\Delta H^0(T)$  applying the Kirchhoff equation [133, 134]:

$$\frac{-\Delta G^0(T)}{T} = \frac{-\Delta G^0(T_{ref})}{T_{ref}} + \int_{T_{ref}}^T \frac{\Delta H^0(T)}{T^2} dT \quad (2.11)$$

$$\Delta H^0(T) = \Delta H^0(T_{ref}) + \int_{T_{ref}}^T \Delta \tilde{c}_p^0(T) dT \quad (2.12)$$

However, by a sensitivity analysis comparing different literature values of  $\Delta G^0(T_{ref})$  for methanol, Graaf and Winkelmann found that already small changes in this parameter largely influence the equilibrium constant of methanol synthesis [129]. Based on this analysis, the authors determined a semi-empirical set of parameters to calculate the equilibrium constant based on experimental equilibrium data published in scientific literature. The experimental data the authors considered cover the temperature range between 200 °C and 1000 °C as well as pressures between 0 bar and 294 bar. The parameters  $a_1$  to  $a_7$  were provided for CO-hydrogenation ( $K_{eq,CO}$ ) and rWGS ( $K_{eq,rWGS}$ ) for the following equation:

$$\ln(K_{eq}(T)) = \frac{1}{R \cdot T} \cdot \left( a_1 + a_2 \cdot T + a_3 \cdot T^2 + a_4 \cdot T^3 + a_5 \cdot T^4 + a_6 \cdot T^5 + a_7 \cdot T \cdot \ln(T) \right) \quad (2.13)$$

The equilibrium constant of CO<sub>2</sub>-hydrogenation ( $K_{eq,CO_2}$ ) can be calculated by the following correlation [129]:

$$K_{eq,CO_2} = K_{eq,CO} \cdot K_{eq,rWGS} \quad (2.14)$$

Details on the derivation of Eq. 2.13 are provided in Appendix A.1 of this work [129, 133]. The work published by Graaf and Winkelmann in 2016 contains the most recent and comprehensive parameter set for the calculation of the equilibrium constants  $K_{eq,CO_2}$  and  $K_{eq,rWGS}$  [129]. Therefore, the values published within their study will be used throughout this work. From these equilibrium constants chemical equilibrium composition can be calculated iteratively varying the fugacities  $f_j$  of the reactants to fulfill the following criteria [128]:

$$0 \stackrel{!}{=} K_{eq,CO_2} - \left( \frac{f_{MeOH} \cdot f_{H_2O}}{f_{CO_2} \cdot f_{H_2}^3} \right)_{eq} \quad (2.15)$$

$$0 \stackrel{!}{=} K_{eq,rWGS} - \left( \frac{f_{CO} \cdot f_{H_2O}}{f_{CO_2} \cdot f_{H_2}} \right)_{eq} \quad (2.16)$$

In these equations the fugacities  $f_j$  at equilibrium conditions are calculated using the equation of state (EoS) by Soave, Redlich and Kwong (SRK) [128, 129, 135, 136]. Equilibrium composition can be obtained by varying the reaction progress coefficient of CO<sub>2</sub>-hydrogenation  $\zeta_1$  and rWGS  $\zeta_2$  applying a molar balance for the reactants H<sub>2</sub>, CO, CO<sub>2</sub>, MeOH and H<sub>2</sub>O:

$$\dot{n}_{CO,eq} = \dot{n}_{CO,in} + \zeta_2 \quad (2.17)$$

$$\dot{n}_{CO_2,eq} = \dot{n}_{CO_2,in} - \zeta_1 - \zeta_2 \quad (2.18)$$

$$\dot{n}_{H_2,eq} = \dot{n}_{H_2,in} - 3 \cdot \zeta_1 - \zeta_2 \quad (2.19)$$

$$\dot{n}_{MeOH,eq} = \dot{n}_{MeOH,in} + \zeta_1 \quad (2.20)$$

$$\dot{n}_{H_2O,eq} = \dot{n}_{H_2O,in} + \zeta_1 + \zeta_2 \quad (2.21)$$

In Fig. 2.4 the carbon yield of methanol at chemical equilibrium was calculated for gas compositions in the range of  $0.0 \leq COR \leq 1.0$  at SN = 2.0 (A, D) and SN = 4.0 (B, E). To show the influence of inert gas on chemical equilibrium of methanol synthesis, a N<sub>2</sub> content of 40% was applied in Fig. 2.4 (C) and (F) at SN = 4.0. Temperature was varied between  $180^\circ\text{C} \leq T \leq 340^\circ\text{C}$  at the two

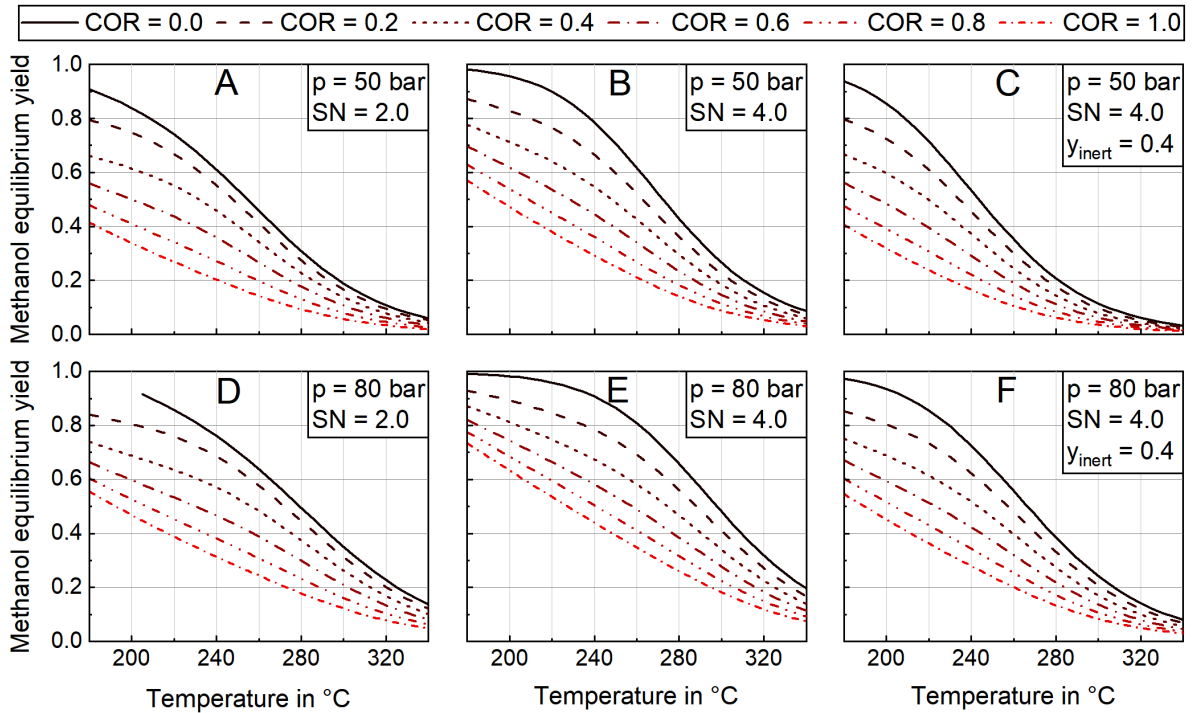


Figure 2.4: Carbon yield of methanol at equilibrium over temperature calculated utilizing the equilibrium constants as published by Graaf and Winkelman [129]; Simulation parameters:  $0.0 < COR < 1.0$ ; SN = 2.0 (A, D), SN = 4.0 (B, E) and SN = 4.0 at  $y_{inert} = 0.4$  (C, F);  $p = 50$  bar (A, B, C) and 80 bar (D, E, F).

pressure levels of 50 bar (A, B, C) and 80 bar (D, E, F). The graphs indicate a strong correlation between synthesis pressure and temperature towards the formation of methanol. Overall, the simulation results are in line with Le Chatelier's principle. While an increase in temperature decreases equilibrium conversion towards methanol, an increase of pressure shifts equilibrium further to the side of the products.

Moreover, a strong correlation between COR and the equilibrium methanol yield can be identified from Fig. 2.4. While at  $COR = 0.0$  the yield approaches a value of 1.0 at low temperature, significantly lower yields are obtained when COR is increased to 1.0. Due to the stoichiometric factor of  $H_2$ , an increase of SN leads to growing methanol yields. In case of an increased inert gases content, the fugacity of the reactants decreases. Therefore, lower equilibrium yields are obtained for syngas with high inert gas content. Overall, some boundary conditions can be defined for methanol synthesis from the analysis of the chemical equilibrium [96]:

1. High pressures and low temperatures are beneficial for the equilibrium conversion towards methanol.
2. Low  $CO_2$  contents shift chemical equilibrium to the side of methanol. Consequently high CO contents in the syngas are desirable.
3. As inert gas decreases equilibrium yield, low inert gas contents are preferable.

#### 2.4.2 Synthesis process

Due to continuous improvements in syngas cleaning technology, Imperial Chemical Industries (ICI, today Nouryon) in 1966 patented a process for the so-called "low pressure" methanol synthesis as it is known today [137]. Higher purities with sulfur contents below 1 ppmw in the synthesis gas enabled the application of  $Cu/Zn/Al_2O_3$  catalysts instead of the formerly applied  $ZnO/Cr_2O_3$  catalyst, which was known to be more robust against sulfur poisoning [16]. Due to its enhanced activity, the more active Cu-catalyst could be industrially applied at temperatures below  $300^\circ C$ . As shown in Sec. 2.4.1, lower temperatures are beneficial for the equilibrium conversion of methanol. Consequently, synthesis pressure of methanol synthesis could be lowered from pressures exceeding 250 bar to below 100 bar when the  $Cu/Zn/Al_2O_3$  catalyst was applied [10, 137]. Even though, the catalyst was modified by numerous companies [138] and researchers, modern commercial catalysts are still based on the catalytic system proposed by ICI in 1966 [14]. Due to the equilibrium limitation shown in Fig. 2.4, today's industrial methanol synthesis is carried out at elevated pressures between 50 bar and 80 bar [14]. Due to the fact that low temperatures do positively affect the equilibrium conversion towards methanol, low temperatures would be beneficial for the synthesis from a thermodynamic point of view. However, state-of-the-art catalysts need to be operated within a temperature range between  $200^\circ C$  and  $280^\circ C$ . On the one hand, temperatures below this operating window lead to inapplicable reaction kinetics for industrial processes. On the other hand, the catalyst is known to be rapidly deactivated at temperatures over  $280^\circ C$  due to thermal sintering [37]. Consequently, an accurate reactor model is obligatory when a methanol synthesis reactor is operated within an industrial process with high requirements towards catalyst stability and productivity.

Optimized methanol plants can show a high level of complexity depending on the plant man-

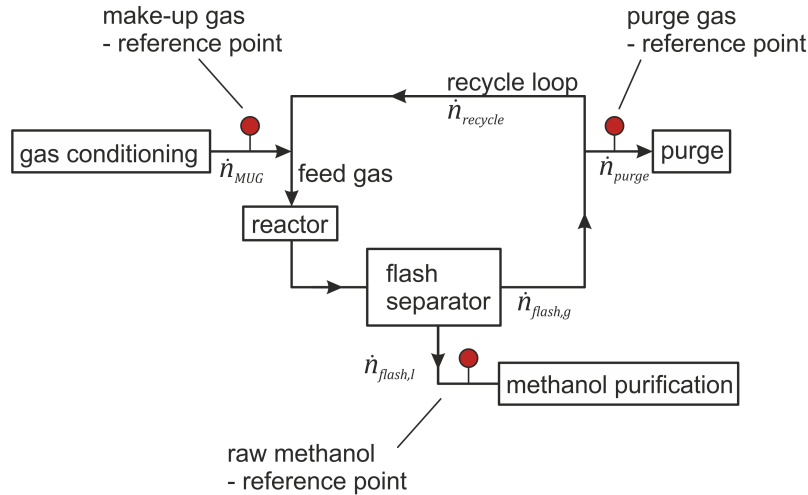


Figure 2.5: Basic scheme of a methanol synthesis process with the main components and the reference points for the calculation of  $LCE$ ,  $LHE_{int}$ , and  $LHE_{ext}$ .

ufacturer’s intellectual property and technological frame conditions as e.g. the connection to other chemical processes [139]. Focusing on the main process equipment, a basic flow scheme of a methanol synthesis loop is provided in Fig. 2.5 as a simplified, demonstrating example. The conditioned syngas enters the process as so-called make-up gas (MUG). After being compressed to synthesis pressure it is mixed with recycled gas from the process loop. This gas stream designated as reactor feed hereafter enters the methanol reactor, where the catalytic conversion according to Eq. 2.1, 2.2 and 2.3 occurs. Downstream the reactor, the product stream is cooled to temperatures between 30 °C and 40 °C to separate unreacted syngas from the liquid product. Condensed liquid raw methanol, i.e. a mixture of methanol, H<sub>2</sub>O, dissolved gases and side products, is removed from the loop in a flash separator. Non-converted gas is returned to the reactor by the recycle loop. The recycle ratio  $RR$  is defined as the ratio between recycle molar flow and MUG molar flow [140]:

$$RR = \frac{\dot{n}_{recycle}}{\dot{n}_{MUG}} \quad (2.22)$$

In order to avoid the accumulation of inert components, a small portion of the recycle gas is purged from the loop. The higher the chosen recycle ratio, the lower the amount of purge gas. The raw methanol product is sent to methanol storage and purification, typically implemented by distillation.

The properties of the syngas described in Sec. 2.2 need to be considered for the technical implementation of methanol production as a direct consequence of the feedstock used (compare Fig. 2.3). Inert components and unreacted syngas leave the process loop via the raw methanol and purge gas stream [57, 91]. Hence, an economical balance between recycle ratio and amount of purge gas has to be found for every individual scenario.

The Loop Carbon Efficiency ( $LCE$ ) indicates the ratio between carbon chemically bound in the raw methanol ( $\dot{n}_{CH_3OH,flash,l}$ ), to the overall amount of carbon oxides in the MUG, i.e. CO ( $\dot{n}_{CO,MUG}$ ) and CO<sub>2</sub> ( $\dot{n}_{CO_2,MUG}$ ) [129, 141–144]. Carbon losses are mainly caused by the purge gas stream, side-product formation and dissolved gases in the raw methanol. The  $LCE$  is

expressed by the following definition:

$$LCE [\%] = \frac{\dot{n}_{CH_3OH,flash,l}}{\dot{n}_{CO,MUG} + \dot{n}_{CO_2,MUG}} \cdot 100 \% \quad (2.23)$$

The LCE as defined in Eq. 2.23 is capable of comparing different loop designs and/or feedstocks. However, carbon efficiency can be defined accordingly at other reference points, e.g. by considering the total amount of carbon bound in the feedstock.

For processes where H<sub>2</sub> is externally generated, another parameter describing the utilization of H<sub>2</sub> concurrent to the LCE is deemed reasonable [118, 141]. However, the definition of a Loop Hydrogen Efficiency (LHE) is more complex. In addition to the above mentioned losses for LCE, it needs to be considered that H<sub>2</sub>O is formed as inevitable byproduct from CO<sub>2</sub>-hydrogenation and rWGS. There are two ways to evaluate the hydrogen efficiency:

- a) An external Loop Hydrogen Efficiency (LHE<sub>ext</sub>) balancing the amount of H<sub>2</sub> solely bound in the methanol produced relative to the amount of H<sub>2</sub> in the MUG ( $\dot{n}_{H_2,MUG}$ ):

$$LHE_{ext} [\%] = \frac{2 \cdot \dot{n}_{CH_3OH,flash,l}}{\dot{n}_{H_2,MUG}} \cdot 100 \% \quad (2.24)$$

This definition is capable of comparing processes utilizing MUG with different COR. As in case of pure CO<sub>2</sub>-feed one third of the H<sub>2</sub> introduced into the process is converted into H<sub>2</sub>O, the theoretical maximum of  $LHE_{ext}$  decreases from 100% towards 66%, when COR is increased from 0.0 towards 1.0. Consequently, gases with a high amount of CO<sub>2</sub> are less-favored with regard to this key indicator.

- b) An internal Loop Hydrogen Efficiency (LHE<sub>int</sub>) considering water in the raw methanol ( $\dot{n}_{H_2O,flash,l}$ ) as a product:

$$LHE_{int} [\%] = \frac{2 \cdot \dot{n}_{CH_3OH,flash,l} + \dot{n}_{H_2O,flash,l}}{\dot{n}_{H_2,MUG}} \cdot 100 \% \quad (2.25)$$

This definition is capable of comparing the efficiency of loop design independently of COR, equivalent to LCE.

In order to illustrate the above described key indicators, gas mixtures with varied COR are introduced into the basic process depicted in Fig. 2.5 and compared by LCE, LHE<sub>ext</sub> and LHE<sub>int</sub> in Fig. 2.6. For this simulation, loop conditions were held constant at RR = 6, T<sub>in</sub> = 230 °C and SN<sub>MUG</sub> = 2.05 at a synthesis pressure of 80 bar. As reactor type, the tubular steam raising reactor was selected with the kinetic model provided by Bussche and Froment [145]. Details on this reactor type as well as the kinetic model will be given later in this chapter, see Sec. 2.4.3 and Sec. 2.5, respectively. The process model was implemented in MATLAB<sup>®</sup> and Simulink<sup>®</sup>. Development of this model was based on prior and parallel academic studies executed within the working group [146–149].

In the process simulation LHE<sub>int</sub> and LCE show a similar, decreasing trend when COR content is increased. This can be explained by the decreased equilibrium yield as well as the slower reaction kinetics at high CO<sub>2</sub> contents. Due to the slight over-stoichiometry in the MUG, more H<sub>2</sub> is purged in comparison to CO<sub>x</sub>, leading to a lower LHE<sub>int</sub> in comparison to LCE. As the process was not optimized by means of an increase in RR for higher CO<sub>2</sub> contents in the MUG, the key

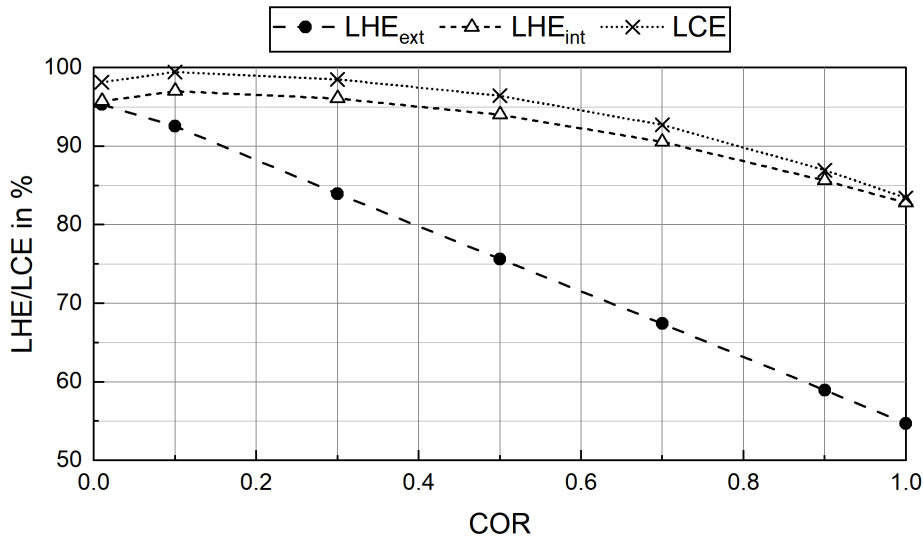


Figure 2.6: Comparison of LCE (x), LHE<sub>ext</sub> (•), and LHE<sub>int</sub> (Δ) computed with varied COR in the MUG at constant loop conditions; Simulation parameters: RR=6; T<sub>in</sub> = T<sub>cool</sub> = 230 °C; p = 80 bar; SN = 2.05.

indicators decrease due to the smaller conversion of the educts in the reactor. Moreover, the increased H<sub>2</sub> demand for CO<sub>2</sub>-rich gas becomes visible considering LHE<sub>ext</sub>. This key indicator decreases faster than LHE<sub>int</sub> over COR due to the byproduct-formation of water.

### 2.4.3 Reactor concepts

Among other equipment as compressors and heat exchangers, the reactor is one key-component in the methanol synthesis process. The combination of geometry, cooling concept as well as gas composition and flow rate largely influences the behavior of the reaction network. One characteristic number quantifying the reactor exploitation independently of pressure and temperature is the gas-hourly-space-velocity *GHSV*. This key indicator correlates the volumetric flow rate of reactor feed at norm conditions to the catalyst bulk volume inside the reactor [140]:

$$GHSV = \frac{\dot{V}_{norm}}{V_{cat}} \quad (2.26)$$

At a high GHSV, residence time in the reactor decreases, leading to reduced contact times between the reactants and the catalyst. As a consequence the gas composition at the reactor exit does not reach thermodynamic equilibrium. Contrary to that, a reduction of GHSV prolongs residence time in the reactor and enables an approach to thermodynamic equilibrium. GHSV as a measure for the reactor load can be optimized depending on the reaction conditions with regard to STY, X<sub>C</sub> or Y<sub>C</sub>. This optimization is, however, besides the reaction kinetics and operation conditions largely depending on the thermal operation of the reactor, i.e. the heat removal from the reaction zone.

Multiple concepts for temperature control and process layout are currently patented or under investigation [14]. As the exothermic heat of the reactions occurring in the methanol synthesis reactor results in a temperature rise, chemical equilibrium would be affected negatively (compare

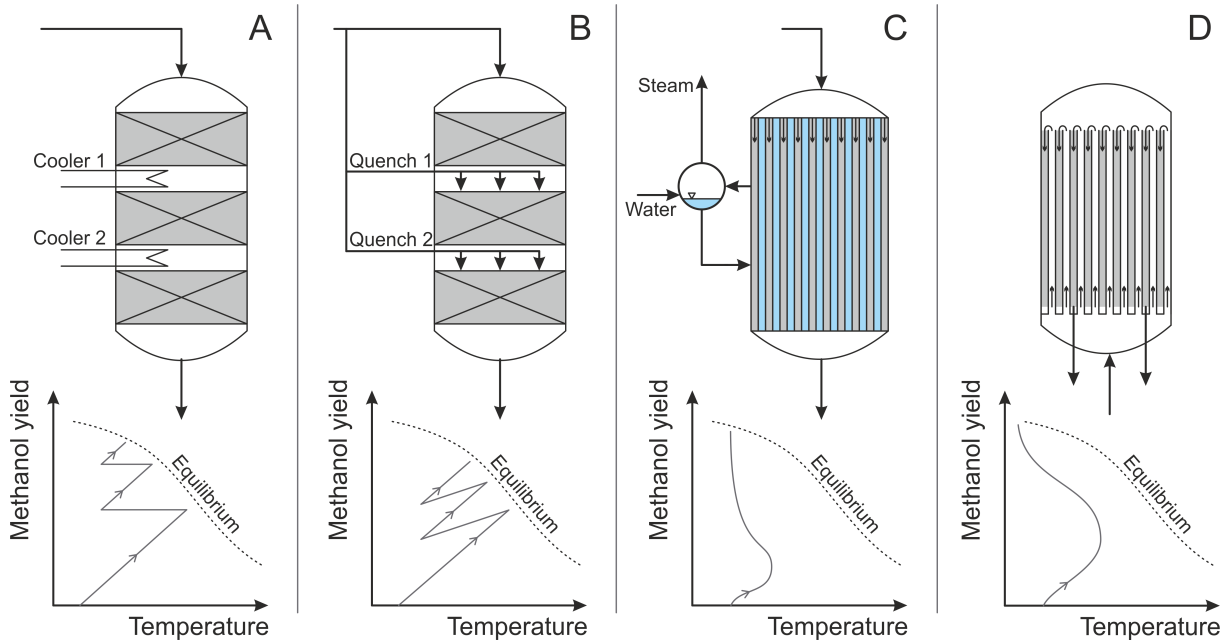


Figure 2.7: Main types of industrially applied methanol synthesis reactors: Adiabatic intercooled reactor (A), adiabatic quench bed reactor (B), steam cooled tubular reactor (C) and the counter-current gas cooled tubular reactor (D); Own illustration based on [9, 53, 159].

Sec.2.4.1). Therefore, measures need to be taken in order to keep the reaction temperature under control. This can be done either by dividing the catalyst bed into intercooled zones or by heat removal along the catalyst bed. The former type of reactor can be described as adiabatic intercooled reactor, while the latter type is of a polytropic nature.

In Fig.2.7, the most commonly applied reactor types in methanol synthesis are depicted with their characteristic temperature-yield profiles. Fig.2.7 shows the adiabatic intercooled reactor as typically applied by Haldor Topsoe (A) [150–152] as well as the adiabatic quench bed reactor as proposed by ICI (B) [141, 142]. In these two reactor types, methanol yield at the adiabatic temperature limit is approached along each fixed bed. By intercooling or quenching of fresh syngas temperature is decreased to enable higher methanol yields. The number and height of catalyst beds as well as the size of the intercooler or the amount of quench gas introduced, respectively, are defined by reactor design in dependence of the gas composition and operating conditions [153–158].

Adiabatic multi-bed reactors have the advantage of a simple design and an easy catalyst replacement [53]. However, these types of reactors have the disadvantages of a more complex startup behavior [153], a possible mal-distribution of the syngas flow and the residence time as well as increased side product formation due to higher synthesis temperatures [159]. Moreover, the high temperatures reached at the exit of each reactor stage lead to faster thermal catalyst degradation in these zones.

The steam raising polytropic tubular reactor depicted in Fig.2.7 (C) was patented in 1971 by Metallgesellschaft AG (later Lurgi, today GEA Group AG) [160]. This reactor type has the advantage of an easier start-up behavior, an improved temperature control and higher possible

yields per pass in comparison to the adiabatic reactor types [153]. Moreover, a decrease in catalyst activity due to catalyst aging can be compensated by an increase of the pressure (and consequently boiling temperature) in the steam drum [161–163]. Today the steam raising reactor is the most commonly applied reactor type in methanol synthesis industry [9, 159]. For this reactor type detailed knowledge of the reaction kinetics is mandatory to optimize the gas load and the coolant temperature. As it is applied in most scientific studies with regard to simulation of industrial methanol synthesis, manifold literature on the geometric dimensions and possible simulation approaches exists in scientific literature [90, 127, 136, 152, 164–171].

Another reactor design commonly applied in methanol synthesis is the counter-current gas cooled tubular reactor schematically depicted in Fig. 2.7 (D). In this type of reactor the incoming reactor feed is introduced into the shell side and directly preheated by the heat of reaction released from the catalyst-filled tubes [172]. In the upper section of the reactor the gas is reversed in direction and enters the reaction zone. Due to the high temperature gradient along the reactor, this reactor type implies an optimal combination of fast reaction kinetics at elevated temperatures (top) and a high equilibrium conversion at low temperatures (bottom). However, the main disadvantages of this reactor emerge from the complex design, the low load flexibility and a difficult start up behavior. Due to the comparably low heat transfer coefficient between tube and shell side, this converter is rather suitable for mild gas conditions.

#### 2.4.4 Dynamic operation

In the synthesis reactor a load point can be defined as a combination of gas composition, i.e. COR, SN and inert gas content, and the quantity of gas passing through the reactor, i.e.  $\dot{n}$  or GHSV, at a certain pressure and temperature. During a load change, one or multiple parameters are varied within a certain time span.

Dynamic load changes in conventional methanol synthesis plants usually appear due to scheduled events as ramp-up at beginning of plant operation, shut-down at the end of the catalyst life time [153] or temperature increase in the steam drum to account for catalyst aging [161–163]. As conventional methanol plants are individually designed for the composition of the exploited resource, i.e. the natural gas field or coal deposit, strong fluctuations in the gas supply are not accounted for in the design of these plants.

However, in case of methanol synthesis from sustainably produced  $H_2$  and captured  $CO_x$ , fluctuation in the gas supply are likely to occur [173]. In case of a decreased production of renewable energy,  $H_2$  supply could decrease drastically. If no appropriate buffer storage for  $H_2$  is available, the shortage in  $H_2$  production would be handed through to the methanol synthesis process. Depending on the control scheme of the plant, the  $H_2$  shortage could be handled by decreasing SN in the MUG ( $SN_{MUG}$ ) or by a reduction of the overall flow rate of MUG. In the latter case, SN would be held constant, however, the process would go into part load with the consequence of a decreased GHSV in the reactor. In case of a decrease in  $SN_{MUG}$ , sub-stoichiometric gas compositions could be reached at the reactor inlet (compare Sec. 2.2.2). When the  $CO_x$  stream is captured from an industrial batch process, e.g. biomass fermentation or steel production, fluctuations in this stream could be another possible source for dynamics in the

gas supply [61] disturbing  $SN_{MUG}$  or, especially in case of steel mill gases, COR in the MUG ( $COR_{MUG}$ ) [174].

To review the development regarding the consideration of dynamics in the scientific community over the past decades, the number of publications explicitly dealing with reactor simulation or experimental campaigns was extracted from the literature data base build during this work. In Fig. 2.8 the number of simulative (turquoise, hatched) and experimental studies (gray, solid) are plotted over the decades from 1970 until today. Both groups are separated by steady state and dynamic studies. The graph indicates, that the majority of scientific studies considers steady state methanol synthesis only. In case of the dynamic simulation studies in the 1990s and 2000s, catalyst deactivation [161, 162, 175–177] and reversed flow reactor configurations, i.e. process concepts where the direction of gas flow in the reactor is periodically reversed to control temperature [178, 179] were in focus of research. From 2005 on, also the topic of process control was addressed by various researchers [169, 180, 181]. Dynamic simulation of a synthesis reactor in the context of PtM was not addressed by any of the simulation studies available in literature.

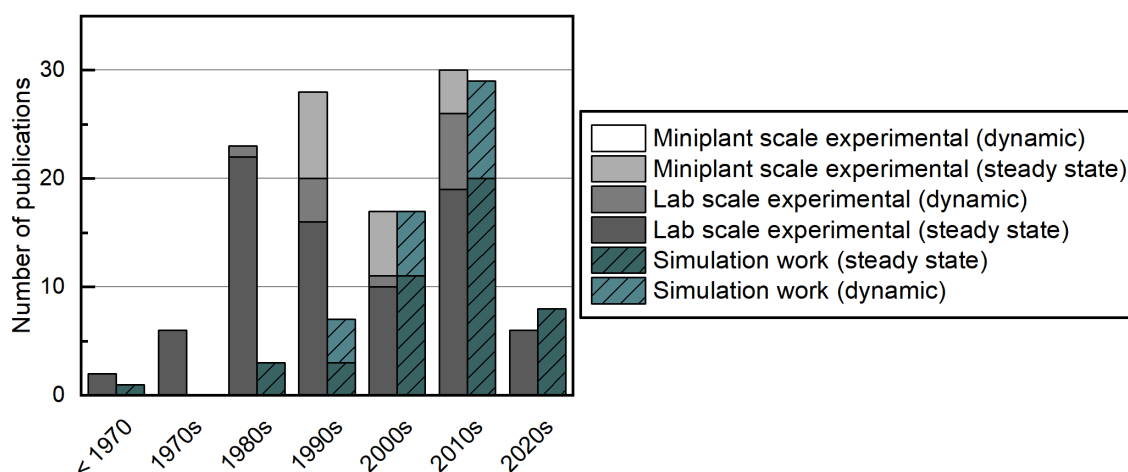


Figure 2.8: Number of publications in the literature data base generated in this work over decades for experimental work (gray) divided by lab scale and miniplant scale work for steady state and dynamic as well as simulation work (turquoise, hatched) for steady state and dynamic consideration.

With regard to experimental investigations, numerous steady state studies describing the reaction kinetics of methanol synthesis were published in the last decades [14, 38, 45, 139, 182]. Contrary to that, only few studies were conducted dealing with its dynamic behavior. While the dynamic experimental studies carried out in the 1980s until the 2000s focus on periodic operation of the synthesis reactor [29, 39, 183–185], some studies considering dynamics in the context of PtM emerged during in the last years [186–189]. Ash-Kulander et al. [186] investigated the influence of a daily startup and shutdown in a  $CO_2$ -rich syngas in a lab scale reactor. In their study they found that the interruption of operation enhanced aging of the catalyst. Besides, their results indicated that flushing of the reactor with  $N_2$  over night enhanced deactivation. However, these findings are in contrast to Ruhland et al. [187] who investigated the effect of load changes on catalyst stability by a variation of SN. In their study no enhancement of deactivation was found

compared to a steady state reference experimental campaign. Seidel and Vollbrecht derived a kinetic model from experimental data obtained from a Micro-Berty type reactor [188, 189]. In their study the authors concluded that a dynamic kinetic model would be beneficial for the description of a methanol synthesis reactor under transient conditions. The dynamic kinetic model derived by the group was characterized by a dynamically changing catalyst morphology, i.e. the fraction of oxidized and reduced active sites, depending on the composition of the syngas. The time-dependent change in the catalyst morphology was included by a differential equation into their kinetic model. However, the authors claimed a lack of experimental data in order to uniquely determine the parameters of their dynamic kinetic model [188]. Due to the high number of model parameters and the computational complexity, the model derived by Seidel and Vollbrecht will not be considered further in this work.

Numerous studies treating the experimental behavior of methanol synthesis on the miniplant or pilot scale are available in literature [81, 84–91]. However, as these studies were exclusively executed under steady state conditions, the behavior of technologically relevant methanol synthesis reactors or processes operated under transient load conditions is one open question in the scientific community.

Overall, it can be concluded from this section, that methanol synthesis is likely to be confronted with fluctuating syngas conditions in the future if PtM technologies are to be implemented on an industrial scale. However, no validated steady state or dynamic reactor model of an industrial sized experimental setup does exist in scientific literature. This research gap must be tackled to enable a stable and economically feasible operation of methanol synthesis process under PtM conditions as described in Sec. 2.3.3.

#### 2.4.5 Capability of reactor types for dynamic operation

Among the reactor types described in Sec. 2.4.3 an assessment regarding their capability for dynamic operation was performed. As already mentioned, the fixed beds of the two adiabatic reactor types (see Fig. 2.7 (A) and (B)) are designed for one load point [158, 190].

In Fig. 2.9, an exemplary simulation of an adiabatic quench bed reactor with three catalyst bed stages was performed for four different load cases. Fig. 2.9 (A) represents the base case at  $p = 80$  bar,  $SN = 2.0$ ,  $COR = 0.8$  and a GHSV of  $8,500 \text{ h}^{-1}$ . The volumetric flow rates and inlet temperatures of the quenched gas streams were adapted to ensure that the critical temperature level of  $280 \text{ }^\circ\text{C}$  was not exceeded. Fig. 2.9 (B) shows the behavior of the reactor at 50% load with the distribution of the quench streams and inlet temperatures held constant. In this scenario the critical temperature level of  $280 \text{ }^\circ\text{C}$  would be exceeded at the end of each catalyst bed stage due to the longer residence times and consequently a higher conversion towards equilibrium. Fig. 2.9 (C) and (D) show an decrease and increase of COR, respectively. At  $COR = 0.7$  (C) temperature in the first reactor stage would exceed  $300 \text{ }^\circ\text{C}$  and therefore lead to serious damage of the catalyst and increased formation of byproducts. However, at  $COR = 0.9$  (D) the reaction would terminate as the cold quench streams would decrease the inlet temperatures of the reaction mixture below  $200 \text{ }^\circ\text{C}$ . Overall, the discussion of the scenarios considered in Fig. 2.9 indicates the requirement of control strategies for the distribution of the feed gas and/or the inlet temperatures

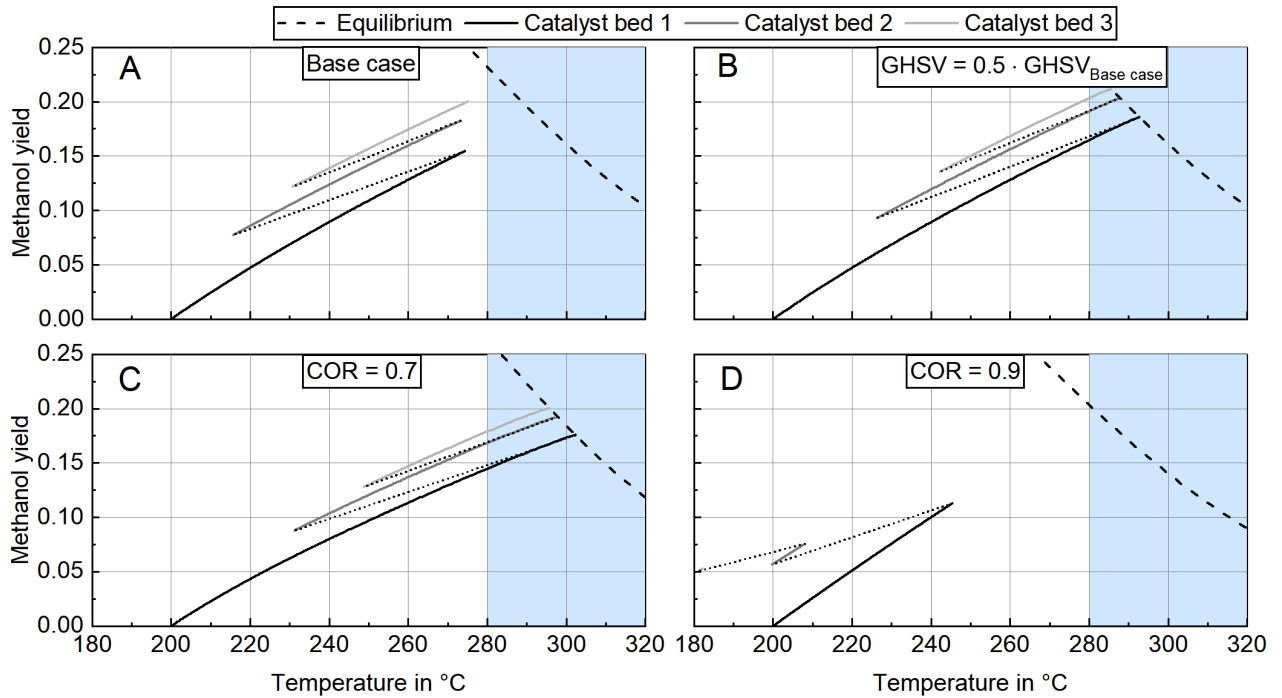


Figure 2.9: Exemplary simulation of a multi-bed adiabatic quench bed reactor at a base case of  $p = 80$  bar,  $SN = 2.0$ ,  $COR = 0.8$  and a  $GHSV$  of  $8,500 \text{ h}^{-1}$  (A), reduced  $GHSV$  to  $4,250 \text{ h}^{-1}$  (B) as well as  $COR = 0.7$  (C) and  $COR = 0.9$  (D); The distribution of the gas streams and the inlet temperatures for the base case were adjusted so that the critical temperature range starting from  $280 \text{ }^\circ\text{C}$  (blue area) was not reached.

to enable the dynamic operation of this reactor type. Therefore, the adiabatic quench bed reactor can be assessed as not viable for rapid load changes if these strategies are not available. Similar conclusions were drawn by Nassirpour et al., who investigated control strategies for different reactor types [190]. In their study the authors found, that both, adiabatic quench bed reactor and adiabatic intercooled reactor are difficult to control on a plant level. Therefore, the adiabatic reactor types will not be considered further within this work.

Similar to the adiabatic multi-bed reactors a strong relation between the cooling strategy and the reaction in the catalyst bed exists for the counter current gas cooled tubular reactor (see Fig. 2.7 (D)). Fluctuations in reactor load or gas composition would influence both, heat transfer coefficients and temperature differences. As the heat transfer coefficient is limited due to the gas-wall-gas heat exchange characteristics and inlet temperature into the catalyst bed is directly affected by the heat produced during the reaction, this reactor type was also assessed not preferable for dynamic operation.

In comparison to the other three reactor types presented in Sec. 2.4.3, the steam cooled tubular reactor was found to be less sensitive towards fluctuations in load. On the one hand this is due to the adjustable heat removal provided by the steam cooling. On the other hand, the high heat transfer coefficient of the boiling steam on the shell side enables high heat fluxes to be removed from the reaction volume. As it is well documented in scientific literature and comparably robust

against dynamic load changes, the steam cooled tubular reactor was selected to be in focus of this work.

## 2.5 Kinetic validation in methanol synthesis

For a proper design of the methanol synthesis reactor and the process, detailed knowledge on the reaction kinetics of methanol synthesis is necessary. Multiple kinetic models based on different mechanism and rate determining steps were published in scientific literature, a detailed overview is provided elsewhere [14]. Most of these models are based on Langmuir-Hinshelwood-Hougen-Watson mechanisms, where the reactants adsorb on an active site before the step-wise reaction towards the product occurs [14, 191]. As the nature of the methanol synthesis mechanism was not yet resolved by the scientific community, all proposed rate equations are based on assumptions and semi-empirical parameters fitted to experimental data. As these parameters are related to various different catalysts, a cross-correlation of different experimental data is usually not possible. In order to evaluate kinetic rate expressions capable of describing industrial methanol synthesis reactors, kinetic models based on commercial catalysts are in focus of this work.

The kinetic model proposed by Graaf in 1988 is mechanistically based on the stepwise hydration of adsorbed CO and CO<sub>2</sub> on two active sites [192]. The parameter set for the model was updated by the authors in 1990 [193]. In their experimental studies the authors utilized a spinning basket reactor filled with a commercial MK-101 catalyst produced by Haldor Topsoe. Even though their kinetic model was published over 30 years ago, it is still applied within recent simulation studies [136, 194–196]. The mechanism, kinetic rate equations and parameter set are provided in Sec. 3.1.2.

In 1996, Bussche and Froment [145] published a kinetic model which became another important literature standard through the last decades [136, 197–200]. The authors proposed a mechanism via the carbonate species on one active site. In their kinetic measurements a fixed bed reactor filled with the ICI 51-2 catalyst was used. Other than in the model of Graaf, no direct CO-hydrogenation reaction was considered. By doing so, the authors accounted for current research results stating that methanol is mainly produced by CO<sub>2</sub>-hydrogenation [201]. Further details on the kinetic model by Bussche et al. are given in Sec. 3.1.2 and Appendix A.18.

In 2011, Graaf's kinetic model was updated by Henkel during his PhD studies performing a comprehensive kinetic study utilizing a commercial catalyst by Südchemie (today Clariant) [202]. Henkel used two different experimental setups, i.e. a Berty reactor and a micro fixed bed reactor. Due to results published by the scientific community and the quality of his parameter fitting, CO-hydrogenation was not considered within his final kinetic model. The mechanism for rWGS and CO<sub>2</sub>-hydrogenation was overtaken from Graaf's kinetic model. Details on this model are provided in Sec. 3.1.2.

Park et al. used a commercial Clariant state-of-the-art catalyst within their kinetic fixed bed studies in 2014 [203]. The kinetic model they proposed was based on the original reaction mechanism provided by Graaf [192] coupled with an additional DME kinetic model published by Chadwick et al. [204].

The kinetic models considered within this work are displayed with their respective validated

data range in Fig. 2.10 with regard to temperature (A), pressure (B), SN (C) and COR (D). All kinetic models cover the temperature ranges relevant for industrial methanol synthesis. In terms of synthesis pressure, Graaf and Bussche only validated their kinetic model for pressures up to 50 bar, whereas Henkel and Park considered higher synthesis pressures up to 75 bar and 90 bar, respectively. As industrial methanol synthesis is usually carried out at pressures exceeding 50 bar, this is a major drawback of the two literature standard models proposed by Bussche and Graaf [157].

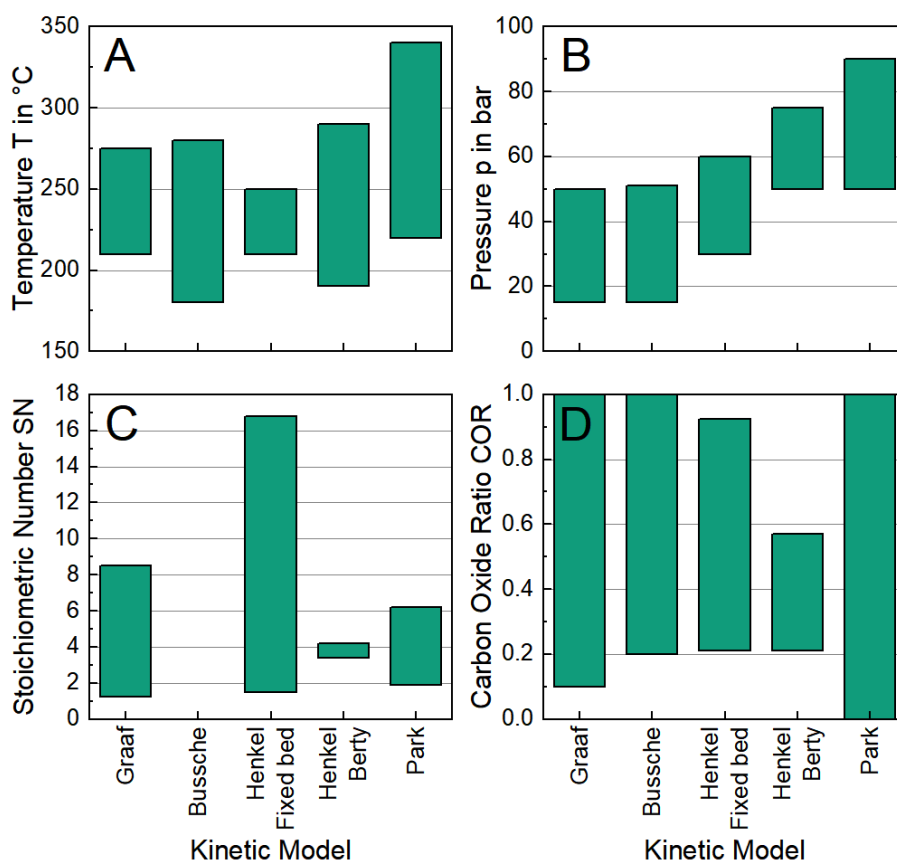


Figure 2.10: Range of experimental validation conditions applied by Graaf [192], Bussche [145], Henkel [202] and Park [203] with regard to temperature (A), synthesis pressure (B), stoichiometric number (C) and carbon oxide ratio (D).

Another important factor for the kinetic performance emerges from SN applied in the kinetic studies. Unfortunately, for this key parameter no data were provided by Bussche et al. [145]. Therefore it is left unclear, for which SN-range their kinetic model was derived. While Graaf and Henkel measured both, sub- and over-stoichiometric conditions, Park et al. did not investigate the reaction kinetics at H<sub>2</sub> shortage for their model (i.e. SN < 2.0).

Besides stoichiometry, COR largely influences the kinetics of methanol synthesis as water produced by CO<sub>2</sub>-hydrogenation considerably limits the reaction kinetics [38]. This effect is enhanced with increasing COR [205]. In the context of PtM technologies, it therefore needs to be mentioned that Henkel's kinetic model probably does not account for these limitations as he performed measurements only until COR = 0.57 (Berty reactor) and COR = 0.93 (fixed bed reactor).

Among all kinetic models published in scientific literature, the kinetic models by Graaf [192]

and Bussche [145] are the most important literature standards, as these two models are used throughout numerous publications with regard of methanol synthesis simulation (compare Appendix A.2). However, both models show deficits for the application in the simulation of PtM reactors due to the usage of probably outdated catalysts [170, 206] and the insufficient validation range (compare Fig. 2.10). As it seemed most promising among the kinetic models considered in this work, an attempt was made to implement the kinetic model proposed by Park et al. [203]. However, an implementation of this model was found impossible due to the lack of some kinetic parameters in their original publication.

Thus, for the modeling of reactors in PtM processes with CO<sub>2</sub>-rich syngas no kinetic model covering the relevant range of reaction conditions exists in scientific literature. However, for the design of an economical and technologically feasible methanol synthesis process detailed knowledge on optimized reactor working conditions and technological limitations is obligatory. Therefore, a new kinetic model using a state-of-the-art commercial catalyst in the PtM-relevant parameter range needs to be derived.

## 2.6 Problem definition and scientific approach

Design and operation of PtM-based methanol synthesis processes will be impacted by the shift in syngas supply from fossil-based towards sustainable feedstocks. Higher CO<sub>2</sub> contents in the MUG will decrease both, equilibrium yield (compare Fig. 2.4) and reaction kinetics due to increased water contents in the product as a consequence of CO<sub>2</sub>-hydrogenation (compare Eq. 2.1). As discussed in Sec. 2.5 a new kinetic model covering the relevant parameter range of PtM processes will be necessary for reactor design under these new boundary conditions.

Moreover, fluctuations in the supply of syngas obtained from alternative feedstocks are likely to occur in future PtM processes (compare Sec. 2.4.4). Therefore, detailed knowledge on the dynamic behavior of a methanol synthesis reactor will necessary for the implementation of this technology.

For this purpose, a new kinetic model will be experimentally derived and discussed for its suitability regarding steady state and dynamic reactor design. In order to maximize the practical relevance of this work, the kinetic model will be derived and validated with experimental data obtained from a miniplant setup. This miniplant was designed using a simulation platform including state-of-the-art kinetic models (extrapolated from their original validation range) as well as a detailed heat transfer and diffusion model to obtain a high level of agreement to the kinetic and thermal behavior of an industrial methanol synthesis reactor.

A well documented steam cooled tubular methanol synthesis reactor was selected as industrial reference for the scale-down as this reactor type was found suitable for dynamic operation (see Sec. 2.4.3). To obtain detailed validation data on the axial thermal behavior of this reactor under both steady state and dynamic load conditions, the miniplant reactor was equipped with a sensor for highly resolved fiber optic temperature measurement [207] in addition to a FTIR online product analysis.

To demonstrate the significance of the herein introduced methodology, the kinetic model adjusted to the miniplant experimental data will be compared against a kinetic model obtained from

a "classic" integral kinetic setup. Furthermore, the kinetic model obtained under steady state conditions will be held against the dynamic experimental data obtained from the miniplant setup to investigate the necessity for dynamic reaction kinetics for the description of methanol synthesis reactor as proposed by other research groups [188] (compare Sec. 2.4.4). Finally, the differential kinetic model will be discussed on industrial scale to demonstrate the impact of this work towards technical reactor and process design.



### 3 Materials and Methods

In this chapter, the reactor model as the basis of the here presented methodology including the simulation-based scale-down, the validation of the kinetic models and the transfer of the results to industrial scale will be explained. Subsequently, details on the design and characteristics of the miniplant setup will be provided. Finally, the methodology for the model validation will be presented.

#### 3.1 Simulation platform

Both, steady state and dynamic reactor model were built on a common modeling basis, wrapped by a simulation platform (see Fig. 3.1). This platform includes the sub-models for heat transfer, powder kinetics and diffusion. Thermodynamic properties for the gas phase are calculated by a sub-module based on NIST- and DIPPR-database [208, 209] with the mixing rules referenced by VDI Heat Atlas [210] as well as the Soave Redlich Kwong equation of state (SRK EoS) for the calculation of gas phase density and fugacity [135]. The thermodynamic models were validated against the data obtained by commercial process simulation software in previous work [211]. To keep the simulation platform flexible for different sizes and reactor types, geometrical parameters are selected from a parameter data-base.

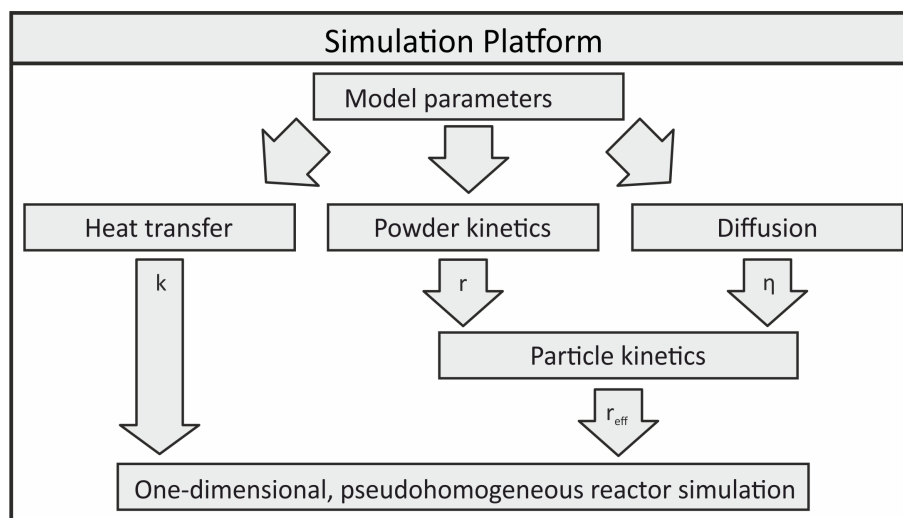


Figure 3.1: Simulation platform applied in this work.

As both, the steady-state and the dynamic reactor model rely on common sub-models, adaptations and enhancements in the sub-models are automatically updated in the whole simulation platform. This has the advantage, that improved models, e.g. for a kinetic expression, can directly be discussed on various design scales and simulation cases. The reactor model was built applying the following assumptions:

1. Radial gradients in concentration and temperature along the catalyst bed are neglected (one-dimensional simulation).

2. Bulk phase and gas phase are considered as one pseudo-homogeneous mixed phase.
3. Ideal plug flow behavior is assumed; Axial dispersion is neglected (see 3.3).
4. No external diffusion limitation is present at the catalyst surface; Only internal diffusion is accounted for by the efficiency factor  $\eta_{eff,j}$  (see Sec. ??).

### 3.1.1 Heat transfer model

The sub-model accounting for the heat transfer between reaction zone and cooling medium was referenced from VDI Heat Atlas providing established state-of-the-art approaches for engineering heat transfer problems [210]. This sub-model provides semi-empirical approaches for heat transfer in packed beds with gas flow ( $\lambda_{rad}$ ,  $\alpha_{int}$ ) and the heat transfer outside the reactor tube ( $\alpha_{ext}$ ). In case of the miniplant  $\alpha_{ext}$  was expressed by convective thermal oil heat transfer, while for the industrial scale a correlation for a steam cooling was applied, respectively. Overall heat transfer coefficient  $U$  was calculated as follows [212]:

$$\frac{1}{U} = \frac{1}{\alpha_{int}} + \frac{d_{int}}{8 \cdot \lambda_{rad}} + \frac{d_{int} \cdot \ln\left(\frac{d_{ext}}{d_{int}}\right)}{2 \cdot \lambda_{wall}} + \frac{d_{int}}{\alpha_{ext} \cdot d_{ext}} \quad (3.1)$$

The calculation of the effective thermal conductivity of the fixed bed as well as the convective heat transfer coefficients inside and outside the reactor wall will be discussed in the following sections.

#### 3.1.1.1 Heat transfer in the catalyst bed

Heat transfer in the catalyst bed was calculated in accordance to VDI Heat Atlas sections D6.3 and M7 [210]. Properties of the activated methanol catalyst were extracted from the PhD thesis by Henkel [202], where the efficient thermal conductivity ( $\lambda_{cat}$ ) and the heat capacity ( $c_{p,cat}$ ) of the catalyst were measured.

The calculation of the effective heat conductivity of the catalyst bed was based on the work by Zehner and Schlünder [213] who investigated thermal conductivity in packed beds without fluid flow. In their work the shape of the particles and the porosity of the fixed bed are transformed to a model cell representing fluid phase and solid phase in cylindrical coordinates (see Appendix A.4). The deformation parameter  $B$  in the heat transfer model is defined as follows:

$$B = C_f \cdot \left[ \frac{1 - \varepsilon}{\varepsilon} \right]^{10/9} \quad (3.2)$$

The semi-empirical shape factor  $C_f$  in this equation must be determined by experiments. Based on literature data Zehner and Schlünder determined values for  $C_f$  as follows [213]:

- a) Spherical particles:  $C_f = 1.25$
- b) Crushed particles:  $C_f = 1.4$
- c) Cylinders and Raschig rings:  $C_f = 2.5$

Due to wall effects, the mean porosity ( $\varepsilon$ ) of a fixed bed in a containment with a low diameter-to-particle-ratio can be higher than in an infinite containment ( $\varepsilon_\infty$ ). In the reactor tube  $\varepsilon$  can be calculated by applying the following semi-empirical correlation for cylindrical particles [210]:

$$\varepsilon = \varepsilon_\infty + (1 - \varepsilon_\infty) \cdot \frac{0.480}{d_{in}/d_{cat}} \quad (3.3)$$

The reduced thermal conductivity of the core of the unit cell  $k_c$ , i.e. the ratio of the heat conductivity of the core of the model unit cell  $\lambda_c$  in relation to the heat conductivity in the fluid phase  $\lambda_f$  is calculated as follows [213]:

$$k_c = \frac{\lambda_c}{\lambda_f} = \frac{2}{N} \cdot \left[ \frac{B}{N^2} \cdot \frac{(k_p - 1)}{k_p} \cdot \ln\left(\frac{k_p}{B}\right) - \frac{(B + 1)}{2} - \frac{B - 1}{N} \right] \quad (3.4)$$

In Eq. 3.4, the parameters  $k_p$  and  $N$  are defined by:

$$k_p = \frac{\lambda_{cat}}{\lambda_f} \quad (3.5)$$

$$N = 1 - \frac{B}{k_p} \quad (3.6)$$

Finally, the reduced thermal conductivity of the catalyst bed without gas flow  $k_{bed}$ , i.e. the ratio of the effective heat conductivity of the catalyst bed  $\lambda_{bed}$  to the heat conductivity of the fluid phase is calculated as follows:

$$k_{bed} = \frac{\lambda_{bed}}{\lambda_f} = 1 - \sqrt{1 - \varepsilon} + \sqrt{1 - \varepsilon} \cdot k_c \quad (3.7)$$

This equation can then be rearranged to calculate the effective heat conductivity of the fixed bed without gas flow. In a subsequent study, Schlünder, Bauer and Zehner adapted the model presented above by inclusion of secondary parameters like the heat radiation between the particles and the influence of pressure [214, 215]. This model is also provided by VDI Heat Atlas, however, the effect towards the overall heat transfer coefficient was found to be negligible by a simulative comparison for the conditions applied within this work. Consequently the secondary parameters of the model were neglected, in order to decrease the number of semi-empirical influence parameters. For the influence of fluid flow on the effective radial heat transfer the following correlation is proposed by VDI Heat Atlas [210]:

$$\lambda_{rad} = \lambda_f \cdot \left( k_{bed} + \frac{Pe_0}{K_r} \right) \quad (3.8)$$

In this equation, the reciprocal of the slope parameter  $K_r$  together with the molecular Péclet number  $Pe_0$  represent the diffusion of the gas with regard to the particle shape as well as gas properties and velocity. Calculation of  $K_r$  is formulated as follows:

$$K_r = K_{r,\infty} \cdot \left( 2 - \left( \frac{2}{d_{in}/d_p} \right)^2 \right) \quad (3.9)$$

The reciprocal slope parameter in an infinitely expanded containment is defined for different particle shapes [210]:

- a) Spherical particles:  $K_{r,\infty} = 7$
- b) Crushed particles:  $K_{r,\infty} = 5.7$
- c) Cylindrical particles:  $K_{r,\infty} = 4.6$

The molecular Péclet number in Eq. 3.8 is calculated as:

$$Pe_0 = \frac{u_0 \cdot \rho_f \cdot c_{p,f} \cdot d_p}{\lambda_f} \quad (3.10)$$

Nusselt number at the inner reactor wall  $Nu_{int}$  can be calculated according to Martin and Nilles by the following semi-empirical equation [216]:

$$Nu_{int} = \left( 1.3 + \frac{5}{d_{in}/d_p} \right) \cdot \frac{\lambda_{bed}}{\lambda_f} + 0.19 \cdot Re_p^{0.75} \cdot Pr^{1/3} \quad (3.11)$$

In Eq. 3.11, Reynolds particle number  $Re_p$  and Prandtl  $Pr$  number are calculated as follows:

$$Re_p = \frac{u_0 \cdot d_p}{\nu_f} \quad (3.12)$$

$$Pr = \frac{\nu_f \cdot \rho_f \cdot \tilde{c}_{p,f}}{\lambda_f \cdot M_f} \quad (3.13)$$

The empty tube fluid velocity  $u_0$  in the reactor was calculated by continuity equation applying the empty tube cross sectional area  $A_R$  and the volumetric flow rate  $\dot{V}$  at rated pressure and temperature:

$$u_0 = \frac{\dot{V}}{A_R} \quad (3.14)$$

Thermophysical properties of the gas phase as the molar heat capacity  $\tilde{c}_{p,f}$ , density  $\rho_f$ , kinematic viscosity  $\nu_f$  and molar mass  $M_f$  were calculated according to DIPPR equations, SRK EoS [135] and VDI Heat Atlas [210]. The heat transfer coefficient at the inner reactor wall  $\alpha_{int}$  can then be calculated by:

$$\alpha_{int} = \frac{Nu_{int} \cdot \lambda_f}{d_p} \quad (3.15)$$

Sensitivity of the model input parameters on the overall heat transfer coefficient will be discussed in Sec. 3.1.1.4.

## 3.1.1.2 External heat transfer coefficient of the industrial reactor

In the steam cooled industrial tubular reactor nucleate boiling can be assumed to appear on the shell side of the reactor [136]. Numerous calculation methods exist in scientific literature to calculate the heat transfer in a boiling liquid based on semi-empirical correlations derived from lab scale measurements [210, 217, 218]. Three different calculation methods were considered in this work:

## 1. Method by Fritz [217]:

The calculation method for the boiling heat transfer coefficient proposed by Fritz is based on heat transfer measurements on horizontal and vertical tubes. The vapor pressure of the boiling liquid  $p_{b,H_2O}$  at cooling temperature  $T_{cool}$  was calculated based on NIST Webbook [208].

$$\alpha_{ext} = 77.8 \cdot \left( \frac{T_{wall,ext} - T_{cool}}{K} \right)^{2.57} \cdot \left( \frac{p_{b,H_2O}}{Pa} \cdot 10^{-6} \right)^{0.857} \text{ W m}^{-2} \text{ K}^{-1} \quad (3.16)$$

## 2. Method by Holman [218]:

The calculation by Holman is structurally similar to the approach proposed by Fritz. However, it discriminates between two semi-empirical equations depending on the range of  $\alpha_{ext}$  and accounts for the orientation of the heat transfer area. For a vertical geometry as it is found in an industrial tube bundle reactor the calculation is performed as follows:

- For  $0 \text{ W m}^{-2} \text{ K}^{-1} < \alpha_{ext} < 670 \text{ W m}^{-2} \text{ K}^{-1}$ :

$$\alpha_{ext} = 537 \cdot \left( \frac{T_{wall,ext} - T_{cool}}{K} \right)^{1/7} \cdot \left( \frac{p_{b,H_2O}}{Pa} \cdot 10^{-5} \right)^{0.4} \text{ W m}^{-2} \text{ K}^{-1} \quad (3.17)$$

- For  $680 \text{ W m}^{-2} \text{ K}^{-1} < \alpha_{ext} < 6680 \text{ W m}^{-2} \text{ K}^{-1}$ :

$$\alpha_{ext} = 7.96 \cdot \left( \frac{T_{wall,ext} - T_{cool}}{K} \right)^3 \cdot \left( \frac{p_{b,H_2O}}{Pa} \cdot 10^{-5} \right)^{0.4} \text{ W m}^{-2} \text{ K}^{-1} \quad (3.18)$$

## 3. Method proposed by VDI Heat Atlas Sec. H2 [210]:

This calculation method for  $\alpha_{ext}$  is more complex compared to those by Fritz and Holman. With regard to VDI Heat Atlas,  $\alpha_{ext}$  is determined from a fluid-specific normalized state (for water  $\alpha_{ext,ref} = 5,6 \text{ kW m}^{-2} \text{ K}^{-1}$ ) as follows:

$$\alpha_{ext} = \alpha_{ext,ref} \cdot F_q \cdot F_p \cdot F_{wall} \quad (3.19)$$

In this equation, correction factors are provided for the heat flow density  $\dot{q}$  ( $F_q$ ), for pressure of the boiling heat exchange fluid ( $F_p$ ) and characteristics of the wall ( $F_{wall}$ ) as follows:

$$F_q = \left( \frac{\dot{q}}{\dot{q}_{ref}} \right)^{0.9-0.3 \cdot p_r^{0.15}} \quad (3.20)$$

$$F_p = 1.73 \cdot p_r^{0.27} + \left(6.1 + \frac{0.68}{1 - p_r}\right) \cdot p_r^2 \quad (3.21)$$

According to VDI Heat Atlas calculation of  $F_{wall}$  is objected to significant inaccuracies, as it is weakly validated by experiments [210]. Therefore, this correction factor was set to 1.0, however, better knowledge of the material factor could be gathered by a comparison with measured data from an industrial reactor.

In Eq. 3.20 the normalized heat flow density is defined as  $\dot{q}_{ref} = 20 \text{ kW m}^{-2}$ . The heat flow density at the working point  $\dot{q}$  can be calculated as follows:

$$\dot{q} = U_{wall,ext} \cdot (T_R - T_{wall,ext}) \quad (3.22)$$

$U_{wall,ext}$  as the overall heat transfer between the catalyst bed and the outer reactor wall outside can be calculated removing  $\alpha_{ext}$  from Eq. 3.1:

$$\frac{1}{U_{wall,ext}} = \frac{1}{\alpha_{int}} + \frac{d_{int}}{8 \cdot \lambda_{rad}} + \frac{d_{int} \cdot \ln\left(\frac{d_{ext}}{d_{int}}\right)}{2 \cdot \lambda_{wall}} \quad (3.23)$$

Relative pressure  $p_r$  in Eq. 3.20 and 3.21 is calculated by relating the critical pressure of water of  $p_{crit,H_2O} = 220.64 \text{ bar}$  to the vapor pressure at  $T_{cool}$  as follows:

$$p_r = \frac{p_{b,H_2O}}{p_{crit,H_2O}} \quad (3.24)$$

Fig. 3.2 shows  $\alpha_{ext}$  calculated by applying the three calculation methods by Fritz [217], Holman [218] and VDI Heat Atlas [210] over the temperature difference between reactor wall and cooling medium for  $T_{cool} = 200^\circ\text{C}$  and  $T_{cool} = 280^\circ\text{C}$ . The two temperature levels of the steam cooling correlate to vapor pressures of 14.6 bar and 64.5 bar, respectively [208]. The graph shows that for all three models an increase of  $\Delta T$  and  $T_{cool}$  leads to a rise of  $\alpha_{ext}$ . However, while the correlation by Holman does only show a low sensitivity towards  $T_{cool}$ , the calculations by VDI Heat Atlas and Fritz are influenced by the temperature of the cooling medium more strongly.

Overall, the correlation by Holman shows a different trend compared to Fritz and VDI Heat Atlas. At low temperature differences between reactor wall and cooling medium higher heat transfer coefficients are calculated with a offset of approx.  $1,000 \text{ W m}^{-2} \text{ K}^{-1}$  or  $2,000 \text{ W m}^{-2} \text{ K}^{-1}$  at  $200^\circ\text{C}$  and  $280^\circ\text{C}$ , respectively, while at higher  $\Delta T$  this correlation calculated the lowest heat transfer coefficients. At  $T_{cool} = 200^\circ\text{C}$  the correlations by VDI Heat Atlas and Fritz show a similar behavior, however, at  $T_{cool} = 280^\circ\text{C}$  VDI Heat Atlas predicts significantly higher heat transfer coefficients than the formula by Fritz. Measured data from an industrial steam cooled reactor would be necessary to select the best correlation for  $\alpha_{ext}$ . For the reactor simulation in this work, the correlation by VDI Heat Atlas was selected, as it provides the most adjustable and up-to-date model for the heat transfer coefficient in boiling medium.

As shown in Fig. 3.2,  $\alpha_{ext}$  depends on the temperature difference between  $T_{wall,ext}$  and  $T_{cool}$ . Vice versa  $T_{wall,ext}$  is dependent on  $\alpha_{ext}$ , as the external heat transfer influences the radial temperature profile along the reactor. Therefore, an iterative determination of  $T_{wall,ext}$  needs to

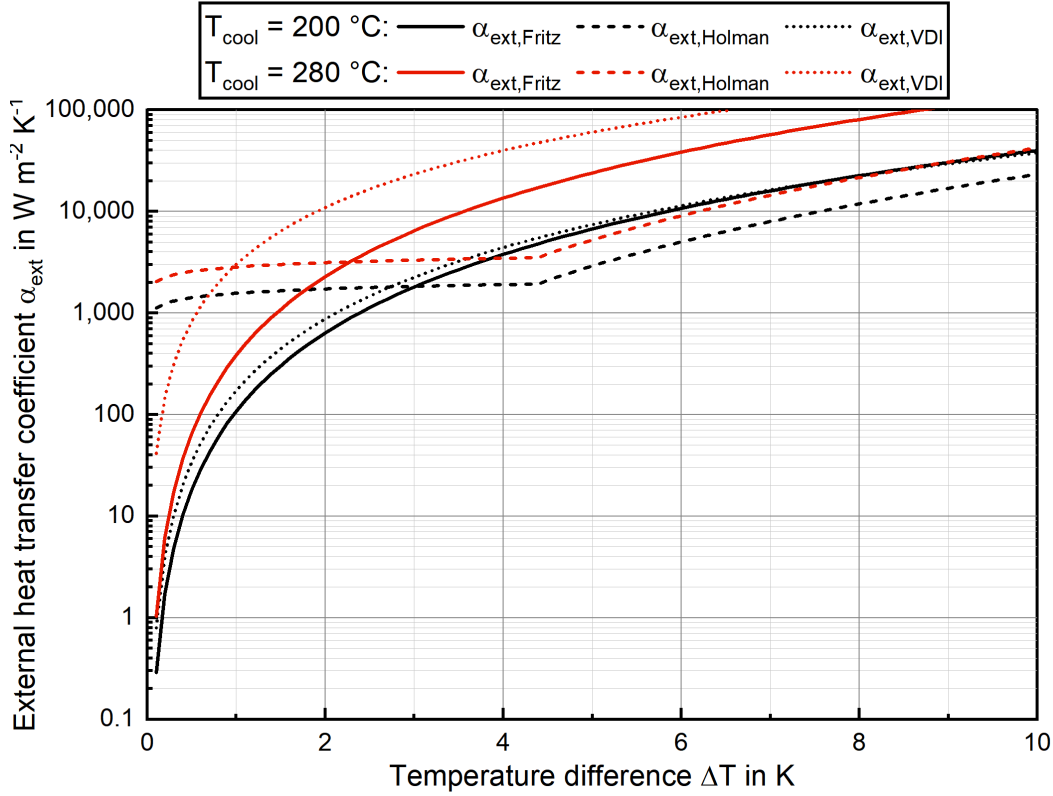


Figure 3.2: External heat transfer coefficient calculated using the correlations by Fritz [217], Holman [218] and VDI Heat Atlas [210] over the temperature difference between outer reactor wall and cooling fluid for  $T_{cool} = 200\text{ °C}$  and  $T_{cool} = 280\text{ °C}$ .

be applied. This iteration can be performed by equating the calculation for the heat flux density from inside the reactor to the outer wall with the heat flux density from the outer wall towards the cooling medium as follows:

$$U_{wall,ext} \cdot (T_R - T_{wall,ext}) \stackrel{!}{=} \alpha_{ext} \cdot (T_{wall,ext} - T_{cool}) \quad (3.25)$$

In case of a correct value for  $T_{wall,ext}$ , both heat flux densities are equal. Therefore, a minimization of the difference between the two heat flux densities can be performed varying  $T_{wall,ext}$  in the boundary  $T_R > T_{wall,ext} > T_{cool}$ .

### 3.1.1.3 External heat transfer coefficient of the miniplant reactor

As the experimental miniplant setup described in Sec. 3.4 is cooled by forced convection of thermal oil flowing through an annular gap around the catalyst-filled reactor tube, calculation of  $\alpha_{ext}$  for the miniplant differs significantly from the previously described methodology for the industrial reactor. The calculation method was taken from the Nusselt correlations of VDI Heat Atlas in Sec. G2 for laminar flow, transition region and turbulent flow [210]. Calculation of the Reynolds number of the thermal oil  $Re_{oil}$  in the annular is performed as follows:

$$Re_{oil} = \frac{u_{oil} \cdot d_{hydr}}{\nu_{oil}} \quad (3.26)$$

In case of the annular gap, the hydraulic diameter  $d_{hydr}$  is defined as the difference between the inner diameter of the annular tube  $d_{ann}$  and the external diameter of the reactor tube  $d_{ext}$  [210]:

$$d_{hydr} = d_{ann} - d_{ext} \quad (3.27)$$

Velocity of the thermal oil  $u_{oil}$  is calculated using the continuity equation as follows:

$$u_{oil} = \frac{4 \cdot \dot{V}_{oil}}{\pi \cdot (d_{ann}^2 - d_{ext}^2)} \quad (3.28)$$

Insertion of Eq. 3.27 and Eq. 3.28 into Eq. 3.26 leads to the following expression for the  $Re_{oil}$  [210]:

$$Re_{oil} = \frac{4 \cdot \dot{V}_{oil}}{\pi \cdot (d_{ann} + d_{ext}) \cdot \nu_{oil}} \quad (3.29)$$

Besides the width of the annular gap,  $Re_{oil}$  depends on the volumetric flow rate of the thermal oil  $\dot{V}_{oil}$  and the kinematic viscosity of the thermal oil  $\nu_{oil}$ . For the determination of  $\dot{V}_{oil}$ , an experimental campaign was performed measuring the volumetric flow rate of the thermal oil rotameter in dependence of oil temperature and rotational speed of the shaft of the thermostat pump. Moreover, the pressure in the thermal oil cycle was measured and compared to a pressure loss simulation of the thermal oil cycle performed with the software "Druckverlust" [219] to verify plausibility of the measurement. Details regarding the measurement of  $\dot{V}_{oil}$  are provided in Appendix A.8. The volumetric flow rate of the thermostat in dependence of temperature was implemented into the simulation platform by a 3rd order polynomial (see Eq. A.21 in Appendix A.8). Thermophysical data of the thermal oil provided by manufacturer [220] were transformed into a temperature dependent polynomial and integrated into the simulation platform (see Appendix A.9).

#### 3.1.1.4 Sensitivity of the heat transfer model parameters

In Fig. 3.3 a sensitivity analysis for the overall heat transfer coefficient calculated with regard to Eq. 3.1 was carried out for both, industrial reactor (A) and the miniplant reactor (B) at a base case of  $T_R = 260^\circ\text{C}$ ,  $T_{cool} = 240^\circ\text{C}$  and  $\text{GHSV} = 10,000 \text{ h}^{-1}$  at a pressure of 65 bar. A gas composition of  $\text{SN} = 4.0$  and  $\text{COR} = 0.9$  was selected for the sensitivity analysis. Details on the dimensions of the industrial and miniplant reactor will be provided in Sec. 3.3 and 3.4, respectively. For the sensitivity analysis, the input parameters influencing the heat transfer through the catalyst bed and the reactor wall were varied in a range of  $\pm 50\%$ . As the heat transfer in the annular gap of the miniplant reactor was found to be largely influenced by  $\dot{V}_{oil}$  (compare Sec. 3.1.1.3) this parameter was included into the analysis for the miniplant reactor. The graphs indicate the importance of the correct determination of particle size for the simulation of heat transfer for both, industrial and miniplant reactor. The larger sensitivity of this parameter for the industrial heat transfer model is due to the larger particle size and therefore larger range varied for this reactor type. A flotation particle size measurement was executed for the particles used in the miniplant experiments in order to accurately determine this parameter (see App. A.10). Besides particle diameter, the semi-empirical inverse slope parameter  $K_{r,\infty}$  applied in Eq. 3.9

does affect the overall heat transfer coefficient. By decreasing the value of  $K_{r,\infty}$ , higher heat transfer coefficients are obtained. Moreover, thermal conductivities of both, the reactor wall  $\lambda_{wall}$  and the catalyst  $\lambda_{cat}$  do influence the heat transfer coefficient for industrial and miniplant reactor. While  $\lambda_{wall}$  was obtained from VDI Heat Atlas of stainless steel [210],  $\lambda_{cat}$  needs to be determined by experiments. As Henkel determined this parameter during his PhD thesis for the activated catalyst, this parameter was overtaken from his work [202].

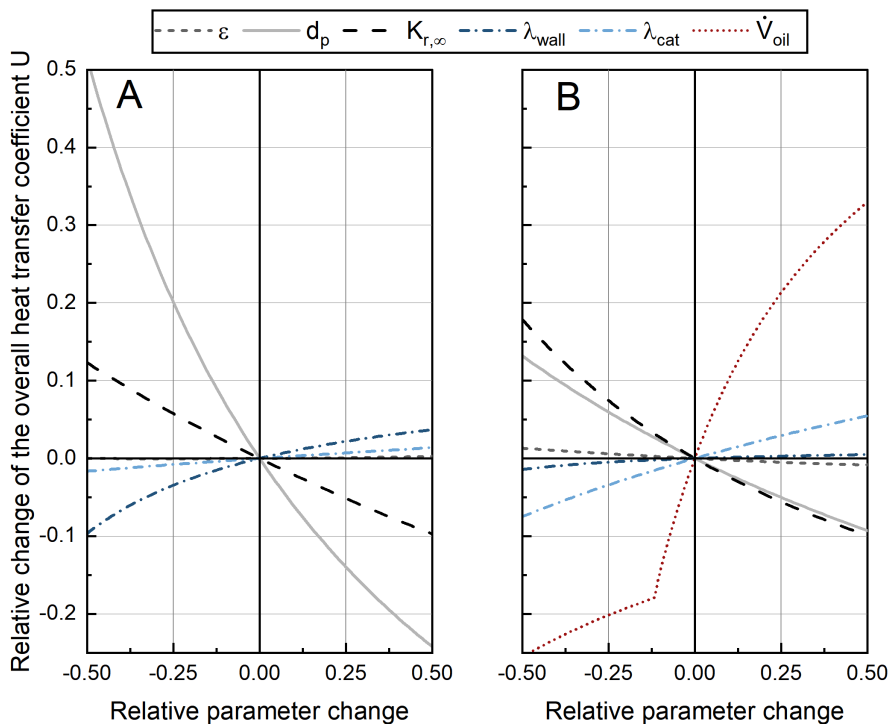
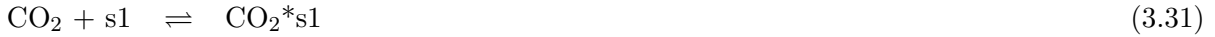


Figure 3.3: Sensitivity of the parameters of the heat transfer model towards the overall heat transfer coefficient  $U_{overall}$  for the industrial reactor (A) and the miniplant reactor (B); Simulation parameters:  $T_{cool} = 240\text{ }^{\circ}\text{C}$ ;  $T_R = 260\text{ }^{\circ}\text{C}$ ;  $GHSV = 10,000\text{ h}^{-1}$ ;  $p = 65\text{ bar}$ ;  $SN = 4.0$ ;  $COR = 0.9$ ; For reactor design parameters see Tab. 3.5 and Tab. 3.6

The parameter influencing the heat transfer coefficient of the miniplant most strongly was found to be  $\dot{V}_{oil}$ . Therefore, this parameter was determined by experiments as described in Sec. 3.1.1.3.

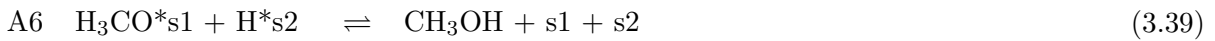
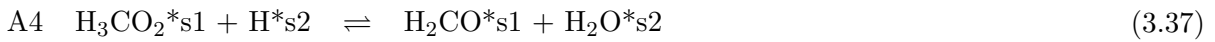
### 3.1.2 Kinetic models

Some of the most commonly used kinetic models for methanol synthesis are the models provided by Graaf [192, 195, 196, 221, 222] and Bussche-Froment [145, 199, 200, 223, 224] (compare Appendix A.2). Graaf's kinetic model is based on dual-site Langmuir-Hinshelwood-Hougen-Watson mechanism. In this mechanism, CO and CO<sub>2</sub> adsorb competitively on site one (s1), while H<sub>2</sub> and H<sub>2</sub>O adsorb on site two (s2) competitively as follows:

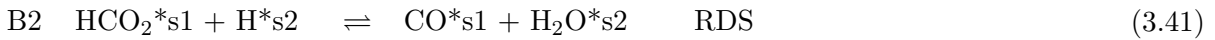


For  $\text{H}_2$ , a dissociative adsorption is assumed for the mechanism. The adsorption of methanol as the reaction product is assumed to be negligible in comparison to the other reactants. Adsorbed on s1, CO and  $\text{CO}_2$  are stepwisely hydrated. The elementary steps of the reaction network can be expressed as follows [192].

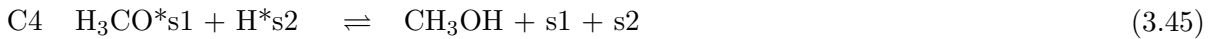
$\text{CO}_2$ -hydrogenation



rWGS



CO-hydrogenation



The rate determining steps (RDS) A3B2C3 were determined by Graaf by means of an error discussion of the 48 possible combinations of RDS for CO-hydrogenation,  $\text{CO}_2$ -hydrogenation and rWGS [191, 192, 225]. The kinetic model by Graaf is formulated by the following rate equations [192]:

$$r_{\text{CO}_2} = \frac{k_1 \cdot K_2 \cdot EQ_1}{(1 + K_1 \cdot f_{\text{CO}} + K_2 \cdot f_{\text{CO}_2}) (f_{\text{H}_2}^{0.5} + K_3 \cdot f_{\text{H}_2\text{O}})} \quad (3.46)$$

$$r_{\text{rWGS}} = \frac{k_2 \cdot K_2 \cdot EQ_2}{(1 + K_1 \cdot f_{\text{CO}} + K_2 \cdot f_{\text{CO}_2}) (f_{\text{H}_2}^{0.5} + K_3 \cdot f_{\text{H}_2\text{O}})} \quad (3.47)$$

$$r_{\text{CO}} = \frac{k_3 \cdot K_1 \cdot EQ_3}{(1 + K_1 \cdot f_{\text{CO}} + K_2 \cdot f_{\text{CO}_2}) (f_{\text{H}_2}^{0.5} + K_3 \cdot f_{\text{H}_2\text{O}})} \quad (3.48)$$

The equilibrium terms for CO<sub>2</sub>-hydrogenation (EQ<sub>1</sub>), rWGS (EQ<sub>2</sub>) and CO-hydrogenation (EQ<sub>3</sub>) can be expressed as follows according to Graaf et al. [129]:

$$EQ_1 = 1 - \frac{f_{CH_3OH} \cdot f_{H_2O}}{f_{CO_2} \cdot f_{H_2}^3 \cdot K_{eq,1}} \quad (3.49)$$

$$EQ_2 = 1 - \frac{f_{CO} \cdot f_{H_2O}}{f_{CO_2} \cdot f_{H_2} \cdot K_{eq,2}} \quad (3.50)$$

$$EQ_3 = 1 - \frac{f_{CH_3OH}}{f_{CO} \cdot f_{H_2}^2 \cdot K_{eq,3}} \quad (3.51)$$

The fugacities were calculated using the Soave-Redlich-Kwong equation of state (SRK EoS) [135]. The model parameters of the above mentioned kinetic models are expressed by an Arrhenius correlation as follows for the kinetic rate constants  $k_i$  and adsorption constants  $K_j$  [226]:

$$k_i = A_{ki} \cdot \exp\left(-\frac{B_{ki}}{R \cdot T}\right) \quad (3.52)$$

$$K_j = A_{Kj} \cdot \exp\left(-\frac{B_{Kj}}{R \cdot T}\right) \quad (3.53)$$

The semi-empirical constants  $A_{ki}$  and  $B_{ki}$  as well as  $A_{Kj}$  and  $B_{Kj}$  in Eq. 3.52 and 3.53, respectively, can be tuned in order to obtain agreement between experimental data and reactor simulation [226]. The parameters determined by Graaf are listed in Tab. 3.1 [193].

Table 3.1: Kinetic parameters proposed by Graaf et al. [193].

Unit	Parameters
$k_1$ mol · kg <sup>-1</sup> · s <sup>-1</sup> · bar <sup>-1</sup>	$1.09 \cdot 10^5 \cdot \exp\left(\frac{-87,500}{R \cdot T}\right)$
$k_2$ mol · kg <sup>-1</sup> · s <sup>-1</sup> · bar <sup>-0.5</sup>	$9.64 \cdot 10^{11} \cdot \exp\left(\frac{-152,900}{R \cdot T}\right)$
$k_3$ mol · kg <sup>-1</sup> · s <sup>-1</sup> · bar <sup>-1</sup>	$4.89 \cdot 10^7 \cdot \exp\left(\frac{-113,000}{R \cdot T}\right)$
$K_1$ bar <sup>-1</sup>	$2.16 \cdot 10^{-5} \cdot \exp\left(\frac{46,800}{R \cdot T}\right)$
$K_2$ bar <sup>-1</sup>	$7.05 \cdot 10^{-7} \cdot \exp\left(\frac{61,700}{R \cdot T}\right)$
$K_3$ bar <sup>-0.5</sup>	$6.37 \cdot 10^{-9} \cdot \exp\left(\frac{84,000}{R \cdot T}\right)$

In contrast to the mechanism applied by Graaf, Bussche and Froment considered a different reaction mechanism based only on CO<sub>2</sub>-hydrogenation coupled with rWGS via the formyl species on a single active site [145]. From the mechanism in combination with the RDS (details see Appendix A.18) the authors derived the following rate equations:

$$r_{CO_2} = \frac{k_1 \cdot f_{CO_2} \cdot f_{H_2} \cdot EQ_1}{\left(1 + K_1 \cdot \left(\frac{f_{H_2O}}{f_{H_2}}\right) + K_2 \cdot f_{H_2}^{0.5} + K_3 \cdot f_{H_2O}\right)^3} \quad (3.54)$$

$$r_{rWGS} = \frac{k_2 \cdot f_{CO_2} \cdot EQ_2}{\left(1 + K_1 \cdot \left(\frac{f_{H_2O}}{f_{H_2}}\right) + K_2 \cdot f_{H_2}^{0.5} + K_3 \cdot f_{H_2O}\right)} \quad (3.55)$$

The parameters Bussche et al. fitted towards their measured data are provided in Tab. 3.2. Further details on this kinetic model are given in Appendix A.18.

Table 3.2: Kinetic parameters proposed by Bussche et al. [145].

	Unit	Parameters
$k_1$	$mol \cdot kg^{-1} \cdot s^{-1} \cdot bar^{-2}$	$1.07 \cdot \exp\left(\frac{36,696}{R \cdot T}\right)$
$k_2$	$mol \cdot kg^{-1} \cdot s^{-1} \cdot bar^{-1}$	$1.22 \cdot 10^{10} \cdot \exp\left(\frac{-94,765}{R \cdot T}\right)$
$K_1$	—	3,453.38
$K_2$	$bar^{-0.5}$	$0.499 \cdot \exp\left(\frac{17,197}{R \cdot T}\right)$
$K_3$	$bar^{-1}$	$6.62 \cdot 10^{-11} \cdot \exp\left(\frac{124,119}{R \cdot T}\right)$

In 2011, Henkel proposed a kinetic model based on the mechanism by Graaf, however, with direct CO-hydrogenation neglected [202]. In agreement to Graaf's finding, the steps A3 and B2 were considered rate determining by Henkel. The following set of rate equations was derived by Henkel:

$$r_{CO_2} = \frac{k_1 \cdot K_2 \cdot f_{CO_2} \cdot f_{H_2}^{1.5} \cdot EQ_1}{(1 + K_1 \cdot f_{CO} + K_2 \cdot f_{CO_2}) \left( f_{H_2}^{0.5} + K_3 \cdot f_{H_2O} \right)} \quad (3.56)$$

$$r_{rWGS} = \frac{k_2 \cdot K_2 \cdot f_{CO_2} \cdot f_{H_2} \cdot EQ_2}{(1 + K_1 \cdot f_{CO} + K_2 \cdot f_{CO_2}) \left( f_{H_2}^{0.5} + K_3 \cdot f_{H_2O} \right)} \quad (3.57)$$

As Henkel could not obtain one kinetic parameter set for the two experimental setups used within his studies (compare Sec. 2.5) he proposed the two parameter sets listed in Tab. 3.3.

Table 3.3: Kinetic parameters fitted by Henkel for the Berty reactor and the micro fixed bed reactor [202].

	Unit	Berty	Micro fixed bed
$k_1$	$mol \cdot kg^{-1} \cdot s^{-1} \cdot Pa^{-1}$	$4.629 \cdot 10^{-4} \cdot \exp\left(\frac{-47,472}{R \cdot T}\right)$	$3.172 \cdot 10^{-4} \cdot \exp\left(\frac{-45,893}{R \cdot T}\right)$
$k_2$	$mol \cdot kg^{-1} \cdot s^{-1} \cdot Pa^{-0.5}$	$12.975 \cdot \exp\left(\frac{-60,609}{R \cdot T}\right)$	$2.021 \cdot 10^6 \cdot \exp\left(\frac{-112,322}{R \cdot T}\right)$
$K_1$	$Pa^{-1}$	$2.743 \cdot 10^{-17} \cdot \exp\left(\frac{108,082}{R \cdot T}\right)$	$2.420 \cdot 10^{-14} \cdot \exp\left(\frac{81,976}{R \cdot T}\right)$
$K_2$	$Pa^{-1}$	$1.935 \cdot 10^{-4}$	$1.000 \cdot 10^{-4}$
$K_3$	$Pa^{-0.5}$	$5.797 \cdot 10^{-14} \cdot \exp\left(\frac{112,322}{R \cdot T}\right)$	$1.040 \cdot 10^{-8} \cdot \exp\left(\frac{61,856}{R \cdot T}\right)$

In 2014, Park et al. published a kinetic model based on the rate equations as provided by Graaf [203, 227]. As the authors used a catalyst similar to the one applied in this study and covered a wide parameter range by their experiments their kinetic model was considered highly relevant for this work. However, the kinetic model proposed by the authors entailed some weaknesses:

- a) In contrast to the models proposed by Bussche and Henkel, their kinetic rate equations still did account for CO-hydrogenation. This topic is discussed controversially in the scientific community [49].
- b) The authors included the DME kinetics originally measured over a different catalyst [204] in order to close their mass balances.
- c) The parameter set derived from their parameter fitting was not provided completely within their original publication (see parameters in Appendix A.19).

Therefore, the kinetic model published by Park et al. is not explicitly treated within this study. Nonetheless, as the authors published a complete set of integral experimental data, this data can be used for validation and parameter regression (for details see Sec. 3.5.1).

### 3.1.3 Diffusion model

Methanol synthesis is known to be subjected to mass transfer limitations depending on particle size and reaction conditions applied [139, 228]. The Thiele modulus [229]  $\phi_M$  is frequently applied in scientific literature to describe the diffusion limitation caused by the reactants passing through the porous structure of the catalyst towards the active sites [14, 168, 230]. Calculation methodology was adopted from Lommerts et al. [230] who discussed the applicability of Thiele modulus against the Dusty Gas Model: In their study the authors stated Thiele modulus as an appropriate compromise between computational time and accuracy. Thiele modulus was calculated via the pseudo-first order reaction rate with  $K'_{eq,H_2O}$  and  $K'_{eq,MeOH}$  representing the pseudo equilibrium constant [230] as well as  $k'_{H_2O}$  and  $k'_{MeOH}$  as pseudo-first-order rate constant [231]:

$$\phi_{M,j} = \frac{d_p}{6} \sqrt{\frac{k'_j \cdot (K'_{eq,j} + 1)}{D_{m,j}^e \cdot K'_{eq,j}}} \quad (3.58)$$

The effective diffusion coefficients for water and methanol in the mixture were obtained as follows [230, 231]:

$$\frac{1}{D_{m,j}^e} = \frac{\tau}{\varepsilon_p} \cdot \sum_{\substack{j=1 \\ j \neq k}}^N \frac{1}{D_{j,k}} + \frac{1}{D_{K,j}} \quad (3.59)$$

The diffusion coefficients for the single components in the reaction mixture  $D_{j,k}$  were calculated according to Fuller et al. [232] while calculation of the Knudsen diffusion coefficients  $D_{K,j}$  was performed with regard to Westerterp et al. [231]. Tortuosity  $\tau$  and porosity of the catalyst  $\varepsilon_p$  overtaken from Henkel [202] are listed in Tab. 3.4.

Table 3.4: Characteristic catalyst properties for the calculation of Thiele modulus determined by Henkel [202].

Parameter	Unit	Value
$\tau$	-	2.99
$\varepsilon_p$	-	0.58

The efficiency factor  $\eta_{eff}$  of the reactions  $i$  is calculated for the components  $j$  water and methanol as follows [230, 231]:

$$\eta_{eff,j} = \frac{r_{eff,i}}{r_i} = \frac{3 \phi_{M,j} \cdot \coth(3 \phi_{M,j}) - 1}{3 \phi_{M,j}^2} \quad (3.60)$$

Amongst the two efficiency factors obtained for water and methanol, the smaller value was considered for the effective reaction rate in order to describe the maximum overall diffusion limitation in the reaction network. Sensitivity of the efficiency factor towards  $\tau$ ,  $\varepsilon_p$  and  $d_p$  was discussed by a singular variation of these influence parameters within a one-dimensional reactor simulation for one representative working point (see Appendix A.5).

### 3.1.4 Steady state reactor model

Based on the sub-models for heat transfer, powder kinetics and diffusion, a steady state reactor model can be built utilizing the following ordinary differential equations (ODE) for mass, energy, and momentum balance [210]:

a) Material balance:

$$\frac{d\dot{n}_j}{dz} = \rho_{bulk} \cdot A_R \cdot \sum v_j \cdot r_i \quad (3.61)$$

b) Energy balance:

$$\frac{dT}{dz} = \frac{\sum \Delta H_{R,i} \cdot r_i \cdot A_R \cdot \rho_{bulk}}{\tilde{c}_{p,f} \cdot \dot{n}_{tot}} + \frac{\pi \cdot d_{int} \cdot U \cdot (T_{cool} - T)}{\tilde{c}_{p,f} \cdot \dot{n}_{tot}} \quad (3.62)$$

c) Momentum balance [210]:

$$\frac{dp}{dz} = - \left( 1.75 + 150 \cdot \frac{1 - \varepsilon_{bulk}}{Re_p} \right) \cdot \frac{1 - \varepsilon_{bulk}}{\varepsilon_{bulk}^3 \cdot d_p} \cdot \rho_f \cdot u_0^2 \quad (3.63)$$

Reynolds particle number  $Re_p$  applied in Ergun's equation (Eq. 3.63) was calculated by Eq. 3.12. The reactor model was verified by a comparison with other publications performing similar simulations with the proposed kinetic models [136, 145, 211, 233].

Due to the nature of the one-dimensional model, radial gradients inside the reactor were neglected in the simulation. However, the effect of this assumption towards the parameter fitting and scale-up may be investigated in future studies, utilizing more powerful computational resources.

### 3.1.5 Dynamic reactor model

Compared to the steady state reactor model, for the dynamic reactor model the storage term  $dx/dt$  is calculated in order to account for the transition of heat and mass from one load point to another. Consequently, the differential equations cannot be handled as ordinary differential

equations, but must be treated as partial differential equations (PDE). The following system of PDEs was applied for the dynamic reactor model:

$$\frac{dx_j}{dt} = \frac{-\frac{\dot{m}_{in}}{A_R} \cdot \frac{dx_j}{dz} + M_j \cdot \sum v_j \cdot r_i \cdot \rho_{bulk}}{\varepsilon_{bulk} \cdot \rho_f} \quad (3.64)$$

$$\frac{dT}{dt} = \frac{-\frac{\dot{m}_{in} \cdot c_{p,f}}{A_R} \cdot \frac{dT}{dz} + \frac{4 \cdot U}{d_{in}} \cdot (T_{cool} - T) + \sum \Delta H_{R,i} \cdot r_i \cdot \rho_{bulk}}{\rho_{bulk} \cdot c_{p,cat} + \varepsilon_{bulk} \cdot \rho_f \cdot c_{p,f}} \quad (3.65)$$

In comparison to the steady state model, for the dynamic reactor model mass fractions  $x_j$  were used to account for the mole reduction of the reaction more easily [180, 234]. The first-order derivative in the z-coordinate is solved using the two-point upwind finite difference method, where the axial grid is stepped through as follows [169, 235]:

$$\frac{dx_j}{dz} \approx \frac{x_{j,n} - x_{j,n-1}}{\Delta z} \quad (3.66)$$

$$\frac{dT}{dz} \approx \frac{T_n - T_{n-1}}{\Delta z} \quad (3.67)$$

For the first element of the grid the boundary conditions  $x_1 = x_{in}$  and  $T_1 = T_{in}$  were applied [235]. Due to the discretization of axial dimension of the PDE, the problem is transferred into the structure of an ODE and can be handled by the solvers implemented in MATLAB<sup>®</sup>. In order to define both, temperature and concentration of the reactants in every grid point, the grid is filled with starting values obtained from a steady state simulation at  $t = 0$ .

In Eq. 3.65 the heat capacity of the catalyst  $c_{p,cat}$  significantly influences the speed of adaption of the reactor towards a new load point. A comprehensive analysis of  $c_{p,cat}$  was performed by Henkel [202] who measured the heat capacity of the activated catalyst by temperature modulated differential scanning calorimetry. As a result Henkel provided a temperature dependent trend of  $c_{p,cat}$  which can be expressed by the following linear correlation:

$$c_{p,cat} = 428.584 \frac{J}{kg \cdot K} - 0.264 \frac{J}{kg \cdot K^2} \cdot T \quad (3.68)$$

Comparison between the steady state reactor model and the dynamic reactor model under steady state conditions showed similar simulation outputs. Small deviations in the reaction and temperature profile can be explained by the error of the two-point upwind difference method. However, this deviation was mitigated by a decrease of the step size of the axial grid. The behavior of the dynamic reactor model is discussed by means of a dynamic simulation campaign in App. A.24.

### 3.1.6 Process simulation model

To evaluate the impact of the kinetic model used in the reactor model introduced in Sec. 3.1.4 towards the operation of the methanol synthesis loop process, it was included into a process simulation performed in MATLAB<sup>®</sup> Simulink. The synthesis loop was implemented as depicted in Fig. 2.5. In the flow diagram, the loop balance was closed by calculation of the purge gas molar

flow  $\dot{n}_{purge}$  from the difference of the molar flow of non-condensed gas after the flash separator  $\dot{n}_{flash,g}$  and the desired molar flow for the recycle loop  $\dot{n}_{recycle}$  expressed via the molar flow of the MUG  $\dot{n}_{MUG}$  multiplied by the recycle ratio  $RR$  as follows:

$$\dot{n}_{purge} = \dot{n}_{flash,g} - \dot{n}_{recycle} = \dot{n}_{flash,g} - RR \cdot \dot{n}_{MUG} \quad (3.69)$$

The calculation of fluid phase equilibrium in the flash separator was performed using SRK EoS [135].

## 3.2 Numerical methods

The differential equations of the pseudo-homogeneous reactor model for both steady state and dynamic simulation were calculated by the solvers for ordinary differential equations implemented into MATLAB<sup>®</sup>. A selection of the solvers was performed with regard to MATLAB<sup>®</sup> documentation [236]. Since non-stiff solvers as "ode45" and "ode23" took long calculation times to solve the differential equations, "ode15s" as a non-stiff equation solver was selected instead. All three solvers led to the same profiles for molar fractions, temperature and pressure along the reactor, however, with ode15s being the most efficient solver.

Performance of the reactor model was found to be a key-element for the simulation platform, as complex analyses as e.g. the parameter fitting of a kinetic model on a large experimental data set requires numerous reactor simulations and consequently simulation time. Therefore, once implemented and tested, the reactor model was analyzed for issues in computational time. These issues were addressed during the development progress of the simulation platform as shown in Fig. 3.4 depicting the simulation time for four model revisions. For the comparison, a sensitivity analysis covering 480 steady state reactor simulations was carried out for the industrial reactor model.

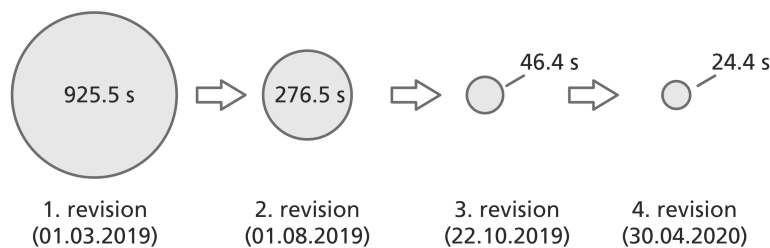


Figure 3.4: Speed-up of the simulation platform exemplified by a sensitivity analysis covering 480 reactor simulations.

The bottle-neck of the simulation with regard to computational time was identified as the sub-module for calculation of the thermodynamic data due to the high number of function calls in the integrator. Among the most important measures taken in order to speed-up the simulation code were:

1. Identification of slow program passages and MATLAB<sup>®</sup> commands, e.g. "roots()", nested for-loops or "xlsread()" (Tool: MATLAB<sup>®</sup> Profiler).

2. Replacement by faster calculation methods, e.g. Cardano's formula for determination of the zero points of a 3rd-order polynomial for SRK EoS instead of "roots()".
3. Vectorization of (nested) for-loops wherever possible.
4. Reduction of function calls by pre-definition of vectors and matrices in the main program and hand-through, e.g. for thermodynamic parameters.
5. Parallelization of "for"-loops (Tool: Parallel Computing Toolbox).
6. Translation of MATLAB<sup>®</sup>-code into c-code (Tool: MATLAB<sup>®</sup> Coder Toolbox).

All of these measures were applied to the source code of the simulation platform as the sub-models were developed further over time and complexity of the simulations increased. It is to be denoted, that the simulation time displayed in Fig. 3.4 was obtained for a sensitivity analysis using the industrial reactor model. As approximately 35 % of the calculation time of the industrial reactor model was consumed by the iterative approximation of the outer wall temperature of the steam cooled reactor (compare Sec. 3.1.1.2) the miniplant reactor model was less time consuming as this iteration is not necessary for convective thermal oil cooling. Due to the speed-up measures described in this section, the accuracy and convergence of the reactor model was not influenced. As a consequence, a parameter fitting requiring approximately 1 Mio. reactor simulations was possible in less than one day overall simulation time on a regular desktop computer.

### 3.2.1 Optimization methodology

Within this work, several optimization issues arose during the reactor simulation and design of the miniplant setup, e.g. for determination of the outer wall temperature in case of the steam cooled industrial reactor (see Sec. 3.1.1.2) or the simulation-based scale-down of the industrial reactor to miniplant size (see Sec. 3.3). While these problems did only feature one-dimensional optimization problems, i.e. optimization problems with one variable, the parameter fitting of kinetic models was a more complex issue. As the kinetic models considered within this study feature ten to twelve variables (compare Sec. 3.1.2), the optimization becomes a multi-dimensional problem. The selection of the optimization algorithm is of high importance for an efficient treatment of the problem in hand. As the simulation platform builds a reactor model resulting in a non-smooth behavior of simulation outputs for example due to numerical noise caused by tolerance of the ode-solvers, gradient-based optimization methods as the "fmincon"-algorithm implemented into MATLAB<sup>®</sup> Optimization Toolbox were unsuitable for the estimation of the kinetic parameters [237].

The "fminsearch"-algorithm as a direct search method was selected for the parameter fitting of the kinetic models instead [237, 238]. This algorithm suggests new variables around the initial starting values defined for the optimization problem. This so-called "simplex" is then moved by the operations "reflect", "expand", "contract inside", "contract outside" and "shrink" until the objective function is constant within a certain threshold or the minimum step size for the variation of the optimization problem is reached [237].

One main drawback of the "fminsearch"-algorithm in connection to the parameter fitting of the kinetic models was identified as the tendency of the solver to settle inside local minima. In order to mitigate this problem, the global "State Transition Algorithm" (STA) published by Zhou et

al. [239] was implemented into MATLAB<sup>®</sup> and tested for the purpose of the kinetic parameter fitting. This algorithm is based on random numbers spread around the local optimum by a Gaussian normal distribution. On the one hand this method led towards lower objective functions than the "fminsearch"-algorithm. On the other hand, the STA was found very inefficient resulting in impractical computational effort. Therefore, the STA was not applied further during this work.

Instead, it was found that a restart of the "fminsearch"-algorithm led to lower values for the objective function. This finding is based on to the fact that the simplex was expanded by the restart of the algorithm and thus able to overcome local minima. Therefore, it was concluded that "fminsearch" could be applied as a quasi-global optimizer within this work. Further research applying evolutionary optimization algorithms in combination with "fminsearch" are planned for future work.

### 3.3 Scale-down of the industrial reactor

Design of reactors for kinetic measurements is a complex topic subjected by numerous scientific studies [240–242]. In general, dimensions of kinetic setups are determined by dimensionless index number as e.g.:

- a) The Bodenstein number  $Bo$  with the axial dispersion coefficient calculated according to Kraume [243]

$$Bo = \frac{u_0 \cdot h_{cat}}{D_{ax}} \quad (3.70)$$

- b) The Reynolds particle number (see Eq. 3.12)  
 c) The reactor-particle diameter ratio [244].

$$\varphi = \frac{d_{int}}{d_p} \quad (3.71)$$

However, already in 1938 Damköhler et al. found that the scale-down of heterogeneous fixed bed reactors is not possible without violation of the terms of similarity [245]. Therefore, in classical kinetic setups ideal conditions by means of fluid dynamics, thermal operation and diffusion are acquired which, however, significantly differ from the industrial scale [241]. Hence, multiple experimental campaigns need to be executed to accurately transfer the results of small-scale measurements towards industrial scale.

The reactor of Shiraz methanol synthesis plant in Iran was used as a reference for the industrial scale in this study, as it is well documented in scientific literature [74, 164, 171, 246]. The steam cooled reactor is part of a conventional methanol synthesis facility producing methanol from a syngas obtained by NG reforming [74]. Design parameters for the industrial synthesis reactor are given in Tab. 3.5 [74, 169, 246, 247].

With regard to methanol synthesis as one of the oldest high pressure reactions, versatile research has been performed and rich knowledge on the modelling of heat transfer, kinetics and diffusion was published in the past decades [14, 44]. Therefore, a simulation-based approach was realized in this work in order to design an experimental miniplant setup with a high transferability of the

Table 3.5: Design parameters of the Shiraz methanol synthesis reactor based on scientific literature [74, 169, 246, 247].

Parameter	Unit	Value
$d_{\text{int}}$	m	0.038
$d_{\text{ext}}$	m	0.042
$h_{\text{cat}}$	m	7.022
$d_{\text{p}}$	m	0.0054
$\varepsilon_{\text{bulk}}$	-	0.39
$\rho_{\text{bulk}}$	$\text{kg m}^{-3}$	1132

experimental results towards industrial scale. As a key parameter, the GHSV was held equal for both industrial and miniplant reactor simulation to obtain similar residence times inside the reactor on both scales.

Based on this approach and infrastructural boundary conditions, the miniplant setup used within this work was designed and built. The following procedure was applied to design the reactor dimensions:

1. Definition of the miniplant scale considering the lab infrastructure
2. Design of a cooling system for a comparable heat transfer in the miniplant related to the industrial scale
3. Optimization of the reactor dimensions by minimizing the difference between the simulated temperature profiles of the industrial reactor and the miniplant using the simulation platform

In contrast to the industrial reactor implemented as multi tubular steam cooled reactor, the miniplant reactor consists of a double pipe arrangement with thermal oil circulated through the annular gap while the catalyst is placed inside the inner tube. The idea behind the thermal oil cooling of the miniplant was to counter-balance the higher cooling-area-to-catalyst-volume ratio of the miniplant in comparison to the industrial reactor by the lower external heat transfer coefficient  $\alpha_{\text{ext}}$  of the miniplant. The overall objective of this advanced cooling concept was to achieve a temperature profile inside the miniplant reactor comparable to that of the industrial reactor. Further details on the design of the miniplant are provided in Sec. 3.4.

In order to determine the reactor dimensions for a maximized comparability of the miniplant setup to the industrial scale, the diameter of the miniplant setup was varied with the catalyst bed length adjusted to the catalyst volume  $V_{\text{cat}}$  defined in the conceptual design of the miniplant correspondingly:

$$h_{\text{cat}} = \frac{4 \cdot V_{\text{cat}}}{\pi \cdot d_{\text{int}}^2} \quad (3.72)$$

The temperature profile inside the reactor was identified one key indicator for the similarities between industrial and miniplant reactor. Therefore, the RMSE between the temperature profiles was considered as objective function for the optimization of the miniplant geometry:

$$RMSE_T = \sqrt{\frac{\sum_{i=1}^{N_{T,inc}} (T_{x,i,ind} - T_{x,i,miniplant})^2}{N_{T,inc}}} \quad (3.73)$$

$RMSE_T$  was minimized by the Nelder Mead algorithm implemented as a "fminsearch"-algorithm in MATLAB® [238]. By performing simulations for both, industrial and miniplant setup, the dimensions listed in Tab. 3.6 were iteratively defined.

Table 3.6: Design parameters determined for the miniplant setup determined by the simulation-based scale-down and experiments.

Parameter	Unit	Value
$d_{int}$	m	$1.3 \cdot 10^{-2}$ *
$d_{ext}$	m	$1.6 \cdot 10^{-2}$ *
$h_{cat}$	m	1.14 *
$d_p$	m	$1.0 \cdot 10^{-3}$ (see App. A.10)
$\varepsilon_{bulk}$	-	0.395 [248]
$\rho_{bulk}$	kg m <sup>-3</sup>	1134 [248]
$d_{shell}$	m	$2.1 \cdot 10^{-2}$ *
$\dot{V}_{oil}$	l min <sup>-1</sup>	17.1 (see App.A.8)

\* determined by simulation-based scale-down

The dimensionless index numbers defined previously are provided for both, industrial and miniplant setup in Tab. 3.7.

Table 3.7: Dimensionless index numbers for the industrial and the miniplant reactor; Bodenstein number  $Bo$  and Reynolds particle number  $Re_p$  were calculated at the following working point:  $T_{in} = 240$  °C;  $p = 80$  bar;  $COR = 0.9$ ;  $SN = 4.0$ ;  $GHSV = 6,000$  h<sup>-1</sup>.

Parameter	Unit	Industrial reactor[74]	Miniplant reactor
$Bo$	-	1014	900
$\varphi$	-	7.04	13
$Re_p$	-	1185	36

Comparison of the dimensionless indices shows that both reactor scales satisfy the criteria for ideal plug flow [212], i.e.  $Bo > 80$ , and non-laminar particle flow, i.e.  $Re_p > 10$ . The difference of the  $Re_p$  numbers between industrial and miniplant reactor due to the adjusted reactor and catalyst geometries was considered in the simulation of pressure loss as well as convective heat transfer inside the reactor. As the reactor-particle-ratio satisfies the criterion  $\varphi > 10$ , wall effects in the miniplant were neglected [212, 241]. However, in case of the industrial reactor  $\varphi$  was below this critical threshold. Measured data obtained from this reactor would be helpful to quantify

possible deviations from the herein assumed ideal plug flow behavior for the industrial reactor. The inner diameter of 13 mm for the miniplant reactor was obtained by the simulation-based scale-down utilizing the kinetic model by Bussche-Froment [145] at high CO<sub>2</sub> contents. As the choice of the kinetic model was found to influence the optimal reactor dimensions significantly, optimized miniplant dimensions applying the kinetic model derived within this work will be presented in Sec. 4.2.6. These were determined for a wide range of synthesis conditions covering two different pressure levels of 50 bar and 80 bar at GHSV = 9,000 h<sup>-1</sup>. Feed gas composition was varied in the range  $2.0 \leq \text{SN} \leq 8.0$  and  $0.5 \leq \text{COR} \leq 1.0$ .

### 3.4 Miniplant setup

Concept design of the miniplant setup was performed before the final reactor diameter and length were defined by the simulation-based scale-down described in Sec. 3.3. In order to be able to directly measure the reaction product from both, steady state and dynamic experiments, the recycle loop of the industrial process was not included into the miniplant setup. On the one hand this simplification moves the behavior of the miniplant setup away from the industrial precursor as non-condensed recycled products like water and methanol are not present in the reactor feed and the diluting effect of the recycle loop is not accounted for. On the other hand, the once-through operation enables a scale-independent consideration of load changes and simplifies gas phase measurement as well as mass balancing of the miniplant. Moreover, the control strategy and the miniplant behavior are easier to handle compared to a setup including the recycle loop [249]. Emulation of the recycle loop, however, was possible by the flexible gas dosing capable of accounting for the complex interplay between CO<sub>2</sub>-hydrogenation and rWGS in the industrial loop process.

A simplified flow sheet of the miniplant setup utilized within this work is given in Fig. 3.5. The reaction educts CO, CO<sub>2</sub>, H<sub>2</sub> as well as the inert gas nitrogen (N<sub>2</sub>) can be flexibly and precisely dosed into the system. Due to the high synthesis pressures up to 80 bar applied to the system, a liquid dosing of CO<sub>2</sub> utilizing an HPLC-pump coupled with a Coriolis flow meter was designed for the system [250]. The liquid CO<sub>2</sub> was mixed with the other educts and evaporated along a heated line towards the reactor. The correct calibration of the gas dosing unit was verified by gas phase measurements through the bypass line at the beginning of each experimental day.

The heat released by the reaction inside the inner tube was removed by thermal oil circulating along the annular gap in counter current flow. Volumetric flow rate of the oil was measured by a rotameter calibrated for the thermal oil used inside the cooling system (Fragoltherm X-400-A). Temperature of the thermal oil was controlled by a closed-cycle thermostat.

The reactor was filled with a commercial Cu-based catalyst provided by Clariant AG. The pelletized catalyst particles were ground and sieved to a particle size of  $d_p = 1$  mm to avoid wall effects inside the reactor. The analysis of the particle size distribution of the catalyst is provided in Appendix A.10. An inert bed of  $\alpha$ -alumina supplied by Merck KGaA was placed above and below the catalyst bed. The fixed bed was held inside the reactor with a porous stainless steel support disc. Blind tests introducing syngas into the heated reactor only filled with the inert material confirmed the inert behavior of this material, as no trace compounds were detected by

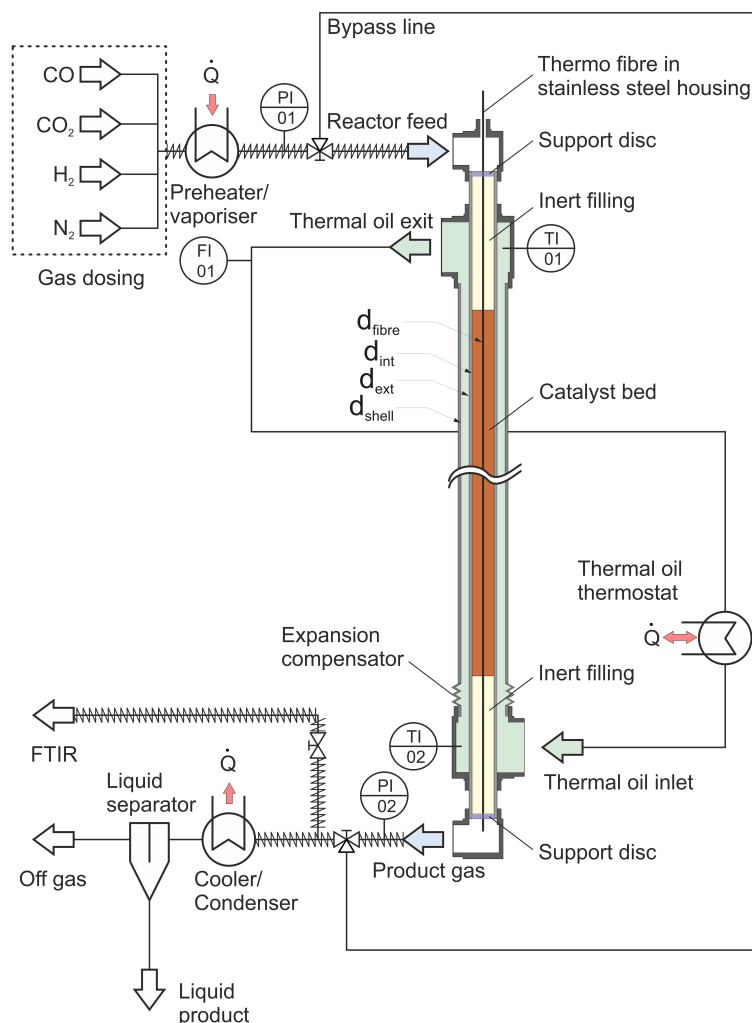


Figure 3.5: Simplified flow sheet of the experimental miniplant setup.

the gas phase measurement.

In order to gather axial information about the reaction kinetics, the reactor was equipped with a system for fiber optical temperature measurement described in detail in Sec. 3.4.1. The glass fiber was placed inside a 0.8 mm steel capillary; the optical signal was generated and processed by a Luna ODiSI 6102 unit. An axial resolution of  $\Delta z = 2.6$  mm was selected for the measurement campaign leading to 438 measurement increments for temperature measurement ( $N_{T,inc}$ ) inside the catalyst bed with a length of 1.14 m. Calibration of the fiber was carried out by heating the thermal oil cycle to constant temperature levels between 50 °C and 265 °C. The oil inlet and outlet temperatures were measured by two Pt-100 temperature sensors at the oil inlet (TI02) and outlet (TI01); a heat loss resulting in a temperature decrease of approximately 1.5 K between thermal oil inlet and outlet was regarded by a linear temperature decrease along the reactor. The cooling temperature  $T_{cool}$  was adjusted to the reading of TI01. As a result of the calibration a polynomial of 3rd degree was determined for each increment along the fiber. Extrapolation of these polynomials was performed for temperatures exceeding 265 °C as the thermal oil did not allow for higher calibration temperatures due to reasons related to plant safety.

For analysis of the reaction products a MKS MultiGas<sup>TM</sup> 2030 on-line Fourier-transform infrared

spectrometer (FTIR) with an optical path length of 35 cm was used for quantitative product analysis. Since H<sub>2</sub> as a homonuclear gas cannot be detected by FTIR, the molar fraction of this gas was determined by the component balance as follows:

$$y_{H_2} = 1 - \sum_{j=1}^{N_{comp}} y_j \quad (3.74)$$

Besides the main reactants CO, CO<sub>2</sub>, H<sub>2</sub>O and MeOH, side products such as methyl formate, methane, ethanol, acetone and acetic acid were calibrated and analyzed by the FTIR. However, their concentrations below 100 ppm in the product gas made an exact quantification in the gas phase impossible with the FTIR applied in this work. Therefore, the side products mentioned above were excluded from the mass balance over the reactor.

Besides the gas phase analysis, the main product stream was led through a cooler-condenser unit at an operating temperature of 10 °C to separate the liquid products from the gas phase for qualitative analysis of condensable trace compounds. Analysis of the liquid phase was carried out using Nuclear magnetic resonance spectroscopy (NMR).

All real time information on sensor properties such as volumetric flow rates, inlet and outlet pressures, temperature profile as well as gas phase composition were logged with a sample rate of 1 Hz.

### 3.4.1 Fiber optic temperature measurement

One key-element of the miniplant setup is the fiber optic temperature measurement. The measurement principle of this technology is based on axial variation of the refractive index along a glass fiber due to impurities or local defects [207]. Application of Fourier transformation to a back-scattered light signal leads to continuous information about the (thermal) expansion of the fiber and thereby delivers a highly resolved temperature information.

Measured data obtained from the fiber was acquired with a frequency of 1 Hz. However, in order to remove time-resolved noise from the signal, the maximum measurement frequency of 128 Hz was applied for five values in a sequence. The median value was used to remove outliers from the temporally resolved signal.

To account for the non-linearity and possible mechanical tension of the fiber optic temperature sensor, calibration of the measurement system was executed [248]. Due to axial irregularities in the displayed output values, the calibration had to be performed separately for each increment along the fiber. The thermal oil cycle was adjusted to fixed temperature levels to set a constant temperature along the axial reactor length. During calibration the reactor was filled with N<sub>2</sub>, however, without gas flow to prevent convective heat transfer phenomena at the gas inlet zone. In order to transform the uncalibrated temperature reading into an accurate output signal, the following temperature dependent 3rd-order polynomial was fitted for each increment along the fiber:

$$T_{calib} = A \cdot T^3 + B \cdot T^2 + C \cdot T + D \quad (3.75)$$

The inlet and outlet temperature of the thermal oil were measured by Pt-100 temperature sensors. Depending on the temperature level, the oil outlet temperature was 1.0 K to 2.0 K below the oil inlet temperature. As the temperature difference increased by rising temperature level, this phenomena was ascribed to heat losses through the axial insulation of the reactor. These losses were accounted by a linear interpolation of the temperature profile of thermal oil between the Pt-100 temperature sensors.

Calibration was executed between temperatures of 50 °C and 265 °C. Higher temperatures were not possible as the flame point of the thermal oil was specified by the manufacturer to 275 °C [220]. With regard to the safety concept, temperature was kept 10 °C below the flame point to have a buffer for a possible emergency turn-off or a control overshoot of the thermostat. Calibration temperature was increased by steps of 25 K from 50 °C until 200 °C and by increments of 5 K for temperatures exceeding 200 °C to achieve a maximum accuracy in the relevant temperature range. As a consequence of the conversion error of the analogue-digital converters of the Pt-100 temperature sensors, the measurement error accounted to  $\pm 0.4$  K. In Fig. 3.6 the temperature offset between calibrated and displayed temperature is plotted over the calibrated temperature for one measurement increment of the fiber. The calibration polynomial is displayed as dashed line.

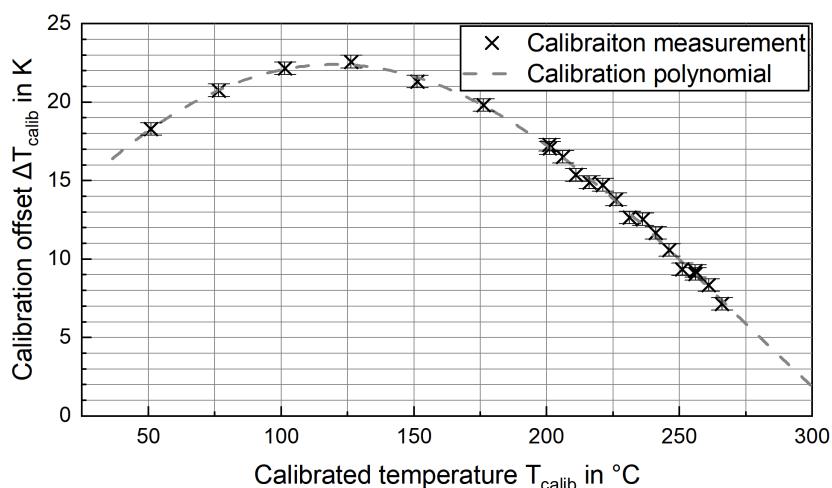


Figure 3.6: Calibration offset over the calibrated temperature between 50 °C and 265 °C together with the fitted 3rd-order polynomial extrapolated to 25 °C and 300 °C at one measurement increment along the fiber.

As temperatures exceeding 265 °C occurred in the reactor during the kinetic experiments, the polynomial had to be extrapolated. Extrapolation could result in an error, however, this procedure was inevitable due to the reasons of plant safety mentioned above. Overall, the calibration set resulted in 580 polynomials in the heated zone of the reactor covering the height of the catalyst bed and the inert bed approximately 20 cm above and below the catalyst bed. In order to obtain information on the temperature profile along the inert bed outside the heating zone, the mean values of the polynomial parameters fitted inside the heated zone were applied as calibration parameters. However, these zones were not relevant for the validation of the kinetic reactor model.

Issues for the calibration of the measurement system arose from  $H_2$  diffusing through the shell of the stainless-steel capillary into the glass fiber. This phenomenon led to a long-term drift of the calibration. Repetition of the calibration procedure showed, that this drift could be addressed by adjustment of the offset  $D$  in Eq. 3.75. Moreover, a leakage was detected during the kinetic measurements at the bottom soldering point at the end of the fiber. This issue, however, could be fixed by an in situ repair applying tungsten inert gas welding inside the bottom flange of the reactor. The problem probably arose, as the bottom of the fiber was sealed by copper instead of stainless-steel by the manufacturer.

The temperature profiles measured by the fiber optic processing unit were subjected to fluctuations caused by slight heterogeneity of the distribution of the catalyst particles along the fiber. Among other possible smoothing filters as e.g. the moving median or a Gaussian weighted moving average [236], the Savitzky-Golay filter [251] was identified as the most robust and least distorting algorithm.

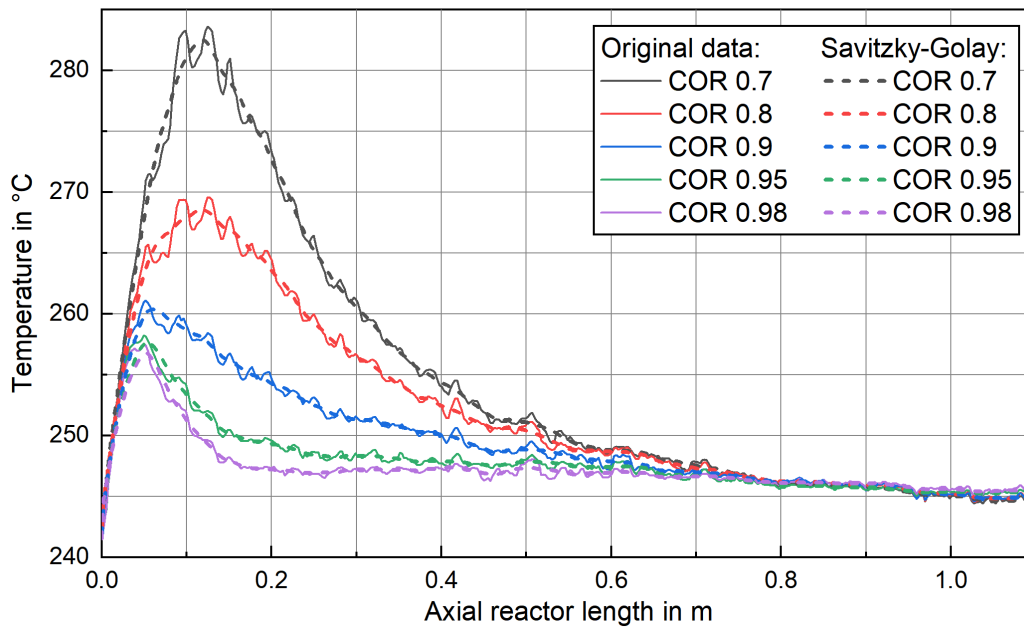


Figure 3.7: Calibrated temperature profile measured by the fiber optic processing unit and Savitzky-Golay smoothed temperature profile obtained with a moving window of 40 elements at  $p = 80$  bar;  $T_{\text{cool}} = 240$  °C;  $SN = 5.0$  and  $GHSV = 9,000$   $h^{-1}$  for  $COR = 0.7, 0.8, 0.9, 0.95$  and  $0.98$ .

In Fig. 3.7 the calibrated original data as obtained by the fiber optic processing unit is displayed together with the Savitzky-Golay smoothed data. The working points were obtained at a working pressure of 80 bar and a cooling temperature of 240 °C at  $GHSV = 9,000$   $h^{-1}$ .  $SN$  was held constant at 5.0, while  $COR$  was varied between 0.7 and 0.98. The graph indicates that the smoothing filter is capable of removing noise from the signal without losing the core information obtained from the measurements. During the parameter fitting of the kinetic models described in Sec. 3.5.2.2, better results with less conflicts due to local minima were obtained with the smoothed data instead of the original data. For the algorithm a moving window of 40 elements

was applied. Smaller moving windows increased the noise on the signal, while higher values led to loss of information on the hot spot position and temperature.

### 3.5 Experimental validation

To evaluate the impact of the herein proposed methodology, a steady state kinetic model was derived from both, integral measured data taken from literature [203] and differential temperature data in combination with the integral FTIR product measurement from the miniplant. The methodology for both approaches will be explained in Sec. 3.5.1 and 3.5.2, respectively.

#### 3.5.1 Integral literature data

In order to obtain a kinetic model applicable towards a wide working range of conventional and renewable feedstock-based methanol synthesis, a kinetic model was derived from the experimental data published by Park et al. [203]. Application of the kinetic rate equations published by Henkel (i.e. Eq. 3.56 and Eq. 3.57) refitted to the experimental data was presumed to lead to a highly relevant kinetic model based on a commercial state-of-the-art catalyst. The model parameters will be compared to those elaborated by Henkel in Sec. 4.1. The macroscopic effect of the integral kinetic model derived within this work in comparison to state-of-the-art models will be discussed within a comprehensive sensitivity study utilizing the one-dimensional model of an industrial methanol synthesis reactor in Sec. 4.1.2. Details on the experimental setup used by Park et al. are provided elsewhere [203].

For the re-fitting of the kinetic model to the measured data provided in the publication by Park et al. [203], a parameter screening and pre-selection of the data was performed. As the mechanism proposed by Henkel does not consider direct CO-hydrogenation, measured values with  $COR = 0.00$  were not considered within this study. Four experimental points were therefore excluded from the data set. The remaining quantity of 114 experimental points ( $N_{data\ pt}$ ) were used for the parameter fitting within this study (see App. A.6). Based on C, H, O balances, the mole fractions at the reactor exit were determined from the CO and CO<sub>2</sub> conversion given in the original publication. This calculation procedure was performed in order to decrease the sensitivity of the parameter fitting towards measurement errors at low concentrations. Before this procedure was applied, high conversion rates at low total concentrations did largely affect the resulting model parameters especially when measurements at low COR were included to the fitting. Therefore, it is concluded that the measurement campaign by Park et al. could be affected by measurement errors especially at low concentrations of CO<sub>2</sub>. This statement, however, needs to be validated by additional experimental data.

For the fitting procedure, the data were imported into a MATLAB<sup>®</sup> reactor model of the kinetic reactor as documented by Park et al. [203]. The simulated output values ( $y_{j,sim}$ ) were then compared against the measured data ( $y_{j,exp}$ ) by means of the root mean square error (RMSE). RMSE was calculated for the molar fractions of CO and CO<sub>2</sub> as follows:

$$f(x) = RMSE_{CO_2} + RMSE_{CO} \quad (3.76)$$

$$RMSE_{CO_2} = \sqrt{\frac{\sum_{i=1}^{N_{data\ pt}} (y_{CO_2, sim, i} - y_{CO_2, exp, i})^2}{N_{data\ pt}}} \quad (3.77)$$

$$RMSE_{CO} = \sqrt{\frac{\sum_{i=1}^{N_{data\ pt}} (y_{CO, sim, i} - y_{CO, exp, i})^2}{N_{data\ pt}}} \quad (3.78)$$

The objective function  $f(x)$  defined as the sum of  $RMSE_{CO}$  and  $RMSE_{CO_2}$  was minimized by adaption of the ten model parameters with the starting values taken from Henkel's original parameter set (see Tab. 3.3). For minimization, the multidimensional unconstrained non-linear Nelder-Mead algorithm implemented within the "fminsearch"-method by MATLAB<sup>®</sup> was applied [238].

### 3.5.2 Differential miniplant data

For deeper insights into the kinetic performance of methanol synthesis on industrial scale, a novel approach for the validation of reaction kinetics using the miniplant described in Sec. 3.4 was investigated within this work. In comparison to classic kinetic setups as e.g. the one applied by Park et al. [203], this setup was intentionally held under polytropic operating conditions by a thermal oil cooling system. Application of fiber optical temperature measurement delivered highly resolved axial information on the differential catalytic activity which was used in connection with FTIR product measurement for the validation and adjustment of kinetic models. The experimental campaign executed with the miniplant setup as well as the validation procedure will be presented in the following sections.

#### 3.5.2.1 Experimental plan

In order to determine the reaction kinetics over a wide parameter range relevant for application with CO<sub>2</sub>-rich syngas, a comprehensive experimental plan was executed. Besides pressure, the parameters GHSV, COR and SN were varied in the experimental campaign due to their relevance for reaction kinetics [206]. The variation ranges of the experimental parameters are provided in Tab. 3.8. All combinations of the parameters listed were applied to the experimental setup at a cooling temperature of 240 °C.

Table 3.8: Parameters applied for the experimental campaign at the miniplant setup.

Parameter	Varied range
p	50 bar; 65 bar; 80 bar
GHSV	6,000 h <sup>-1</sup> ; 9,000 h <sup>-1</sup> ; 12,000 h <sup>-1</sup>
COR	0.7; 0.8; 0.9; 0.95; 0.98
SN	2.0; 3.0; 4.0; 5.0; 6.0; 7.0; 8.0

To consider the effect of lower cooling temperatures the parameter variation at 50 bar was also executed at  $T_{cool} = 220$  °C in a COR range between 0.7 and 0.95 and SN between 2.0 and 8.0.

When the experimental campaign was executed, 24/7 operation of the miniplant facility was not implemented yet. Therefore, the campaign was interrupted, when no operation was possible, e.g. over night, weekend or during maintenance intervals. While the miniplant setup was held at 160 °C and flushed with N<sub>2</sub> over night (hot standby), it was blocked with N<sub>2</sub> at ambient temperature (cold standby) for longer downtime periods. However, the activity of the catalyst was benchmarked at the beginning and end of each experimental day – no effects due to hot or cold standby could be observed. The chronological progress of the overall experimental campaign is provided in App. A.12.

Due to instability of some experimental points as a result of oscillations in CO<sub>2</sub> dosing or hot spot temperatures expected to exceed the critical threshold of 280 °C, some of the data points could not be included into the validation resulting in an overall set of 324 data points ( $N_{data\ pt}$ ). To account for activity changes during the experimental campaign a benchmark measurement was repeatedly executed. The benchmark condition was defined at COR = 0.9, SN = 4.0, GHSV = 12,000 h<sup>-1</sup> and T<sub>cool</sub> = 240 °C in coordination with project partners [252].

The experimental plan was executed in seven phases as follows:

1. Ramp-up at benchmark conditions at 50 bar:  
p = 50 bar; T<sub>cool</sub> = 240 °C; SN = 4.0; COR = 0.9; GHSV = 12,000 h<sup>-1</sup>;
2. Parameter variation at 50 bar and 240 °C:  
p = 50 bar; T<sub>cool</sub> = 240 °C; 2.0 ≤ SN ≤ 8.0; 0.7 ≤ COR ≤ 0.95; 6,000 h<sup>-1</sup> ≤ GHSV ≤ 12,000 h<sup>-1</sup>
3. Parameter variation at 65 bar and 240 °C:  
p = 65 bar; T<sub>cool</sub> = 240 °C; 2.0 ≤ SN ≤ 8.0; 0.7 ≤ COR ≤ 0.95; 6,000 h<sup>-1</sup> ≤ GHSV ≤ 12,000 h<sup>-1</sup>
4. Parameter variation at 80 bar and 240 °C:  
p = 80 bar; T<sub>cool</sub> = 240 °C; 2.0 ≤ SN ≤ 8.0; 0.7 ≤ COR ≤ 0.95; 6,000 h<sup>-1</sup> ≤ GHSV ≤ 12,000 h<sup>-1</sup>
5. Parameter variation at COR = 0.98 and 240 °C:  
50 bar ≤ p ≤ 80 bar; T<sub>cool</sub> = 240 °C; 2.0 ≤ SN ≤ 8.0; COR = 0.98; 6,000 h<sup>-1</sup> ≤ GHSV ≤ 12,000 h<sup>-1</sup>
6. Parameter variation at 50 bar and 220 °C:  
p = 50 bar; T<sub>cool</sub> = 220 °C; 2.0 ≤ SN ≤ 8.0; 0.7 ≤ COR ≤ 0.95; 6,000 h<sup>-1</sup> ≤ GHSV ≤ 12,000 h<sup>-1</sup>
7. Benchmark at conditions of phase 1.)

During phase 1.) the benchmark conditions were held constant for 56 h time-on-stream (ToS). In phase 5.) COR was held constant at 0.98 at the three pressure levels considered. This variation was not included into phases 2.) to 4.) as catalyst deactivation was expected during these experiments due to the high CO<sub>2</sub> content. After the parameter variation was terminated, the benchmark point of phase 1.) was held constant for another 12 h.

### 3.5.2.2 Validation and parameter fitting

To validate the performance of the kinetic models proposed by Bussche and Graaf (see Sec. 3.1.2) as well as the integral kinetic model derived in Sec. 4.1, reactor simulations utilizing these models were executed for all working points gathered during the experimental campaign. In order to quantify the deviations between these models and the experimental data, RMSE values considering both, information on the thermal behavior and the composition of the gas phase were calculated. The objective function  $f(x)$  for the parameter fitting was formulated as the

sum of the weighted root mean square errors for temperature profile ( $RMSE_{T,profile}$ ), hot spot temperature ( $RMSE_{T,hs}$ ) and gas phase composition at reactor outlet ( $RMSE_y$ ):

$$f(x) = \alpha \cdot RMSE_{T,profile} + \beta \cdot RMSE_{T,hs} + \gamma \cdot RMSE_y \quad (3.79)$$

$RMSE_{T,profile}$  in Eq. 3.79 was calculated considering all working points  $i$  along the axial temperature measurement increments  $j$  from the start to end of the catalystr bed as follows:

$$RMSE_{T,profile} = \sqrt{\frac{\sum_{i=1}^{N_{data\ pt}} \left( \frac{\sum_{j=1}^{N_{T,inc}} |T_{exp,i,j} - T_{sim,i,j}|}{N_{T,inc}} \right)^2}{N_{data\ pt}}} \quad (3.80)$$

$RMSE_{T,hs}$  was calculated for the maximum temperature measured and simulated for the working points using the following equation:

$$RMSE_{T,hs} = \sqrt{\frac{\sum_{i=1}^{N_{data\ pt}} (T_{hs, exp,i} - T_{hs, sim,i})^2}{N_{data\ pt}}} \quad (3.81)$$

To account for the gas phase composition,  $RMSE_y$  was calculated for all working points considering the molar fractions of the components  $j$  in the product gas mixture:

$$RMSE_y = \sqrt{\frac{\sum_{i=1}^{N_{data\ pt}} \left( \frac{\sum_{j=1}^{N_{comp}} |y_{exp,i,j} - y_{sim,i,j}| \cdot 100\%}{N_{comp}} \right)^2}{N_{data\ pt}}} \quad (3.82)$$

The weighting factors  $\alpha$ ,  $\beta$  and  $\gamma$  were fixed to constant values of  $\alpha = 2 \text{ K}^{-1}$ ,  $\beta = 3 \text{ K}^{-1}$  and  $\gamma = 25$  by an empirical approach in order to balance the RMSE of temperature and composition to comparable numerical values [253].

Fig. 3.8 right shows a comparison between the experimental data obtained at the benchmark gas composition at 50 bar and the reactor simulation using the kinetic model as proposed by Bussche [145]. As the model by Bussche was derived from a different catalyst using integral experimental data, strong deviations between the experimental data and the simulation are present in temperature profile, hot spot temperature and product composition. A detailed discussion on the deviation between the experimental data and the simulation results obtained using the original kinetic models proposed by Bussche and Graaf as well as the integral kinetic model fitted to Park's experimental data is given in Sec. 4.2.2.

To minimize the deviation between the reactor simulation and the experimental data, the kinetic constants and adsorption constants of the kinetic models were adjusted by a parameter fitting minimizing the objective function  $f(x)$  defined in Eq. 3.79.

A flow diagram indicating the procedure of the parameter fitting is provided in Fig. 3.8 on the left. The initial parameter set for the rate equations considered was overtaken from the original publications by Graaf and Bussche as well as from the integral kinetic model derived in Sec. 4.1. The objective function, i.e. the deviation between the experimental data and the reactor

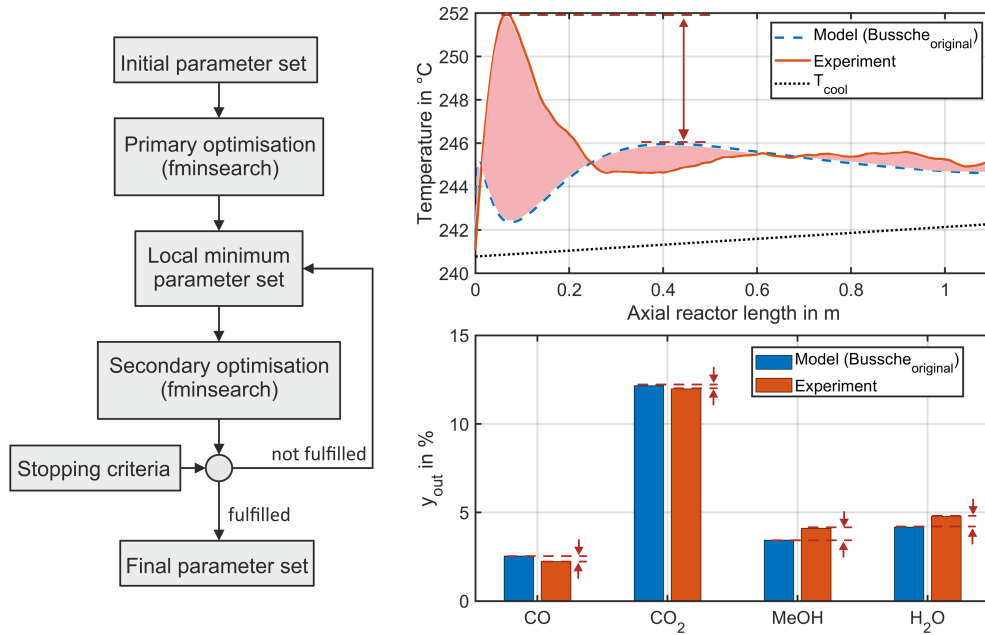


Figure 3.8: Illustration of the parameter fitting methodology applied in this work (left) and an exemplary working point a benchmark conditions at 50 bar showing the temperature profile (right, top) and gas phase molar fractions (right bottom) obtained from the experiment (solid, red) and the miniplant reactor simulation (dotted, blue) using the kinetic model as proposed by Bussche [145]; Red arrows and areas indicate the deviations between the simulation and the experimental data addressed by the parameter fitting; The measured temperature profile is smoothed by the Savitzky-Golay filter [251].

simulation results, was then minimized during the primary optimization by the "fminsearch" algorithm (see Sec. 3.2.1). Starting from the improved parameter set, the optimization algorithm was repeated (secondary optimization) until the objective function was not improved further to mitigate local minima. Once a set of kinetic parameters was found fulfilling the stopping criteria, this set was subjected to a further analysis.

### 3.5.2.3 Impact on industrial reactor design

For the demonstration of the impact of the differential kinetic model on the industrial scale reactor in comparison to the integral kinetic model [206], a simulation study was performed analyzing hot spot position and temperature as well as product composition, in an industrial reactor simulation at the pressure levels 50 bar and 80 bar at  $GHSV = 6,000 \text{ h}^{-1}$ . For the gas composition the range applied in the experimental campaign was considered (see Tab. 3.8). Inlet and cooling temperatures were set to  $240 \text{ }^\circ\text{C}$ .



## 4 Results and Discussion

In this chapter the main results of the kinetic parameter fitting performed for integral and differential experimental data will be discussed Sec. 4.1 and Sec. 4.2, respectively. As both sets of measured data are based on a similar catalyst, a comparison between the derived kinetic models will be performed in order to demonstrate their deviations originating from the different methodical approaches. The integral model based on Henkel's kinetic model and fitted to the measured data published by Park et al. will be designated as "Nestler<sub>integ</sub>" from hereon. The differential kinetic model based on Nestler<sub>integ</sub> fitted to the miniplant data will be labeled "Nestler<sub>diff</sub>".

In Sec. 4.3, the performance of the dynamic reactor simulation including the Nestler<sub>diff</sub> kinetic model will be validated against one representative load change experiment measured at the miniplant setup. Finally, in Sec. 4.4, the differential kinetic model derived within this work will be held against one important literature standard on the process scale.

### 4.1 Kinetic model derived from integral literature data

In Fig. 4.1 the final fitting result is presented for the Nestler<sub>integ</sub> kinetic model in a parity plot comparing the measured and simulated molar fractions of CO and CO<sub>2</sub> at the exit of the reactor. The plot illustrates that most values lie within the 20 % error region. RMSE values of 0.042 for the CO molar fractions and 0.084 for CO<sub>2</sub> molar fractions were obtained applying the kinetic model after the parameter estimation. These deviations could be based on analytical inaccuracies

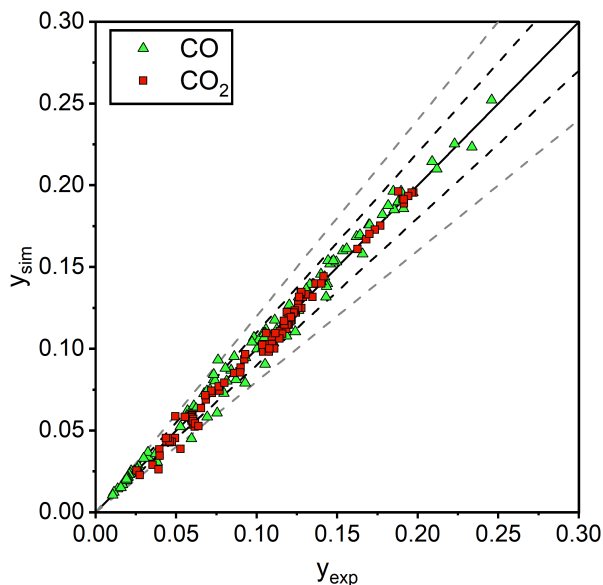


Figure 4.1: Parity plot of the kinetic model fitted to the measured data published by Park et al. [203] including the error lines for 0 % (solid, black), 10 % (dashed, black) and 20 % (dashed, gray).

or systematic errors as e.g. the deactivation of the catalyst or temperature gradients along the fixed bed. However, these possible issues were not discussed by Park et al. [203]. Moreover, the remaining error could be due to insufficient mechanistic assumption within the proposed model equation.

Generally, the model describes the whole range of the measured data set in acceptable range. Importantly, the kinetic model  $Nestler_{integ}$  proposed within this section does not constitute a final kinetic expression, but rather a working base which can will compared to the kinetic model derived from the differential miniplant experimental data in Sec. 4.2.

The kinetic parameters obtained from the fitting procedure are given in Tab. 4.1.

Table 4.1: Parameters for the  $Nestler_{integ}$  kinetic model proposed within this work.

	Unit	$Nestler_{integ}$ kinetic parameters
$k_1$	$mol \cdot kg^{-1} \cdot s^{-1} \cdot Pa^{-1}$	$5.411 \cdot 10^{-4} \cdot \exp\left(\frac{-45,458}{R \cdot T}\right)$
$k_2$	$mol \cdot kg^{-1} \cdot s^{-1} \cdot Pa^{-0.5}$	$4.701 \cdot \exp\left(\frac{-54,970}{R \cdot T}\right)$
$K_1$	$Pa^{-1}$	$3.321 \cdot 10^{-18} \cdot \exp\left(\frac{109,959}{R \cdot T}\right)$
$K_2$	$Pa^{-1}$	$8.262 \cdot 10^{-6}$
$K_3$	$Pa^{-0.5}$	$6.430 \cdot 10^{-14} \cdot \exp\left(\frac{119,570}{R \cdot T}\right)$

In agreement with literature findings the reaction rate constants for CO<sub>2</sub>-hydrogenation ( $k_1$ ) and rWGS ( $k_2$ ) increase with increasing temperature [145, 192, 254].

While the adsorptions constants for CO ( $K_1$ ) as well as H<sub>2</sub>O and H<sub>2</sub> ( $K_3$ ) decrease with increasing temperature, the adsorption constant for CO<sub>2</sub> ( $K_2$ ) does not show any temperature dependence. This finding is in line with the parameter estimation by Henkel who also did not determine a temperature dependence of this constant [202].

In Tab. 4.2 the RMSE values for the measured data published by Park and the kinetic models by Graaf, Bussche and Henkel as well as  $Nestler_{integ}$  are listed. It can be concluded that the model by Graaf shows the highest deviation from the measured data and is therefore not appropriate for the description of the kinetic data considered in this study. A better fitting result could be achieved with the models by Bussche and Henkel. However, by application of the fitting

Table 4.2: Comparison of the RMSE for the molar fractions measured by Park [203] and simulated using the kinetic models by Graaf [192], Bussche [145] and Henkel [202] as well as the kinetic model  $Nestler_{integ}$ .

Kinetic model	RMSE <sub>CO</sub> in %	RMSE <sub>CO2</sub> in %
Graaf	2.453	0.917
Bussche	1.085	0.528
Henkel, Berty	0.833	0.529
Henkel, fixed bed	0.877	0.522
$Nestler_{integ}$	0.605	0.441

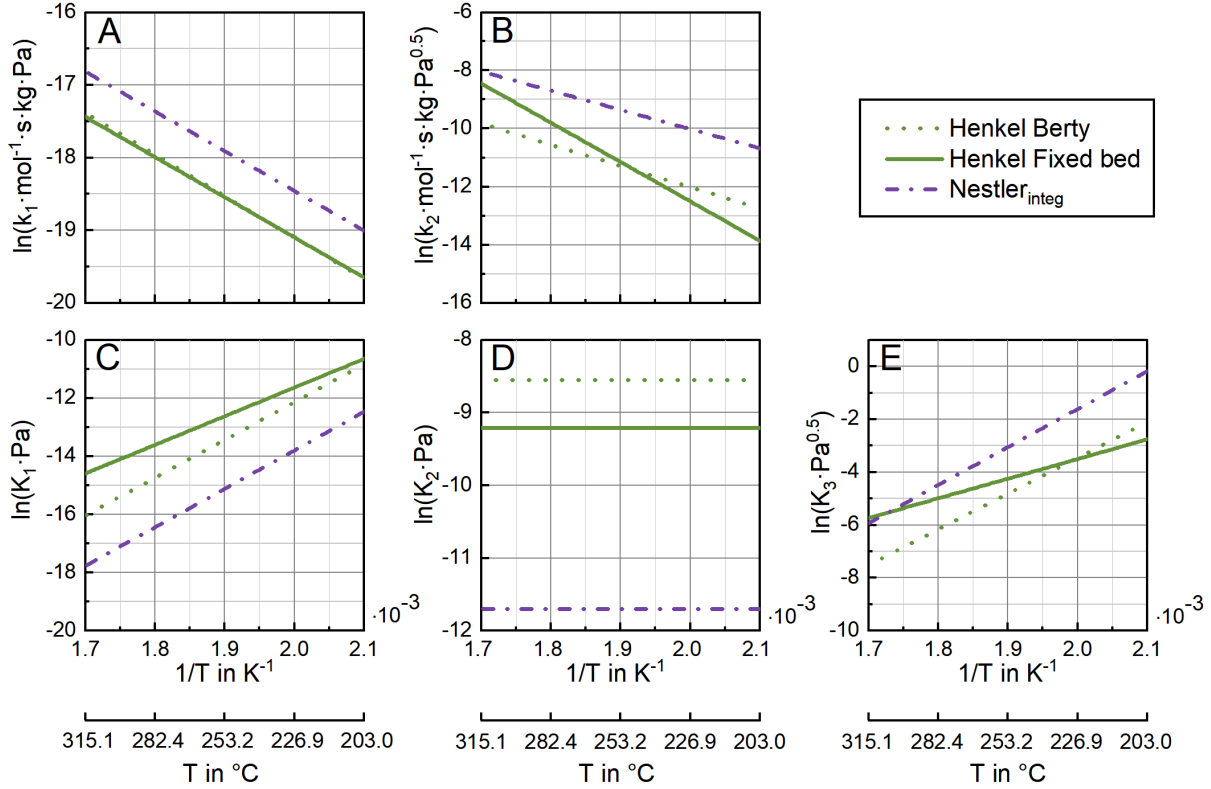


Figure 4.2: Arrhenius plot of the kinetic constants  $k_1$  (A),  $k_2$  (B),  $K_1$  (C),  $K_2$  (D), and  $K_3$  (E) for the  $\text{Nestler}_{\text{integ}}$  model in comparison to those calculated with the model by Henkel [202] between 203 °C and 315 °C.

procedure to the kinetic parameters of the model proposed by Henkel it was possible to decrease the RMSE by 27.4% for CO and 16.6% for CO<sub>2</sub> with regard to the closest literature model, i.e. Henkel Berty.

The kinetic parameters determined by Henkel (see Tab. 3.3) are compared to the parameter set listed in Tab. 4.1 in Fig. 4.2 by means of Arrhenius diagrams between 203 °C and 315 °C. The graphs show differences in the temperature dependence of both, reaction (A, B) and adsorption constants (C, D, E) between the  $\text{Nestler}_{\text{integ}}$  kinetic model and Henkel's kinetic models obtained for Berty and fixed bed reactor. For the  $\text{Nestler}_{\text{integ}}$  model  $k_1$  (CO<sub>2</sub>-hydrogenation) and  $k_2$  (rWGS) are higher in comparison to those by Henkel over the whole temperature range considered.  $K_1$ , i.e. the adsorption constant for CO, of the  $\text{Nestler}_{\text{integ}}$  kinetic model is below the parameter range determined by Henkel for both, Berty and fixed bed reactor.  $K_2$  representing the adsorption constant of CO<sub>2</sub> was computed at a lower value in comparison to Henkel.  $K_3$  representing the adsorption constant of water and H<sub>2</sub> has due to the structure of Eq. 3.56 and 3.57 the highest sensitivity on the reaction rate for CO<sub>2</sub>-rich syngas. At temperatures exceeding 300 °C the values for  $K_3$  are in a comparable range to those obtained by Henkel with the fixed bed reactor. At lower temperatures, however, increased values for  $K_3$  were determined leading to decreased reaction kinetics at high partial pressures of water in the reacting gas mixture in comparison to the model by Henkel. As high partial pressures of water are known to occur with increasing COR, this finding may be explained by the experimental range covered by Henkel and Park. While Park et

al. considered COR up 1.0 in their experimental campaign, Henkel did not perform experiments at COR exceeding 0.9 within his study (see Fig. 2.10). As the kinetic model proposed by Henkel does not account for the kinetic inhibition caused by water adsorption on the active sites of the catalyst, it can be concluded, that experimental data with  $COR > 0.9$  is necessary in order to accurately describe this effect. Therefore, kinetic models applied for the design of PtM processes should be validated at high  $CO_2$  in the synthesis gas.

#### 4.1.1 Analysis of the reaction rates

In order to show the influence of product formation on the reaction rates, the  $Nestler_{integ}$  kinetic model is discussed in comparison to the kinetic models by Graaf, Bussche and Henkel for different levels of reaction products formed (see Fig. 4.3). Temperature dependent reaction rates were calculated for  $CO_2$ -hydrogenation at 50 bar with a feed composition of  $COR = 1.0$  and  $SN = 2.0$ . Three cases were considered, (A) without product, (B) with 0.5 mol-% of methanol and 1.7 mol-% of water and (C) 1.6 mol-% of methanol and 4.5 mol-% of water. The increased product contents in (B) and (C) correspond to typical gas compositions formed along an industrial reactor at this composition of the feed gas. Fig. 4.3 (A) shows that the reaction rate of  $CO_2$ -hydrogenation without products in the gas mixture calculated by Bussche's kinetic model is more than one order of magnitude higher than those calculated with the other kinetic models. The reaction rates calculated with Henkel's parameter set show a similar trend as the  $Nestler_{integ}$  model, however, at a lower level. The lowest reaction rates were calculated using Graaf's kinetic model.

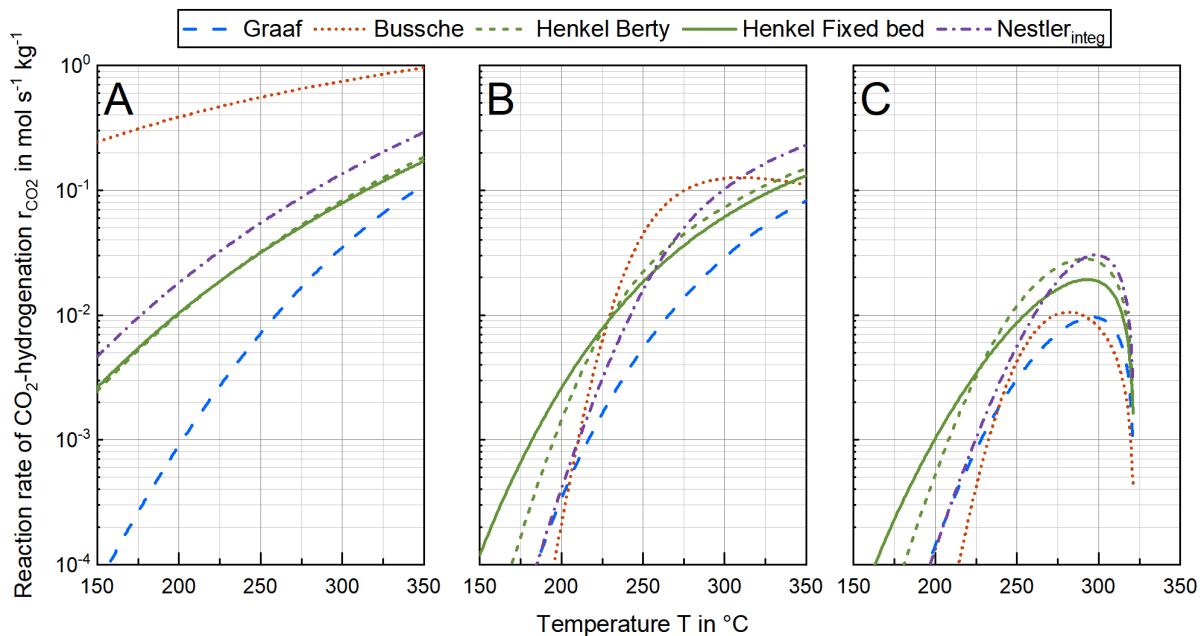


Figure 4.3: Reaction rates of the kinetic models considered within this study at  $SN = 2.0$ ,  $COR = 1.0$ ,  $p = 50$  bar without product (A), with approx. 0.5 mol-% methanol and 1.7 mol-% water (B), and 1.6 mol-% methanol and 4.5 mol-% water (C).

At increased product formation (i.e. 1.7 mol-% water and 0.5 mol-% methanol, (Fig. 4.3 (B)) the reaction rates calculated by Bussche drop significantly. While Bussche’s kinetic model shows a maximum reaction rate at approx. 300 °C the reaction rate of the Nestler<sub>integ</sub> model increases with rising temperature comparable to the models by Henkel and Graaf. At temperatures below 270 °C the reaction rate of the Nestler<sub>integ</sub> model falls below that of Henkel’s models.

The limiting effect of the products formed towards the reaction rates for the model by Bussche and the Nestler<sub>integ</sub> model is enhanced when more water and methanol are formed within the reactor (Fig. 4.3 (C)). Below 300 °C the reaction rates calculated with the models by Henkel and Graaf are moderately decreasing while temperature is reduced, however, the limiting effect of water is not as strongly developed as in the model published by Bussche and the model proposed within this section. At 1.6 mol-% of methanol and 4.5 mol % of H<sub>2</sub>O the equilibrium limitation of the reaction can be determined at approx. 325 °C.

Concerning the influence of COR on the reaction rates, in scientific literature a maximum reaction rate of methanol formation was reported for a educt gas with approx. 2 mol-% of CO<sub>2</sub> [28, 30, 31, 38, 42–44, 46–48, 185]. In Fig. 4.4 the carbon conversion ( $X_C$ ) of an ideally cooled isothermal reactor was calculated at a pressure of 50 bar and a constant temperature of 250 °C for the kinetic models considered. COR was varied from 0.001 to 1.0 with SN fixed at 2.0. In order to compare the  $X_C$  within the kinetic regime, a GHSV of 20,000 h<sup>-1</sup> was selected.

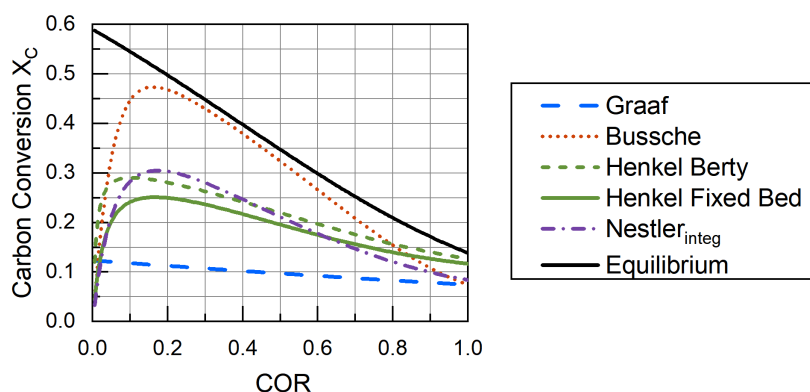


Figure 4.4: Carbon conversion over COR in the reactor feed for the kinetic models by Graaf [192], Bussche [145], Henkel [202] and the Nestler<sub>integ</sub> model at a reaction pressure of 50 bar; SN adjusted to 2.0; reaction temperature of 250 °C; GHSV of 20,000 h<sup>-1</sup>; ideal isothermal reactor.

The simulation results show a maximum  $X_C$  at low COR for all kinetic models, however, with Graaf’s model indicating the lowest sensitivity towards COR, i.e.  $X_C = 12.3\%$  and  $X_C = 7.5\%$  for  $COR = 0.001$  and  $COR = 1.0$ , respectively. In comparison to the other kinetic models the activity of Graaf’s kinetic model is at the lowest level. This finding is in good agreement with those by other researchers stating a low activity of Graaf’s kinetic model [170]. Bussche’s model indicates the highest influence of COR towards  $X_C$  with a maximum of  $X_C = 47.4\%$  achieved at  $COR = 0.16$  (i.e. 5.1 mol-% of CO<sub>2</sub>). This maximum is, however, not based on kinetic measurements as Bussche et al. did not consider gas compositions with  $COR < 0.2$ . At  $COR = 1.0$  (i.e. 25.0 mol-% of CO<sub>2</sub>)  $X_C$  calculated with Bussche’s model decreases towards the values obtained by Graaf.

While the simulations with Henkel’s kinetic models show lower activities than the kinetic model by Bussche for low COR, higher conversions are obtained at COR exceeding 0.80 and 0.84 for the Berty and the fixed bed parameters, respectively. These high conversions predicted by Henkel’s kinetic model again show the necessity to provide an appropriate data basis especially for the rate limiting effect of water at high COR.

The kinetic model  $Nestler_{integ}$  shows a maximum  $X_C$  of 30.5 % at  $COR = 0.18$  (i.e. 5.5 mol-% of  $CO_2$ ) in the reactor feed and is therefore within the range of the models proposed by Henkel (fixed bed) and Bussche with regard to the gas composition. The considerably higher  $X_C$  of Bussche’s kinetic model in comparison to that of Henkel and the  $Nestler_{integ}$  model could be due to weak validation data of the kinetic data set by Bussche at low COR and  $SN = 2.0$ . Slightly increased  $X_C$  is obtained at  $COR = 1.0$  by the  $Nestler_{integ}$  model in comparison to Bussche and Graaf. With 8.4 % this value is, however, well below the prediction made by the Henkel’s kinetic models at 12.7 % and 11.7 % for Berty and fixed bed parameters, respectively.

Overall, it can be concluded from the discussion of the kinetic performance of the kinetic models considered in this section, that the validation at high  $CO_2$  contents in the educt gas is of high importance to account for the rate limitation of water in the derived kinetic model. Therefore, the kinetic models proposed by Henkel should not be applied for PtM-simulations with a high COR in the syngas. Moreover, the discussion showed, that the kinetic model by Graaf calculated significantly lower reaction rates in comparison to the other rate equations and is therefore very likely based on an outdated catalyst. Analysis of the kinetic performance with regard to COR showed that all kinetic models with the exception of Graaf show a maximum in catalytic activity at low COR and, thus, behave plausible with respect to literature findings [48].

#### 4.1.2 Comparison of reactor simulations

To demonstrate the consequences of the  $Nestler_{integ}$  kinetic model on reactor design, a simulative sensitivity study varying the reaction conditions was conducted. The  $Nestler_{integ}$  kinetic model is directly compared with the kinetic models by Graaf, Bussche as well as Henkel. The parameter range of the sensitivity analysis is provided in Tab. 4.3; A wide range of COR and SN was considered for three pressure levels. Data analysis was performed with focus on the hot spot temperature and position, as the temperature profile is one key feature for industrial reactor design and largely affected by the reaction kinetics [136, 167, 169, 170, 234]. Dimensions of the reactor were applied with regard to Tab. 3.5.

All combinations of COR and SN were varied with the result of 20 simulation runs for each kinetic model and pressure level. The diffusion model presented in Sec. ?? was not applied for

Table 4.3: Parameter set varied within the sensitivity study in this section.

Parameter	Unit	Values
p	bar	50; 65; 80
COR	-	0.25; 0.5; 0.75; 1.0
SN	-	1.5; 2.0; 2.5; 3.0; 3.5

this analysis to simplify the interpretation of the simulation results. With regard to Kordabadi et al. [74] the temperatures of the reactor feed  $T_{\text{in}}$  and the cooling steam  $T_{\text{cool}}$  were set to  $T_{\text{in}} = 230\text{ }^{\circ}\text{C}$  and  $T_{\text{cool}} = 252\text{ }^{\circ}\text{C}$ , respectively.

1D-temperature and product concentration profiles simulated for a steam cooled tubular reactor utilizing the  $\text{Nestler}_{\text{integ}}$  kinetic model and Bussche's kinetic model are provided in Fig. 4.5. As inlet parameters for the syngas  $\text{COR} = 0.75$  and  $\text{SN} = 3.0$  at a pressure of 65 bar were selected.

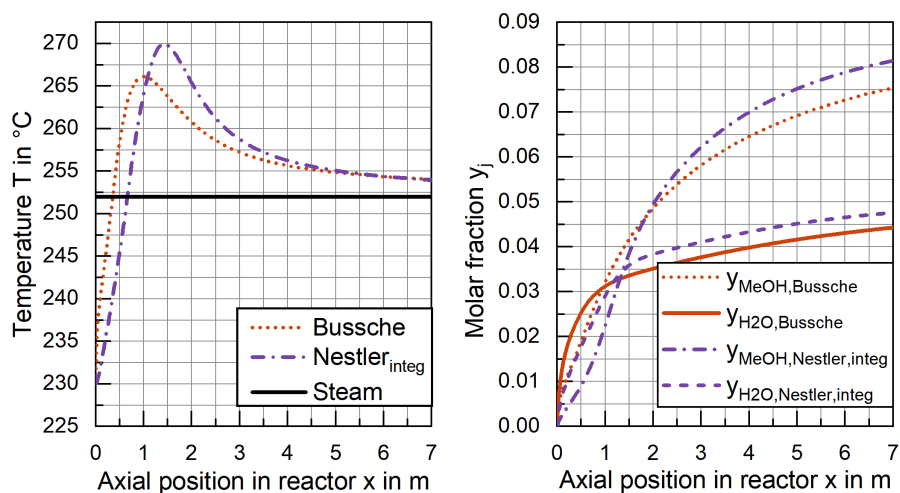


Figure 4.5: Comparison of the one-dimensional temperature profiles (left) and product molar fraction profiles (right) obtained by a reactor simulation at  $\text{COR} = 0.75$ ,  $\text{SN} = 3.0$ ,  $\text{GHSV} = 10,000\text{ h}^{-1}$  at a pressure of 65 bar utilizing the kinetic model by Bussche and the  $\text{Nestler}_{\text{integ}}$  kinetic model; Inlet temperature of the feed  $T_{\text{in}}$  was set to  $230\text{ }^{\circ}\text{C}$ , temperature of the cooling medium (steam) was set to  $T_{\text{cool}} = 252\text{ }^{\circ}\text{C}$  with respect to Kordabadi et al. [74]; Design parameters were applied according to Tab. 3.5.

The concentration profiles of the products are closely linked to the temperature profiles in the reactor. The kinetic model by Bussche shows a higher rate of methanol and water formation at the reactor entry in comparison to the  $\text{Nestler}_{\text{integ}}$  model. Nonetheless, both simulations approach equilibrium at cooling temperature at the reactor exit, however, with an overall lower conversion and therefore slower reaction kinetics of the Bussche model in comparison to  $\text{Nestler}_{\text{integ}}$ .

Based on the previously shown results, hot spot position and magnitude were used for an advanced analysis of the model behavior depending on  $\text{COR}$ ,  $\text{SN}$  and synthesis pressure for the parameter range listed in Tab. 4.3. The data on position and temperature of the hot spot are presented in Fig. 4.6. As the kinetic model Henkel determined from the Berty reactor experiments is validated over a wider temperature range and higher pressures than the fixed bed model, the latter was not considered within the sensitivity study. Pressures exceeding the valid range of the kinetic models were applied in the simulation as the extrapolation of the pressure range is commonly done in scientific publications performing reactor simulations [136, 194, 195, 255, 256]. To indicate the extrapolation of the kinetic models in the simulation study regarding temperature, pressure,  $\text{SN}$  and  $\text{COR}$ , the data points exceeding the validated data ranges of the kinetic models with respect to Fig. 2.10 were bleached out in the diagram.

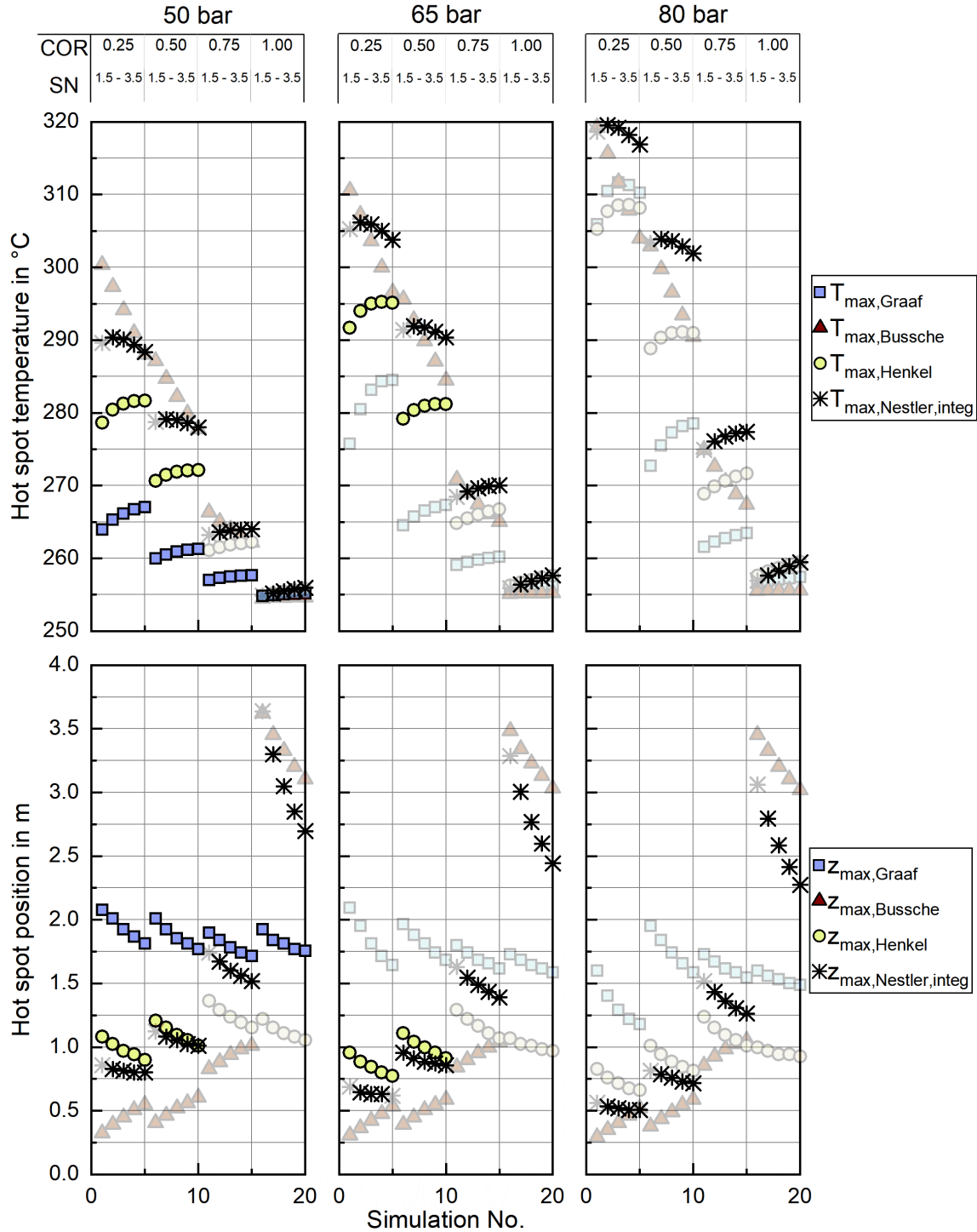


Figure 4.6: Sensitivity study discussing the hot spot temperatures (top) and positions (bottom) obtained from the simulation of an industrial scale tubular reactor with the kinetic models by Graaf [192], Bussche [145] and Henkel (Berty) [202] as well as with the Nestler<sub>integ</sub> kinetic model for the parameter range between  $0.25 \leq \text{COR} \leq 1$ ,  $1.5 \leq \text{SN} \leq 3.5$  at  $\text{GHSV} = 10,000 \text{ h}^{-1}$  at the pressure levels of 50 bar, 65 bar and 80 bar; SN was varied in steps of 0.5; Inlet temperature of the feed  $T_{\text{in}}$  was set to  $230 \text{ }^\circ\text{C}$ , temperature of the cooling medium (steam) was set to  $T_{\text{cool}} = 252 \text{ }^\circ\text{C}$  with respect to Kordabadi et al. [74]; Data points exceeding the validated data range of the kinetic models with regard to Fig. 2.10 were bleached out; Design parameters were applied according to Tab. 3.5.

Overall results from the sensitivity study show that hot spot temperature rises with increasing pressure and decreasing COR for all kinetic models. This behavior is in line with literature findings regarding the maximum methanol reaction rates and the increased exothermic heat at high CO contents in the reactor feed gas. The increase of reaction kinetics with increasing pressure is in agreement with Le Chatelier's principle. However, big differences in position and temperature of the hot spot were determined between the different kinetic models proving the necessity of an appropriate description of reaction kinetics for reactor design purposes. Among all considered kinetic models the lowest sensitivity of hot spot temperature and position towards COR is predicted by Graaf. In addition, this model delivers the lowest hot spot temperatures for the COR range between 0.25 and 0.75. The poor activity of Graaf's model was already documented within the scientific community [170] and could be due to the fact that the catalyst for Graaf's kinetic model was less active than those applied by other researchers. Therefore, this model should be used with caution for the description of state-of-the-art methanol synthesis.

The kinetic model by Bussche provides a higher sensitivity towards changes in COR in comparison to Graaf. The highest temperatures are achieved at low SN-values for COR between 0.25 and 0.75. A strong decrease of the hot spot temperature can be denoted with increasing SN. This behavior is in contrast to the other kinetic models depicted in Fig. 4.6 as these show a slight increase of the catalytic activity, i.e. higher hot spot temperatures and further upstream positions, with rising SN. An increase of the reaction rates with rising SN was also found by Chanchlani et al. who performed an experimental study on the influence of H<sub>2</sub> on the rate of methanol formation [31]. As the SN-range of the kinetic study was not documented within the publication by Bussche et al., the diverging behavior of this model could be explained by a missing variation of SN in their experimental campaign. Therefore, it can be stated, that the model by Bussche should be carefully applied with regard to variations in SN.

The hot spot temperatures and positions simulated with the model proposed by Henkel ranges between those predicted by Bussche and Graaf at COR between 0.25 and 0.75. The Nestler<sub>integ</sub> model shows a comparable sensitivity towards COR as the model by Bussche, however, with the hot spot formed further downstream for COR ranging between 0.25 and 0.75 (also see Fig. 4.5). Synthesis pressure is predicted with a higher effect towards hot spot temperature as compared to Bussche. This is most likely due to the higher pressures applied in the experimental campaign by Park et al. setting the validation basis for the Nestler<sub>integ</sub> kinetic model (compare Fig. 2.10). The insufficient description of the reaction kinetics by Bussche at pressures exceeding 50 bar was already claimed by Mignard et al. proposing a pressure extension for this model [38, 157]. However this extension was based on the measured data by Klier from 1982 and therefore most likely based on a different catalyst than the one applied within Bussche's study.

Due to the low reaction enthalpy of CO<sub>2</sub>-hydrogenation coupled with the low equilibrium conversion, all kinetic models show low hot spot temperatures for the case of COR = 1.0. However, the maximum temperature rise slightly increases with rising SN. For the cases with COR = 1.0 the positions of the hot spots for the kinetic models by Bussche and the Nestler<sub>integ</sub> kinetic model are almost similar, while Graaf and Henkel show the hot spot further upstream. The kinetic model by Henkel is most active for high CO<sub>2</sub> contents by means of hot spot temperature and position. This is most probably due to the fact that Henkel did not perform measurements at

high COR. Therefore, this model cannot account for the inhibiting effect of water at high COR appropriately [31, 38, 205].

Generally, the Nestler<sub>integ</sub> kinetic model was proven to behave plausibly in comparison to the other kinetic models considered in this study. As this model covers the technical relevant pressure and COR range for methanol synthesis, it is likely that the trends shown by the sensitivity analysis are more realistic than those given by the other models.

#### 4.1.3 Concluding remarks on the integral kinetic model

For the application of kinetic models for methanol synthesis it is of significant importance that the relevant parameter range is considered in the experimental data used for derivation of the kinetic model. The extrapolation of the catalytic activity is not necessarily valid as long as the mechanism of methanol synthesis is not understood completely. In this section, a kinetic model based on recent experimental data published by Park et al. [203] was presented. The performance of this kinetic model was systematically compared against the kinetic models proposed by Graaf, Bussche and Henkel to identify the potential of the model for the application at operation conditions relevant for both conventional and PtM-based methanol synthesis.

Furthermore, a sensitivity analysis on the industrial reactor scale was conducted to compare the performance of the kinetic models with regard to pressure, COR and SN. The results demonstrated that Bussche's kinetic model shows an inverse sensitivity towards SN compared to the other kinetic models indicating an important inconsistency within this model. The kinetic model by Graaf was proven to be less active and sensitive towards COR than the other models considered in this section. Therefore, special caution should be taken applying this model for the description of modern methanol synthesis reactors. As water is known to have a strong rate-inhibiting effect on the kinetics of methanol synthesis, measurements with high CO<sub>2</sub> contents should be included into kinetic measurement campaigns, especially with regard to PtM applications. Exclusion of high CO<sub>2</sub> contents from the kinetic measurement could lead to an overestimated model activity as shown with the kinetic models proposed by Henkel.

Consequently, the Nestler<sub>integ</sub> kinetic model based on Park's experimental data and the rate equations proposed by Henkel covers the widest parameter range of kinetic models available in scientific literature for methanol synthesis on a commercial catalyst. Therefore, this model can be applied for reactor and process design covering the complete range of pressure, temperature, SN and COR with a high level of confidence.

However, the experimental data set published by Park et al. is mainly based on gas phase measurements at GHSVs between 9,000 h<sup>-1</sup> and 23,000 h<sup>-1</sup>. This leads to possible model weaknesses with regard to the axial catalytic performance and, thus, inaccuracies in the calculation of the temperature profile in industrial reactors. Therefore, measurements at higher GHSVs would be necessary in order to accurately describe the reaction kinetics at low conversion. Moreover, only a small quantity of experimental points was measured by Park et al. at elevated CO<sub>2</sub> contents in the feed gas (compare Fig. A.5 in App. A.6). To obtain a more reliable kinetic model for the design of methanol synthesis reactors in PtM applications, an improved methodical

approach delivering differential experimental data along the reactor of a polytropic miniplant will be presented in the next section.

## 4.2 Kinetic model derived from differential miniplant data

In order to gain experimental data for the adjustment of the kinetic model  $Nestler_{integ}$ , the miniplant described in Sec. 3.4 was operated with the experimental plan presented in Sec. 3.5.2. Besides an analysis of the reaction product, the experimental data obtained from the miniplant setup provide axially resolved information on the temperature profile inside the reactor – a direct output of the interplay between the reaction kinetics and the heat flux into the thermal oil. Due to the high resolution of the temperature data, a detailed picture of the kinetic performance along the catalyst fixed bed is provided (compare Fig. 3.7). This data set will be used to derive an axially validated kinetic model ( $Nestler_{diff}$ ) for CO<sub>2</sub>-rich syngas as further evolution of  $Nestler_{integ}$ .

### 4.2.1 Experimental results

The experimental data obtained from the miniplant setup indicated strong sensitivities of hot spot temperature, product composition and space time yield (STY) towards pressure, stoichiometry and COR. However, the measurement campaign was overlaid by a continuous deactivation of the catalyst. In Fig. 4.7 STY is plotted over experimental ToS for the benchmark composition of SN = 4.0 and COR = 0.9 at the three pressure levels as well as the two cooling temperatures applied in this study. The graph indicates that STY stabilized during ramp up after approx. 50 h ToS. However, stronger deactivation of the catalyst was observed during the experimental plan at 80 bar (phase 4.) and COR = 0.98 (phase 5.). As both, the highest temperatures and the highest water contents were measured during these phases, based on these observations it can be concluded that the deactivation of the catalyst was mainly correlated to these two factors. This is in good agreement to the work of Fichtl et al. who considered hydrothermal degradation of the active sites as the main reason for catalyst deactivation in cleaned syngas [37]. However, their group showed the necessity for longer experimental campaigns exceeding 1,600 h ToS to obtain satisfactory information about deactivation kinetics. As this, though, was not in the scope of this study, the influence of catalyst deactivation was not yet included consequently leading to inaccuracies for the kinetic fitting. However, the strong decrease of the catalyst's activity during the formation phase (phase 1. in Fig. 4.7) was excluded from the kinetic parameter fitting. Future research is planned to derive advanced axially resolved deactivation kinetics using the miniplant setup.

In Fig. 4.8 the molar fractions of water and methanol obtained from the experiments at GHSV = 12,000 h<sup>-1</sup> and a cooling temperature of 240 °C at the three pressure levels for COR = 0.7 (left) and COR = 0.95 (right) are depicted over SN. Thermodynamic equilibrium for the data points was calculated at reactor outlet temperature applying the equilibrium constants published by Graaf et al. as described in Sec. 2.4.1 [129]. As shown by the difference between equilibrium and measured molar fraction of methanol, all experiments at this GHSV were carried out within the kinetic regime of the methanol reaction. However, water production did reach the thermody-

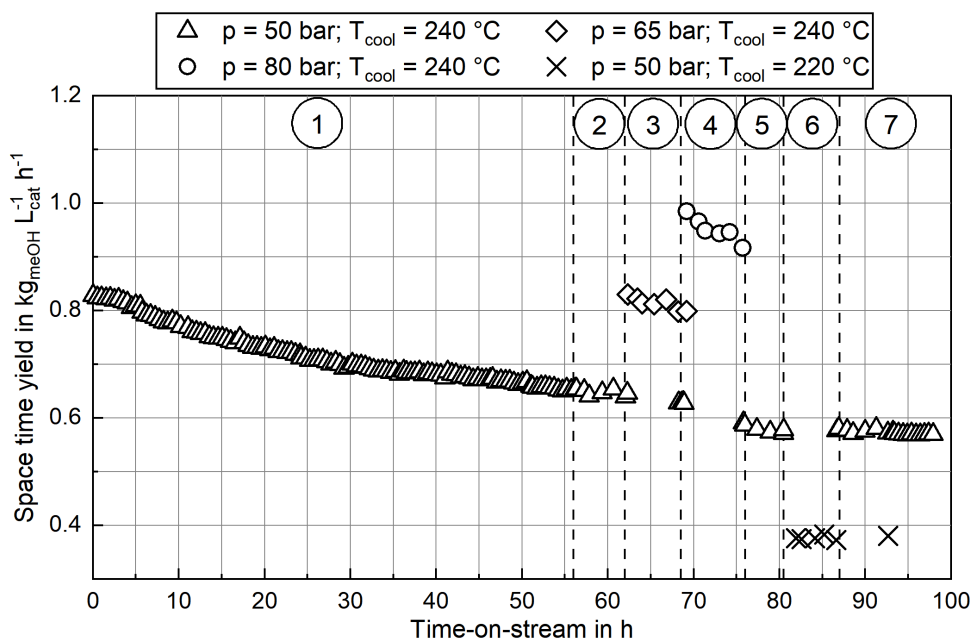


Figure 4.7: Trend of the space time yield over time-on-stream at benchmark conditions COR = 0.9; SN = 4.0; GHSV = 12,000 h<sup>-1</sup> at 50 bar, 65 bar and 80 bar; Sectors marked: 1.) ramp up, benchmark at 50 bar, T<sub>cool</sub> = 240 °C; 2.) experimental plan at 50 bar, T<sub>cool</sub> = 240 °C; 3.) experimental plan at 65 bar, T<sub>cool</sub> = 240 °C; 4.) experimental plan at 80 bar, T<sub>cool</sub> = 240 °C; 5.) variation of SN at COR = 0.98, T<sub>cool</sub> = 240 °C and 50 bar to 80 bar; 6.) experimental plan at 50 bar, T<sub>cool</sub> = 220 °C; 7.) benchmark at 50 bar, T<sub>cool</sub> = 240 °C.

dynamic equilibrium, probably due to faster reaction kinetics of rWGS. As expected considering Le Chatelier's principle, increased synthesis pressures led to increased equilibrium molar fractions of methanol and water and consequently to faster reaction kinetics due to an enhanced driving force. The highest methanol molar fraction was obtained at COR = 0.7 and SN = 2.0. While at COR = 0.7 an increase of SN led to a decrease of methanol molar fraction, the molar fraction of methanol was not sensitive to SN at COR = 0.95. This finding can be explained with the rate inhibiting effect of high water partial pressures that was already recorded in literature [32, 49, 51].

Besides product concentration, another indicator for the catalytic activity can be gathered from the temperature profile inside the reactor. In Fig. 4.9 the hot spot temperatures for the three pressure levels at GHSV = 12,000 h<sup>-1</sup> and COR = 0.7 and COR = 0.95 are plotted over SN. The graph indicates a strong correlation between COR and the achieved temperatures inside the reactor. While at COR = 0.7 a maximum hot spot temperature of 278 °C was reached (SN = 2.0; p = 80 bar), temperatures were on a significantly lower level at COR = 0.95 with a maximum hot spot temperature of 257 °C at SN = 5.0 and p = 80 bar. This can be explained as an increase of CO molar fraction in the feed gas decreases the amount of water produced and consequently increases the reaction rates for methanol synthesis. Due to the higher exothermic heat released inside the reactor (Eq. 2.3), heat removal requires a higher temperature difference between cooling fluid and catalyst, leading to an increase of hot spot temperature. The hot spot position was

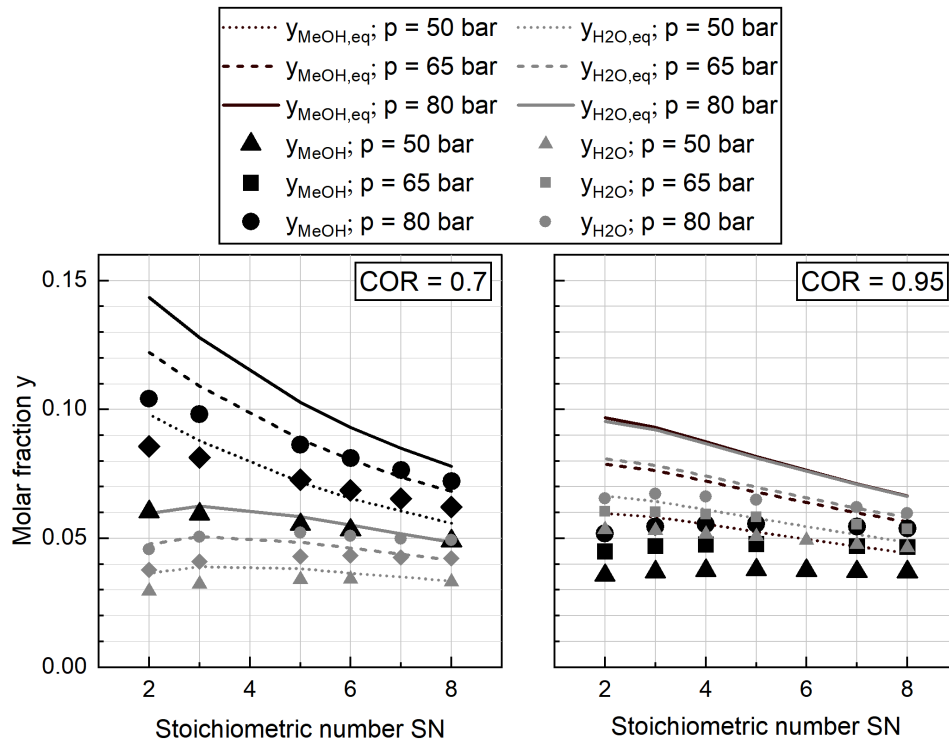


Figure 4.8: Equilibrium and measured molar fraction of methanol (black) and water (grey) at  $COR = 0.7$  (left) and  $COR = 0.95$  (right); Equilibrium molar fractions at 50 bar (dotted), 65 bar (dashed) and 80 bar (solid); measured molar fractions of methanol and water at  $GHSV = 12,000 \text{ h}^{-1}$  at 50 bar (triangle), 65 bar (diamond) and 80 bar (circle).

measured between 0.1 m and 0.2 m downstream the inlet of the catalyst bed at  $COR = 0.7$  and at 0.06 m at  $COR = 0.95$ , respectively. Due to the heterogeneities of the particle distribution along the temperature sensor, a clear sensitivity of hot spot position towards SN could not be derived (compare raw data in Fig. 3.7).

At  $COR = 0.7$  an increase of SN led to a decrease of hot spot temperature at 65 bar and 80 bar, whereas it was almost constant at 50 bar. This can be explained by chemical equilibrium of methanol synthesis decreasing by rising SN and temperature as well as the acceleration of reaction kinetics at increased temperature and pressure. Most probably hot spot temperature was limited by chemical equilibrium at 65 bar and 80 bar when SN exceeded a value of 3.0. Downstream the hot spot, temperature in the reactor approaches the temperature of the cooling fluid. As shown in Sec. 2.4.1, lower temperatures enable higher equilibrium conversions. However, due to the decrease in reaction kinetics at decreasing temperature, equilibrium at the cooling temperature is not reached inside the reactor (compare Fig. 4.8).

While at  $COR = 0.7$  an increase of synthesis pressure from 50 bar to 65 bar as well as from 65 bar to 80 bar increased the hot spot temperature by at least 7 K, at  $COR = 0.95$  only a small rise of hot spot temperature of less than 3.5 K was measured. Moreover, sensitivity towards SN was weaker at  $COR = 0.95$  with the highest hot spot temperature obtained at  $SN = 5.0$  for all three pressure levels. Overall, the sensitivities of hot spot temperatures towards  $COR$  and SN are in

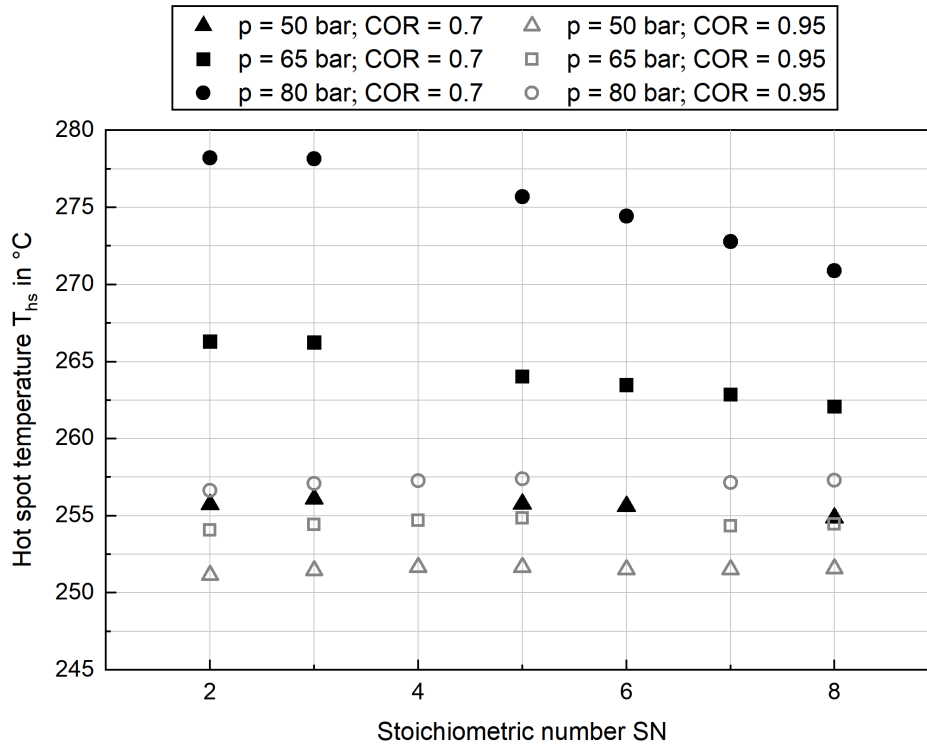


Figure 4.9: Hot spot temperature measured at COR = 0.7 (black) and COR = 0.95 (gray) and GHSV = 12,000 h<sup>-1</sup>; pressure levels: 50 bar (triangle), 65 bar (diamond) and 80 bar (circle).

good agreement with the results previously shown in Fig. 4.6 using the kinetic model  $Nestler_{integ}$ . NMR side-product analysis of the liquid product showed the presence of low concentrations of ethanol, propanol and formic acid (see Appendix A.16), which is in good agreement with Göhna et al. who analyzed the side-products of CO<sub>2</sub>-based methanol synthesis [84]. However, as non-condensable side-products as methane and DME could not be trapped in the liquid phase, no comprehensive analysis could be drawn from the liquid phase measurements executed. Further side-product gas phase measurements utilizing a FTIR with a longer optical path length to identify possible traces of these components could be applied in future studies.

Overall, the experimental results obtained from the miniplant setup were plausible regarding the trends in hot spot temperature and product composition. Therefore, the measured data provide a reliable data basis for the validation and adjustment of kinetic models.

#### 4.2.2 Validation of literature kinetics

In order to discuss the ability of the kinetic models available in literature for the description of the measured data obtained from the miniplant setup, reactor simulations using the kinetic models as proposed by Graaf [193] and Bussche [145] as well as the  $Nestler_{integ}$  kinetic model, were performed for all experimental working points. For the sake of clarity, the kinetic models with the parameter set applied as published Graaf and Bussche are hereon labeled with the index "original".

In Fig. 4.10 parity plots for the three models are provided for the product molar fractions of

methanol (A) and water (B) as well as hot spot temperature (C) and position (D), with a confidence interval of 10%. The graphs for the outlet molar fraction of water and methanol show a high level of agreement between experiment and simulation in terms of the kinetic model  $Nestler_{integ}$ . The models  $Bussche_{original}$  and  $Graaf_{original}$ , however, show strong deviations from the experiments with the tendency of underestimated reaction kinetics.

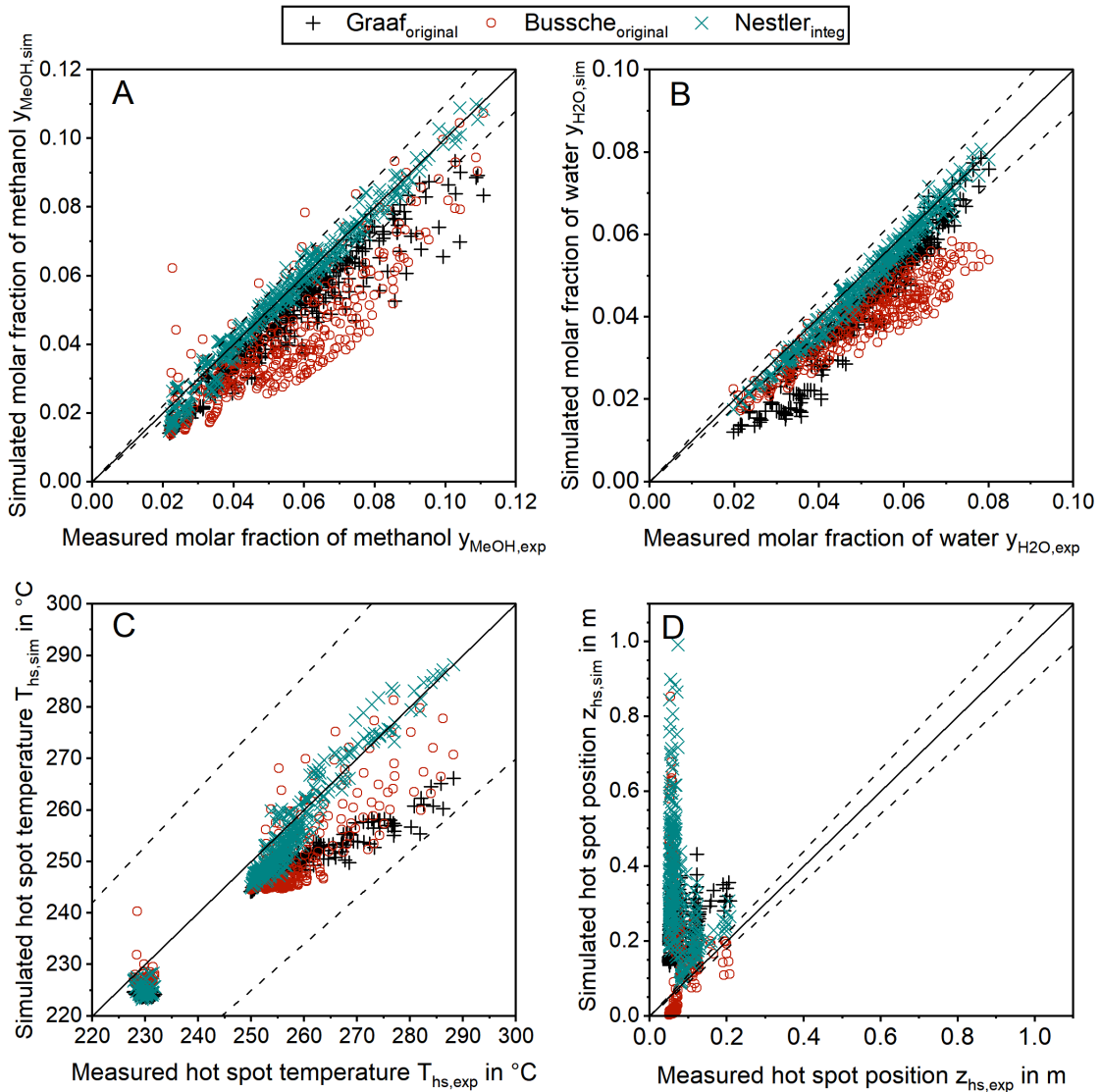


Figure 4.10: Parity plots for the outlet molar fractions of methanol (A) and water (B) as well as hot spot temperature (C) and axial hot spot position (D) including error lines for 0% (solid line) and for 10% (dashed line); Experiments were carried out with the miniplant setup; Simulation was performed using the kinetic models by Graaf (+) and Bussche (o) as published as well as the  $Nestler_{integ}$  kinetic model (x).

Interestingly, none of the models considered in Fig. 4.10 was able to precisely describe the thermal behavior of the reactor. Even though the hot spot temperatures of all kinetic models lie within the 10% confidence interval, position of the hot spot was estimated further downstream in the catalyst bed for all kinetic models considered here. The strong disagreement between the experimentally obtained temperature profiles and the simulations performed with the  $Nestler_{integ}$  kinetic model

underlines the requirement of kinetic measurements either at high GHSV ( $> 40,000 \text{ h}^{-1}$ ) or with a high axial resolution.

In Tab. 4.4 the objective function obtained from Eq. 3.79 is shown for the three original models considered in this study together with the respective RMSE-values (compare Eq. 3.79 to Eq. 3.82).

Table 4.4: Objective function and RMSEs calculated between the experimental data and the reactor simulations using the original kinetic models by Graaf and Bussche as well as the Nestler<sub>integ</sub> kinetic model.

Parameter	Unit	Graaf <sub>original</sub>	Bussche <sub>original</sub>	Nestler <sub>integ</sub>
$f(x)$	-	52.06	59.54	24.25
$RMSE_{T,profile}$	K	2.3	2.5	2.6
$RMSE_{T,hs}$	K	9.2	8.4	4.0
$RMSE_y$	%	0.79	1.18	0.27

The value obtained for  $RMSE_y$  proves the high accuracy of the Nestler<sub>integ</sub> model for calculation of the product composition in comparison to the literature standards Graaf<sub>original</sub> and Bussche<sub>original</sub>. While these models predict product composition with a mean error of 0.79% and 1.18%, respectively, a smaller mean error of 0.22% is obtained when the Nestler<sub>integ</sub> model is applied. Besides composition, the Nestler<sub>integ</sub> kinetic model delivers a better description of the temperature profile and hot spot position in comparison to Graaf<sub>original</sub> and Bussche<sub>original</sub>. However, hot spot temperature of this model is still predicted with a mean error of 4 K. As the temperature profile is coupled with the conversion of synthesis gas towards methanol, wrong outlet concentrations could be calculated when the original kinetic models considered here are transferred towards different reactor geometries, working conditions or even other reactor types, e.g. an adiabatic quench bed reactor. Even though, the Nestler<sub>integ</sub> kinetic model delivers a satisfactory description of the outlet concentration for the experimental conditions applied, high deviations could be the case, especially when the kinetic model is used for high COR and higher GHSV.

Summarizing the behavior of the kinetic models discussed in this section it can be stated, that the kinetic models Graaf<sub>original</sub> and Bussche<sub>original</sub> show a higher disagreement towards the kinetic performance measured with the miniplant setup compared to Nestler<sub>integ</sub>. This finding can be led back on different catalysts considered in the studies by Graaf and Bussche and missing validation data at pressures exceeding 50 bar. The simulations carried out with the Nestler<sub>integ</sub> kinetic model shows lower deviations with regard to product composition and hot spot temperature. However, a more accurate prediction of the temperature profile is necessary if this kinetic model should be applied for reactor design.

The three kinetic models considered in this section are based on different assumptions regarding the mechanism, RDS and presence of CO-hydrogenation. As these assumptions are controversially discussed within the scientific community, a parameter fitting of these models to the experimental data of the miniplant is reasonable to analyze their validity.

### 4.2.3 Fitted kinetic model

In order to enhance the applicability of the kinetic models described previously, their semi-empirical parameters (see Eq. 3.52 and Eq. 3.53) were fitted to the experimental results measured with the miniplant. The parameter fitting was subjected to the weighting factors in Eq. 3.79. Other weighting factors could influence the fitting result along the Pareto front of the optimization problem [257]. The kinetic models by Bussche and Graaf refitted to the experimental data will be denoted with the index "fit" hereafter; The kinetic model adapted from Nestler<sub>integ</sub> will be labeled Nestler<sub>diff</sub> from hereon.

In Tab. 4.5 the results of the parameter fitting are listed by means of the objective function and the respective RMSE values.

Table 4.5: Objective function and RMSEs calculated between the experimental data and the reactor simulations using the fitted kinetic models.

Parameter	Unit	Graaf <sub>fit</sub>	Bussche <sub>fit</sub>	Nestler <sub>diff</sub>
$f(x)$	-	17.50	24.97	17.93
$RMSE_{T,profile}$	K	1.4	1.8	1.5
$RMSE_{T,hs}$	K	1.7	3.4	1.8
$RMSE_y$	%	0.38	0.45	0.38

Comparison of the fitted kinetic models shows similar remaining errors for the models Graaf<sub>fit</sub> and Nestler<sub>diff</sub>, while for the model Bussche<sub>fit</sub> larger deviations remain for temperature profile and product concentration. This can be explained by the reaction mechanisms and RDS of the kinetic models. Graaf<sub>fit</sub> and Nestler<sub>diff</sub> rely on a common mechanism and similar RDS, however with Nestler<sub>diff</sub> not considering CO-hydrogenation. In contrast, Bussche's rate equation is based on a different mechanism. Due to the high remaining errors after the parameter fitting (compare Tab. 4.5) the rate equations of the Bussche-model were found not applicable for the description of methanol synthesis kinetics on the catalyst considered in this study.

The remaining RMSE values show that the fitted models Graaf<sub>fit</sub> and Nestler<sub>diff</sub> predict the temperature profile with a mean error of 1.4 K or 1.5 K, respectively, and therefore with a higher accuracy than the original literature models. A deeper look into the reaction rate of the fitted kinetic models at  $T_{cool} = 240^\circ\text{C}$  over the whole considered parameter range showed, that the direct CO-hydrogenation in the Graaf<sub>fit</sub> kinetic model can be neglected due to a very small reaction rate ( $|\bar{r}_{CO}| < 6.0 \cdot 10^{-8} \text{ mol s}^{-1} \text{ kg}_{cat}^{-1}$ ) obtained in comparison to CO<sub>2</sub>-hydrogenation ( $|\bar{r}_{CO_2}| > 3.2 \cdot 10^{-3} \text{ mol s}^{-1} \text{ kg}_{cat}^{-1}$ ) and rWGS ( $|\bar{r}_{WGS}| > 1.5 \cdot 10^{-3} \text{ mol s}^{-1} \text{ kg}_{cat}^{-1}$ ). Due to this finding, it can be stated, that CO-hydrogenation can be neglected for the description of the kinetic behavior inside the reactor, which is in good agreement to the findings of the scientific community [49, 258]. Consequently, the kinetic model Nestler<sub>diff</sub> will be used throughout the following discussion of this work.

The set of fitted kinetic parameters for the proposed kinetic model based on the rate equations of Eq. 3.56 and Eq. 3.57 is given in Tab. 4.6. The parameter sets of the fitted kinetic models Graaf<sub>fit</sub> and Bussche<sub>fit</sub> are listed in Appendix A.17 and A.18, respectively.

Table 4.6: Parameters for the kinetic model Nestler<sub>diff</sub>.

	Unit	Proposed kinetic parameters
$k_1$	$\text{mol kg}^{-1} \text{ s}^{-1} \text{ Pa}^{-1}$	$2.385 \cdot 10^{-5} \cdot \exp\left(\frac{-14,709}{R \cdot T}\right)$
$k_2$	$\text{mol kg}^{-1} \text{ s}^{-1} \text{ Pa}^{-0.5}$	$244.433 \cdot \exp\left(\frac{-53,741}{R \cdot T}\right)$
$K_1$	$\text{Pa}^{-1}$	$1.440 \cdot 10^{-17} \cdot \exp\left(\frac{-570}{R \cdot T}\right)$
$K_2$	$\text{Pa}^{-1}$	$4.223 \cdot 10^{-6}$
$K_3$	$\text{Pa}^{-0.5}$	$6.407 \cdot 10^{-13} \cdot \exp\left(\frac{126,843}{R \cdot T}\right)$

In Fig. 4.11 the parity plots for the outlet concentrations of methanol (A), water (B) as well as the hot spot temperature (C) and position (D) simulated with the Nestler<sub>diff</sub> kinetic model are provided. The graphs indicate that the description of both, hot spot position and temperature were improved significantly in comparison to the original model (compare Fig. 4.10). However, while the description of the temperature profile was enhanced with the proposed model, a slightly higher error can be observed regarding the composition of the products methanol and water. This is most likely due to inaccuracies in the measurements of axial temperature profile and product composition. Besides, the remaining error could be a consequence of inaccuracies in the reactor model, e.g. the diffusion or heat transfer sub-models. Application of the validation methodology presented within this study to other reactor geometries could help identifying possible simulation issues and improve the simulation platform.

A comparison between the experimental data and the simulation results applying the kinetic models Graaf<sub>original</sub>, Bussche<sub>original</sub>, Nestler<sub>integ</sub> and Nestler<sub>diff</sub> is provided in App. A.23 for data points at SN = 5.0 at a pressure of 80 bar over the whole COR range considered in this study. Despite the slightly lower accuracy of the proposed model in comparison to Nestler<sub>integ</sub> for the calculation of product composition, it is worth pointing out, that the correct description of reaction kinetics along the reactor is vital to enable a reliable transfer of the kinetic model towards industrial scale. To the best of the authors' knowledge, the herein proposed kinetic model delivers such a description and is therefore of a high value for reactor design problems. However, the validity of the herein proposed kinetic model was only confirmed within the parameter range applied for the experimental campaign (compare Tab. 3.8). Expansion of the validated parameter range should only be applied with caution [206]; More experimental data will be obtained from the miniplant for a wider COR range in future work to obtain a kinetic model applicable also for conventional gas compositions.

#### 4.2.4 Impact on industrial scale

To quantify the behavior of the herein proposed kinetic model on the industrial scale, a comprehensive simulation study was executed. As the Nestler<sub>integ</sub> kinetic model is based on a similar catalyst, though exclusively based on the measurement of the outlet concentration of a kinetic reactor [206], a comparison to this model is capable of showing the impact of the herein proposed

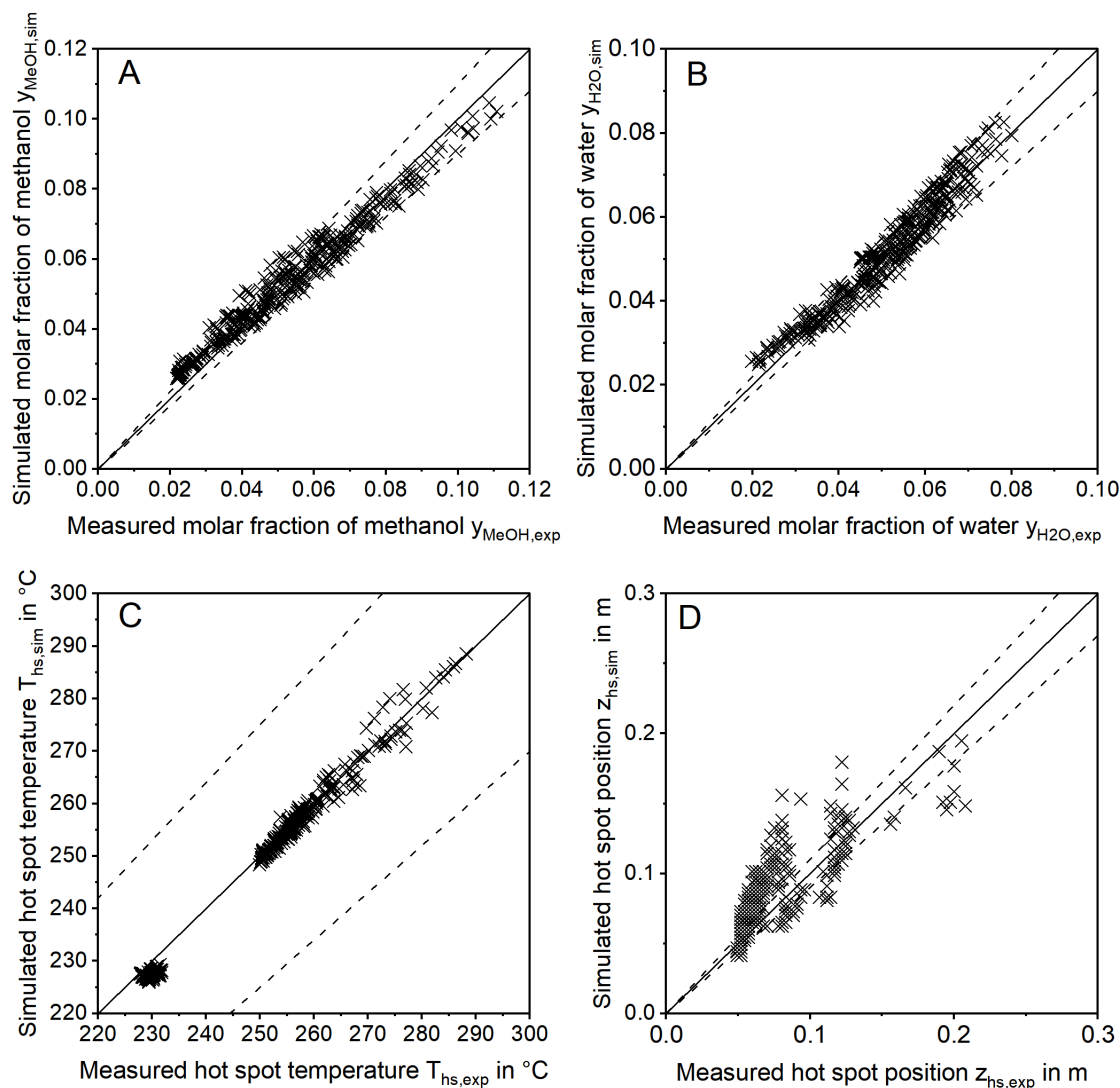


Figure 4.11: Parity plots of the refitted kinetic model  $\text{Nestler}_{\text{diff}}$  for outlet molar fractions of methanol (A) and water (B) as well as hot spot temperature (C) and axial hot spot position (D) including error lines for 0% (solid line) and for 10% (dashed line); Experiments were carried out with the miniplant setup.

validation approach. In Fig. 4.12 industrial reactor simulations applying both, the kinetic model  $\text{Nestler}_{\text{integ}}$  and the proposed adapted kinetic model  $\text{Nestler}_{\text{diff}}$  are compared by means of hot spot temperature (A, B) and position (C, D) as well as methanol (E, F) and water outlet molar fraction (G, H) at synthesis pressures of 50 bar (left side) and 80 bar (right side). The graphs A and B indicate a lower sensitivity of the  $\text{Nestler}_{\text{diff}}$  model with regard to the dependency of hot spot position and temperature towards COR in comparison to  $\text{Nestler}_{\text{integ}}$ . While hot spot temperatures of both models are comparable at  $\text{COR}=0.8$  the  $\text{Nestler}_{\text{diff}}$  kinetic model shows lower hot spot temperatures at  $\text{COR}=0.7$  and increased temperatures at higher COR.

As expected from the comparison of the parity plots of  $\text{Nestler}_{\text{integ}}$  model and  $\text{Nestler}_{\text{diff}}$  model in Fig. 4.10 and Fig. 4.11, respectively, high deviations between the kinetic models are observed with regard to hot spot position. This shows that large inaccuracies on the industrial reactor scale

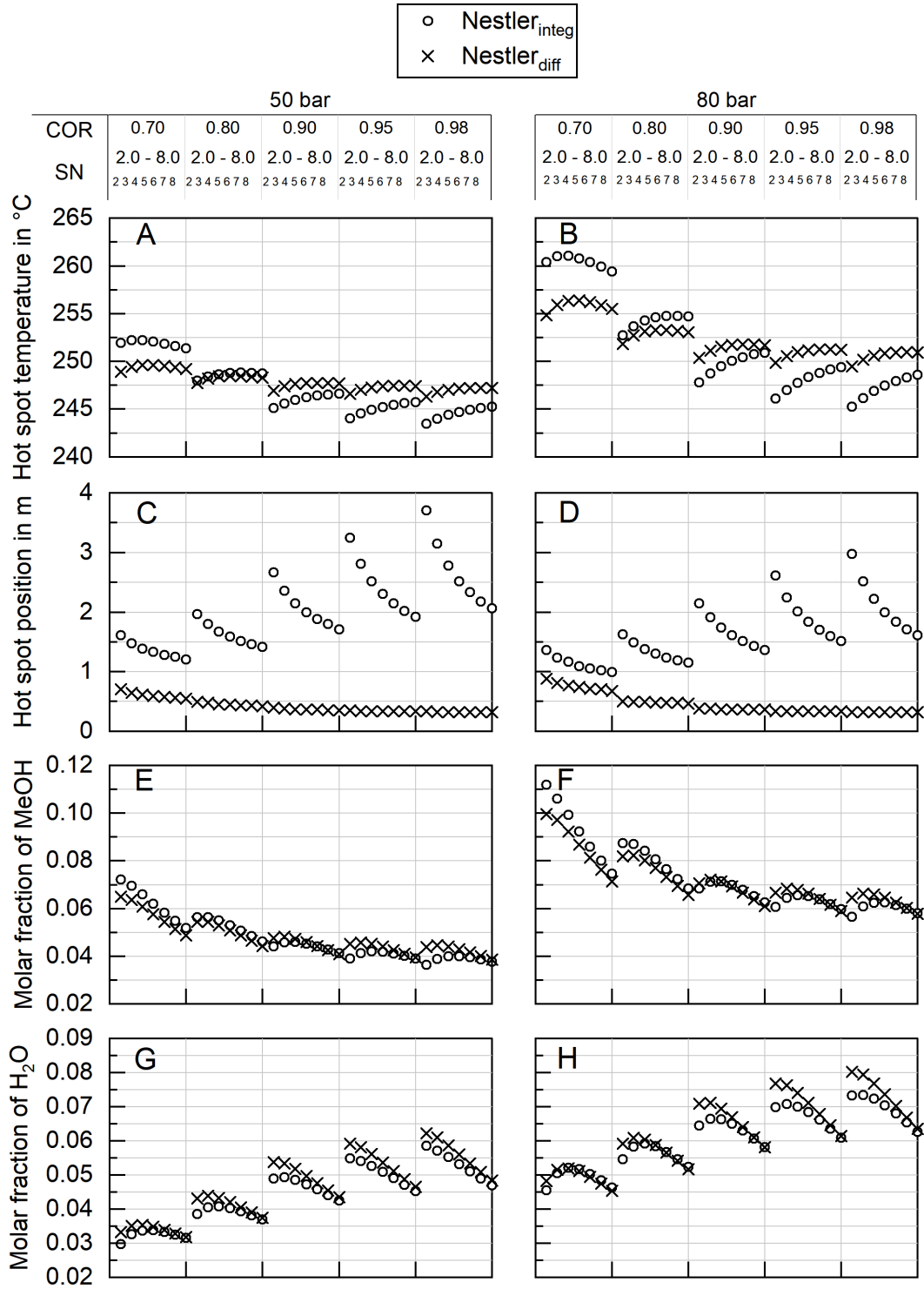


Figure 4.12: Sensitivity study discussing the behavior of the kinetic models Nestler<sub>integ</sub> (o) and Nestler<sub>diff</sub> (x) by means of hot spot temperature (A, B) and position (C, D) as well as product molar fraction of methanol (E, F) and water (G, H) at a synthesis pressure of 50 bar (A, C, E, G) and 80 bar (B, D, F, H) in the range  $0.7 \leq \text{COR} \leq 0.98$ ,  $2.0 \leq \text{SN} \leq 8.0$  at  $\text{GHSV} = 6,000 \text{ h}^{-1}$ .

can be obtained with kinetic models derived from experimental data measured in traditional integral reactors. Differential measurement of concentration or, as presented here, highly resolved temperature measurements add information to the data set which are advantageous when a transfer from lab to industrial scale is performed. The more accurate and reliable description of the thermal behavior inside the reactor provides increased security for reactor and process design on the industrial scale. Looking at the product molar fraction of methanol (E, F) and water (G, H) increasing deviations between the two models are present with decreasing SN. This is probably due to larger deviations in hot spot position predicted with decreasing SN. On the one hand this finding again shows the importance of the interlink between a correct kinetic axial description and accurate calculation of product formation. On the other hand, detailed knowledge of the product composition at the reactor exit is of high importance, when the synthesis reactor is embedded in a loop process.

#### 4.2.5 Co-verification of the kinetic model $Nestler_{diff}$

In order to verify the new methodology proposed in this work, the kinetic model fitted to the differential miniplant data was compared to the integral experimental data measured by Park et al. [203]. In Fig. 4.13 a parity plot is shown comparing this set of experimental data to the simulation using the kinetic model  $Nestler_{diff}$ .

Comparison of Fig. 4.1 to Fig. 4.13 shows that both integral and differential kinetic model are capable of describing the experimental data published by Park et al. [203]. This finding is remarkable as the validity range of the differential kinetic model obtained from the miniplant data is largely exceeded in terms of COR – while Park et al. covered the whole COR-range from 0.0 until 1.0, the miniplant-data only covers the range  $0.7 \leq COR \leq 1.0$ . However, in terms of product composition the  $Nestler_{diff}$  kinetic model is still capable of describing the experimental data by Park.

Compared to the  $Nestler_{integ}$  kinetic model, a slightly higher scatter can be observed in Fig. 4.13. A look at the remaining errors for both kinetic models in Tab. 4.7, shows higher deviations for the  $Nestler_{diff}$  kinetic model in comparison to  $Nestler_{integ}$ . However, still the errors are below those by the literature kinetic models listed in Tab. 4.2.

Table 4.7: Comparison of the RMSE for the measured molar fractions published by Park [203] and the simulated molar fractions utilizing the kinetic models derived in Sec. 4.1 ( $Nestler_{integ}$ ) and in this section ( $Nestler_{diff}$ ).

Kinetic model	RMSE <sub>CO</sub> in %	RMSE <sub>CO2</sub> in %
$Nestler_{integ}$	0.605	0.441
$Nestler_{diff}$	0.784	0.437

Therefore, it can be concluded that the  $Nestler_{diff}$  kinetic model can be extrapolated towards higher COR to describe the reactor outlet composition. However, as no validation using the temperature profile was performed for  $COR < 0.7$  with this model, it should be applied with caution for reactor design purposes at these gas compositions.

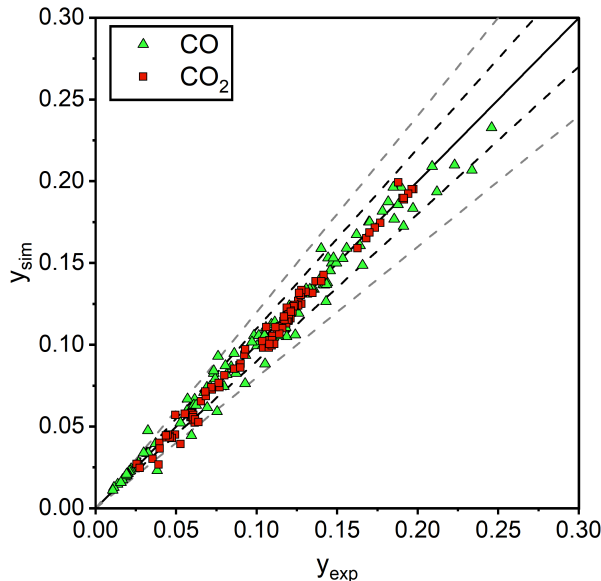


Figure 4.13: Parity plot comparing the kinetic model  $Nestler_{diff}$  fitted to the miniplant experimental data to the integral experimental data published by Park et al. [203]; Error lines for 0% (solid, black), 10% (dashed, black) and 20% (dashed, gray).

Finally, the high degree of agreement between the integral experimental data and the two kinetic models shows that multiple combinations of parameter sets can be found to deliver an appropriate kinetic description when only the reactor outlet concentration is measured (integral measurement). However, the fact that the axial performance of the two models  $Nestler_{integ}$  and  $Nestler_{diff}$  differs significantly (compare Fig. 4.12) emphasizes the necessity of kinetic data gathered at high GHSVs ( $GHSV > 40,000 \text{ h}^{-1}$ ) or at differential axial positions along the reactor in methanol synthesis. From this finding it can be concluded, that differential measurement of the temperature profile along the reactor is one valid methodology to tackle this requirement. Moreover, this finding shows the potential of the here proposed miniplant-based validation approach for the transfer towards the kinetic validation of other fixed bed syntheses as e.g. Fischer Tropsch synthesis, methanation or  $\text{NH}_3$  synthesis.

#### 4.2.6 Optimal design for the miniplant setup

In order to optimize the miniplant geometry for an improved agreement between industrial and miniplant scale, scale-down from industrial scale to the miniplant dimensions was repeated applying the  $Nestler_{diff}$  kinetic model. In Fig. 4.14 the optimized reactor diameters determined at  $GHSV = 9,000 \text{ h}^{-1}$  and the pressure levels of 50 bar (A) and 80 bar (B) are shown in a 2D contour plot. The graphs indicate that scale-down of the industrial reactor to miniplant scale is correlated to the working range applied. While pressure and COR reveal higher sensitivities towards optimal reactor dimensions, SN does affect the diameter less significantly. With regard to the methodology applied, an inner reactor diameter of  $9 \text{ mm} \leq d_{in} \leq 12 \text{ mm}$  would be beneficial for the miniplant setup to improve the similarity towards the industrial reactor scale. Moreover, the smaller reactor diameter would lead to a better heat removal from the reactor and consequently

enable the setup to be used for syngas with lower COR. However, wall effects (Eq. 3.71) as well as other relevant design criteria [241] must be considered when the geometry of the miniplant reactor is changed to the dimensions proposed here.

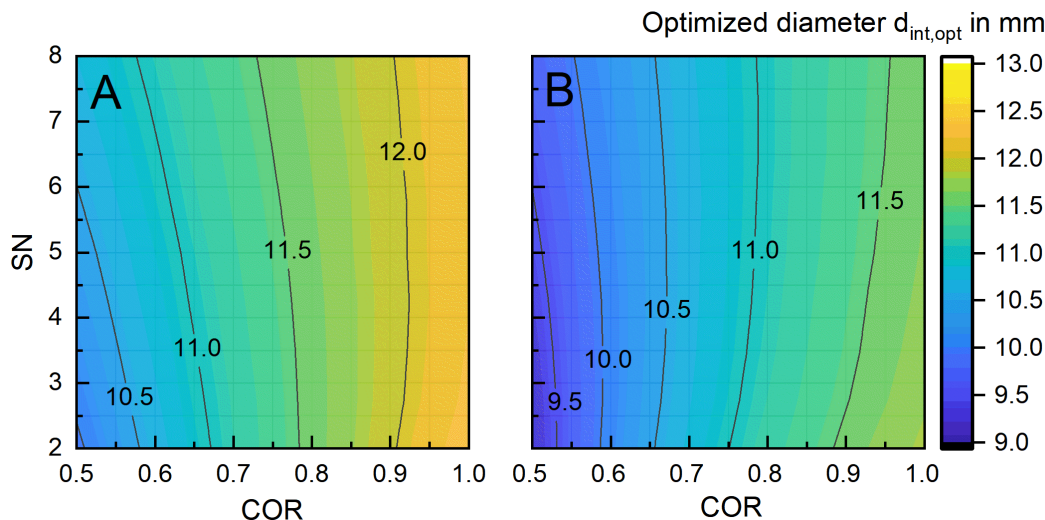


Figure 4.14: Optimized inner reactor diameter of the miniplant over COR and SN at  $\text{GHSV} = 9,000 \text{ h}^{-1}$  and  $T_{\text{cool}} = 240 \text{ }^\circ\text{C}$  for maximized comparability towards the industrial reactor (see Tab. 3.5) at 50 bar (A) and 80 bar (B); Color code indicates the optimized reactor diameter.

As the implementation of Thiele modulus for the description of the diffusion limitation showed to significantly influence the results of the scale-down, further research will be necessary in order to validate the diffusion model against experimental data. This could be done by introduction of larger catalyst particles into the miniplant reactor in future work or by comparing the reactor simulation to measured data obtained from a pilot/commercial scale facility.

#### 4.2.7 Concluding remarks on the differential kinetic model

In this section, a novel approach for kinetic model validation and parameter estimation using experimental data from a miniplant setup featuring a highly resolved fiber optic temperature measurement in a polytropic miniplant combined with FTIR product analysis was presented.

In Fig. 4.15, the smoothed temperature profiles obtained from the miniplant setup at  $\text{GHSV} = 9,000 \text{ h}^{-1}$  and  $\text{SN} = 5.0$  at a pressure level of 80 bar over the whole COR range considered in the miniplant experiments (for raw data see Fig. 3.7) are compared against the reactor simulation using the kinetic models  $\text{Graaf}_{\text{original}}$  (A),  $\text{Bussche}_{\text{original}}$  (B),  $\text{Nestler}_{\text{integ}}$  (C) and  $\text{Nestler}_{\text{diff}}$  (D). The graphs indicate strong deviations between the temperature profiles obtained from the miniplant experiments and the simulations performed with kinetic models  $\text{Graaf}_{\text{original}}$  and  $\text{Bussche}_{\text{original}}$  known to be the most frequently used kinetic models on the current-state-of-science in methanol synthesis (compare Sec. 2.5). A better description of hot spot temperature and gas phase composition (see also Fig. A.19) is achieved by the  $\text{Nestler}_{\text{integ}}$  kinetic model based on the experimental data published by Park et. al. [203]. However, as this model was not validated against data at a high GHSV (compare Fig. A.5 (C)), the position of

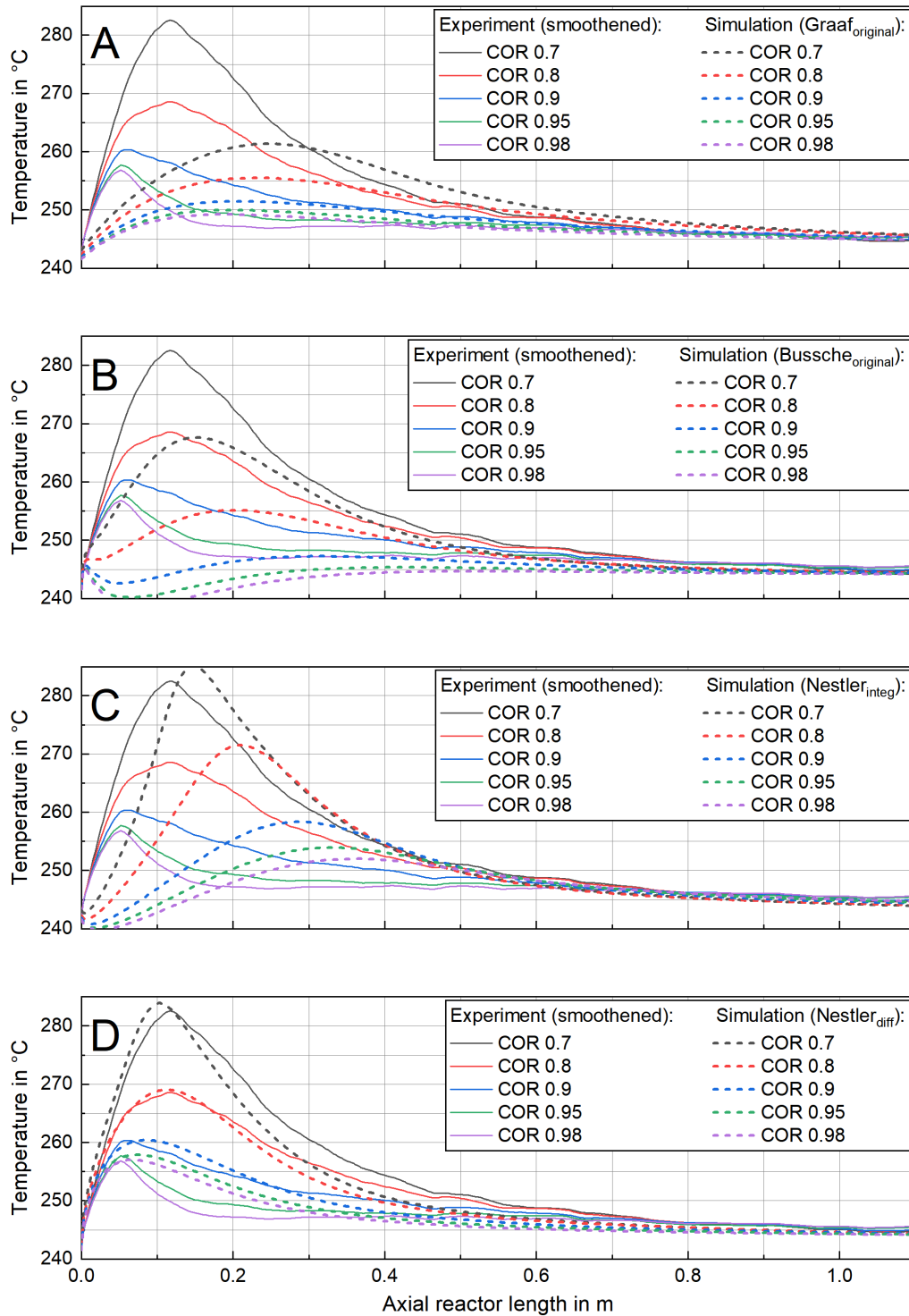


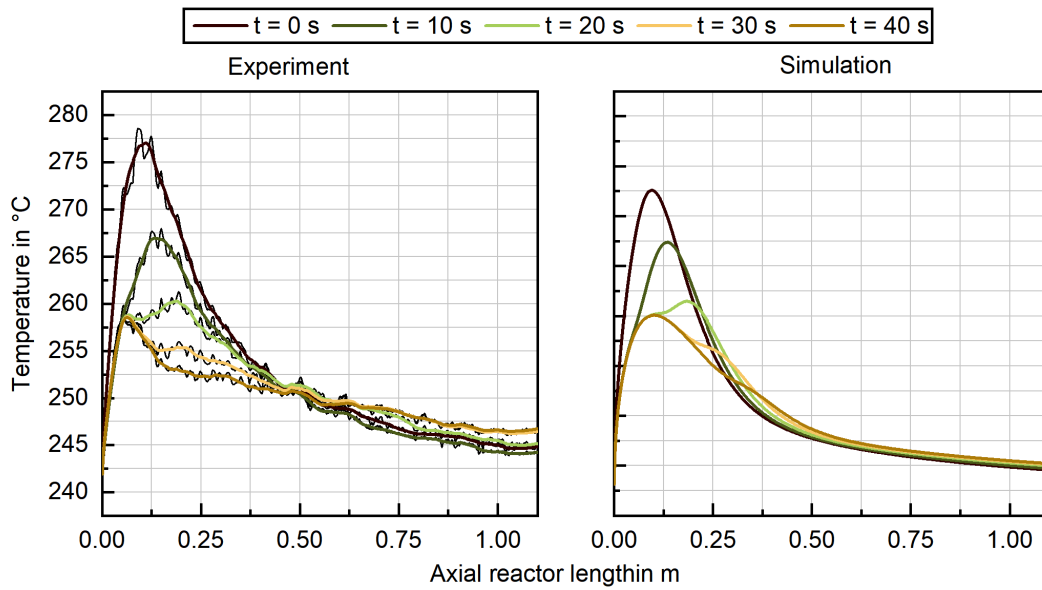
Figure 4.15: Smoothened temperature profiles obtained from the miniplant experiments and simulated temperature profiles using the kinetic models by Graaf [192] (A), Bussche [145] (B) as well as the kinetic model Nestler<sub>integ</sub> (compare Sec. 4.1, C) and Nestler<sub>diff</sub> (compare Sec. 4.2, D) at  $p = 80$  bar;  $T_{\text{cool}} = 240$  °C,  $SN = 5.0$  and  $GHSV = 9,000$  h<sup>-1</sup> for  $COR = 0.7, 0.8, 0.9, 0.95$  and  $0.98$ .

the hot spot is estimated too far downstream in the reactor. This could consequently lead to large inaccuracies in the design of industrial methanol synthesis reactors for PtM applications. The kinetic model  $Nestler_{diff}$  fitted to the differential temperature data along the miniplant reactor and the product composition provides the highest accuracy with regard to the axial kinetic performance of all kinetic models considered in this work. This result emphasizes the high practical relevance of the  $Nestler_{diff}$  kinetic model for the implementation of methanol synthesis from  $CO_2$ -rich gases and  $H_2$  on industrial scale. To the best of the author's knowledge the herein proposed novel approach for the validation of reaction kinetics of fixed bed reactions is a significant improvement over state-of-the-art kinetic measurements as it offers an enhanced methodology for bridging between experimental and industrial reactors.

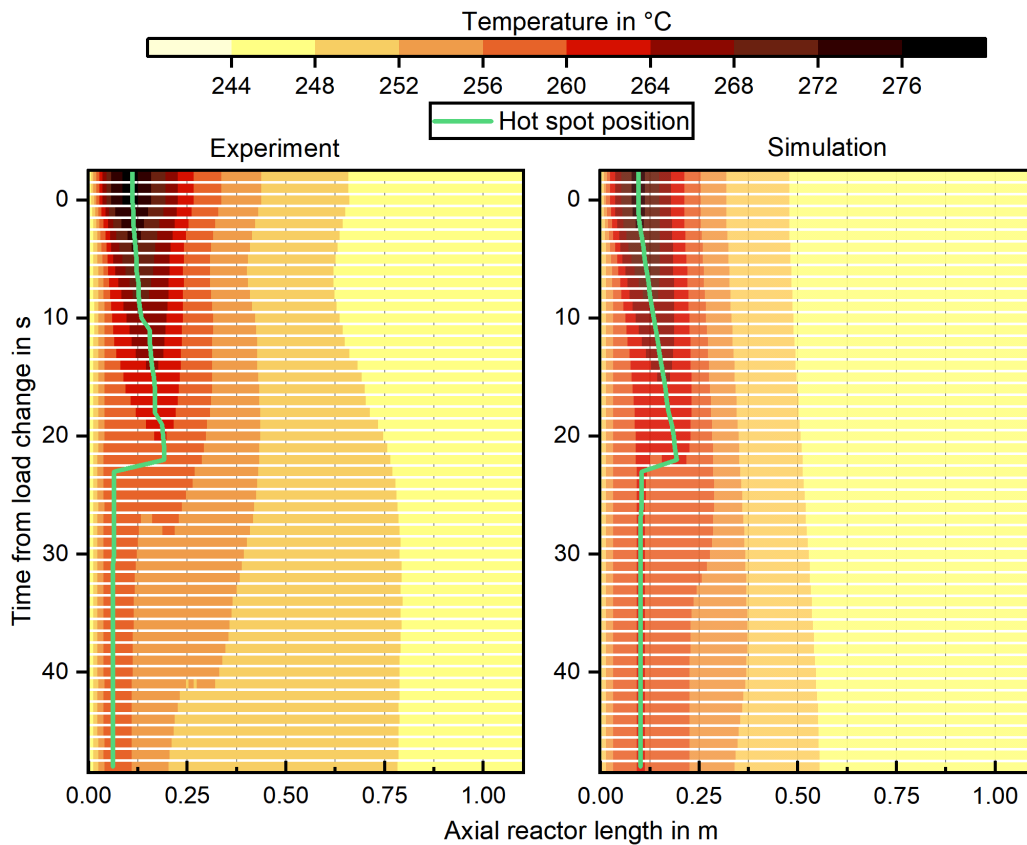
### 4.3 Validation of the dynamic reactor model

In this section, the behavior of the dynamic reactor model presented in Sec. 3.1.5 will be validated using experimental data from the miniplant setup and comparing the temperature profiles of both, experiment and simulated data. A detailed analysis regarding the behavior of the dynamic reactor model during sharp load transitions was executed prior to the validation in order to verify the plausible behavior of the model. The results of this analysis are provided in App. A.24. Dynamic load changes were experimentally observed at the miniplant setup during every transition from one steady state working point to another. During these load changes no temperature over-swing could be observed at any of the load changes performed. However, as Seidel et al. [188] observed a dynamic kinetic behavior of the catalyst in their Berty reactor (compare Sec. 2.4.4), the research question arises, whether a steady state kinetic model as the one proposed in Sec. 4.2 is sufficient for the description of a dynamically operated fixed bed reactor in methanol synthesis. Therefore, the simulation using this kinetic model will be held against one load change simultaneously altering COR, SN and GHSV measured with the miniplant setup. In this section, only the temperature profile measured inside the reactor will be used for the analysis. The FTIR measurement as implemented at the miniplant was found inappropriate for the analysis of dynamic experiments, as dynamic adsorption/desorption processes would lead to a change in the total flow rate of the reactor product. Moreover, the gas flow through the FTIR was objected to backmixing behavior due to the volume of the measurement cell. A continuous measurement of the flow rate of the reaction product would be necessary in order to accurately obtain the dead-time behavior of the analyzed gas stream.

The load change analyzed in this section was performed at a synthesis pressure of 80 bar and a cooling temperature of 240 °C. COR was varied from 0.8 to 0.9, SN from 2.0 to 4.0 and GHSV from 6,000  $h^{-1}$  to 12,000  $h^{-1}$ . In Fig. 4.16 a) left, the measured axial temperature profile is displayed directly before the load change(0s) as well as 10s, 20s, 30s and 40s after the load change. The graph indicates that the hot spot temperature decreases by 17K in the first 20s after the load change. After this period, the hot spot temperature decreases by only 3K in the following 20s. However, during this period the position of the hot spot is shifted to the reactor inlet. Besides the decrease of the maximum temperature in the reactor, it can be observed, that the temperature at the reactor outlet is increased by approx. 3K. This behavior can be explained



a) Temperature profiles in the reactor over the axial reactor length for the time steps  $t = 0$  s, 10 s, 20 s, 30 s and 40 s; thin black lines in the experimental data (left) mark the non-smoothened, originally measured temperature profiles.



b) Heat map representing the temperature shift over the axial reactor length; color code represents the temperature along the relative axial length of the reactor (x-axis) over time (y-axis); the green line marks the hot spot position.

Figure 4.16: Shift of the temperature profile during a load change from  $COR = 0.8$ ;  $SN = 2.0$ ;  $GHSV = 6,000 \text{ h}^{-1}$  to  $COR = 0.9$ ;  $SN = 4.0$ ;  $GHSV = 12,000 \text{ h}^{-1}$  at 80 bar and a cooling temperature of  $240^\circ\text{C}$  obtained by experiment (left) and simulation (right); experimental values were smoothed by the Savitzky-Golay filter [251].

by the higher GHSV as well as the increased COR. While the reaction was approaching chemical equilibrium at the reactor outlet before the load change, the higher load of synthesis gas as well as the slower reaction kinetics extend the kinetic zone to the outlet of the reactor.

In the steady state after the load change, the temperature directly downstream the hot spot drops from 257 °C to 253 °C. This decrease was caused by a strong reduction of the reaction rate at this point in the reactor. After this temperature reduction, reaction kinetics are obtained at a low, slightly decreasing level from  $z/h_{\text{cat}} = 0.12$ . The fact that activity of the catalyst is obtained at a low level leading to higher outlet temperatures than the steady state before the load change shows that the rapid axial temperature decrease is rather of a kinetic nature than due to an equilibrium limitation. A similar behavior was observed during all experimental points with  $\text{COR} \geq 0.9$  and  $\text{SN} \leq 5.0$  (compare Fig. 4.15). Therefore, this rapid axial decrease of reaction kinetics could very likely be linked to a mechanistic switch in reaction kinetics due to the increased partial pressure of water. Advanced analyses measuring the axial concentration profile could confirm this hypothesis in future work.

On the right side of Fig. 4.16 a), the transition of the temperature profile obtained with the dynamic reactor model is displayed during the same dynamic load change. Compared to the measured data, the shift of the temperature profile over time follows a similar trend. Within 20 s after the load change the temperature of the hot spot decreases significantly and its position moves downstream in the catalyst bed. Then, between 20 s and 40 s after the load change, the primary hot spot vanishes and a new hot spot forms near the reactor inlet. Due to the remaining inaccuracy of the kinetic model obtained from the steady state measurements in Sec. 4.2, deviations remain in both steady states before and after the load change. However, the overall dynamic behavior of the reactor is well described with the dynamic model explained in Sec 3.1.5.

In Fig. 4.16 b), the temperature profiles are displayed over time for both, experimental data (left) and simulation (right) as a heat map. In these graphs, the color code represents the reactor temperature. This kind of graphical illustration was found to be advantageous in displaying deviations of the temperature profiles over time. The two graphs show slight deviations in the steady states of the simulations ( $t = 0$  s and  $t = 40$  s). While the measured temperature in the hot spot is higher before the load change compared to the simulation, lower temperatures are predicted downstream the hot spot by the simulation model after the load change. A closer look at the position of the hot spot (solid green line) shows a comparable dynamic behavior of simulation and experiment. Within the first 22 s after the load change, the hot spot moves to the back of the reactor. Simultaneously, the new hot spot is formed further upstream the reactor. 23 s after the load change, the temperature of the newly formed, secondary hot spot exceeds the temperature of the vanishing primary hot spot. This time is marked in Fig. 4.16 b) by the shift of the hot spot position to the reactor inlet. Interestingly, this shift appears at the same time for both experiment and dynamic simulation. Overall it can be concluded that the characteristic of the load change considered here is well described by the dynamic reactor model.

With regard to Eq. 3.65, the speed of the temperature shift inside the reactor is determined by density and heat capacity of both catalyst and gas phase. While the density of the gas phase was determined by SRK EoS (see Sec. 3.1), the solid density of the catalyst and porosity of the

fixed bed were measured during the filling of the reactor [248]. Therefore, the heat capacity of the activated catalyst inside the reactor can be considered as the determinant parameter for the speed of the load change inside the reactor. In Fig. 4.17 a) three dynamic reactor simulations were carried out varying the heat capacity of the catalyst. For the base case (middle), the heat capacity was overtaken as measured by Henkel [202]. In Fig. 4.17 a) left, the heat capacity was reduced by 30 %, while it was increased by 30 % on the right. The graphs show the temperature profiles before the load change (0s) as well as 10s, 20s and 30s after it was performed.

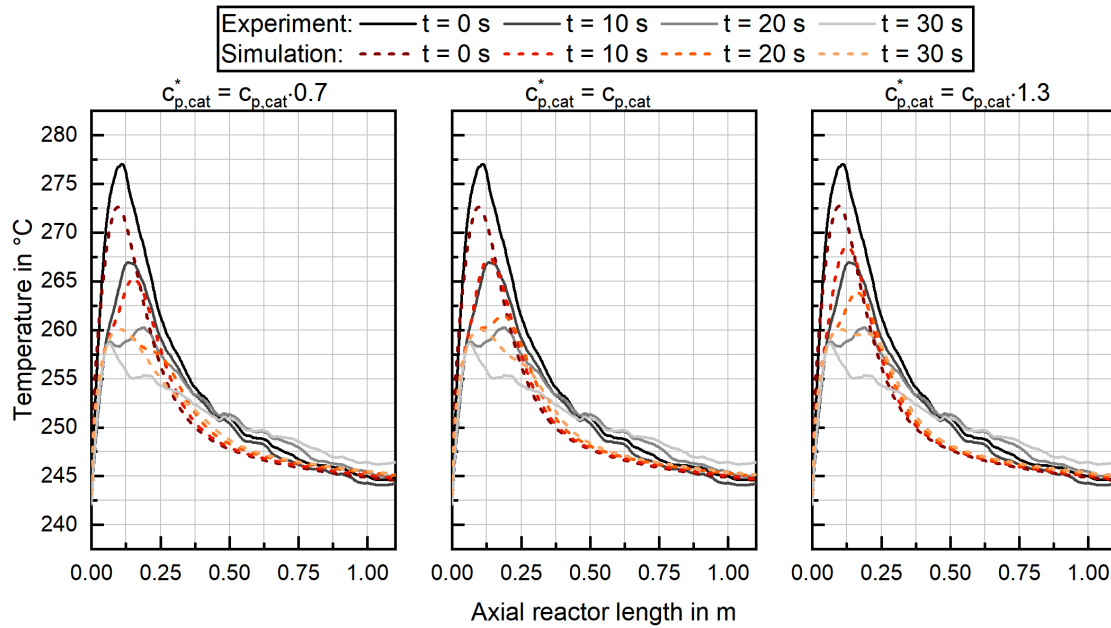
With regard to the steady state working point before the load change, the graphs show, that the heat capacity of the catalyst does not influence the dynamic simulation model in agreement to Eq. 3.62. This finding also confirms that the stability of the ODE-solver was not influenced by the variation of this parameter.

In terms of the dynamic behavior of the simulations, only small deviations in hot spot temperature at 10s and 20s are shown between the base case simulation and the experimental data. Between 20s and 30s the hot spot obtained by the simulation moves to the reactor inlet in a comparable manner as the experimental data.

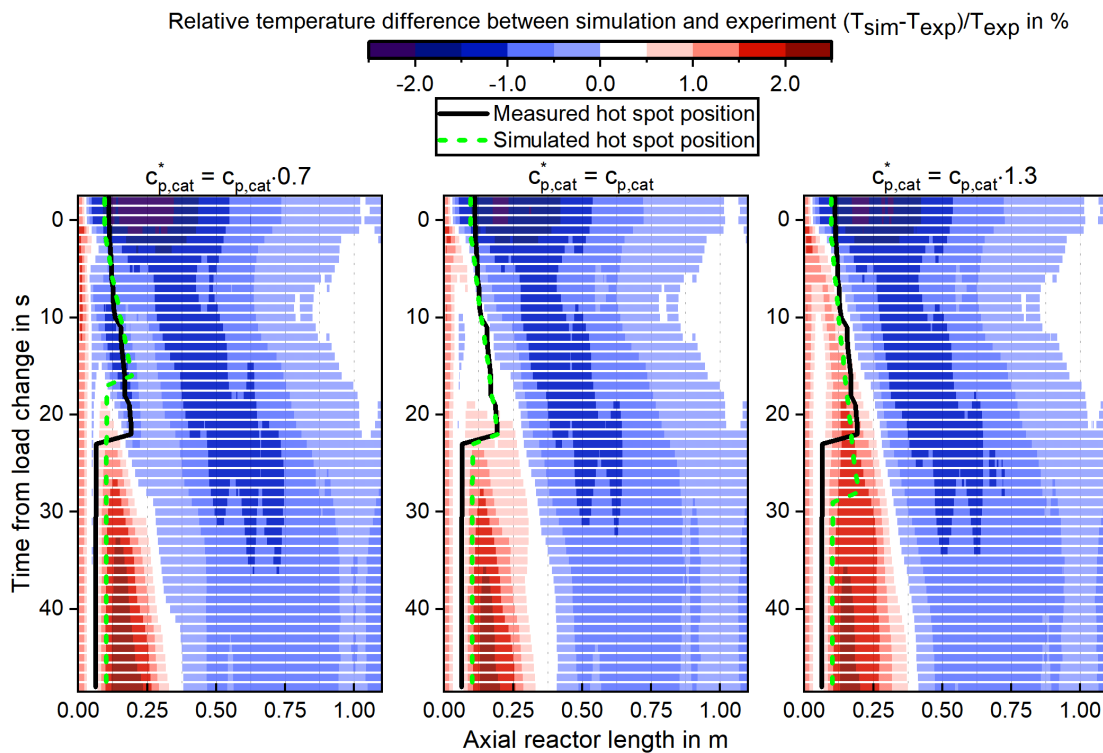
Compared to the base case, the reduction of the catalyst's heat capacity decreased the time for the adaption to the new load point significantly. In this case, the temperature and position of the hot spot approach the steady state already after 20s, i.e. 10s ahead of the base case simulation and the experimental data. On the other hand, the increase of the catalyst's heat capacity extends the time for adaption to the new load point compared to the base case. Hot spot temperature for this case exceeds the temperature of the experiment already 10s after the load change. The fact that this difference increases over time shows that heat capacity is overestimated when heat capacity is increased from the base case.

In Fig. 4.17 b), a heat map symbolizing the relative deviations between the experiment and simulation is shown for the three heat capacities considered. In the graphs, the color code represents the relative temperature deviation between simulation and experiment. Blue color represents a underestimation of the temperature obtained by the simulation, while the red color marks overestimated temperatures. In the areas of white color, a relative deviation of 0 % between simulation and experiment was obtained. All three graphs show that the temperature of the steady state before the load change is underestimated by the reactor simulation. Besides, the graphs indicate a weakness of the model for the steady state working point at  $COR = 0.9$  after the load change. Here, the kinetic model is not capable of following the sharp decrease of the experimentally obtained temperature at 0.06 m reactor length downstream the hot spot. Further research will be necessary to include this kinetic shift probably caused by the increased water in the gas mixture into a kinetic model for methanol synthesis.

With regard to the deviation between simulation and experimental data, the graphs clearly indicate the sensitivity of the heat capacity of the catalyst on the reactor performance. In case of the base case, the lowest deviations are obtained after the load change, especially at the hot spot position (dotted line: simulation; dashed line: experimental data). Remarkably, the positions as well as the previously mentioned shift of the hot spot only show minor deviations. Contrary to that, in the simulation case with decreased heat capacity, Fig. 4.17 b) (left) indicates an underestimation of the temperature around the hot spot. This can be interpreted as a too



a) Temperature profiles obtained by experiments (solid lines) and dynamic simulation (dashed lines) before the load change (0 s) as well as 10 s, 20 s and 30 s after the load change.



b) Heat map on the relative temperature difference along the axial reactor length (x-axis) between simulation and experiment over time (y-axis); the color code represents the relative temperature difference: blue – temperature obtained by simulation is lower than the measured temperature; white – temperature of simulation and experiment are equal; red – temperature obtained by simulation exceeds the experimental data; Lines mark the measured (solid) and simulated (dashed) hot spot position.

Figure 4.17: Comparison of experimental and simulation data obtained during a load change from  $COR = 0.8$ ;  $SN = 2.0$ ;  $GHSV = 6,000 \text{ h}^{-1}$  to  $COR = 0.9$ ;  $SN = 4.0$ ;  $GHSV = 12,000 \text{ h}^{-1}$  at 80 bar and  $T_{cool} = 240 \text{ }^\circ\text{C}$  using different heat capacities for the catalyst particle; Heat capacity of the simulation was reduced by 30 % (left) and increased by 30 % (right) from the base case (middle) representing the heat capacity as published by Henkel [202].

fast load change when the catalyst heat capacity is reduced in the simulation. This statement is supported by the development of hot spot position obtained by experiment (dashed line) and simulation (dotted line). In this case, the shift of the hot spot to the reactor inlet obtained from the simulation is observed 6 s ahead of the experiment.

On the other hand, an increase of the heat capacity leads to an overestimation of the temperature of the hot spot after the load change. This behavior shows that the temperature profile obtained by the simulation with increased  $c_{p,cat}$  decreases slower compared to the experimental data. Besides, the shift of the hot spot temperature in the simulation appears 6 s after the simulation. Overall, it can be concluded from the analysis of the load change performed here that the heat capacity measured by Henkel is well applicable to the catalyst used within this work. Moreover, the dynamic model presented in Sec. 3.1.5 was validated by the detailed comparison with experimental data. The herein proposed differential steady state kinetic model seems suitable to describe the experimental data with an appropriate accuracy. This finding is in contradiction to the work published by Seidel et al. proposing the necessity of a dynamic kinetic model to accurately describe the dynamic behavior of methanol synthesis. These differences, however, are very likely due to the differences in the experimental setups. While in this work, the load change is largely determined by temperature change depending on the heat capacity of the catalyst, Seidel et al. used an ideal isothermal Berty-type reactor. Probably, the researchers were able to observe dynamic effects caused by the change of catalyst morphology as the influence of temperature was eliminated in their measurement. The results of this work, however, propose that a dynamic kinetic model is not necessary for the description of an industrial reactor under transient load conditions. Further research including a dynamic quantitative gas phase measurement would be necessary in order to further support this statement.

#### 4.4 Application on process scale

To demonstrate the effect of the differential kinetic model derived in this work on design of the synthesis process schematically depicted in Fig. 2.5, a simulation study was performed integrating the adapted reactor model into the process model implemented in MATLAB® Simulink with regard to Sec. 3.1.6. In order to account for a load case using a CO<sub>2</sub>-based synthesis gas (compare Sec. 2.3.4), COR = 1.0 was applied for the MUG. For this simulation study, the stoichiometry of the MUG was varied in the range  $0.5 \leq SN_{MUG} \leq 4.0$  to demonstrate the influence of syngas stoichiometry on process design (see also Sec. 2.4.4). As another important parameter for process design, the recycle ratio (see Eq. 2.22) was varied as second parameter in the range  $1.0 \leq RR \leq 14.0$ . The cooling temperature was held constant at  $T_{cool} = 240^\circ\text{C}$  as this temperature was applied within the validation experiments presented in Sec. 4.2. GHSV in the reactor was fixed to  $10,000\text{ h}^{-1}$ .

In Fig. 4.18 the sensitivity of  $SN_{MUG}$  and the RR on the operating conditions of the synthesis process are discussed. By an increase of RR, conversion of the syngas is increased as the gas mixture is led through the reactor more often. However, increased values for RR entail the drawback of larger process equipment, as the amount of gas in the loop process strongly increases. Moreover, RR strongly influences the composition of the gases in the loop. At high RR, inert

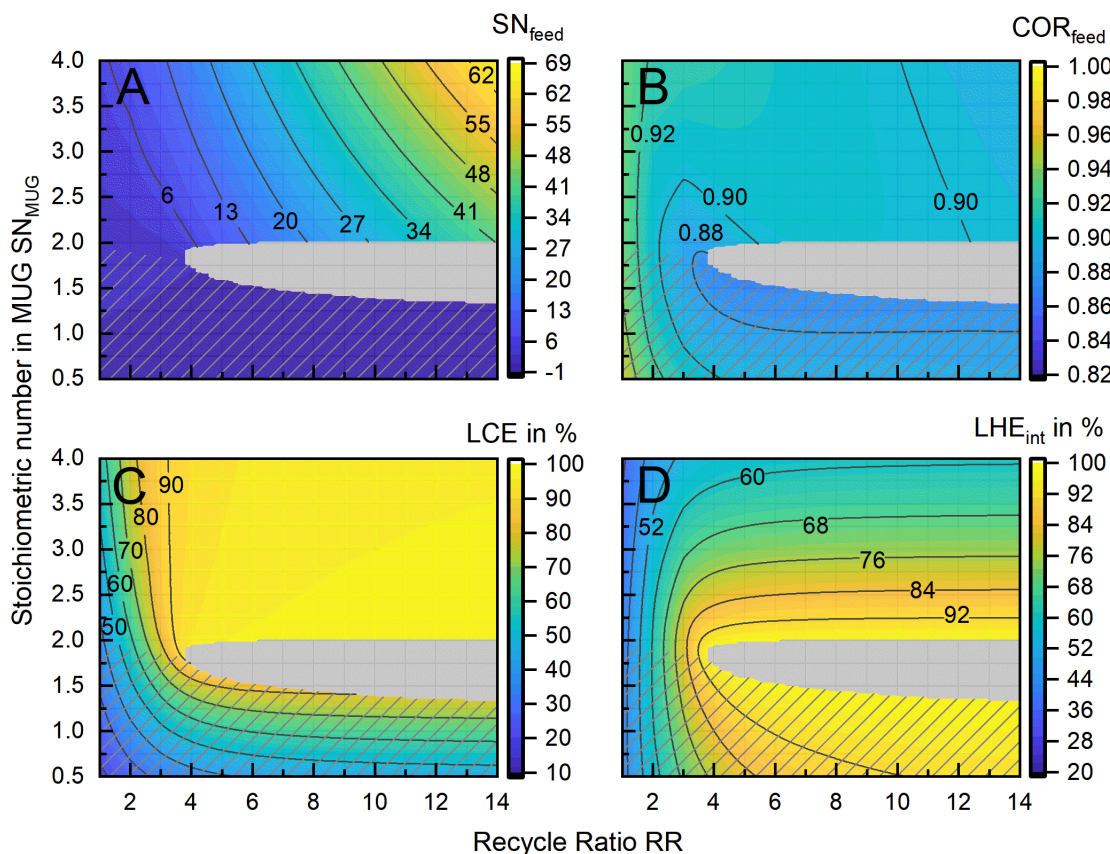


Figure 4.18: Sensitivity of  $SN_{MUG}$  and RR on the operating condition of the process; Color represents the simulated values for  $SN_{feed}$  (A) and  $COR_{feed}$  (B) balancing in the synthesis loop as well as LCE (C) and  $LHE_{int}$  (D); Hatched area marks sub-stoichiometric gas mixtures at reactor inlet; gray area indicates unstable working points where the recycle ratio could not be adjusted due to full loop conversion; Simulation parameters:  $GHSV = 10,000 \text{ h}^{-1}$ ;  $p = 65 \text{ bar}$ ;  $T_{cool} = 240 \text{ }^\circ\text{C}$ ;  $COR_{MUG} = 1.0$ ;  $T_{flash} = 40 \text{ }^\circ\text{C}$ ; kinetic model:  $Nestler_{diff}$ .

gases and the excessive reactant species, i.e.  $H_2$  for over-stoichiometric gas mixtures and  $CO_x$  for sub-stoichiometric gas mixtures, are accumulated in the loop.

In Fig. 4.18 (A) the influence of  $SN_{MUG}$  and RR to SN of the reactor feed ( $SN_{feed}$ ) is discussed. The hatched area marks the values with  $SN_{feed} < 2.0$ , which was not experimentally investigated within this work, as this gas composition was expected to lead to an increased formation of reaction byproducts [10, 55]. The border line of the marked area for  $SN < 2.0$  slightly decreases from  $RR = 1.0$  to  $RR = 3.8$  due to the solubility of  $CO_2$  in the liquid raw methanol at the flash separator of the process. At  $RR > 3.8$  and  $SN < 2.0$  a blank area is displayed in the graph indicating unstable process parameters, where the set recycle ratio cannot be adjusted due to full conversion of the reactants towards raw methanol. In a real process the full conversion of the educts towards methanol and water achieved at these process conditions would lead to a decrease in process pressure. At  $SN_{MUG} > 2.0$ ,  $H_2$  is accumulated in the synthesis loop, while it is depleted for  $SN_{MUG} < 2.0$ . Accumulation of excess  $H_2$  in the loop is strongly enhanced by an

increase of RR, ending up at gas compositions, where exclusively  $\text{H}_2$  is present in the reactor feed.

Fig. 4.18 (B) shows the development of  $\text{COR}_{\text{feed}}$  in dependence of  $\text{SN}_{\text{MUG}}$  and RR. The graph indicates a decrease of COR when RR is increased from 1.0 to 3.8. This change can be led back to the equilibrium of the rWGS reaction which is shifted towards CO and  $\text{H}_2\text{O}$  by the removal of water in the flash separator. A minimal value of  $\text{COR}_{\text{feed}}$  of 0.87 is reached in the sub-stoichiometric (hatched) area at  $\text{RR} = 5.1$  and  $\text{SN}_{\text{MUG}} = 1.6$ . However, validation measurements would be necessary in order to determine the kinetic activity of the rWGS for sub-stoichiometric gas mixtures. Overall, the simulation shows, that the COR-range investigated within the experimental campaign at the miniplant (see Tab. 3.8) does represent the gas composition on process scale.

With regard to the educt utilization, LCE (compare Eq. 2.23) and  $\text{LHE}_{\text{int}}$  (compare Eq. 2.25) were considered as key indicators for conversion of the educt gases into raw methanol obtained at the flash separator. LCE and  $\text{LHE}_{\text{int}}$  are depicted in Fig. 4.18 (C) and (D), respectively. Comparison of the two efficiencies shows opposing trends in dependence of  $\text{SN}_{\text{MUG}}$ . While both key indicators increase with increasing RR, LCE approaches 100 % at  $\text{SN}_{\text{MUG}} > 2.0$ , while  $\text{LHE}_{\text{int}}$  reaches a maximum at the border of the unstable (gray) area and at  $\text{SN}_{\text{MUG}} < 2.0$ . As the price of methanol produced from electrolytic  $\text{H}_2$  is mainly determined by the operating cost of  $\text{H}_2$  production [13, 15, 259],  $\text{LHE}_{\text{int}}$  is of higher importance for PtM processes than LCE. Therefore, in future experimental studies special attention should be drawn on the gas compositions in the hashed area of Fig. 4.18.

In order to demonstrate the influence of the kinetic model on process design, the kinetic model by Bussche was integrated into the process and subjected to the same sensitivity analysis. In Fig. 4.19 the results of the analysis are displayed applying the same color code as in Fig. 4.18. With regard to  $\text{SN}_{\text{feed}}$  (A), the graph indicates that less  $\text{H}_2$  is enriched within the loop at  $\text{SN}_{\text{MUG}} > 2.0$  in comparison to Fig. 4.18 (A). Considering  $\text{COR}_{\text{feed}}$  (Fig. 4.19 (B)) the lower values for  $\text{SN}_{\text{feed}}$  can be explained by an increased activity of the rWGS in the kinetic model by Bussche for over-stoichiometric gas compositions. The lower activity of the kinetic model by Bussche in comparison to the here proposed model  $\text{Nestler}_{\text{diff}}$  (compare Fig. 4.10) is reflected by the unstable (gray) area shifting to higher RR. As a consequence, process design based on Bussche's kinetic model would lead to an unnecessarily large dimensioned synthesis loop.

Consideration of two different kinetic models on process scale showed, that selection of the kinetic model does largely influence gas composition and process design. This results emphasized the significance of kinetic validation and the herein proposed approach for the technological implementation of PtM-processes.

Application of the differential kinetic model derived within this work ( $\text{Nestler}_{\text{diff}}$ ) on the process scale showed that the parameters of the validation campaign presented in Tab. 3.8 represent the synthesis conditions in a  $\text{CO}_2$ -based process. With regard to  $\text{SN}_{\text{feed}}$ , values exceeding the validated range of the kinetic model could be reached in case of high RR and  $\text{SN}_{\text{MUG}} > 2$ . However, from an economical point of view, increased RR would lead to growing equipment cost. As shown in Fig. 4.18 (D), the optimum  $\text{LHE}_{\text{int}}$  would be reached along the unstable area already at  $\text{RR} = 3.8$ . Consequently higher RR would not lead to an increase of  $\text{H}_2$  utilization

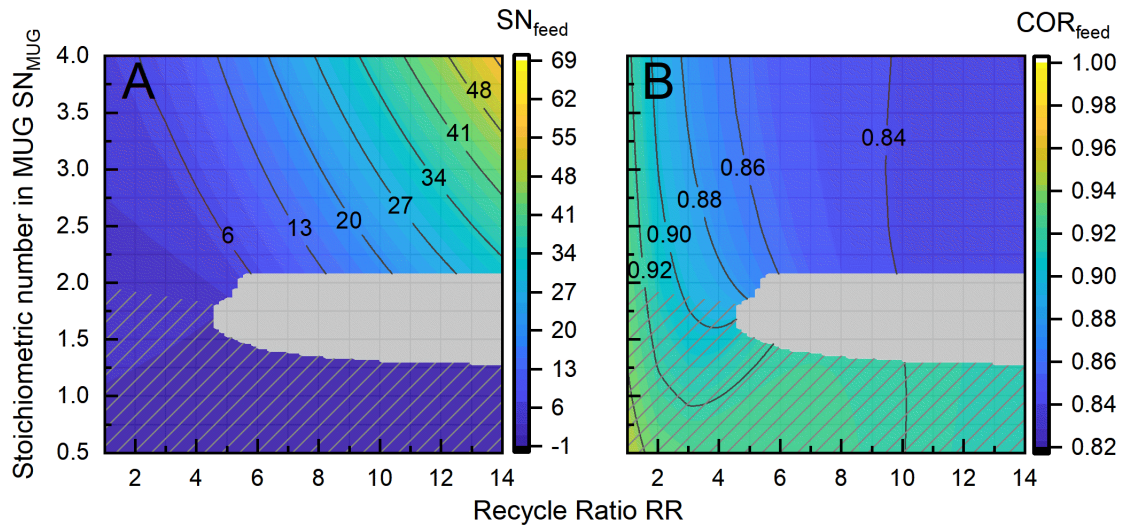


Figure 4.19: Sensitivity of  $SN_{MUG}$  and  $RR$  on the operating condition of the process; Color represents the simulated values for  $SN_{feed}$  (A) and  $COR_{feed}$  (B) balancing in the synthesis loop; Hatched area marks sub-stoichiometric gas mixtures at reactor inlet; gray area indicates unstable working points where the recycle ratio could not be obtained due full loop conversion; Simulation parameters:  $GHSV = 10,000 \text{ h}^{-1}$ ;  $T_{cool} = 240 \text{ }^\circ\text{C}$ ;  $COR_{MUG} = 1.0$ ;  $T_{Flash} = 40 \text{ }^\circ\text{C}$ ; kinetic model: Bussche<sub>orig</sub> [145].

and therefore probably negatively affect the overall plant economics.  $SN > 8.0$  would therefore be unlikely to occur in a  $\text{CO}_2$ -based methanol synthesis process.

$SN < 2.0$  seems a promising option for  $\text{CO}_2$ -based PtM processes with regard to  $LHE_{int}$  (compare Fig. 4.18 (D)). However, sub-stoichiometric gas compositions remain one open research question for an experimental validation and an extension of the validated data range of the differential kinetic model derived in this work. Advanced gas phase analysis as e.g. an FTIR with a longer optical path length would be necessary for sub-stoichiometric experimental campaigns in order to accurately determine the formation of side-products in dependence of  $SN$ . If these experiments could verify a stable catalytic activity and a lower formation of side-products than expected, PtM process could be operated within a wider range of economic operating conditions.

Finally, control and design strategies could be enhanced to dynamically operated PtM-process in future work. In order to verify the behavior of the catalyst and the reactor under fluctuating MUG-conditions on process scale, the miniplant setup could be connected with a dynamic process model.



## 5 Conclusion and Outlook

For the implementation of dynamically operated PtX processes, a deep understanding of the behavior of the process equipment under varying load conditions is necessary. With regard to Power-to-Methanol (PtM) processes using CO<sub>2</sub>-rich syngas and electrolytically produced H<sub>2</sub> supplied by fluctuating renewable energy, the simulative description of the stationary and dynamically operated synthesis reactor was identified one core-challenge. The complex interplay between the thermodynamically and kinetically limited CO<sub>2</sub>-hydrogenation and reverse water-gas-shift reaction at non-conventional gas compositions required for a detailed kinetic study.

Four kinetic models were investigated closer within this work due to their role as literature standard, i.e. Graaf [192] and Bussche [145], or due to their validation on a modern commercial catalyst, i.e. Henkel [202] and Park [203]. However, the experimental data used by Graaf, Bussche and Henkel to derive their kinetic models were found not representative for the parameter ranges relevant for PtM processes, either by pressure, COR and/or SN (compare Fig. 2.10). The kinetic model published by Park et al. is based on experimental data captured over a wide parameter range for both conventional and PtM-based methanol synthesis – however, this model was found not usable due to missing kinetic model parameters and inconsistencies in the kinetic description (for details see Sec. 3.1.2). Therefore, the experimental data measured by Park et al. with an integral kinetic reactor was used to derive the kinetic model "Nestler<sub>integ</sub>" based on the rate equation proposed by Henkel. Due to the wide validation range, this model was shown to be a significant improvement in comparison to the kinetic models available in scientific literature for methanol synthesis.

However, the Nestler<sub>integ</sub> kinetic model was scarcely validated at high GHSVs and elevated COR with the possible consequence of an inappropriate description of the axial kinetic performance of the catalyst and consequently improper sizing of the reactor. In order to further validate and improve the kinetic model, a novel experimental approach including a highly resolved axial temperature measurement in a polytropic miniplant-scale reactor coupled with a FTIR gas phase analysis was implemented. To ensure a high relevance of this work for the application on industrial scale, the miniplant reactor was designed for a maximized thermochemical agreement to a steam cooled tube bundle reactor by a simulation-based scale-down (see Sec. 3.3). By means of a comprehensive experimental campaign covering 324 experimental points for pressures between 50 bar and 80 bar over the complete PtM-relevant COR-, SN- and GHSV-range, a data set for the validation of kinetic models was gathered. During the experimental campaign, temperature gradients up to 50 K between cooling medium and catalyst bed as well as methanol molar fractions in the product of up to 11 % were observed depending on the load conditions applied underlining the high transferability of the miniplant data to industrial scale.

A comparison of the experimental miniplant data to simulations using the kinetic models by Graaf and Bussche showed strong deviations with regard to temperature profile and product composition. Compared to those, the kinetic model Nestler<sub>integ</sub> showed a better agreement to the data obtained from the miniplant setup in terms of hot spot temperature and product

composition, though, with significant deviations in the calculation of hot spot position.

As none of the three kinetic models considered for the validation of the miniplant experimental data was capable of sufficiently describing the axial kinetic performance with their original kinetic parameters, these models were subjected to a parameter fitting. As a result, the fitted kinetic models Graaf<sub>fit</sub> and Nestler<sub>diff</sub> were able to describe the experimental data by a high level of agreement. In comparison to these models, the kinetic model Bussche<sub>fit</sub> showed strong deviations from the experimental data after the parameter estimation, underlining the capability of the herein proposed miniplant validation approach to verify mechanistic assumptions of complex reaction networks. Therefore, the rate equation proposed by Bussche was identified unsuitable for the kinetic description methanol synthesis.

Since the reaction velocity of CO-hydrogenation calculated with the adjusted kinetic model Graaf<sub>fit</sub> was found to be negligible, it was concluded that the Nestler<sub>diff</sub> model based on the same mechanism, however, neglecting CO-hydrogenation was appropriate to describe methanol synthesis from CO<sub>2</sub>-rich gases. Consequently, the kinetic model Nestler<sub>diff</sub> was identified the most adequate description for the reaction kinetics of methanol synthesis with an average root mean square error (RMSE) of 0.4% with regard to product composition and 1.5 K in the axial temperature profile.

Application of the final kinetic model in the dynamic reactor simulation delivered a highly accurate description of an exemplary load change performed with the miniplant setup. Thus, it was concluded, that a steady state kinetic model can be appropriate for the kinetic description of an industrial fixed bed reactor under fluctuating load conditions.

In a final step, consideration of the Nestler<sub>diff</sub> kinetic model on process scale showed that the applied ranges for SN and COR in the experimental campaign represent the gas composition balancing in an industrial CO<sub>2</sub>-based PtM process underlining the high reliability of the kinetic model. Implementation of a detailed economic model into the process model is currently in progress to optimize the process layout and operation conditions for improved competitiveness of PtM processes operated under fluctuating load. Moreover, this result proved the capability of the miniplant setup for the analysis of dynamic load changes in polytropically operated fixed bed reactors.

Besides possible enhancements of the reactor simulation platform, e.g. by upgrading from the one-dimensional towards a two-dimensional model, the deactivation of the catalyst was identified as an important field for further research (see also Fig. A.12). As the experimental campaign executed with the miniplant setup was subjected to catalyst degradation, especially at high pressures and CO<sub>2</sub> contents in the feed gas, a better accuracy for the kinetic model could be obtained when this influence was described by a deactivation model. Furthermore, a better understanding of the catalyst deactivation mechanisms using the axially resolved experimental data from the miniplant setup could contribute to prolong the catalyst lifetime by enhanced operating conditions and improved catalyst formulation. Consequently, a detailed study on the catalyst deactivation is likely to increase the competitiveness of PtM-based methanol in comparison to the conventionally produced counterpart.

Even though a high level of agreement was obtained between the reactor simulation using the Nestler<sub>diff</sub> kinetic model and the experimental data from the miniplant setup, further research

on the influence of water on the reaction kinetics will be necessary to improve the accuracy of the kinetic model at high COR and catalyst formulation. Moreover, a better understanding of the rate inhibiting effect of water would enable the adaption of the process operating conditions to accelerate reaction kinetics on the industrial scale.

To reinforce the herein presented methodology for the simulation-based scale-down, experimental data obtained from a large scale methanol reactor would be helpful to enhance the model of the industrial reactor with regard to diffusion and heat transfer in future work. This could contribute to enhance the comparability of the performance of the miniplant reactor and the industrial scale by a higher level of confidence.

Finally, this work proved that a miniplant experimental setup featuring a highly resolved temperature measurement can be used to derive detailed kinetic models for exothermic equilibrium limited reactions which can be applied under steady state and dynamic load conditions. Moreover, it was shown that this measurement method can be superior over "classic" kinetic measurements in isothermal integral reactors if appropriate models for heat transfer, diffusion and reaction kinetics are available. Transfer of this new methodology towards other syntheses as e.g. methanation, Fischer-Tropsch synthesis or  $\text{NH}_3$  synthesis in future studies could make an important contribution to evaluate the potential of a flexible operation of these processes in the context of Power-to-X technology.



# Bibliography

- [1] United Nations, ed. *Kyoto Protocol to the United Nations Framework Convention on Climate Change*. 1998. URL: <https://unfccc.int/sites/default/files/resource/docs/cop3/107a01.pdf>.
- [2] United Nations, ed. *Paris agreement*. 2015. URL: [http://unfccc.int/files/essential\\_background/convention/application/pdf/english\\_paris\\_agreement.pdf](http://unfccc.int/files/essential_background/convention/application/pdf/english_paris_agreement.pdf).
- [3] Remus Pravalie and Georgeta Bandoc. “Nuclear energy: Between global electricity demand, worldwide decarbonisation imperativeness, and planetary environmental implications”. In: *Journal of environmental management* 209 (2018), pp. 81–92. DOI: 10.1016/j.jenvman.2017.12.043.
- [4] Ministerial Council on Renewable Energy, Hydrogen and Related Issues, ed. *Basic Hydrogen Strategy*. 2017. URL: [https://www.meti.go.jp/english/press/2017/pdf/1226\\_003b.pdf](https://www.meti.go.jp/english/press/2017/pdf/1226_003b.pdf).
- [5] Bundesministerium für Wirtschaft und Technologie, ed. *Die Nationale Wasserstoffstrategie*. 2020. URL: <https://www.bmwi.de/Redaktion/DE/Publikationen/Energie/die-nationale-wasserstoffstrategie.pdf>.
- [6] Alexis Michael Bazzanella and Florian Ausfelder. *Low carbon energy and feedstock for the European chemical industry*. Ed. by DECHEMA, Gesellschaft für Chemische Technik und Biotechnologie e.V. 2017. URL: [http://dechema.de/Low\\_carbon\\_chemical\\_industry.html](http://dechema.de/Low_carbon_chemical_industry.html).
- [7] A. Valera-Medina et al. “Ammonia for power”. In: *Progress in Energy and Combustion Science* 69 (2018), pp. 63–102. ISSN: 03601285. DOI: 10.1016/j.pecs.2018.07.001.
- [8] Stefan Rönsch et al. “Review on methanation – From fundamentals to current projects”. In: *Fuel* 166 (2016), pp. 276–296. ISSN: 00162361. DOI: 10.1016/j.fuel.2015.10.111.
- [9] Vincent Dieterich et al. “Power-to-liquid via synthesis of methanol, DME or Fischer–Tropsch-fuels: a review”. In: *Energy & Environmental Science* 13.10 (2020), pp. 3207–3252. ISSN: 1754-5692. DOI: 10.1039/D0EE01187H.
- [10] George A. Olah, Alain Goepfert, and G. K. Surya Prakash. *Beyond Oil and Gas: The Methanol Economy*. 2nd ed. Wiley Chichester et al, 2009.
- [11] Martin Bertau, ed. *Methanol: The basic chemical and energy feedstock of the future: Asinger’s vision today*. Berlin and Heidelberg: Springer, 2014. ISBN: 978-3-642-39709-7.
- [12] B. Anicic, P. Trop, and D. Goricanec. “Comparison between two methods of methanol production from carbon dioxide”. In: *Energy* 77 (2014), pp. 279–289. ISSN: 03605442. DOI: 10.1016/j.energy.2014.09.069.
- [13] Judit Nyári et al. “Techno-economic barriers of an industrial-scale methanol CCU-plant”. In: *Journal of CO<sub>2</sub> Utilization* 39 (2020), p. 101166. ISSN: 22129820. DOI: 10.1016/j.jcou.2020.101166.

- [14] Giulia Bozzano and Flavio Manenti. “Efficient methanol synthesis: Perspectives, technologies and optimization strategies”. In: *Progress in Energy and Combustion Science* 56 (2016), pp. 71–105. ISSN: 03601285. DOI: 10.1016/j.pecs.2016.06.001.
- [15] Christoph Hank et al. “Economics & carbon dioxide avoidance cost of methanol production based on renewable hydrogen and recycled carbon dioxide – power-to-methanol”. In: *Sustainable Energy & Fuels* 2.6 (2018), pp. 1244–1261. ISSN: 2398-4902. DOI: 10.1039/C8SE00032H.
- [16] G. Natta. “Synthesis of Methanol”. In: *Catalysis*. Ed. by Paul H. Emmett. Vol. 3. New York: Emmett, Paul H., 1955, pp. 349–411.
- [17] OCI N.V., ed. *OCI N.V. Investor Presentation*. 2016. URL: <https://www.sec.gov/Archives/edgar/data/1324404/000119312516490022/d140313d425.htm>.
- [18] USGS, ed. *Mineral Commodity Summaries 2020*. 2020. URL: <https://pubs.usgs.gov/periodicals/mcs2020/mcs2020.pdf>.
- [19] Steve Lewandowski. *Ethylene - Global*. Ed. by IHS Markit. 2016. URL: <https://cdn.ihs.com/www/pdf/Steve-Lewandowski-Big-Changes-Ahead-for-Ethylene-Implications-for-Asia.pdf>.
- [20] Marc Alvarado. *Methanol*. Ed. by IHS Markit. 2016. URL: <http://www.methanol.org/wp-content/uploads/2016/07/Marc-Alvarado-Global-Methanol-February-2016-IMPCA-for-upload-to-website.pdf>.
- [21] Florian Ausfelder et al. *Technology Roadmap "Energy and GHG Reductions in the Chemical Industry via Catalytic Processes"*. Ed. by DECHEMA. 2013. URL: <https://dechema.de/industrialcatalysis.html>.
- [22] Statista, ed. *CO2-Emissionen weltweit in den Jahren 1960 bis 2019*. 2021. URL: <https://de.statista.com/statistik/daten/studie/37187/umfrage/der-weltweite-co2-ausstoss-seit-1751/>.
- [23] Andreas Bode et al. “Methane Pyrolysis and CO<sub>2</sub> Activation - Technologies with Application Options for Hydrogen, Carbon and Synthesis Gas Production”. In: *Chemie Ingenieur Technik* 88.9 (2016), p. 1342. ISSN: 0009-286X. DOI: 10.1002/cite.201650483.
- [24] Guenter Harp. “Methanol as Key for Industrial Symbiosis between Chemistry and Steel”. In: *6th Conference on Carbon Dioxide as Feedstock for Fuels, Chemistry and Polymers*. Ed. by nova-Institut GmbH. 2018.
- [25] Jerzy Skrzypek et al. “Thermodynamics and kinetics of low pressure methanol synthesis”. In: *The Chemical Engineering Journal and the Biochemical Engineering Journal* 58.2 (1995), pp. 101–108. ISSN: 09230467. DOI: 10.1016/0923-0467(94)02955-5.
- [26] Godfrey C. Chinchin et al. “Mechanism of methanol synthesis from CO<sub>2</sub>/CO/H<sub>2</sub> mixtures over copper/zinc oxide/alumina catalysts: Use of <sup>14</sup>C-labelled reactants”. In: *Applied Catalysis* 30.2 (1987), pp. 333–338. ISSN: 01669834. DOI: 10.1016/S0166-9834(00)84123-8.

- [27] Yu B. Kagan et al. “Mechanism of methanol synthesis from carbon dioxide and hydrogen. Tracer study of conversion over Cu–Zn–aluminium oxide SNM-1 catalyst”. In: *Dokl. Chem. (Engl. Transl.); (United States)* 221 (1975), pp. 254–256.
- [28] Jae Sung Lee et al. “A Comparative Study of Methanol Synthesis from CO<sub>2</sub>/H<sub>2</sub> and CO/H<sub>2</sub> over a Cu/ZnO/Al<sub>2</sub>O<sub>3</sub> Catalyst”. In: *Journal of Catalysis* 144.2 (1993), pp. 414–424. ISSN: 00219517. DOI: 10.1006/jcat.1993.1342.
- [29] Martin Muhler et al. “On the role of adsorbed atomic oxygen and CO<sub>2</sub> in copper based methanol synthesis catalysts”. In: *Catalysis Letters* 25.1-2 (1994), pp. 1–10. DOI: 10.1007/BF00815409.
- [30] George Liu. “The rate of methanol production on a copper-zinc oxide catalyst: The dependence on the feed composition”. In: *Journal of Catalysis* 90.1 (1984), pp. 139–146. ISSN: 00219517. DOI: 10.1016/0021-9517(84)90094-0.
- [31] K. G. Chanchlani. “Methanol synthesis from H<sub>2</sub>, CO, and CO<sub>2</sub> over Cu/ZnO catalysts”. In: *Journal of Catalysis* 136.1 (1992), pp. 59–75. ISSN: 00219517. DOI: 10.1016/0021-9517(92)90106-R.
- [32] James T. Sun, Ian S. Metcalfe, and Mortaza Sahibzada. “Deactivation of Cu/ZnO/Al<sub>2</sub>O<sub>3</sub> Methanol Synthesis Catalyst by Sintering”. In: *Industrial & Engineering Chemistry Research* 38.10 (1999), pp. 3868–3872. ISSN: 0888-5885. DOI: 10.1021/ie990078s.
- [33] E. A. Volnina and M. A. Kipnis. “Modern View of the Mechanism of Methanol Synthesis on Cu-Containing Catalysts”. In: *Kinetics and Catalysis* 61.1 (2020), pp. 119–129. ISSN: 0023-1584. DOI: 10.1134/S0023158420010115.
- [34] Harold H. Kung. “Deactivation of methanol synthesis catalysts - a review”. In: *Catalysis Today* 11.4 (1992), pp. 443–453. ISSN: 09205861. DOI: 10.1016/0920-5861(92)80037-N.
- [35] Jürgen Ladebeck, Jon P. Wagner, and Toshio Matsuhisa. “Custom made catalysts for low pressure methanol synthesis”. In: *Natural Gas Conversion IV*. Vol. 107. Studies in Surface Science and Catalysis. Elsevier, 1997, pp. 73–78. ISBN: 9780444823526. DOI: 10.1016/S0167-2991(97)80319-9.
- [36] Jingang Wu et al. “The stability of Cu/ZnO-based catalysts in methanol synthesis from a CO<sub>2</sub>-rich feed and from a CO-rich feed”. In: *Applied Catalysis A: General* 218.1-2 (2001), pp. 235–240. ISSN: 0926860X. DOI: 10.1016/S0926-860X(01)00650-0.
- [37] Matthias B. Fichtl et al. “Kinetics of deactivation on Cu/ZnO/Al<sub>2</sub>O<sub>3</sub> methanol synthesis catalysts”. In: *Applied Catalysis A: General* 502 (2015), pp. 262–270. ISSN: 0926860X. DOI: 10.1016/j.apcata.2015.06.014.
- [38] K. Klier. “Catalytic synthesis of methanol from CO/H<sub>2</sub>: IV. The effects of carbon dioxide”. In: *Journal of Catalysis* 74.2 (1982), pp. 343–360. ISSN: 00219517. DOI: 10.1016/0021-9517(82)90040-9.
- [39] A. Nappi et al. “Influence of forced feed composition cycling on catalytic methanol synthesis”. In: *The Canadian Journal of Chemical Engineering* 63.6 (1985), pp. 963–970. DOI: 10.1002/cjce.5450630613.

- [40] V. Ostrovskii. “Mechanisms of methanol synthesis from hydrogen and carbon oxides at Cu–Zn-containing catalysts in the context of some fundamental problems of heterogeneous catalysis”. In: *Catalysis Today* 77.3 (2002), pp. 141–160. ISSN: 09205861. DOI: 10.1016/S0920-5861(02)00241-9.
- [41] Aleksandr Ya Rozovskii. “Fundamentals of Methanol Synthesis and Decomposition”. In: *Topics in Catalysis* 22.3/4 (2003), pp. 137–150. ISSN: 10225528. DOI: 10.1023/A:1023555415577.
- [42] B. Denise, R.P.A. Sneed, and C. Hamon. “Hydrocondensation of carbon dioxide: IV”. In: *Journal of Molecular Catalysis* 17.2-3 (1982), pp. 359–366. ISSN: 03045102. DOI: 10.1016/0304-5102(82)85047-5.
- [43] M. Takagawa. “Study on reaction rates for methanol synthesis from carbon monoxide, carbon dioxide, and hydrogen”. In: *Journal of Catalysis* 107.1 (1987), pp. 161–172. ISSN: 00219517. DOI: 10.1016/0021-9517(87)90281-8.
- [44] Godfrey C. Chinchin et al. “Synthesis of Methanol”. In: *Applied Catalysis* 36 (1988), pp. 1–65. ISSN: 01669834. DOI: 10.1016/S0166-9834(00)80103-7.
- [45] Melanie A. McNeil, Carl J. Schack, and Robert G. Rinker. “Methanol synthesis from hydrogen, carbon monoxide and carbon dioxide over a CuO/ZnO/Al<sub>2</sub>O<sub>3</sub> catalyst”. In: *Applied Catalysis* 50.1 (1989), pp. 265–285. ISSN: 01669834. DOI: 10.1016/S0166-9834(00)80841-6.
- [46] Zao-Xin Ren et al. “Effect of carbon dioxide on methanol synthesis over different catalysts”. In: *Applied Catalysis* 49.1 (1989), pp. 83–90. ISSN: 01669834. DOI: 10.1016/S0166-9834(00)81424-4.
- [47] C. Kuechen and U. Hoffmann. “Investigation of simultaneous reaction of carbon monoxide and carbon dioxide with hydrogen on a commercial copper/zinc oxide catalyst”. In: *Chemical Engineering Science* 48.22 (1993), pp. 3767–3776. ISSN: 00092509. DOI: 10.1016/0009-2509(93)80219-G.
- [48] A. Coteron and A. N. Hayhurst. “Kinetics of the synthesis of methanol from CO + H<sub>2</sub> and CO + CO<sub>2</sub> + H<sub>2</sub> over copper-based amorphous catalysts”. In: *Chemical Engineering Science* 49.2 (1994), pp. 209–221. ISSN: 00092509. DOI: 10.1016/0009-2509(94)80039-1.
- [49] Mortaza Sahibzada, Ian S. Metcalfe, and D. Chadwick. “Methanol Synthesis from CO/CO<sub>2</sub>/H<sub>2</sub> over Cu/ZnO/Al<sub>2</sub>O<sub>3</sub> at Differential and Finite Conversions”. In: *Journal of Catalysis* 174.2 (1998), pp. 111–118. ISSN: 00219517. DOI: 10.1006/jcat.1998.1964.
- [50] Malte Behrens. “Chemical hydrogen storage by methanol: Challenges for the catalytic methanol synthesis from CO<sub>2</sub>”. In: *Recyclable Catalysis* 2.1 (2015), p. 3343. ISSN: 2084-7629. DOI: 10.1515/recat-2015-0009.
- [51] Masahiro Saito and Kazuhisa Murata. “Development of high performance Cu/ZnO-based catalysts for methanol synthesis and the water-gas shift reaction”. In: *Catalysis Surveys from Asia* 8.4 (2004), pp. 285–294. ISSN: 1571-1013. DOI: 10.1007/s10563-004-9119-y.

- [52] Emil Supp. *How to Produce Methanol from Coal*. Berlin and Heidelberg: Springer, 1990. ISBN: 978-3-662-00895-9. DOI: 10.1007/978-3-662-00895-9.
- [53] Jean-Paul Lange. “Methanol synthesis: A short review of technology improvements”. In: *Catalysis Today* 64.1-2 (2001), pp. 3–8. ISSN: 09205861. DOI: 10.1016/S0920-5861(00)00503-4.
- [54] Wolff Balthasar, Dierk Müller, and Ulrich Wagner. “Verfahren zur Synthese von Methanol”. Pat. EP Patent 000003205622A1. 11.02.2016.
- [55] Amjad Riaz, Gholamreza Zahedi, and Jiří Jaromír Klemesš. “A review of cleaner production methods for the manufacture of methanol”. In: *Journal of Cleaner Production* 57 (2013), pp. 19–37. ISSN: 09596526. DOI: 10.1016/j.jclepro.2013.06.017.
- [56] I. Dybkjær and Thomas S. Christensen. “Syngas for Large Scale Conversion of Natural Gas to Liquid Fuels”. In: *Natural Gas Conversion VI. Studies in Surface Science and Catalysis*. Elsevier, 2001, pp. 435–440. ISBN: 9780444505446. DOI: 10.1016/S0167-2991(01)80342-6.
- [57] Jens R. Rostrup-Nielsen. “Syngas in perspective”. In: *Catalysis Today* 71.3-4 (2002), pp. 243–247. ISSN: 09205861. DOI: 10.1016/S0920-5861(01)00454-0.
- [58] Yun Hang Hu and Eli Ruckenstein. “Catalytic Conversion of Methane to Synthesis Gas by Partial Oxidation and CO<sub>2</sub> Reforming”. In: *Advances in Catalysis* 48 (2004), pp. 297–345. DOI: 10.1016/S0360-0564(04)48004-3.
- [59] Xin-Mei Liu et al. “Recent Advances in Catalysts for Methanol Synthesis via Hydrogenation of CO and CO<sub>2</sub>”. In: *Industrial & Engineering Chemistry Research* 42.25 (2003), pp. 6518–6530. ISSN: 0888-5885. DOI: 10.1021/ie020979s.
- [60] Martyn V. Twigg. “Deactivation of Copper Metal Catalysts for Methanol Decomposition, Methanol Steam Reforming and Methanol Synthesis”. In: *Topics in Catalysis* 22.3/4 (2003), pp. 191–203. ISSN: 10225528. DOI: 10.1023/A:1023567718303.
- [61] Julian Schittkowski et al. “Methanol Synthesis from Steel Mill Exhaust Gases: Challenges for the Industrial Cu/ZnO/Al<sub>2</sub>O<sub>3</sub> Catalyst”. In: *Chemie Ingenieur Technik* 90.10 (2018), pp. 1419–1429. ISSN: 0009-286X. DOI: 10.1002/cite.201800017.
- [62] Dierk Müller and Jörg Ott. “Verfahren und Anlage zur Herstellung von Methanol”. Pat. DE Patent 102007030440A1. 29.06.2007.
- [63] Melissa Manning. *Global Methanol Demand Growth Driven by Methanol to Olefins as Chinese Thirst for Chemical Supply Grows, IHS Markit Says*. Ed. by IHS Markit. 2017. URL: <http://news.ihsmarkit.com/press-release/country-industry-forecasting-media/global-methanol-demand-growth-driven-methanol-olefi>.
- [64] G. L. Farina. “Produce syngas for methanol”. In: *Hydrocarbon Processing* 71.3 (1992), pp. 77–79. ISSN: 00188190.
- [65] N. Muradov and T. Veziroglu. “From hydrocarbon to hydrogen: Carbon to hydrogen economy”. In: *International Journal of Hydrogen Energy* 30.3 (2005), pp. 225–237. ISSN: 03603199. DOI: 10.1016/j.ijhydene.2004.03.033.

- [66] Christopher Higman and Maarten van der Burgt. *Gasification*. 2nd ed. Burlington: Elsevier Science, 2011. ISBN: 9780750685283.
- [67] Stijn Effting. *Waste to chemicals*. Ed. by Port of Rotterdam. 2018. URL: <https://www.portofrotterdam.com/de/geschaefsmoeglichkeiten/hafen-der-zukunft/energiewende/kreislaufwirtschaft/waste-to-chemicals> (visited on 10/02/2018).
- [68] D. Toporov and R. Abraham. “Entrained Flow Gasifiers: The ThyssenKrupp’s Prenflo Technology”. In: *12th International Conference on Energy for a Clean Environment*. 5. -09. 2015.
- [69] D. Toporov and R. Abraham. “Gasification of low-rank coal in the High-Temperature Winkler (HTW) process”. In: *Journal of the Southern African Institute of Mining and Metallurgy* 115.7 (2015), pp. 589–597. ISSN: 24119717. DOI: 10.17159/2411-9717/2015/v115n7a5.
- [70] M. Pieterman. “The historical development of innovative and energy efficient synthesis gas production technology”. Report. 2001.
- [71] George A. Olah and G. K. Surya Prakash. “Efficient and selective conversion of carbon dioxide to methanol, dimethyl ether and derived products”. Pat. US Patent 000007605293B2. 12.04.2006.
- [72] R. A. Periana. “Platinum Catalysts for the High-Yield Oxidation of Methane to a Methanol Derivative”. In: *Science (New York, N. Y.)* 280.5363 (1998), pp. 560–564. ISSN: 1095-9203. DOI: 10.1126/science.280.5363.560.
- [73] George A. Olah et al. “Bi-reforming of methane from any source with steam and carbon dioxide exclusively to metgas (CO-2H<sub>2</sub>) for methanol and hydrocarbon synthesis”. In: *Journal of the American Chemical Society* 135.2 (2013), pp. 648–650. ISSN: 0002-7863. DOI: 10.1021/ja311796n.
- [74] H. Kordabadi and Abdolhossein Jahanmiri. “Optimization of methanol synthesis reactor using genetic algorithms”. In: *Chemical Engineering Journal* 108.3 (2005), pp. 249–255. ISSN: 13858947. DOI: 10.1016/j.cej.2005.02.023.
- [75] W. S. Ernst et al. “Push syngas production limits”. In: *Hydrocarbon Processing* 79.3 (2000), pp. 100C–100. ISSN: 00188190.
- [76] Gerald Ondrey. “Making much more methanol”. In: *Chemical Engineering* 108.5 (2001), p. 29.
- [77] Zhen Qin et al. “Carbon footprint evaluation of coal-to-methanol chain with the hierarchical attribution management and life cycle assessment”. In: *Energy Conversion and Management* 124 (2016), pp. 168–179. ISSN: 01968904. DOI: 10.1016/j.enconman.2016.07.005.
- [78] Florian Ausfelder and Hanna Ewa Dura. *Optionen für ein nachhaltiges Energiesystem mit Power-to-X Technologien*. 1. Auflage. Frankfurt am Main: DECHEMA Gesellschaft für Chemische Technik und Biotechnologie e.V., 2018. ISBN: 978-3-89746-212-0. URL: <https://edocs.tib.eu/files/e01fn18/1034723774.pdf>.

- [79] Hironori Arakawa, J.-L. Dubois, and Kazuhiro Sayama. “Selective conversion of CO<sub>2</sub> to methanol by catalytic hydrogenation over promoted copper catalyst”. In: *Energy Conversion and Management* 33.5-8 (1992), pp. 521–528. ISSN: 01968904. DOI: 10.1016/0196-8904(92)90051-W.
- [80] Masahiro Fujiwara et al. “Hydrogenation of Carbon Dioxide over Cu–Zn–Cr Oxide Catalysts”. In: *Bulletin of the Chemical Society of Japan* 67.2 (1994), pp. 546–550. ISSN: 0009-2673. DOI: 10.1246/bcsj.67.546.
- [81] Kenji Ushikoshi et al. “Methanol synthesis from CO<sub>2</sub> and H<sub>2</sub> in a bench-scale test plant”. In: *Applied Organometallic Chemistry* 14.12 (2000), pp. 819–825. ISSN: 0268-2605.
- [82] Jae Sung Lee et al. “Modified Cu/ZnO/Al<sub>2</sub>O<sub>3</sub> catalysts for methanol synthesis from CO<sub>2</sub>/H<sub>2</sub> and CO/H<sub>2</sub>”. In: *Catal. Lett. (Catalysis Letters)* 34.1-2 (1995), pp. 93–99. DOI: 10.1007/BF00808326.
- [83] Oh-Shim Joo et al. “Carbon Dioxide Hydrogenation To Form Methanol via a Reverse-Water-Gas-Shift Reaction (the CAMERE Process)”. In: *Industrial & Engineering Chemistry Research* 38.5 (1999), pp. 1808–1812. ISSN: 0888-5885. DOI: 10.1021/ie9806848.
- [84] Hermann Göhna and Peter König. “Producing methanol from CO<sub>2</sub>”. In: *Chemtech* 24.6 (1994), pp. 36–39.
- [85] Masahiro Saito et al. “Methanol synthesis from CO<sub>2</sub> and H<sub>2</sub> over a multicomponent catalyst”. In: *Energy Conversion and Management* 38 (1997), pp. 403–408. ISSN: 01968904. DOI: 10.1016/S0196-8904(96)00302-0.
- [86] Oh-Shim Joo, Kwang-Deog Jung, and Jung Yonsoo. “CAMERE Process for methanol synthesis from CO<sub>2</sub> hydrogenation”. In: *Carbon Dioxide Utilization for Global Sustainability, Proceedings of 7th the International Conference on Carbon Dioxide Utilization*. Vol. 153. Studies in Surface Science and Catalysis. Elsevier, 2004, pp. 67–72. ISBN: 9780444516008. DOI: 10.1016/S0167-2991(04)80221-0.
- [87] Gabriele Centi and Siglinda Perathoner. “Opportunities and prospects in the chemical recycling of carbon dioxide to fuels”. In: *Catalysis Today* 148.3-4 (2009), pp. 191–205. ISSN: 09205861. DOI: 10.1016/j.cattod.2009.07.075.
- [88] Brandon Doss, Christopher Ramos, and Steve Atkins. “Optimization of Methanol Synthesis from Carbon Dioxide and Hydrogen: Demonstration of a Pilot-Scale Carbon-Neutral Synthetic Fuels Process”. In: *Energy & Fuels* 23.9 (2009), pp. 4647–4650. ISSN: 0887-0624. DOI: 10.1021/ef900466u.
- [89] Jamil Toyir et al. “Sustainable process for the production of methanol from CO<sub>2</sub> and H<sub>2</sub> using Cu/ZnO-based multicomponent catalyst”. In: *Physics Procedia* 2.3 (2009), pp. 1075–1079. ISSN: 18753892. DOI: 10.1016/j.phpro.2009.11.065.
- [90] Hye-Won Lim et al. “Optimization of methanol synthesis reaction on Cu/ZnO/Al<sub>2</sub>O<sub>3</sub>/ZrO<sub>2</sub> catalyst using genetic algorithm: Maximization of the synergetic effect by the optimal CO<sub>2</sub> fraction”. In: *Korean Journal of Chemical Engineering* 27.6 (2010), pp. 1760–1767. ISSN: 0256-1115. DOI: 10.1007/s11814-010-0311-7.

- [91] Florian Pontzen et al. “CO<sub>2</sub>-based methanol and DME – Efficient technologies for industrial scale production”. In: *Catalysis Today* 171.1 (2011), pp. 242–250. ISSN: 09205861. DOI: 10.1016/j.cattod.2011.04.049.
- [92] thyssenkrupp Industrial Solutions AG, ed. *Methanol plants: How you profit from our one-stop shop*. 2017. URL: [https://www.thyssenkrupp-industrial-solutions.com/media/download\\_1/methanol\\_plants\\_eng.pdf](https://www.thyssenkrupp-industrial-solutions.com/media/download_1/methanol_plants_eng.pdf).
- [93] Jürgen Ladebeck. “Improve methanol synthesis”. In: *Hydrocarbon Processing;(United States)* 72.3 (1993), pp. 89–91.
- [94] Masahiro Saito et al. “Advances in joint research between NIRE and RITE for developing a novel technology for methanol synthesis from CO<sub>2</sub> and H<sub>2</sub>”. In: *Applied Organometallic Chemistry* 14.12 (2000), pp. 763–772. ISSN: 0268-2605. DOI: 10.1002/1099-0739(200012)14:12<763::AID-AOC98>3.0.CO;2-4.
- [95] Yiping Zhang et al. “Methanol synthesis from CO<sub>2</sub> hydrogenation over Cu based catalyst supported on zirconia modified lamda-Al<sub>2</sub>O<sub>3</sub>”. In: *Energy Conversion and Management* 47.18-19 (2006), pp. 3360–3367. ISSN: 01968904. DOI: 10.1016/j.enconman.2006.01.010.
- [96] Robert Schlögl. *Chemical energy storage*. Berlin: De Gruyter, 2013. ISBN: 9783110266320.
- [97] Mohammad Reza Rahimpour. “A two-stage catalyst bed concept for conversion of carbon dioxide into methanol”. In: *Fuel Processing Technology* 89.5 (2008), pp. 556–566. ISSN: 03783820. DOI: 10.1016/j.fuproc.2007.10.011.
- [98] Hermann Goehna and Peter Koenig. “Verfahren zur Erzeugung von Methanol”. Pat. DE Patent 000004416425A1. 10.05.1994.
- [99] Oh-Shim Joo. “CAMERE process for carbon dioxide hydrogenation to form methanol”. In: *Energy and Fuels*. Ed. by American Chemical Society. Vol. 45(4). 2000, pp. 686–689.
- [100] Oddur Ingolfsson et al. “Process for producing liquid fuel from carbon dioxide and water”. Pat. WO Patent 002007108014A1. 20.03.2007.
- [101] Christoph Hank et al. “Energy efficiency and economic assessment of imported energy carriers based on renewable electricity”. In: *Sustainable Energy & Fuels* 4.5 (2020), pp. 2256–2273. ISSN: 2398-4902. DOI: 10.1039/D0SE00067A.
- [102] ECN. *FReSMe - From Residual Steel gases to Methanol*. 2017. URL: <https://www.sintef.no/globalassets/project/tccs-9/presentasjoner/d5/7---20170614-fresme-h2020-project---dissemination.pdf>.
- [103] Steelanol, ed. *Steelanol recycles carbon into sustainable, advanced bio-ethanol*. 2018. URL: <http://www.steelanol.eu/en>.
- [104] Carbon2Value, ed. *Carbon2Value: Development and demonstration of low carbontechnologies to transform CO<sub>2</sub> and CO streams from the steel industry into new value chains*. 2018. URL: <https://www.carbon2value.be/en>.
- [105] Markus Oles et al. “Carbon2Chem - Ein cross-industrieller Ansatz zur Reduzierung der Treibhausgasemissionen”. In: *Chemie Ingenieur Technik* 90.1-2 (2018), pp. 169–178. ISSN: 0009-286X. DOI: 10.1002/cite.201700112.

- [106] H2Future, ed. *H2Future: Green Hydrogen*. 2018. URL: <http://www.h2future-project.eu/>.
- [107] Thomas Bürgler, Wolfgang Eder, and Peter Schwab. “Verfahren zum Erzeugen von Stahl und Verfahren zum Speichern diskontinuierlich anfallender Energie”. Pat. DE Patent 102012109284A1. 28.09.2012.
- [108] Abdul M. Quader, S. Ahmed, and R.A.R. Ghazillaa. “Recent progress and future trends of CO<sub>2</sub> breakthrough iron and steelmaking technologies for CO<sub>2</sub> mitigation”. In: *Ironmaking and Steelmaking Processes: Greenhouse Emissions, Control, and Reduction*. Springer International Publishing, 2016, pp. 373–388. ISBN: 9783319395296.
- [109] E. A. Mousa et al. “Recent trends in ironmaking blast furnace technology to mitigate CO<sub>2</sub> emissions: Tuyeres injection”. In: *Ironmaking and Steelmaking Processes: Greenhouse Emissions, Control, and Reduction*. Springer International Publishing, 2016, pp. 173–197. ISBN: 9783319395296.
- [110] Pasquale Cavaliere and Alessio Silvello. “CO<sub>2</sub> Emission Reduction in Blast Furnaces”. In: *Ironmaking and Steelmaking Processes: Greenhouse Emissions, Control, and Reduction*. Ed. by Pasquale Cavaliere. Cham: Springer International Publishing, 2016, pp. 151–171. ISBN: 978-3-319-39529-6. DOI: 10.1007/978-3-319-39529-6\_9.
- [111] thyssenkrupp AG. *Statistical Analysis of Steel Mill Gases: (Internal Communication)*. In collab. with Carbon2Chem. 2017.
- [112] Ana-Maria Iosif et al. “Physicochemical modelling of the classical steelmaking route for life cycle inventory analysis”. In: *The International Journal of Life Cycle Assessment* 15.3 (2010), pp. 304–310. ISSN: 0948-3349. DOI: 10.1007/s11367-010-0160-y.
- [113] Guenter Harp et al. “Application of Power to Methanol Technology to Integrated Steelworks for Profitability, Conversion Efficiency, and CO<sub>2</sub> Reduction”. In: *Proceedings of METEC and 2* (2015).
- [114] Joakim Lundgren et al. “Methanol production from steel-work off-gases and biomass based synthesis gas”. In: *Applied Energy* 112 (2013), pp. 431–439. ISSN: 03062619. DOI: 10.1016/j.apenergy.2013.03.010.
- [115] Marina Bukhtiyarova et al. “Methanol Synthesis from Industrial CO<sub>2</sub> Sources: A Contribution to Chemical Energy Conversion”. In: *Catalysis Letters* 147.2 (2017), pp. 416–427. ISSN: 1011-372X. DOI: 10.1007/s10562-016-1960-x.
- [116] José M. Bermúdez et al. “An overview of novel technologies to valorise coke oven gas surplus”. In: *Fuel Processing Technology* 110 (2013), pp. 150–159. ISSN: 03783820. DOI: 10.1016/j.fuproc.2012.12.007.
- [117] Fred Joseck, Michael Wang, and Ye Wu. “Potential energy and greenhouse gas emission effects of hydrogen production from coke oven gas in U.S. steel mills”. In: *International Journal of Hydrogen Energy* 33.4 (2008), pp. 1445–1454. ISSN: 03603199. DOI: 10.1016/j.ijhydene.2007.10.022.

- [118] José M. Bermúdez et al. “New process for producing methanol from coke oven gas by means of CO<sub>2</sub> reforming. Comparison with conventional process”. In: *Fuel Processing Technology* 115 (2013), pp. 215–221. ISSN: 03783820. DOI: 10.1016/j.fuproc.2013.06.006.
- [119] Jianzhong Guo et al. “Production of Syngas via Partial Oxidation and CO<sub>2</sub> Reforming of Coke Oven Gas over a Ni Catalyst”. In: *Energy & Fuels* 22.3 (2008), pp. 1444–1448. ISSN: 0887-0624. DOI: 10.1021/ef7003865.
- [120] Jun Shen et al. “A New Technology for Producing Hydrogen and Adjustable Ratio Syngas from Coke Oven Gas”. In: *Energy & Fuels* 21.6 (2007), pp. 3588–3592. ISSN: 0887-0624. DOI: 10.1021/ef700217j.
- [121] José M. Bermúdez et al. “Dry reforming of coke oven gases over activated carbon to produce syngas for methanol synthesis”. In: *Fuel* 89.10 (2010), pp. 2897–2902. ISSN: 00162361. DOI: 10.1016/j.fuel.2010.01.014.
- [122] José M. Bermúdez, Ana Arenillas, and J. Angel Menéndez. “Equilibrium prediction of CO<sub>2</sub> reforming of coke oven gas: Suitability for methanol production”. In: *Chemical Engineering Science* 82 (2012), pp. 95–103. ISSN: 00092509. DOI: 10.1016/j.ces.2012.07.012.
- [123] Bundesministerium für Wirtschaft und Technologie, ed. *Energiekonzept: für eine umweltschonende, zuverlässige und bezahlbare Energieversorgung*. 2010. URL: <https://www.bmwi.de/Redaktion/DE/Downloads/E/energiekonzept-2010.pdf>.
- [124] A.SPIRE aisbl, ed. *Sustainable Process Industry: SPIRE - Sustainable Process Industry through Resource and Energy Efficiency*. 2013. URL: <https://www.spire2030.eu/what/walking-the-spire-roadmap/spire-vision>.
- [125] Rocío Pacios and David Cuesta. *MefCO<sub>2</sub>: Methanol from CO<sub>2</sub>: Synthesis of methanol from captured carbon dioxide using surplus electricity*. 2016. URL: <http://www.mefco2.eu/pdf/mefco2-teaser.pdf>.
- [126] Jens R. Rostrup-Nielsen, Jens Sehested, and Jens K. Nørskov. “Hydrogen and synthesis gas by steam- and CO<sub>2</sub> reforming”. In: *Advances in Catalysis* 47 (2002), pp. 65–139. DOI: 10.1016/S0360-0564(02)47006-X.
- [127] Frank Hartig and Frerich J. Keil. “Large-scale spherical fixed bed reactors: Modeling and optimization”. In: *Industrial & Engineering Chemistry Research* 32.3 (1993), pp. 424–437. ISSN: 0888-5885. DOI: 10.1021/ie00015a005.
- [128] Geert H. Graaf et al. “Chemical equilibria in methanol synthesis”. In: *Chemical Engineering Science* 41.11 (1986), pp. 2883–2890. ISSN: 00092509. DOI: 10.1016/0009-2509(86)80019-7.
- [129] Geert H. Graaf and Jozef G. M. Winkelman. “Chemical Equilibria in Methanol Synthesis Including the Water–Gas Shift Reaction: A Critical Reassessment”. In: *Industrial & Engineering Chemistry Research* 55.20 (2016), pp. 5854–5864. ISSN: 0888-5885. DOI: 10.1021/acs.iecr.6b00815.
- [130] Raymond H. Ewell. “Calculation of Chemical Equilibrium At High Pressures”. In: *Industrial & Engineering Chemistry* 32.2 (1940), pp. 147–153. ISSN: 0019-7866. DOI: 10.1021/ie50362a004.

- [131] Robert Holub and Petr Voňka. *The Chemical Equilibrium of Gaseous Systems*. Dordrecht: Springer Netherlands, 1976. ISBN: 978-94-010-1775-6.
- [132] Te Chang, Ronald W. Rousseau, and Peter K. Kilpatrick. “Methanol synthesis reactions: Calculations of equilibrium conversions using equations of state”. In: *Industrial & Engineering Chemistry Process Design and Development* 25.2 (1986), pp. 477–481. ISSN: 0196-4305. DOI: 10.1021/i200033a021.
- [133] W. J. Thomas and Stanislaw Portalski. “Thermodynamics in Methanol Synthesis”. In: *Industrial & Engineering Chemistry* 50.6 (1958), pp. 967–970. ISSN: 0019-7866. DOI: 10.1021/ie50582a048.
- [134] Manfred Baerns. *Technische Chemie*. 2., erw. Aufl. Weinheim, Bergstr.: Wiley-VCH, 2013. ISBN: 978-3-527-33072-0.
- [135] Giorgio Soave. “Equilibrium constants from a modified Redlich-Kwong equation of state”. In: *Chemical Engineering Science* 27.6 (1972), pp. 1197–1203. ISSN: 00092509. DOI: 10.1016/0009-2509(72)80096-4.
- [136] Johannes J. Meyer et al. “Modeling of a Methanol Synthesis Reactor for Storage of Renewable Energy and Conversion of CO<sub>2</sub> - Comparison of Two Kinetic Models”. In: *Chemical Engineering & Technology* 39.2 (2016), pp. 233–245. ISSN: 09307516. DOI: 10.1002/ceat.201500084.
- [137] John Thomas Gallagher and John Mitchel Kidd. “Verfahren zur Synthese von Methanol”. Pat. DE Patent 000001568864C3. 16.08.1966.
- [138] Alexandre C. Dimian, Costin Sorin Bildea, and Anton A. Kiss. “Methanol”. In: *Applications in Design and Simulation of Sustainable Chemical Processes*. Elsevier, 2019, pp. 101–145. ISBN: 9780444638762. DOI: 10.1016/B978-0-444-63876-2.00003-6.
- [139] Sunggyu Lee. *Methanol synthesis technology*. Boca Raton, Fla.: CRC Press, 1990. ISBN: 0-8493-4610-X.
- [140] Robert H. Perry, Doon W. Green, and James O. Maloney. *Perry’s chemical engineer’s platinum edition Perry’s chemical engineers’ handbook*. 7. ed. New York: McGraww-Hill, 1999. ISBN: 0-07-049841-5.
- [141] N. J. Macnaughton, Alwin Pinto, and P. L. Rogerson. “Development of methanol technology for future fuel and chemical markets”. In: *Energy Prog.;(United States)* 4.4 (1984), pp. 232–241.
- [142] Alwin Pinto and P. L. Rogerson. “Optimizing the ICI low-pressure methanol synthesis”. In: *Chemical Engineering* 4 (1977), pp. 102–108.
- [143] Irving Wender. “Reactions of synthesis gas”. In: *Fuel Processing Technology* 48.3 (1996), pp. 189–297. ISSN: 03783820. DOI: 10.1016/S0378-3820(96)01048-X.
- [144] Kim Aasberg-Petersen et al. *Large Scale Methanol Production from Natural Gas: Research, Technology, Catalyst*. Ed. by Haldor Topsøe. 2013. URL: <https://www.researchgate.net/file.PostFileLoader.html?id=593cceb0eeae39a7b869898f&assetKey=AS%3A503928378884096%401497157296471>.

- [145] Kurt M. Vanden Bussche and Gilbert F. Froment. “A Steady-State Kinetic Model for Methanol Synthesis and the Water Gas Shift Reaction on a Commercial Cu/ZnO/Al<sub>2</sub>O<sub>3</sub> Catalyst”. In: *Journal of Catalysis* 161.1 (1996), pp. 1–10. ISSN: 00219517. DOI: 10.1006/jcat.1996.0156.
- [146] Andrea Schnabl. “Die Konversion von CO<sub>2</sub> und H<sub>2</sub> zu Methanol als nachhaltigem chemischen Energiespeicher”. Master thesis. Technical University of Munich, 2015.
- [147] Rafael Mayorga-González. “Dynamische Modellierung und Analyse einer Miniplant zur Methanol-Produktion aus Hüttengas”. Master thesis. Karlsruhe Institute of Technology, 2018.
- [148] Siraj Eddine Chahbani. “Simulation based techno-economic assessment of Power-to-X-processes”. Bachelor thesis. University of Carthage, 2019.
- [149] Lars Felix Müller. “Simulationsbasierte techno-ökonomische Analyse eines dynamisch betriebenen Power-to-Methanol Prozesses”. Master thesis. Mannheim University of Applied Sciences, 2021.
- [150] I. Dybkjær. “Topsoe methanol technology”. In: *Chem. Econ. Engng. Rev* 13.6 (1981), pp. 17–25.
- [151] Klaas Roelof Westerterp. “A Process for producing methanol”. Pat. EP Patent 000000326718A1. 5.02.1988.
- [152] Klaas Roelof Westerterp et al. “Neue Konvertersysteme für die Methanol-Synthese”. In: *Chemie Ingenieur Technik* 61.3 (1989), pp. 193–199. ISSN: 0009-286X. DOI: 10.1002/cite.330610303.
- [153] Emil Supp. “Improved Methanol Process”. In: *Hydrocarbon Processing* 60.3 (1981), pp. 71–75. ISSN: 00188190.
- [154] W. B. Earl and K. A. Islam. “Steady-state model of a methanol synthesis reactor”. In: *Chemeca 86: The Fourteenth Australasian Chemical Engineering Conference; Chemical Engineering; Initiatives, Attitudes, Cycles*. 1986, p. 129.
- [155] Geert H. Graaf and A.A.C.M. Beenackers. “Comparison of two-phase and three-phase methanol synthesis processes”. In: *Chemical Engineering and Processing: Process Intensification* 35.6 (1996), pp. 413–427. ISSN: 02552701. DOI: 10.1016/S0255-2701(96)04147-5.
- [156] S. V. Sinadinovic-Fiser, Jankovic, and R. Z. Radicevic. “Simulation of the Fixed-Bed Reactor for Methanol Synthesis”. In: *Petroleum and Coal* 43.1 (2001), pp. 31–34.
- [157] Dimitri Mignard and Colin Pritchard. “On the use of electrolytic hydrogen from variable renewable energies for the enhanced conversion of biomass to fuels”. In: *Chemical Engineering Research and Design* 86.5 (2008), pp. 473–487. ISSN: 02638762. DOI: 10.1016/j.cherd.2007.12.008.
- [158] D. L. O. Santangelo, V. R. R. Ahón, and A. L. H. Costa. “Optimization of Methanol Synthesis Loops with Quench Reactors”. In: *Chemical Engineering & Technology* 31.12 (2008), pp. 1767–1774. ISSN: 09307516. DOI: 10.1002/ceat.200800374.

- [159] Vincenzo Palma et al. “State of the Art of Conventional Reactors for Methanol Production”. In: *Methanol*. Elsevier, 2018, pp. 29–51. ISBN: 9780444639035. DOI: 10.1016/B978-0-444-63903-5.00002-9.
- [160] Wilhelm Herbert, Roland Marcks, and Helmut Liebgott. “Verfahren zur Herstellung von Methanol in Röhrenofen”. Pat. DE Patent 000002123950A. 14.05.1971.
- [161] Gholamreza Zahedi, Ali Elkamel, and Ali Lohi. “Dynamic Optimization Strategies of a Heterogeneous Reactor for CO<sub>2</sub> Conversion to Methanol”. In: *Energy & Fuels* 21.5 (2007), pp. 2977–2983. ISSN: 0887-0624. DOI: 10.1021/ef700361m.
- [162] Ingvild Løvik, Magne Hillestad, and Terje Hertzberg. “Long term dynamic optimization of a catalytic reactor system”. In: *Computers & Chemical Engineering* 22 (1998), S707–S710. ISSN: 00981354. DOI: 10.1016/S0098-1354(98)00130-6.
- [163] Mohd Nazri Mohd Fuad, Mohd Azlan Hussain, and Adam Zakaria. “Optimization strategy for long-term catalyst deactivation in a fixed-bed reactor for methanol synthesis process”. In: *Computers & Chemical Engineering* 44 (2012), pp. 104–126. ISSN: 00981354. DOI: 10.1016/j.compchemeng.2012.05.003.
- [164] N. Rezaie et al. “A comparison of homogeneous and heterogeneous dynamic models for industrial methanol reactors in the presence of catalyst deactivation”. In: *Chemical Engineering and Processing: Process Intensification* 44.8 (2005), pp. 911–921. ISSN: 02552701. DOI: 10.1016/j.cep.2004.10.004.
- [165] P. Parvasi, Mohammad Reza Rahimpour, and Abdolhossein Jahanmiri. “Incorporation of Dynamic Flexibility in the Design of a Methanol Synthesis Loop in the Presence of Catalyst Deactivation”. In: *Chemical Engineering & Technology* 31.1 (2008), pp. 116–132. ISSN: 09307516. DOI: 10.1002/ceat.200700209.
- [166] Suzana Yusup, N. Phuong Anh, and Haslinda Zabiri. “A simulation study of an industrial methanol reactor based on simplified steady-state model”. In: *IJRRAS* 5.3 (2010), pp. 213–222.
- [167] L. Chen et al. “Optimization of Methanol Yield from a Lurgi Reactor”. In: *Chemical Engineering & Technology* 34.5 (2011), pp. 817–822. ISSN: 09307516.
- [168] Sidharth Abrol and Courtland M. Hilton. “Modeling, simulation and advanced control of methanol production from variable synthesis gas feed”. In: *Computers & Chemical Engineering* 40 (2012), pp. 117–131. ISSN: 00981354. DOI: 10.1016/j.compchemeng.2012.02.005.
- [169] Flavio Manenti and Giulia Bozzano. “Optimal Control of Methanol Synthesis Fixed-Bed Reactor”. In: *Industrial & Engineering Chemistry Research* 52.36 (2013), pp. 13079–13091. ISSN: 0888-5885. DOI: 10.1021/ie401511e.
- [170] Andrea Montebelli et al. “Enabling small-scale methanol synthesis reactors through the adoption of highly conductive structured catalysts”. In: *Catalysis Today* 215 (2013), pp. 176–185. ISSN: 09205861. DOI: 10.1016/j.cattod.2013.02.020.

- [171] Fereshteh Samimi et al. “Phase stability analysis on green methanol synthesis process from CO<sub>2</sub> hydrogenation in water cooled, gas cooled and double cooled tubular reactors”. In: *Fuel Processing Technology* 181 (2018), pp. 375–387. ISSN: 03783820. DOI: 10.1016/j.fuproc.2018.10.004.
- [172] Joseph D. Korchnak. “Advances in Methanol Technology”. In: *Methane Conversion, Proceedings of a Symposium on the Production of Fuels and Chemicals from Natural Gas*. Ed. by D. M. Bibby et al. Vol. 36. Studies in Surface Science and Catalysis. Elsevier, 1988, pp. 647–661. ISBN: 9780444429353. DOI: 10.1016/S0167-2991(09)60563-2.
- [173] Mathias Beek and Matthias Sadlowski. “Transient Optimization of Coproduction Systems for Steel and Value-Added Chemicals”. In: *Chemie Ingenieur Technik* 92.10 (2020), pp. 1431–1443. ISSN: 0009-286X. DOI: 10.1002/cite.202000064.
- [174] Stefan Schlüter and Christian Geitner. “Simulation of Methanol and Urea Production from Catalytic Conversion of Steel Mill Gases”. In: *Chemie Ingenieur Technik* 92.10 (2020), pp. 1403–1415. ISSN: 0009-286X. DOI: 10.1002/cite.202000068.
- [175] Mohammad Reza Rahimpour et al. “A dynamic kinetic model for methanol synthesis on deactivated catalyst”. In: *Computers & Chemical Engineering* 22 (1998), S675–S678. ISSN: 00981354. DOI: 10.1016/S0098-1354(98)00122-7.
- [176] Mohammad Reza Rahimpour, J. Fathi Kaljahi, and Abdolhossein Jahanmiri. “Selective kinetic deactivation model for methanol synthesis from simultaneous reaction of CO<sub>2</sub> and CO with H<sub>2</sub> on a commercial copper/zinc oxide catalyst”. In: *The Canadian Journal of Chemical Engineering* 76.4 (1998), pp. 753–761. ISSN: 00084034. DOI: 10.1002/cjce.5450760410.
- [177] Gholamreza Zahedi, Ali Elkamel, and Ali Lohi. “Enhancing CO<sub>2</sub> Conversion to Methanol Using Dynamic Optimization, Applied on Shell Temperature and Inlet Hydrogen During Four Years Operation of Methanol Plant”. In: *Energy Sources, Part A: Recovery, Utilization, and Environmental Effects* 29.15 (2007), pp. 1385–1396. ISSN: 1556-7036. DOI: 10.1080/00908310600625285.
- [178] Kurt M. Vanden Bussche et al. “Modelling and simulation of the reversed flow operation of a fixed-bed reactor for methanol synthesis”. In: *Chemical Engineering Science* 48.19 (1993), pp. 3335–3345. ISSN: 00092509. DOI: 10.1016/0009-2509(93)80150-O.
- [179] Kurt M. Vanden Bussche and Gilbert F. Froment. “The STAR configuration for methanol synthesis in reversed flow reactors”. In: *The Canadian Journal of Chemical Engineering* 74.5 (1996), pp. 729–734. ISSN: 00084034. DOI: 10.1002/cjce.5450740524.
- [180] Flavio Manenti et al. “Dynamic modeling of the methanol synthesis fixed-bed reactor”. In: *Computers & Chemical Engineering* 48 (2013), pp. 325–334. ISSN: 00981354. DOI: 10.1016/j.compchemeng.2012.09.013.
- [181] M. Shahrokhi and G. R. Baghmisheh. “Modeling, simulation and control of a methanol synthesis fixed-bed reactor”. In: *Chemical Engineering Science* 60.15 (2005), pp. 4275–4286. ISSN: 00092509. DOI: 10.1016/j.ces.2004.12.051.

- [182] Michal Kuczynski et al. “Reaction kinetics for the synthesis of methanol from CO and H<sub>2</sub> on a copper catalyst”. In: *Chemical Engineering and Processing: Process Intensification* 21.4 (1987), pp. 179–191. ISSN: 02552701. DOI: 10.1016/0255-2701(87)80015-6.
- [183] Shin-ichiro Fujita, Hiroto Ito, and Nobutsune Takezawa. “Methanol Synthesis from CO<sub>2</sub> and H<sub>2</sub> over a ZnO Catalyst. Effect of the Pretreatment with CO–H<sub>2</sub> upon the Reaction”. In: *Bulletin of the Chemical Society of Japan* 66.10 (1993), pp. 3094–3096. ISSN: 0009-2673. DOI: 10.1246/bcsj.66.3094.
- [184] K. G. Chanchlani, R. R. Hudgins, and Peter L. Silveston. “Methanol synthesis under periodic operation: An experimental investigation”. In: *The Canadian Journal of Chemical Engineering* 72.4 (1994), pp. 657–671. ISSN: 00084034. DOI: 10.1002/cjce.5450720416.
- [185] Melanie A. McNeil and Robert G. Rinker. “An experimental study of concentration forcing applied to the methanol synthesis reaction”. In: *Chemical Engineering Communications* 127.1 (1994), pp. 137–149. ISSN: 0098-6445. DOI: 10.1080/00986449408936229. URL: <https://doi.org/10.1080/00986449408936229>.
- [186] Uri Ash-Kurlander et al. “Impact of Daily Startup-Shutdown Conditions on the Production of Solar Methanol over a Commercial Cu-ZnO-Al<sub>2</sub>O<sub>3</sub> Catalyst”. In: *Energy Technology* 4.5 (2016), pp. 565–572. ISSN: 21944288. DOI: 10.1002/ente.201600022.
- [187] Holger Ruhland et al. “CO<sub>2</sub> Hydrogenation with Cu/ZnO/Al<sub>2</sub>O<sub>3</sub>: A Benchmark Study”. In: *Angewandte Chemie* 12.12 (2020), pp. 3216–3222. ISSN: 00448249. DOI: 10.1002/cctc.202000195.
- [188] C. Seidel et al. “Kinetic modeling of methanol synthesis from renewable resources”. In: *Chemical Engineering Science* 175 (2018), pp. 130–138. ISSN: 00092509. DOI: 10.1016/j.ces.2017.09.043.
- [189] B. Vollbrecht. “Zur Kinetik der Methanolsynthese an einem technischen Cu/ZnO/Al<sub>2</sub>O<sub>3</sub>-Katalysator”. Dissertation. Otto-von-Guericke-Universität Magdeburg, 2007.
- [190] Mozhgan Nassirpour and Mohammad Hasan Khademi. “Evaluation of different cooling technologies for industrial methanol synthesis reactor in terms of energy efficiency and methanol yield: An economic-optimization”. In: *Journal of the Taiwan Institute of Chemical Engineers* 113 (2020), pp. 302–314. ISSN: 18761070. DOI: 10.1016/j.jtice.2020.08.029.
- [191] Geert Hilbert Graaf. “The synthesis of methanol in gas-solid and gas-slurry reactors”. PhD thesis. University of Groningen, 1988.
- [192] Geert H. Graaf, E. J. Stamhuis, and A.A.C.M. Beenackers. “Kinetics of low-pressure methanol synthesis”. In: *Chemical Engineering Science* 43.12 (1988), pp. 3185–3195. ISSN: 00092509. DOI: 10.1016/0009-2509(88)85127-3.
- [193] Geert H. Graaf et al. “Intra-particle diffusion limitations in low-pressure methanol synthesis”. In: *Chemical Engineering Science* 45.4 (1990), pp. 773–783. ISSN: 00092509. DOI: 10.1016/0009-2509(90)85001-T.

- [194] Andrea Montebelli et al. “Optimization of compact multitubular fixed-bed reactors for the methanol synthesis loaded with highly conductive structured catalysts”. In: *Chemical Engineering Journal* 255 (2014), pp. 257–265. ISSN: 13858947. DOI: 10.1016/j.cej.2014.06.050.
- [195] F. Samimi et al. “Green methanol synthesis process from carbon dioxide via reverse water gas shift reaction in a membrane reactor”. In: *Chemical Engineering Research and Design* 140 (2018), pp. 44–67. ISSN: 02638762. DOI: 10.1016/j.cherd.2018.10.001.
- [196] Mina Khanipour et al. “A membrane-assisted hydrogen and carbon oxides separation from flare gas and recovery to a commercial methanol reactor”. In: *International Journal of Hydrogen Energy* 45.12 (2020), pp. 7386–7400. ISSN: 03603199. DOI: 10.1016/j.ijhydene.2019.04.149.
- [197] Éverton Simões Van-Dal and Chakib Bouallou. “Design and simulation of a methanol production plant from CO<sub>2</sub> hydrogenation”. In: *Journal of Cleaner Production* 57 (2013), pp. 38–45. ISSN: 09596526. DOI: 10.1016/j.jclepro.2013.06.008.
- [198] Shachit S. Iyer et al. “Generalized thermodynamic analysis of methanol synthesis: Effect of feed composition”. In: *Journal of CO<sub>2</sub> Utilization* 10 (2015), pp. 95–104. ISSN: 22129820. DOI: 10.1016/j.jcou.2015.01.006.
- [199] Rafael Oliveira dos Santos, Lizandro de Sousa Santos, and Diego Martinez Prata. “Simulation and optimization of a methanol synthesis process from different biogas sources”. In: *Journal of Cleaner Production* 186 (2018), pp. 821–830. ISSN: 09596526. DOI: 10.1016/j.jclepro.2018.03.108.
- [200] Grazia Leonzio, Edwin Zondervan, and Pier Ugo Foscolo. “Methanol production by CO<sub>2</sub> hydrogenation: Analysis and simulation of reactor performance”. In: *International Journal of Hydrogen Energy* 44.16 (2019), pp. 7915–7933. ISSN: 03603199. DOI: 10.1016/j.ijhydene.2019.02.0561.
- [201] Godfrey C. Chinchin, K. Mansfield, and Michael S. Spencer. “The methanol synthesis-how does it work”. In: *Chemtech* 20.11 (1990), pp. 692–699.
- [202] Tobias Henkel. “Modellierung von Reaktion und Stofftransport in geformten Katalysatoren am Beispiel der Methanolsynthese”. PhD thesis. Technische Universität München, 2011.
- [203] Nonam Park et al. “Kinetic modeling of methanol synthesis over commercial catalysts based on three-site adsorption”. In: *Fuel Processing Technology* 125 (2014), pp. 139–147. ISSN: 03783820. DOI: 10.1016/j.fuproc.2014.03.041.
- [204] K. L. Ng, D. Chadwick, and B. A. Toseland. “Kinetics and modelling of dimethyl ether synthesis from synthesis gas”. In: *Chemical Engineering Science* 54.15-16 (1999), pp. 3587–3592. ISSN: 00092509. DOI: 10.1016/S0009-2509(98)00514-4.
- [205] Paweł Nowak, Maria Lachowska, and Jerzy Skrzypek. “Influence of water vapour on methanol synthesis over CuO-ZnO-Al<sub>2</sub>O<sub>3</sub> catalyst”. In: *Chemical Engineering Science* 46.12 (1991), pp. 3324–3325. ISSN: 00092509.

- [206] Florian Nestler et al. “Kinetic modelling of methanol synthesis over commercial catalysts: A critical assessment”. In: *Chemical Engineering Journal* 394 (2020), p. 124881. ISSN: 13858947. DOI: 10.1016/j.cej.2020.124881.
- [207] J. Schwarz and D. Samiec. “B3.4 - Fiber-Optic Measurement of Temperature Profiles: AMA Service GmbH, Von-Münchhausen-Str. 49, 31515 Wunstorf, Germany”. In: *Proceedings Sensor 2017* (2017), pp. 212–216. DOI: 10.5162/sensor2017/B3.4.
- [208] National Institute of Standards and Technology, ed. *NIST Chemistry WebBook: NIST Standard Reference Database Number 69*. 2020. URL: <https://webbook.nist.gov/chemistry/>.
- [209] Design Institute for Physical Properties, ed. *DIPPR 801 Database*. 2021. URL: <https://dippr.aiche.org>.
- [210] *VDI Heat Atlas: with 539 tables*. 2. ed. Springer reference. Heidelberg: Springer, 2010. ISBN: 978-3-540-77877-6. DOI: 10.1007/978-3-540-77877-6.
- [211] Stefan Berger. “Implementierung, Verifizierung und Vergleich zweier Kinetikmodelle für die Methanolsynthese mittels MATLAB”. Bachelor thesis. Hochschule München, 2017.
- [212] Andreas Jess and Peter Wasserscheid. *Chemical technology: An integral textbook*. Weinheim: Wiley-VCH, 2013. ISBN: 978-3-527-67062-8.
- [213] P. Zehner and E. U. Schlünder. “Wärmeleitfähigkeit von Schüttungen bei mäßigen Temperaturen”. In: *Chemie Ingenieur Technik* 42.14 (1970), pp. 933–941. ISSN: 0009-286X. DOI: 10.1002/cite.330421408.
- [214] P. Zehner and E. U. Schlünder. “Einfluß der Wärmestrahlung und des Druckes auf den Wärmetransport in nicht durchströmten Schüttungen”. In: *Chemie Ingenieur Technik* 44.23 (1972), pp. 1303–1308. ISSN: 0009-286X. DOI: 10.1002/cite.330442305.
- [215] R. Bauer and E. U. Schluender. “Effective radial thermal conductivity of packings in gas flows- 2. Thermal conductivity of the packing fraction without gas flow”. In: *Int Chem Eng* 18.2 (1978), pp. 189–204. URL: <https://www.scopus.com/inward/record.uri?eid=2-s2.0-0017956059&partnerID=40&md5=3d20d0d8733c90cdeb182c58ffdbcef>.
- [216] Holger Martin and Michael Nilles. “Radiale Wärmeleitung in durchströmten Schüttungsrohren”. In: *Chemie Ingenieur Technik* 65.12 (1993), pp. 1468–1477. ISSN: 0009-286X. DOI: 10.1002/cite.330651206.
- [217] Walter Fritz. “Grundlagen der Wärmeübertragung beim Verdampfen von Flüssigkeiten”. In: *Chemie Ingenieur Technik* 35.11 (1963), pp. 753–764. ISSN: 0009-286X. DOI: 10.1002/cite.330351102.
- [218] Jack Philip Holman. *Heat transfer*. 10. ed. McGraw-Hill series in mechanical engineering. Boston, Mass. [u.a.]: McGraw-Hill Higher Education, 2010. ISBN: 978-0-07-352936-3.
- [219] H. Schmitz. *Druckverlust*. 2018. URL: [www.druckverlust.de](http://www.druckverlust.de).
- [220] Miroslav Babic. *Fragoltherm X-400-A Diagramme: e-Mail*. In collab. with Florian Nestler. 2018-11-09.

- [221] A. Keshavarz et al. “Simultaneous methanol production and separation in the methanol synthesis reactor to increase methanol production”. In: *Chemical Engineering and Processing: Process Intensification* 158 (2020), p. 108176. ISSN: 02552701. DOI: 10.1016/j.cep.2020.108176.
- [222] Pavel Maksimov et al. “Gas phase methanol synthesis with Raman spectroscopy for gas composition monitoring”. In: *RSC Advances* 10.40 (2020), pp. 23690–23701. DOI: 10.1039/D0RA04455E.
- [223] Xiaoti Cui and Søren Knudsen Kær. “A comparative study on three reactor types for methanol synthesis from syngas and CO<sub>2</sub>”. In: *Chemical Engineering Journal* 393 (2020), p. 124632. ISSN: 13858947. DOI: 10.1016/j.cej.2020.124632.
- [224] Shashwata Ghosh et al. “Biogas to methanol: A comparison of conversion processes involving direct carbon dioxide hydrogenation and via reverse water gas shift reaction”. In: *Journal of Cleaner Production* 217 (2019), pp. 615–626. ISSN: 09596526. DOI: 10.1016/j.jclepro.2019.01.171.
- [225] Geert H. Graaf et al. “On chemical equilibria in methanol synthesis”. In: *Chemical Engineering Science* 45.3 (1990), pp. 769–770. ISSN: 00092509.
- [226] G. F. Froment and L. H. Hosten. “Catalysis science and technology”. In: *Catalytic Kinetics Modelling, Springer, Berlin, Heidelberg, New York* (1981), pp. 97–170.
- [227] Nonam Park et al. “Modeling and analysis of a methanol synthesis process using a mixed reforming reactor: Perspective on methanol production and CO<sub>2</sub> utilization”. In: *Fuel* 129 (2014), pp. 163–172. ISSN: 00162361. DOI: 10.1016/j.fuel.2014.03.068.
- [228] Jannike Solsvik and Hugo A. Jakobsen. “Modeling of multicomponent mass diffusion in porous spherical pellets: Application to steam methane reforming and methanol synthesis”. In: *Chemical Engineering Science* 66.9 (2011), pp. 1986–2000. ISSN: 00092509. DOI: 10.1016/j.ces.2011.01.060.
- [229] E. W. Thiele. “Relation between Catalytic Activity and Size of Particle”. In: *Industrial & Engineering Chemistry* 31.7 (1939), pp. 916–920. ISSN: 0019-7866. DOI: 10.1021/ie50355a027.
- [230] B. J. Lommerts, Geert H. Graaf, and A.A.C.M. Beenackers. “Mathematical modeling of internal mass transport limitations in methanol synthesis”. In: *Chemical Engineering Science* 55.23 (2000), pp. 5589–5598. ISSN: 00092509. DOI: 10.1016/S0009-2509(00)00194-9.
- [231] Klaas Roelof Westerterp et al. *Chemical reactor design and operation*. Wiley Chichester et al, 1984.
- [232] Edward N. Fuller, Paul D. Schettler, and J. Calvin. Giddings. “New Method for Prediction of binary gas phase diffusion coefficients”. In: *Industrial & Engineering Chemistry* 58.5 (1966), pp. 18–27. ISSN: 0019-7866. DOI: 10.1021/ie50677a007.
- [233] Salih Obut. “Derivative-Free Optimization of a Fixed-Bed Methanol Synthesis Reactor”. In: *Chemical Engineering & Technology* (2021). ISSN: 09307516. DOI: 10.1002/ceat.202100165.

- [234] Flavio Manenti, Silvia Cieri, and Marco Restelli. “Considerations on the steady-state modeling of methanol synthesis fixed-bed reactor”. In: *Chemical Engineering Science* 66.2 (2011), pp. 152–162. ISSN: 00092509. DOI: 10.1016/j.ces.2010.09.036.
- [235] William E. Schiesser and Graham W. Griffiths. *A compendium of partial differential equation models: Method of lines analysis with Matlab*. Cambridge: Cambridge University Press, 2009. ISBN: 9780521519861.
- [236] *MATLAB: Documentation*. 2020.
- [237] Jeffrey C. Lagarias et al. “Convergence Properties of the Nelder–Mead Simplex Method in Low Dimensions”. In: *SIAM Journal on Optimization* 9.1 (1998), pp. 112–147. ISSN: 1052-6234. DOI: 10.1137/S1052623496303470.
- [238] J. A. Nelder and R. Mead. “A Simplex Method for Function Minimization”. In: *The Computer Journal* 7.4 (1965), pp. 308–313. ISSN: 0010-4620. DOI: 10.1093/comjnl/7.4.308.
- [239] Xiaojun Zhou, Chunhua Yang, and Weihua Gui. “A new transformation into state transition algorithm for finding the global minimum”. In: *2011 2nd International Conference on Intelligent Control and Information Processing*. IEEE, 25.07.2011 - 28.07.2011, pp. 674–678. ISBN: 978-1-4577-0813-8. DOI: 10.1109/ICICIP.2011.6008335.
- [240] Frits M. Dautzenberg. “Ten Guidelines for Catalyst Testing”. In: *Deactivation and Testing of Hydrocarbon-Processing Catalysts*. Ed. by John P. O’Connell, Toru Takatsuka, and Geoffrey L. Woolery. Vol. 411. ACS Symposium Series. Washington, DC: AMERICAN CHEMICAL SOCIETY, 1996, pp. 99–119. ISBN: 0-8412-3411-6. DOI: 10.1021/bk-1989-0411.ch011.
- [241] J. Pérez-Ramírez. “The six-flow reactor technology A review on fast catalyst screening and kinetic studies”. In: *Catalysis Today* 60.1-2 (2000), pp. 93–109. ISSN: 09205861. DOI: 10.1016/S0920-5861(00)00321-7.
- [242] S. T. Sie. “Advantages, Possibilities, and Limitations of Small-Scale Testing of Catalysts for Fixed-Bed Processes”. In: *Deactivation and Testing of Hydrocarbon-Processing Catalysts*. Ed. by John P. O’Connell, Toru Takatsuka, and Geoffrey L. Woolery. Vol. 634. ACS Symposium Series. Washington, DC: AMERICAN CHEMICAL SOCIETY, 1996, pp. 6–41. ISBN: 0-8412-3411-6. DOI: 10.1021/bk-1996-0634.ch002.
- [243] Matthias Kraume. *Transportvorgänge in der Verfahrenstechnik*. Berlin, Heidelberg: Springer Berlin Heidelberg, 2012. ISBN: 978-3-642-25148-1. DOI: 10.1007/978-3-642-25149-8.
- [244] Marko Zlokarnik. *Scale-Up in Chemical Engineering*. Wiley, 2006. ISBN: 9783527314218. DOI: 10.1002/352760815X.
- [245] G. Damköhler and G. Delcker. “Einflüsse der Strömung, Diffusion und des Wärmeüberganges auf die Leistung von Reaktionsöfen”. In: *Zeitschrift für Elektrochemie und angewandte physikalische Chemie* 44.4 (1938), pp. 1938–. URL: <https://onlinelibrary.wiley.com/doi/abs/10.1002/bbpc.19380440403>.

- [246] Ali Elkamel et al. “Optimal Fixed Bed Reactor Network Configuration for the Efficient Recycling of CO<sub>2</sub> into Methanol”. In: *Energies* 2.2 (2009), pp. 180–189. ISSN: 1996-1073. DOI: 10.3390/en20200180.
- [247] Gholamreza Zahedi et al. “Hybrid artificial neural network – First principle model formulation for the unsteady state simulation and analysis of a packed bed reactor for CO<sub>2</sub> hydrogenation to methanol”. In: *Chemical Engineering Journal* 115.1-2 (2005), pp. 113–120. ISSN: 13858947. DOI: 10.1016/j.cej.2005.08.018.
- [248] Viktor Paul Müller. “Experimentelle Validierung eines Modells zur Methanolsynthese aus regenerativen Rohstoffen”. Master thesis. Technische Universität Darmstadt, 2020.
- [249] M. J. Hadrich et al. “Methanolsynthese auf Basis von synthetischen Hüttengasen in einer vollautomatisierten Miniplant - Carbon2Chem”. In: *Chemie Ingenieur Technik* 90.9 (2018), p. 1137. ISSN: 0009-286X. DOI: 10.1002/cite.201855010.
- [250] Sebastian Schäfer. “Planung, Auslegung und Aufbau einer dynamischen Methanolsyntheseanlage”. Bachelor thesis. HTWG Konstanz, 2019.
- [251] Abraham. Savitzky and M. J. E. Golay. “Smoothing and Differentiation of Data by Simplified Least Squares Procedures”. In: *Analytical Chemistry* 36.8 (1964), pp. 1627–1639. ISSN: 0003-2700. DOI: 10.1021/ac60214a047.
- [252] Isabel Kundler and Alexis Michael Bazzanella. *Power to Methanol: Grünes Methanol als "flüssiger Strom" für Speicherung, Transport und als Rohstoff*. 2018. URL: <https://dechema.de/Forschungsförderung/Projekte/Power+to+Methanol-p-20102808.html>.
- [253] Franziska Müller et al. “Is green a Pan-African colour? Mapping African renewable energy policies and transitions in 34 countries”. In: *Energy Research & Social Science* 68 (2020), p. 101551. ISSN: 22146296. DOI: 10.1016/j.erss.2020.101551.
- [254] Maximilian Peter et al. “Detailed kinetic modeling of methanol synthesis over a ternary copper catalyst”. In: *Chemical Engineering Journal* 203 (2012), pp. 480–491. ISSN: 13858947. DOI: 10.1016/j.cej.2012.06.066.
- [255] Joost G. van Bennekom et al. “Modeling and Experimental Studies on Phase and Chemical Equilibria in High-Pressure Methanol Synthesis”. In: *Industrial & Engineering Chemistry Research* 51.38 (2012), pp. 12233–12243. ISSN: 0888-5885. DOI: 10.1021/ie3017362.
- [256] Raquel de María et al. “Industrial Methanol from Syngas: Kinetic Study and Process Simulation”. In: *International Journal of Chemical Reactor Engineering* 11.1 (2013). ISSN: 1542-6580. DOI: 10.1515/ijcre-2013-0061.
- [257] D. A. van Veldhuizen and G. B. Lamont. “Multiobjective evolutionary algorithms: analyzing the state-of-the-art”. In: *Evolutionary computation* 8.2 (2000), pp. 125–147. ISSN: 1063-6560. DOI: 10.1162/106365600568158.
- [258] Godfrey C. Chinchin, P. J. Denny, D. G. Parker, et al. “Activity of Cu-ZnO-Al<sub>2</sub>O<sub>3</sub> methanol synthesis catalyst”. In: *ACS Division of Fuel Chemistry* 29.5 (1984), pp. 178–190.

- [259] D. Bellotti, M. Rivarolo, and L. Magistri. “Economic feasibility of methanol synthesis as a method for CO<sub>2</sub> reduction and energy storage”. In: *Energy Procedia* 158 (2019), pp. 4721–4728. ISSN: 18766102. DOI: 10.1016/j.egypro.2019.01.730.
- [260] Parth Garg. “Experimental Validation of Steady State Heat Transfer Model for Methanol Synthesis”. Master thesis. FAU Nürnberg Erlangen, 2019.
- [261] Arif Reiner Schütze. “Erweiterung und Verifizierung eines Reaktormodells für die Synthese von Methanol aus nachhaltigen Rohstoffen”. Masterarbeit. TH Nürnberg, 2019.
- [262] Minji Son et al. “CFD modeling of a compact reactor for methanol synthesis: Maximizing productivity with increased thermal controllability”. In: *International Journal of Heat and Mass Transfer* 145 (2019), p. 118776. ISSN: 00179310. DOI: 10.1016/j.ijheatmasstransfer.2019.118776.



# Acknowledgements

This thesis was developed during my period as doctoral researcher at Engler-Bunte Institute at KIT in Karlsruhe, my employment as scientific assistant at Fraunhofer Institute for Solar Energy Systems ISE in Freiburg and my time as Deutsche Bundesstiftung Umwelt PhD scholar (20017/517). Many people in these three institutions supported this work during the past years – I would hereby like to express my appreciation and thankfulness to everyone of them.

Special thanks go to my supervisors Prof. Dr. Thomas Kolb and Dr. Siegfried Bajohr at Engler-Bunte Institute for their strong scientific and personal support as well as their time and feedback during this interesting and intense time. I am looking forward to staying in connection with them and their research group for the next joint research projects to come.

Prof. Dr. Jürgen Karl from FAU Nürnberg-Erlangen is sincerely thanked for his agreement to evaluate this thesis as second reviewer.

This work would not have been possible without the strong support of my colleagues at Fraunhofer ISE who invested plenty of their energy and dedication into making this work a success. Special thanks go to Prof. Dr. Christopher Hebling, Dr. Achim Schaadt, Dr. Ouda Salem and Max Hadrich for their supervision, trust, encouragement and organizational support during the past years. Turning scientific ideas into reality demands for a strong and dedicated team. I am grateful for my dear colleagues, students and friends in the whole division Hydrogen Technologies for their support in the construction and automation of the miniplant facility, their great generousness with regard to the sharing of their scientific equipment and knowledge, their assistance in topics related to analytical problems and software bugfixing issues as well as their passion for endless scientific discussions at any daytime.

Acceptance for my scholarship provided by Deutsche Bundesstiftung Umwelt was one of the most motivating and encouraging moments during my professional career so far. Thus, I am grateful to DBU for their financial support and for providing access to the DBU network.

Last but not least, I would like to thank my partner Charlotte as well as my family and friends for their patience, support and care during the past years.

## Verification of the contribution of co-authors

## **Verification of the contribution from the co-authors**

Title: Methanol Synthesis – Industrial Challenges within a Changing Raw Material Landscape

Journal: Chemie Ingenieur Technik (Wiley)

Authors: Florian Nestler, Matthias Krüger, Johannes Full, Max J. Hadrich, Robin J. White, Achim Schaadt

### **Position in the dissertation:**

The content of this paper has been included in Chapter 2.

Contribution of Florian Nestler:

- Literature review on methanol synthesis and syngas generation
- Composition of the manuscript (70%)

Contribution of Matthias Krüger:

- Input of industrial experience
- Composition of the manuscript (30%)

Contribution of Johannes Full:

- Simulation on process scale
- Proofreading and scientific reviewing of the manuscript

Contribution of Max J. Hadrich:

- Proofreading and scientific reviewing of the manuscript

Contribution of Robin J. White:

- Proofreading and scientific/methodical reviewing of the manuscript

Contribution of Achim Schaadt:

- Proofreading and scientific/methodical reviewing of the manuscript

## **Verification of the contribution from the co-authors**

Title: Kinetic modelling of methanol synthesis over commercial catalysts: A critical assessment

Journal: Chemical Engineering Journal (Elsevier)

Authors: Florian Nestler, Arif R. Schütze, Mohamed Ouda, Max J. Hadrich, Achim Schaadt, Siegfried Bajohr, Thomas Kolb

### **Position in the dissertation:**

The content of this paper has been included in Chapters 2, 3 and 4.

Contribution of Florian Nestler:

- Elaboration of the validation methodology
- Implementation of the simulation platform (90%)
- Structuring and implementation of the methodological approach
- Analysis and discussion of experimental data and simulation results
- Composition of the manuscript

Contribution of Arif R. Schütze:

- Implementation of the simulation platform (10%)
- Transfer of the experimental data into the validation toolbox
- Execution of the fitting procedure
- Structuring and composition of the appendix

Contribution of Mohamed Ouda:

- Support in structuring of the manuscript
- Supervision of the research
- Proofreading of the manuscript

Contribution of Max J. Hadrich:

- Proofreading of the manuscript

Contribution of Achim Schaadt:

- Supervision of the research
- Proofreading of the manuscript

Contribution of Siegfried Bajohr:

- Supervision of the research
- Proofreading of the manuscript

Contribution of Thomas Kolb:

- Supervision of the research
- Proofreading of the manuscript

## **Verification of the contribution from the co-authors**

Title: A Novel Approach for Kinetic Measurements in Exothermic Fixed Bed Reactors: Advancements in Non-Isothermal Bed Conditions Demonstrated for Methanol Synthesis

Journal: Reaction Chemistry & Engineering (RSC)

Authors: Florian Nestler, Viktor P. Müller, Mohamed Ouda, Max J. Hadrich, Achim Schaadt, Siegfried Bajohr, Thomas Kolb

### **Position in the dissertation:**

The content of this paper has been included in Chapters 3 and 4.

#### Contribution of Florian Nestler:

- Elaboration of the miniplant design and analytical concept
- Built up and structuring of the simulation platform
- Data extraction, processing and selection
- Implementation of the validation library and parameter fitting scripts (90%)
- Conduction of the miniplant experiments (70%)
- Analysis and discussion of the experimental data and simulation results
- Composition of the manuscript

#### Contribution of Viktor P. Müller:

- Elaboration of weighting factors for the multi objective parameter fitting
- Implementation of the validation library and parameter fitting scripts (10%)
- Conduction of the miniplant experiments (30%)

#### Contribution of Mohamed Ouda:

- Support in structuring of the manuscript
- Critical discussion of the results
- Supervision of the research
- Proofreading of the manuscript

#### Contribution of Max J. Hadrich:

- Support in the design of the miniplant facility
- Proofreading of the manuscript

#### Contribution of Achim Schaadt:

- Supervision of the research
- Proofreading of the manuscript

#### Contribution of Siegfried Bajohr:

- Supervision of the research
- Proofreading of the manuscript

#### Contribution of Thomas Kolb:

- Supervision of the research
- Proofreading of the manuscript

# Publication list

## Journal publications sorted by year

- F. Nestler, V. P. Müller, M. Ouda, M. J. Hadrich, A. Schaadt, S. Bajohr, T. Kolb. "A Novel Approach for Kinetic Measurements in Exothermic Fixed Bed Reactors: Advancements in Non-Isothermal Bed Conditions Demonstrated for Methanol Synthesis". In *RSC Reaction Chemistry & Engineering* 6 (2021), pp. 1092–1107. DOI: 10.5445/IR/1000131790.
- M. Martens, M. J. Hadrich, F. Nestler, M. Ouda, A. Schaadt. "Combination of Refractometry and Densimetry – A Promising Option for Fast Raw Methanol Analysis". In *Chemie Ingenieur Technik* 92.10 (2020), pp. 1474–1481. DOI: 10.1002/cite.202000058.
- F. Nestler, A. R. Schütze, M. Ouda, M. J. Hadrich, A. Schaadt, S. Bajohr, T. Kolb. "Kinetic modelling of methanol synthesis over commercial catalysts: A critical assessment". In *Chemical Engineering Journal* 394 (2020), pp. 124881. DOI: 10.1016/j.cej.2020.124881.
- M. Ouda, C. Hank, F. Nestler, M. J. Hadrich, J. Full, A. Schaadt, C. Hebling. "Power-to-Methanol: Techno-Economical and Ecological Insights". In *Zukünftige Kraftstoffe*. Ed. by Wolfgang Maus. Vol. 55. Berlin, Heidelberg: Springer Berlin Heidelberg, 2019, pp. 380–409. ISBN : 978-3-662-58005-9. DOI: 10.1007/978-3-662-58006-6\_17.
- F. Nestler, M. Krüger, J. Full, M. J. Hadrich, R. J. White, A. Schaadt. "Methanol Synthesis – Industrial Challenges within a Changing Raw Material Landscape". In *Chemie Ingenieur Technik* 90.10 (2018), pp. 1409–1418. DOI: 10.1002/cite.201800026.
- F. Nestler, L. Burhenne, M. J. Amtenbrink, T. Aicher. "Catalytic decomposition of biomass tars. The impact of wood char surface characteristics on the catalytic performance for naphthalene removal". In *Fuel Processing Technology* 145 (2016), pp. 31–41. DOI: 10.1016/j.fuproc.2016.01.020.

## Conference contributions sorted by year

- F. Nestler, M. J. Hadrich, M. Ouda, A. Schaadt, S. Bajohr, T. Kolb "Dynamic behavior of a methanol synthesis reactor under flexible load conditions – Validation of a reactor model using a miniplant setup". *13th European Congress of Chemical Engineering* (2021), Poster contribution.
- F. Nestler, J. Full, M. J. Hadrich, M. Ouda, A. Schaadt, S. Bajohr, C. Hebling, T. Kolb "Experimentelle Validierung eines Kinetikmodells für die Methanolsynthese anhand einer Miniplant-Anlage". *10. ProcessNet Jahrestagung* (2020), Poster contribution.

- F. Nestler, M. Ouda, M. J. Hadrich, A. Schaadt, S. Bajohr, T. Kolb. "Experimentelle Validierung eines dynamischen Modells für die Methanolsynthese". *ProcessNet Energieverfahrenstechnik* (2020), Oral presentation, DOI :10.1002/cite.202055427.
- F. Nestler, R. Mayorga-Gonzalez, J. Full, A. Schaadt, S. Bajohr, T. Kolb. "Dynamische 1D/2D-Analyse kritischer Reaktor-Lastzustände". *ProcessNet Energieverfahrenstechnik* (2019), Oral presentation
- R. Becka, F. Nestler, S. Bajohr, M. Ouda, A. Schaadt, T. Kolb "Methanol synthesis in fixed-bed and slurry bubble column reactors". *ProcessNet Reaktionstechnik* (2019), Poster contribution.

# Appendix

## A.1 Derivation of the equilibrium constant

The derivation of Eq. 2.13 from Eq. 2.10 is based on the work provided by Graaf and Winkelmann [129] and Thomas et al. [133].

Basic expression:

$$\ln(K_{eq}(T)) = -\frac{\Delta G^0(T)}{R \cdot T} \quad (\text{A.1})$$

Calculation of  $\Delta G^0(T)$  by the change in enthalpy from a reference temperature:

$$\frac{-\Delta G^0(T)}{T} = \frac{-\Delta G^0(T_{ref})}{T_{ref}} + \int_{T_{ref}}^T \frac{\Delta H^0(T)}{T^2} dT \quad (\text{A.2})$$

Application of the Kirchhoff equation for  $\Delta H^0(T)$ :

$$\Delta H^0(T) = \Delta H^0(T_{ref}) + \int_{T_{ref}}^T \Delta \tilde{c}_p^0(T) dT \quad (\text{A.3})$$

Temperature dependence of heat capacity can be calculated by 4<sup>th</sup> order polynomial as follows:

$$\Delta \tilde{c}_p^0(T) = \Delta \tilde{c}_p \cdot A + \Delta \tilde{c}_p \cdot B \cdot T + \Delta \tilde{c}_p \cdot C \cdot T^2 + \Delta \tilde{c}_p \cdot D \cdot T^3 + \Delta \tilde{c}_p \cdot E \cdot T^4 \quad (\text{A.4})$$

Insertion of Eq. A.4 and Eq. A.3 into A.2 with subsequent integration delivers:

$$\Delta H^0(T) = I_H + \Delta \tilde{c}_p \cdot A \cdot T + \frac{1}{2} \Delta \tilde{c}_p \cdot B \cdot T^2 + \frac{1}{3} \Delta \tilde{c}_p \cdot C \cdot T^3 + \frac{1}{4} \Delta \tilde{c}_p \cdot D \cdot T^4 + \frac{1}{5} \Delta \tilde{c}_p \cdot E \cdot T^5 \quad (\text{A.5})$$

with  $I_H$  as the integration constant for the lower boundary:

$$\begin{aligned} I_H = \Delta H^0(T_{ref}) - \Delta \tilde{c}_p \cdot A \cdot T_{ref} - \frac{1}{2} \Delta \tilde{c}_p \cdot B \cdot T_{ref}^2 \\ - \frac{1}{3} \Delta \tilde{c}_p \cdot C \cdot T_{ref}^3 - \frac{1}{4} \Delta \tilde{c}_p \cdot D \cdot T_{ref}^4 - \frac{1}{5} \Delta \tilde{c}_p \cdot E \cdot T_{ref}^5 \end{aligned} \quad (\text{A.6})$$

Insertion of Eq. A.5 into Eq. A.2 leads to:

$$\begin{aligned} \frac{-\Delta G^0(T)}{T} = \frac{-\Delta G^0(T_{ref})}{T_{ref}} + \int_{T_{ref}}^T \frac{I_H + \Delta \tilde{c}_p \cdot A \cdot T + \frac{1}{2} \Delta \tilde{c}_p \cdot B \cdot T^2 + \frac{1}{3} \Delta \tilde{c}_p \cdot C \cdot T^3 + \frac{1}{4} \Delta \tilde{c}_p \cdot D \cdot T^4 + \frac{1}{5} \Delta \tilde{c}_p \cdot E \cdot T^5}{T^2} dT \end{aligned} \quad (\text{A.7})$$

Simplification leads towards:

$$\begin{aligned} \frac{-\Delta G^0(T)}{T} &= \frac{-\Delta G^0(T_{ref})}{T_{ref}} + \int_{T_{ref}}^T I_H/T^2 + \Delta\tilde{c}_p \cdot A/T + \frac{1}{2}\Delta\tilde{c}_p \cdot B \\ &\quad + \frac{1}{3}\Delta\tilde{c}_p \cdot C \cdot T + \frac{1}{4}\Delta\tilde{c}_p \cdot D \cdot T^2 + \frac{1}{5}\Delta\tilde{c}_p \cdot E \cdot T^3 dT \end{aligned} \quad (\text{A.8})$$

Integration of Eq. A.8 delivers:

$$\begin{aligned} \frac{-\Delta G^0(T)}{T} &= I_G - \frac{I_H}{T} + \Delta\tilde{c}_p \cdot A \cdot \ln(T) + \frac{1}{2}\Delta\tilde{c}_p \cdot B \cdot T \\ &\quad + \frac{1}{6}\Delta\tilde{c}_p \cdot C \cdot T^2 + \frac{1}{12}\Delta\tilde{c}_p \cdot D \cdot T^3 + \frac{1}{20}\Delta\tilde{c}_p \cdot E \cdot T^4 \end{aligned} \quad (\text{A.9})$$

with  $I_G$  as the integration constant for the lower boundary:

$$\begin{aligned} I_G &= \frac{-\Delta G^0(T_{ref})}{T_{ref}} + \frac{I_H}{T_{ref}} - \Delta\tilde{c}_p \cdot A \cdot \ln(T_{ref}) - \frac{1}{2}\Delta\tilde{c}_p \cdot B \cdot T_{ref} \\ &\quad - \frac{1}{6}\Delta\tilde{c}_p \cdot C \cdot T_{ref}^2 - \frac{1}{12}\Delta\tilde{c}_p \cdot D \cdot T_{ref}^3 - \frac{1}{20}\Delta\tilde{c}_p \cdot E \cdot T_{ref}^4 \end{aligned} \quad (\text{A.10})$$

Substitution in Eq. A.10 with the parameters  $a_1$  bis  $a_7$ :

$$a_1 = -I_H \quad (\text{A.11})$$

$$a_2 = I_G \quad (\text{A.12})$$

$$a_3 = \frac{1}{2}\Delta\tilde{c}_p \cdot B \quad (\text{A.13})$$

$$a_4 = \frac{1}{6}\Delta\tilde{c}_p \cdot C \quad (\text{A.14})$$

$$a_5 = \frac{1}{12}\Delta\tilde{c}_p \cdot D \quad (\text{A.15})$$

$$a_6 = \frac{1}{20}\Delta\tilde{c}_p \cdot E \quad (\text{A.16})$$

$$a_7 = \Delta\tilde{c}_p \cdot A \quad (\text{A.17})$$

Leads towards:

$$\frac{-\Delta G^0(T)}{T} = \frac{a_1}{T} + a_2 + a_3 \cdot T + a_4 \cdot T^2 + a_5 \cdot T^3 + a_6 \cdot T^4 + a_7 \cdot \ln(T) \quad (\text{A.18})$$

Rearrangement towards  $\Delta G^0(T)$ :

$$-\Delta G^0(T) = a_1 + a_2 \cdot T + a_3 \cdot T^2 + a_4 \cdot T^3 + a_5 \cdot T^4 + a_6 \cdot T^5 + a_7 \cdot T \cdot \ln(T) \quad (\text{A.19})$$

Finally insertion into Eq. A.1 leads towards the final expression for  $K_{eq}(T)$ :

$$\ln(K_{eq}(T)) = \frac{1}{R \cdot T} \cdot \left( a_1 + a_2 \cdot T + a_3 \cdot T^2 + a_4 \cdot T^3 + a_5 \cdot T^4 + a_6 \cdot T^5 + a_7 \cdot T \cdot \ln(T) \right) \quad (\text{A.20})$$

## A.2 Literature use of kinetic models

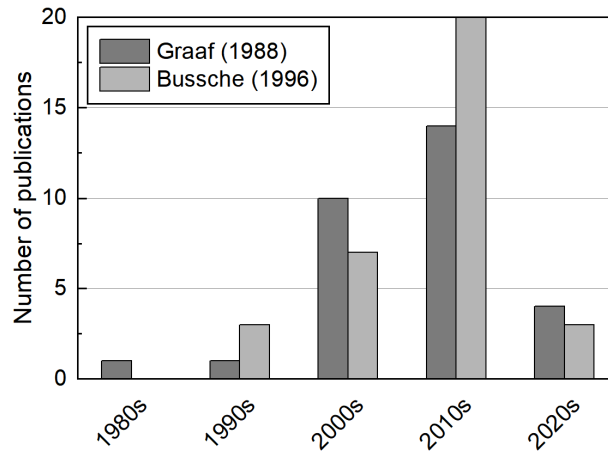


Figure A.1: Literature use of the kinetic models by Bussche [145] and Graaf [192] over decades since 1980.

## A.3 Industrial reactor data available in scientific literature

Table A.1: Design parameters for steam cooled tube bundle reactors available in scientific literature.

Parameter	Unit	Kordabadi et al. 2005	Hartig et al. 1993	Yusup et al. 2010	Chen et al. 2011
References	-	[74, 169, 246, 247]	[127]	[163, 166]	[167]
$d_{\text{int}}$	m	0.038	0.05	0.0445	0.04
$d_{\text{ext}}$	m	-	-	0.0485	-
$h_{\text{cat}}$	m	7.022	5	7.26	7
$N_{\text{tubes}}$	-	2962	9100	4801	1620
$d_p$	m	0.0054	0.0042	0.006	0.0054
$\varepsilon_{\text{bulk}}$	-	0.39	0.4	0.4	0.285
$\rho_{\text{bulk}}$	$\text{kg m}^{-3}$	1132	1062	1100	1190
$T_{\text{in}}$	$^{\circ}\text{C}$	230	238	225	225
$p$	bar	76.98	81.95	82.3	69.7
$T_{\text{cool}}$	$^{\circ}\text{C}$	252	260	250	220

## A.4 Cell model for heat transfer inside the packed bed

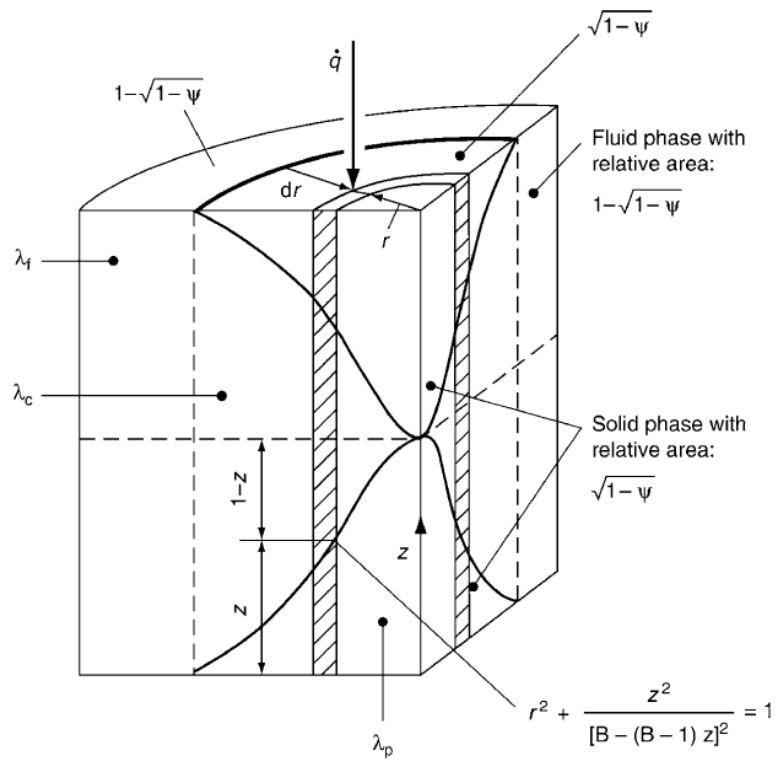


Figure A.2: Schematic of the unit cell model as defined by Zehner and Schlünder [213]; Figure was overtaken from VDI Heat Atlas [210].

## A.5 Sensitivity of Thiele modulus

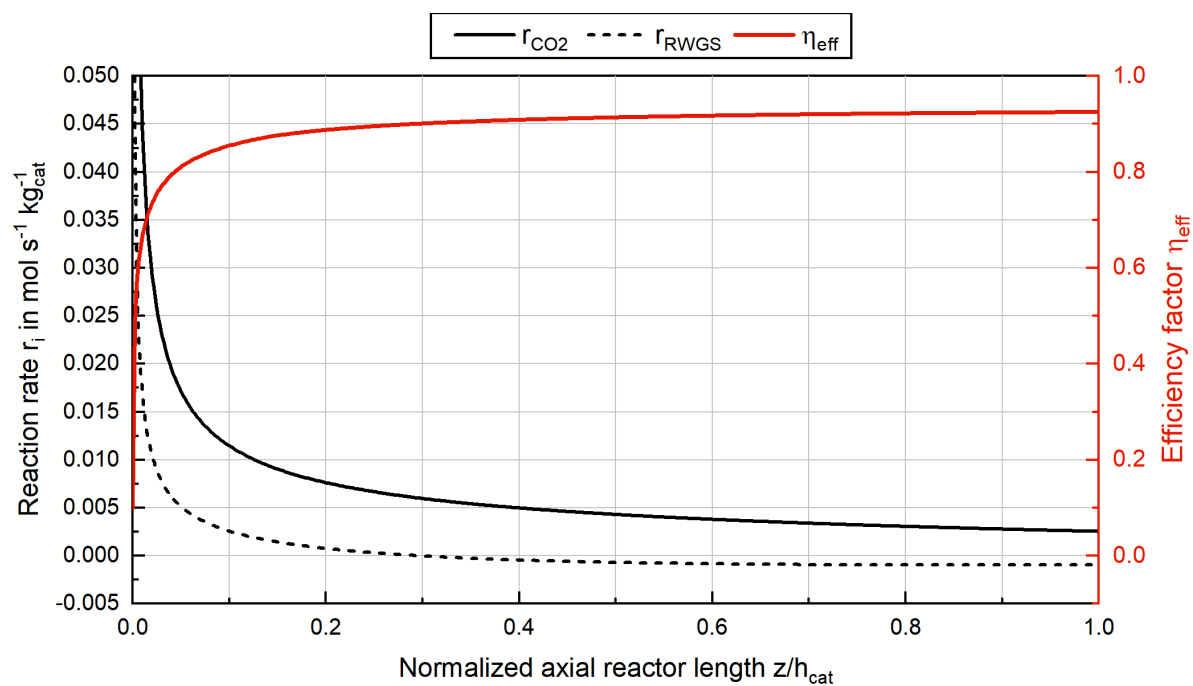


Figure A.3: Intrinsic reaction rate (primary axis) of CO<sub>2</sub>-hydrogenation ( $r_{CO_2}$ ) and rWGs ( $r_{RWGS}$ ) simulated with the kinetic model  $Nest_{diff}$  as well as the efficiency factor calculated by Thiele modulus (secondary axis) for an ideal isothermal reactor at  $T = 240\text{ }^\circ\text{C}$  with the kinetic model  $Nest_{diff}$  at  $SN = 4.0$ ;  $COR = 0.9$ ;  $GHSV = 10,000\text{ h}^{-1}$  and a pressure of 80 bar.

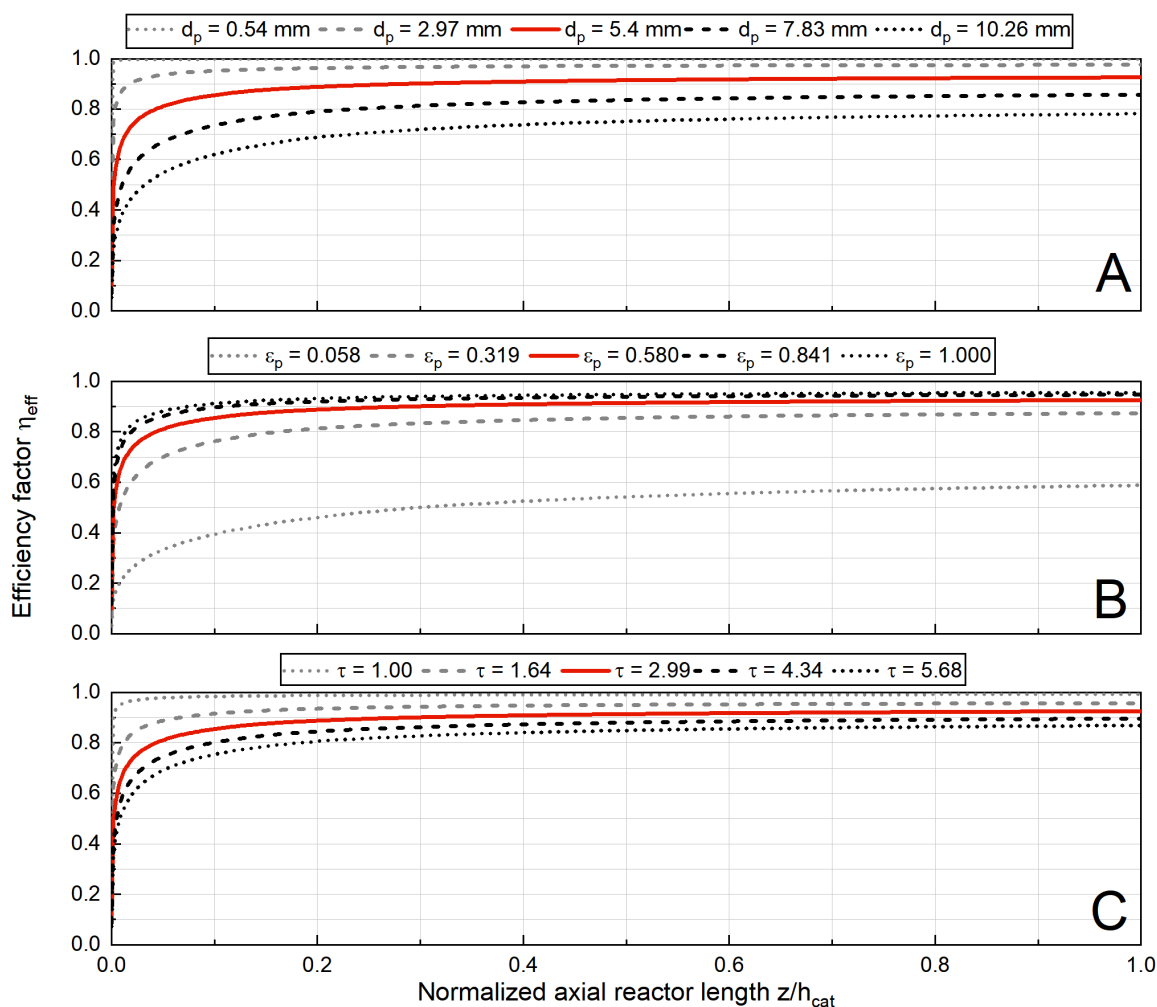


Figure A.4: Sensitivity analysis of efficiency factor calculated using Thiele modulus (compare Sec. ??) towards the catalyst parameters  $d_p$  (A),  $\varepsilon_p$  (B) and  $\tau$  (C); Simulation was performed within an ideal isothermal reactor at  $T = 240^\circ\text{C}$  with the kinetic model  $\text{Nestler}_{\text{diff}}$  at  $\text{SN} = 4.0$ ;  $\text{COR} = 0.9$ ;  $\text{GHSV} = 10,000 \text{ h}^{-1}$  and a pressure of 80 bar; Parameters were varied from the base case (red, solid) towards -45% (dashed, gray), -90% (dotted, gray) as well as +45% (dashed, black), +90% (dotted, black); In case of  $\varepsilon_p$  and  $\tau$  the upper or lower boundary were limited by these parameters physical meaning, respectively.

## A.6 Experimental data used for integral kinetic model

Table A.2: Experimental data taken from Park et al. [203] that was used for the integral kinetic model Nestler<sub>integ</sub>.

N <sub>data pt</sub>	Feed composition				Reactor conditions			Conversion	
	y <sub>CO</sub>	y <sub>CO2</sub>	y <sub>H2</sub>	y <sub>Ar</sub>	p	T	GHSV	X <sub>CO</sub>	X <sub>CO2</sub>
[-]	[-]	[-]	[-]	[-]	[bar]	[°C]	[h <sup>-1</sup> ]	[-]	[-]
1	0.19	0.11	0.70	0.00	50	249.85	22,640	0.4105	0.0784
2	0.19	0.11	0.70	0.00	50	269.85	22,640	0.3378	0.0605
3	0.19	0.11	0.70	0.00	50	299.85	22,640	0.1806	0.0618
4	0.19	0.11	0.70	0.00	50	319.85	22,640	0.0914	0.068
5	0.19	0.11	0.70	0.00	50	339.85	22,640	0.0327	0.0838
6	0.19	0.11	0.70	0.00	50	249.85	9,056	0.5428	0.0946
7	0.19	0.11	0.70	0.00	50	249.85	22,640	0.4121	0.061
8	0.19	0.11	0.70	0.00	50	249.85	33,960	0.3413	0.0482
9	0.19	0.11	0.70	0.00	50	249.85	45,280	0.2893	0.0462
10	0.19	0.11	0.70	0.00	50	249.85	9,056	0.5229	0.1068
11	0.19	0.11	0.70	0.00	70	249.85	9,056	0.6678	0.1005
12	0.19	0.11	0.70	0.00	90	249.85	9,056	0.7478	0.1098
13	0.00	0.24	0.72	0.04	50	249.85	9,056	-0.0936	0.2332
14	0.11	0.16	0.68	0.05	50	249.85	9,056	0.5254	0.1073
15	0.17	0.11	0.67	0.05	50	249.85	9,056	0.526	0.0809
16	0.22	0.07	0.66	0.05	50	249.85	9,056	0.499	0.0037
17	0.26	0.05	0.64	0.05	50	249.85	9,056	0.4562	0.0005
18	0.27	0.03	0.65	0.05	50	249.85	9,056	0.446	0
19	0.28	0.02	0.65	0.05	50	249.85	9,056	0.4221	0
20	0.29	0.02	0.64	0.05	50	249.85	9,056	0.365	0
21	0.18	0.10	0.67	0.05	50	249.85	9,056	0.5755	0.0782
22	0.16	0.09	0.70	0.05	50	249.85	9,056	0.5796	0.08
23	0.13	0.07	0.76	0.04	50	249.85	9,056	0.6231	0.0938
24	0.09	0.05	0.83	0.03	50	249.85	9,056	0.6977	0.1511
25	0.19	0.11	0.70	0.00	50	249.85	9,056	0.5716	0.058
26	0.14	0.08	0.50	0.29	50	249.85	9,056	0.409	0.0432
27	0.14	0.08	0.50	0.29	70	249.85	9,056	0.574	0.0532
28	0.19	0.11	0.70	0.00	70	249.85	9,056	0.7303	0.1101
29	0.00	0.24	0.72	0.04	70	249.85	9,056	-0.074	0.287
30	0.17	0.11	0.67	0.05	70	249.85	9,056	0.6446	0.1002
31	0.22	0.07	0.66	0.05	70	249.85	9,056	0.6085	0.0421
32	0.27	0.03	0.65	0.05	70	249.85	9,056	0.5741	-0.0643
33	0.29	0.02	0.64	0.05	70	249.85	9,056	0.5419	-0.2302

N <sub>data pt</sub>	Feed composition				Reactor conditions			Conversion	
	y <sub>CO</sub>	y <sub>CO2</sub>	y <sub>H2</sub>	y <sub>Ar</sub>	p	T	GHSV	X <sub>CO</sub>	X <sub>CO2</sub>
[-]	[-]	[-]	[-]	[-]	[bar]	[°C]	[h <sup>-1</sup> ]	[-]	[-]
34	0.00	0.24	0.72	0.04	70	269.85	9,056	-0.1022	0.2646
35	0.17	0.11	0.67	0.05	70	269.85	9,056	0.4993	0.0478
36	0.22	0.07	0.66	0.05	70	269.85	9,056	0.4844	-0.0127
37	0.27	0.03	0.65	0.05	70	269.85	9,056	0.4638	-0.3565
38	0.29	0.02	0.64	0.05	70	269.85	9,056	0.4566	-0.4762
39	0.00	0.24	0.72	0.04	50	249.85	9,056	-0.0844	0.2461
40	0.00	0.22	0.74	0.04	50	249.85	9,056	-0.0913	0.2539
41	0.00	0.17	0.80	0.03	50	249.85	9,056	-0.0988	0.3147
42	0.00	0.12	0.86	0.02	50	249.85	9,056	-0.1051	0.4094
43	0.00	0.24	0.72	0.04	60	249.85	9,056	-0.0789	0.2621
44	0.00	0.22	0.74	0.04	60	249.85	9,056	-0.0835	0.28
45	0.00	0.17	0.80	0.03	60	249.85	9,056	-0.0896	0.3423
46	0.00	0.12	0.86	0.02	60	249.85	9,056	-0.0858	0.4515
47	0.00	0.24	0.72	0.04	70	249.85	9,056	-0.073	0.2836
48	0.00	0.22	0.74	0.04	70	249.85	9,056	-0.078	0.3037
49	0.00	0.17	0.80	0.03	70	249.85	9,056	-0.0833	0.3595
50	0.00	0.12	0.86	0.02	70	249.85	9,056	-0.0802	0.4844
51	0.07	0.05	0.62	0.26	80	249.85	9,056	0.7593	0.1675
52	0.07	0.05	0.62	0.26	80	259.85	9,056	0.6736	0.1894
53	0.07	0.05	0.62	0.26	80	269.85	9,056	0.5905	0.2096
54	0.07	0.05	0.62	0.26	80	269.85	11,320	0.5791	0.1701
55	0.19	0.11	0.70	0.00	50	229.85	22,640	0.3712	0.0829
56	0.19	0.11	0.70	0.00	50	239.85	22,640	0.4379	0.0834
57	0.19	0.11	0.70	0.00	50	249.85	22,640	0.4266	0.0832
58	0.19	0.11	0.70	0.00	50	259.85	22,640	0.3842	0.0786
59	0.19	0.11	0.70	0.00	50	269.85	22,640	0.3221	0.0714
60	0.19	0.11	0.70	0.00	50	279.85	22,640	0.2794	0.0685
61	0.19	0.11	0.70	0.00	50	289.85	22,640	0.2375	0.0694
62	0.19	0.11	0.70	0.00	50	299.85	22,640	0.1756	0.0588
63	0.19	0.11	0.70	0.00	50	309.85	22,640	0.1161	0.0577
64	0.19	0.11	0.70	0.00	50	319.85	22,640	0.0842	0.0463
65	0.19	0.11	0.70	0.00	50	339.85	22,640	0.0631	0.0575
66	0.11	0.06	0.83	0.00	50	229.85	22,640	0.5543	0.1562
67	0.11	0.06	0.83	0.00	50	239.85	22,640	0.5282	0.3012
68	0.11	0.06	0.83	0.00	50	249.85	22,640	0.558	0.1529
69	0.11	0.06	0.83	0.00	50	259.85	22,640	0.518	0.1404
70	0.11	0.06	0.83	0.00	50	269.85	22,640	0.4595	0.1212
71	0.11	0.06	0.83	0.00	50	279.85	22,640	0.3914	0.0929

N <sub>data pt</sub>	Feed composition				Reactor conditions			Conversion	
	y <sub>CO</sub>	y <sub>CO2</sub>	y <sub>H2</sub>	y <sub>Ar</sub>	p	T	GHSV	X <sub>CO</sub>	X <sub>CO2</sub>
[-]	[-]	[-]	[-]	[-]	[bar]	[°C]	[h <sup>-1</sup> ]	[-]	[-]
72	0.11	0.06	0.83	0.00	50	289.85	22,640	0.327	0.0742
73	0.11	0.06	0.83	0.00	50	299.85	22,640	0.2675	0.0388
74	0.19	0.11	0.70	0.00	50	229.85	9,056	0.5642	0.1215
75	0.19	0.11	0.70	0.00	50	239.85	9,056	0.5565	0.1128
76	0.19	0.11	0.70	0.00	50	249.85	9,056	0.5137	0.1009
77	0.19	0.11	0.70	0.00	50	269.85	9,056	0.3657	0.0922
78	0.11	0.06	0.83	0.00	50	229.85	9,056	0.7618	0.1888
79	0.11	0.06	0.83	0.00	50	239.85	9,056	0.7228	0.1786
80	0.11	0.06	0.83	0.00	50	249.85	9,056	0.6593	0.1707
81	0.11	0.06	0.83	0.00	50	259.85	9,056	0.5927	0.159
82	0.11	0.06	0.83	0.00	50	269.85	9,056	0.5032	0.1159
83	0.11	0.06	0.83	0.00	50	279.85	9,056	0.4414	0.1024
84	0.11	0.06	0.83	0.00	50	289.85	9,056	0.3976	0.0694
85	0.11	0.06	0.83	0.00	50	299.85	9,056	0.3669	0.0251
86	0.18	0.10	0.67	0.05	70	249.85	22,640	0.5423	0.0545
87	0.18	0.10	0.67	0.05	70	219.85	22,640	0.3172	0.0409
88	0.18	0.10	0.67	0.05	70	229.85	22,640	0.5562	0.0561
89	0.18	0.10	0.67	0.05	70	239.85	22,640	0.5792	0.0561
90	0.18	0.10	0.67	0.05	70	249.85	22,640	0.5321	0.0398
91	0.18	0.10	0.67	0.05	70	259.85	22,640	0.4976	0.0372
92	0.18	0.10	0.67	0.05	70	269.85	22,640	0.443	0.0335
93	0.18	0.10	0.67	0.05	70	279.85	22,640	0.3745	0.0158
94	0.18	0.10	0.67	0.05	70	299.85	22,640	0.2795	0.0031
95	0.18	0.10	0.67	0.05	70	249.85	22,640	0.5318	0.0423
96	0.18	0.10	0.67	0.05	70	299.85	22,640	0.2622	0.0289
97	0.18	0.10	0.67	0.05	70	249.85	22,640	0.5373	0.0518
98	0.18	0.10	0.67	0.05	50	249.85	22,640	0.4126	0.0637
99	0.18	0.10	0.67	0.05	70	249.85	22,640	0.4859	0.0428
100	0.18	0.10	0.67	0.05	90	249.85	22,640	0.5321	0.0398
101	0.00	0.24	0.72	0.04	50	249.85	22,640	-0.1513	0.2564
102	0.11	0.16	0.68	0.05	50	249.85	22,640	0.3355	0.0864
103	0.17	0.11	0.67	0.05	50	249.85	22,640	0.3557	0.0423
104	0.22	0.07	0.66	0.05	50	249.85	22,640	0.3876	0.0629
105	0.27	0.03	0.65	0.05	50	249.85	22,640	0.3045	-0.1195
106	0.29	0.02	0.64	0.05	50	249.85	22,640	0.2893	-0.1501
107	0.18	0.10	0.67	0.05	50	249.85	9,056	0.5392	0.0747
108	0.13	0.07	0.76	0.04	50	249.85	9,056	0.6484	0.1721
109	0.09	0.05	0.83	0.03	50	249.85	9,056	0.7193	0.2426

N <sub>data pt</sub>	Feed composition				Reactor conditions			Conversion	
	y <sub>CO</sub>	y <sub>CO2</sub>	y <sub>H2</sub>	y <sub>Ar</sub>	p	T	GHSV	X <sub>CO</sub>	X <sub>CO2</sub>
[-]	[-]	[-]	[-]	[-]	[bar]	[°C]	[h <sup>-1</sup> ]	[-]	[-]
110	0.18	0.10	0.67	0.05	50	249.85	22,640	0.3036	0.0716
111	0.16	0.09	0.70	0.05	50	249.85	22,640	0.3159	0.0885
112	0.13	0.07	0.76	0.04	50	249.85	22,640	0.3683	0.1402
113	0.11	0.06	0.80	0.03	50	249.85	22,640	0.3871	0.1764
114	0.09	0.05	0.83	0.03	50	249.85	22,640	0.401	0.2091

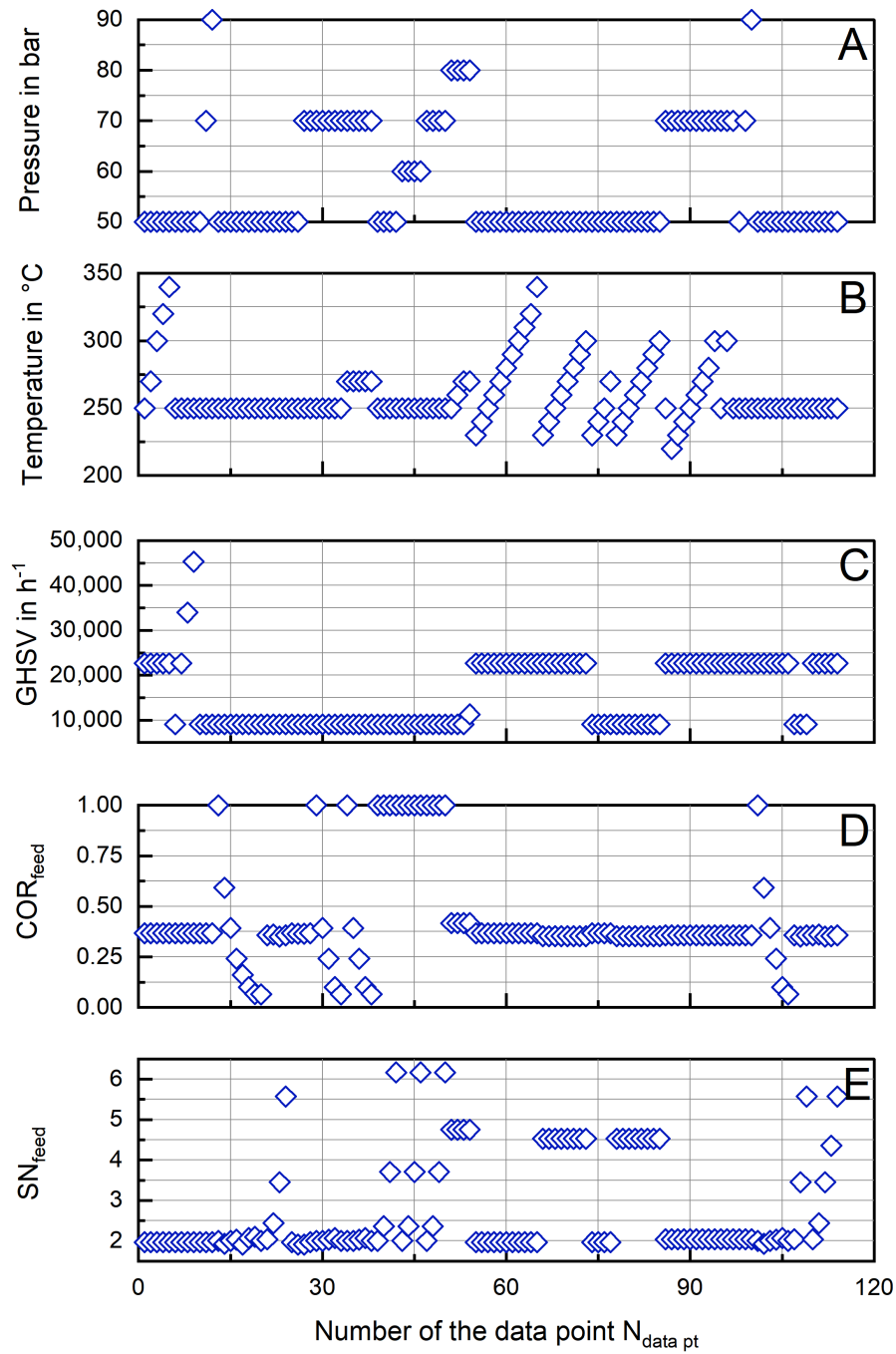


Figure A.5: Experimental data published by Park et al. [203] classified with regard to synthesis pressure (A), reactor temperature (B), GHSV (C),  $\text{COR}_{\text{feed}}$  (D) and  $\text{SN}_{\text{feed}}$  (E).

### A.7 CAD drawing of the miniplant setup

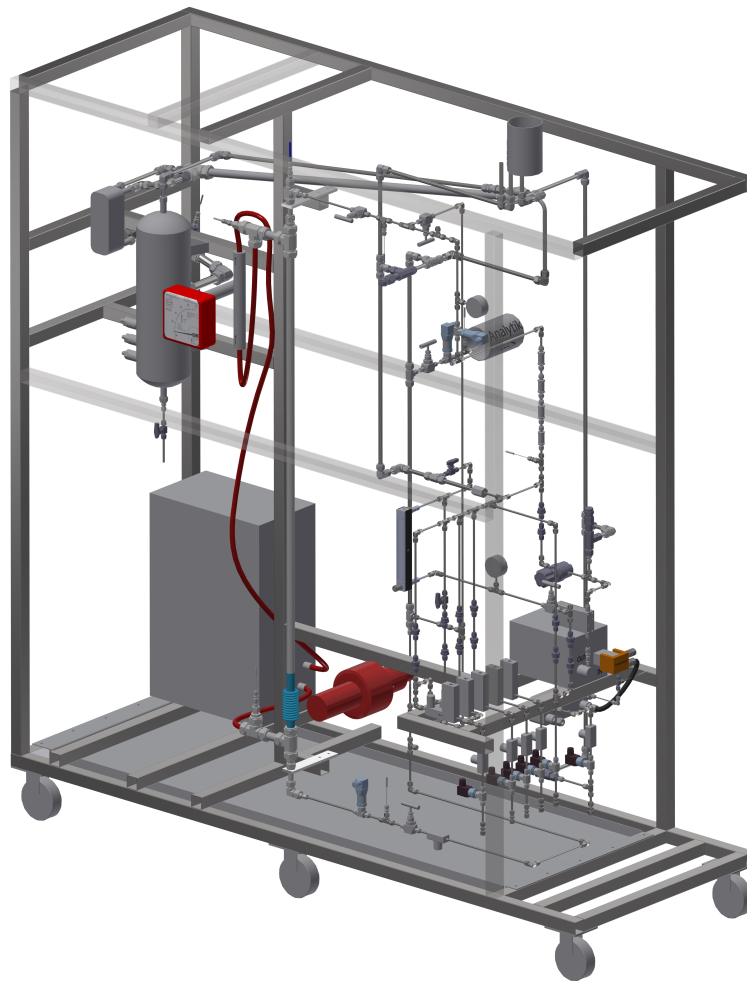


Figure A.6: CAD drawing of the miniplant setup with its most important components [250].

## A.8 Measurement of thermal oil flow rate

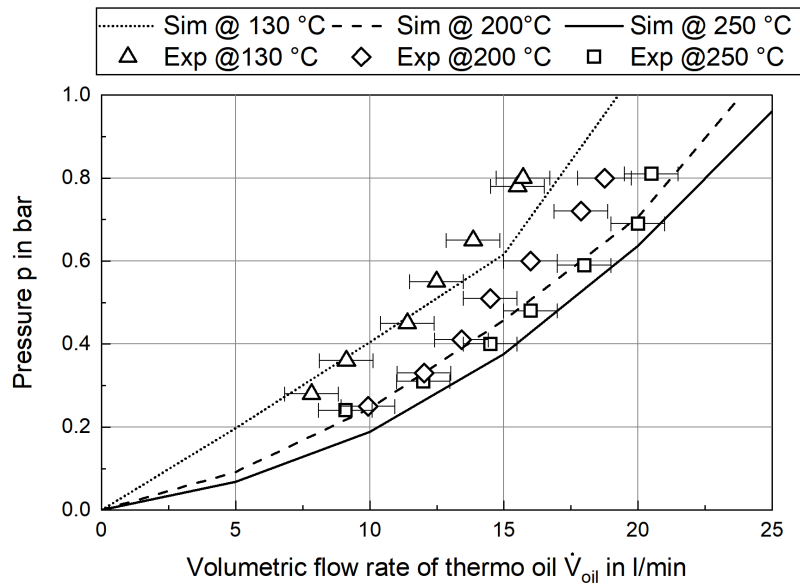


Figure A.7: Measurement (symbols) and simulation of the system characteristic curve of the miniplant setup at 130 °C (triangle / dotted), 200 °C (diamond / dashed) and 250 °C (rectangle / solid); Variation of the volumetric flow rate was performed by variation of the rotating speed of the pump; Pressure was obtained from the pressure sensor of the oil thermostat; Simulation was carried out using the software "druckverlust" [219].

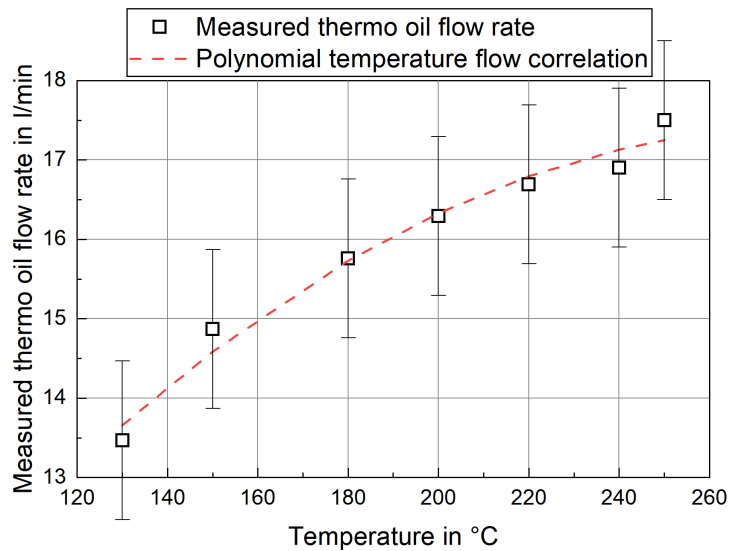


Figure A.8: Temperature-compensated volumetric flow rate obtained in the thermal oil cycle at constant rotational speed of the thermostat pump shaft between 130 °C and 250 °C thermal oil temperature [260].

Obtained temperature-flow correlation:

$$\dot{V}_{oil} = -2.73 \cdot 10^{-9} \cdot T_{cool}^2 \cdot \frac{m^3}{s K^2} + 3.03 \cdot 10^{-6} \cdot T_{cool} \cdot \frac{m^3}{s K} - 5.50 \cdot 10^{-4} \cdot \frac{m^3}{s} \quad (A.21)$$

## A.9 Thermophysical properties of the thermal oil

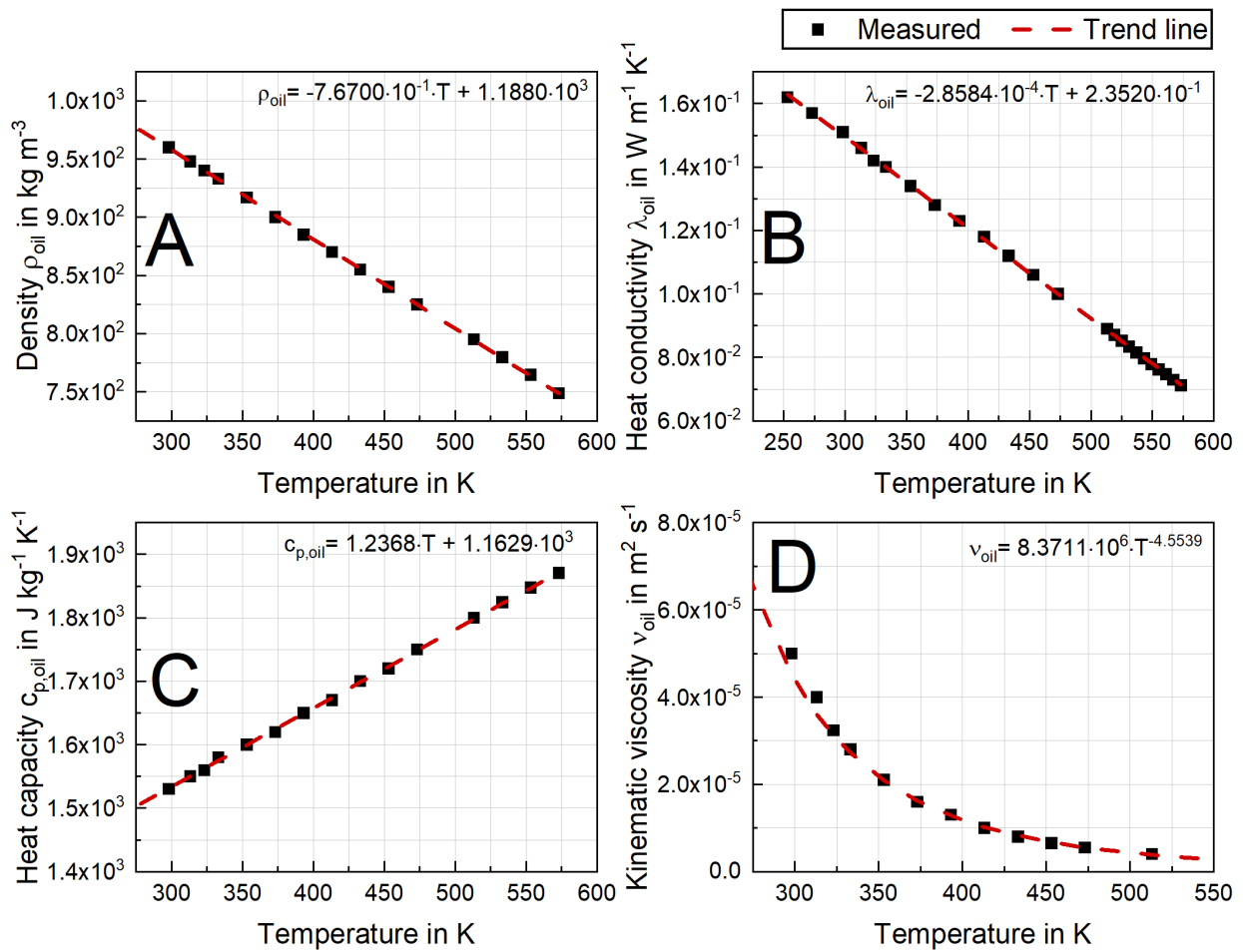


Figure A.9: Thermophysical properties of the thermal oil used in the miniplant setup for density (A), heat conductivity (B), heat capacity (C) and kinematic viscosity (D) with the respective fitted trend line [220].

## A.10 Analysis of the catalyst particle size distribution

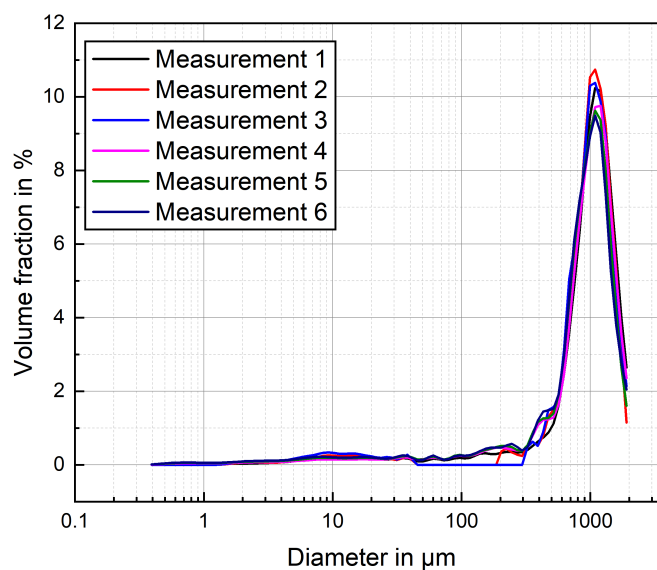


Figure A.10: Particle size distribution of the catalyst obtained by a flotation measurement using the Laser Diffraction Particle Size Analyzer LS 13 320 by Beckman Coulter.

## A.11 Purity of the gases used within the miniplant experiments

Table A.3: Supplier and purity of the technical gases used for the miniplant experiments.

Gas	Supplier	Purity
N <sub>2</sub>	Linde GmbH	5.0 (99.999 %)
CO <sub>2</sub>	Linde GmbH	4.5 (99.995 %)
CO	Linde GmbH	3.7 (99.97 %)
H <sub>2</sub>	Linde GmbH	5.0 (99.999 %)

## A.12 Overview on the experimental campaign executed on the scale down miniplant

Table A.4: Chronological progress of the experimental campaign.

Date	Activity	Comment
02.04.2020	Catalyst preparation and reactor filling	171 g of catalyst filled
03.04.2020	Leakage testing of the miniplant	Pressure tested at 85 bar
06.04.2020	Activation of the catalyst (day 1)	N <sub>2</sub> -blocking over night
07.04.2020	Activation of the catalyst (day 2)	N <sub>2</sub> -blocking over night
09.04.2020	Calibration of the fiber optic temperature sensor	Calibration between 50 °C and 265 °C under N <sub>2</sub> atmosphere
14.04.2020	Formation of the catalyst (day 1)	Benchmark conditions at 50 bar; Time on stream added: 5:45 h; N <sub>2</sub> -blocking over night at hot standby (T <sub>cool</sub> = 160 °C)
15.04.2020	Formation of the catalyst (day 2)	Benchmark conditions at 50 bar; Time on stream added: 5:20 h; N <sub>2</sub> -blocking over night at hot standby (T <sub>cool</sub> = 160 °C)
16.04.2020	Formation of the catalyst (day 3)	Benchmark conditions at 50 bar; Time on stream added: 6:05 h; N <sub>2</sub> -blocking of the miniplant; Ramp-down to cold standby
17.04.2020 - 05.05.2020	Replacement of the process control valve; infrastructure measures in laboratory	N <sub>2</sub> -blocking of the miniplant
06.05.2020	Formation of the catalyst (day 4)	Benchmark conditions at 50 bar; Time on stream added: 7:15 h; N <sub>2</sub> -blocking over night at hot standby (T <sub>cool</sub> = 160 °C)
07.05.2020	Formation of the catalyst (day 5)	Benchmark conditions at 50 bar; Time on stream added: 6:00 h; N <sub>2</sub> -blocking over night at hot standby (T <sub>cool</sub> = 160 °C)

Date	Activity	Comment
08.05.2020	Formation of the catalyst (day 6)	Benchmark conditions at 50 bar; Time on stream added: 6:20 h; N <sub>2</sub> -blocking of the miniplant; Ramp-down to cold standby
12.05.2020	Formation of the catalyst (day 7)	Benchmark conditions at 50 bar; Time on stream added: 4:48 h; N <sub>2</sub> -blocking over night at hot standby (T <sub>cool</sub> = 160 °C)
13.05.2020	Formation of the catalyst (day 8)	Benchmark conditions at 50 bar; Time on stream added: 5:10 h; N <sub>2</sub> -blocking over night at hot standby (T <sub>cool</sub> = 160 °C)
14.05.2020	Formation of the catalyst (day 9)	Benchmark conditions at 50 bar; Time on stream added: 4:40 h; N <sub>2</sub> -blocking of the miniplant; Ramp-down to cold standby
19.05.2020	Formation of the catalyst (day 10)	Benchmark conditions at 50 bar; Time on stream added: 5:10 h; <b>Leakage of the fiber optic temperature sensor detected at the end of the experiment;</b> N <sub>2</sub> -blocking of the miniplant; Ramp-down to cold standby
20.05.2020 - 17.06.2020	Repair of a leakage in the thermo sensor	Reactor flushed with N <sub>2</sub> permanently; Sensor was fixed by tungsten inert gas welding without removal of the catalyst bed
18.06.2020	Leakage testing of the miniplant	Pressure tested at 85 bar
19.06.2020	Parameter variation at 50 bar; T <sub>cool</sub> = 240 °C	N <sub>2</sub> -blocking over night at hot standby (T <sub>cool</sub> = 160 °C)
22.06.2020	Parameter variation at 65 bar; T <sub>cool</sub> = 240 °C	N <sub>2</sub> -blocking over night at hot standby (T <sub>cool</sub> = 160 °C)
23.06.2020	Parameter variation at 80 bar; T <sub>cool</sub> = 240 °C	<b>Experiment was canceled due to a leakage in H<sub>2</sub> gas dosing MFC;</b> <b>Emergency stop;</b> N <sub>2</sub> -blocking of the miniplant; Ramp down to cold standby

Date	Activity	Comment
24.06.2020 - 20.08.2020	Repair of the broken MFC by the manufacturer; replacement of the sealings of the other MFCs	N <sub>2</sub> -blocking of the miniplant
21.08.2020 - 25.08.2020	Leakage testing of the miniplant and commissioning	Pressure tested at 85 bar
26.08.2020	Parameter variation at 80 bar; T <sub>cool</sub> = 240 °C	N <sub>2</sub> -blocking over night at hot standby (T <sub>cool</sub> = 160 °C)
27.08.2020	Parameter variation at COR = 0.98 at the pressure levels 50 bar, 65 bar, 80 bar and T <sub>cool</sub> = 240 °C	N <sub>2</sub> -blocking of the miniplant Ramp-down to cold standby
02.09.2020	Parameter variation at 50 bar; T <sub>cool</sub> = 220 °C	N <sub>2</sub> -blocking over night at hot standby (T <sub>cool</sub> = 160 °C)
03.09.2020	Benchmark conditions at 50 bar	Time on stream added: 5:40 h N <sub>2</sub> -blocking of the miniplant; Ramp-down to cold standby
07.09.2020	Benchmark conditions	Time on stream added: 5:40 h; N <sub>2</sub> -blocking of the miniplant; Ramp-down to cold standby

## A.13 Experimental data obtained from the miniplant experiments

Table A.5: Experimental data obtained during the steady state experiments at the miniplant setup.

N <sub>data pt</sub>	Feed composition			Reactor conditions			Product composition				Hot spot	
	COR	SN	GHSV	TI01	TI02	p	y <sub>CO</sub>	y <sub>CO2</sub>	y <sub>MeOH</sub>	y <sub>H2O</sub>	T <sub>hs</sub>	z <sub>hs</sub>
[-]	[-]	[-]	[h <sup>-1</sup> ]	[°C]	[°C]	[bar]	[mol-%]	[mol-%]	[mol-%]	[mol-%]	[°C]	[m]
1	0.9	8	12,105	240.8	242.3	50	1.27%	5.73%	3.90%	4.36%	251.8	0.057
2	0.9	7	12,105	240.9	242.3	50	1.43%	6.74%	3.96%	4.44%	251.9	0.060
3	0.9	7	9,079	241.0	242.3	50	1.22%	6.54%	4.50%	4.78%	252.6	0.060
4	0.9	6	12,105	240.8	242.2	50	1.63%	7.98%	4.01%	4.59%	251.9	0.057
5	0.9	6	9,079	240.9	242.2	50	1.41%	7.86%	4.60%	4.94%	252.7	0.057
6	0.9	5	12,105	240.8	242.2	50	1.89%	9.69%	4.06%	4.68%	252.0	0.060
7	0.9	5	9,079	241.0	242.2	50	1.64%	9.52%	4.69%	5.03%	252.7	0.057
8	0.9	5	6,053	241.1	242.2	50	1.38%	9.32%	5.47%	5.53%	254.2	0.055
9	0.9	4	12,105	240.9	242.2	50	2.22%	11.94%	4.07%	4.76%	252.1	0.060
10	0.9	4	9,079	241.0	242.2	50	1.95%	11.98%	4.75%	5.14%	252.8	0.057
11	0.9	4	6,053	241.0	242.2	50	1.64%	11.81%	5.61%	5.65%	254.0	0.055
12	0.9	3	12,105	240.9	242.2	50	2.71%	15.42%	4.04%	4.81%	252.0	0.060
13	0.9	3	9,079	240.9	242.2	50	2.38%	15.38%	4.73%	5.15%	252.5	0.057
14	0.9	3	6,053	241.0	242.2	50	2.00%	15.25%	5.68%	5.71%	253.6	0.055
15	0.9	2	12,105	240.9	242.2	50	3.39%	20.35%	3.90%	4.75%	251.7	0.060
16	0.9	2	9,079	241.0	242.2	50	3.04%	20.58%	4.61%	5.08%	252.4	0.060
17	0.8	8	12,105	241.1	242.2	50	1.40%	5.39%	4.33%	3.79%	252.5	0.094
18	0.8	8	6,053	241.1	242.2	50	1.00%	5.00%	5.45%	4.47%	256.9	0.088
19	0.8	7	12,105	241.0	242.2	50	1.61%	6.33%	4.46%	3.87%	252.6	0.088
20	0.8	7	9,079	241.1	242.2	50	1.34%	6.23%	5.08%	4.22%	254.5	0.060
21	0.8	7	6,053	241.2	242.2	50	1.12%	5.86%	5.71%	4.57%	257.4	0.091
22	0.8	6	12,105	241.0	242.2	50	1.87%	7.51%	4.57%	3.92%	252.7	0.094
23	0.8	6	9,079	241.1	242.2	50	1.57%	7.41%	5.27%	4.29%	254.7	0.060
24	0.8	5	12,105	241.1	242.2	50	2.20%	9.02%	4.68%	3.96%	252.9	0.088
25	0.8	5	9,079	241.1	242.2	50	1.85%	9.00%	5.45%	4.36%	254.9	0.088
26	0.8	5	6,053	241.2	242.2	50	1.52%	8.77%	6.29%	4.82%	257.9	0.094
27	0.8	4	12,105	240.8	242.2	50	2.71%	11.39%	4.75%	3.98%	252.7	0.088
28	0.8	4	9,079	241.1	242.2	50	2.27%	11.35%	5.61%	4.35%	254.9	0.088
29	0.8	4	6,053	241.2	242.2	50	1.85%	11.19%	6.60%	4.87%	258.1	0.101
30	0.8	3	12,105	240.9	242.2	50	3.44%	14.58%	4.79%	3.93%	252.8	0.088
31	0.8	3	6,053	241.1	242.2	50	2.33%	14.49%	6.86%	4.83%	258.2	0.101
32	0.8	2	12,105	241.0	242.2	50	4.60%	19.59%	4.72%	3.72%	252.7	0.101
33	0.8	2	9,079	241.1	242.2	50	3.92%	19.87%	5.73%	4.07%	254.6	0.101

Pt. No.	Feed composition			Reactor conditions			Product composition				Hot spot	
	COR	SN	GHSV	TI01	TI02	p	y <sub>CO</sub>	y <sub>CO2</sub>	y <sub>MeOH</sub>	y <sub>H2O</sub>	T <sub>hs</sub>	z <sub>hs</sub>
[-]	[-]	[-]	[h <sup>-1</sup> ]	[°C]	[°C]	[bar]	[mol-%]	[mol-%]	[mol-%]	[mol-%]	[°C]	[m]
34	0.8	2	6,053	241.2	242.2	50	3.15%	20.01%	7.03%	4.53%	258.1	0.101
35	0.7	8	12,105	240.9	242.2	50	1.52%	4.94%	4.90%	3.30%	254.9	0.187
36	0.7	8	6,053	241.0	242.2	50	1.14%	3.98%	5.59%	3.35%	260.1	0.125
37	0.7	7	12,105	241.2	242.2	50	1.07%	4.65%	6.04%	3.91%	263.4	0.101
38	0.7	7	6,053	241.1	242.2	50	1.21%	5.46%	6.40%	4.00%	255.5	0.190
39	0.7	6	12,105	241.2	242.2	50	2.07%	6.90%	5.33%	3.42%	255.6	0.190
40	0.7	6	9,079	240.9	242.2	50	1.70%	6.80%	6.11%	3.73%	259.6	0.125
41	0.7	6	6,053	241.2	242.2	50	1.41%	6.59%	6.80%	4.12%	264.8	0.101
42	0.7	5	12,105	241.2	242.2	50	2.52%	8.39%	5.54%	3.41%	255.8	0.187
43	0.7	5	9,079	240.9	242.2	50	2.06%	8.35%	6.41%	3.75%	260.0	0.125
44	0.7	4	9,079	241.0	242.2	50	2.57%	10.52%	6.76%	3.71%	260.9	0.190
45	0.7	3	12,105	241.2	242.2	50	4.20%	13.63%	5.94%	3.23%	256.1	0.190
46	0.7	3	9,079	241.0	242.2	50	3.05%	12.22%	7.16%	3.56%	262.5	0.187
47	0.7	3	6,053	241.1	242.2	50	2.68%	13.80%	8.36%	3.94%	268.3	0.122
48	0.7	2	12,105	241.2	242.2	50	5.91%	18.52%	6.03%	2.95%	255.7	0.190
49	0.7	2	9,079	240.8	242.2	50	4.85%	18.93%	7.47%	3.25%	261.5	0.190
50	0.7	2	6,053	241.1	242.2	50	3.82%	19.24%	8.89%	3.53%	269.0	0.122
51	0.95	8	12,105	241.2	242.2	50	1.21%	5.99%	3.70%	4.63%	251.6	0.057
52	0.95	8	9,079	240.8	242.2	50	1.06%	5.78%	4.16%	4.93%	252.0	0.052
53	0.95	8	6,053	240.9	242.2	50	0.91%	5.52%	4.69%	5.33%	252.3	0.052
54	0.95	7	12,105	240.8	242.2	50	1.34%	6.91%	3.71%	4.77%	251.5	0.057
55	0.95	7	9,079	241.0	242.2	50	1.16%	6.69%	4.22%	5.08%	252.2	0.052
56	0.95	6	12,105	240.8	242.2	50	1.52%	8.20%	3.76%	4.92%	251.5	0.057
57	0.95	6	9,079	241.0	242.2	50	1.33%	8.06%	4.30%	5.27%	252.1	0.052
58	0.95	5	12,105	240.7	242.2	50	1.76%	9.96%	3.78%	5.07%	251.7	0.060
59	0.95	5	9,079	240.9	242.2	50	1.54%	9.89%	4.35%	5.43%	252.2	0.052
60	0.95	5	6,053	240.7	242.2	50	1.32%	9.60%	5.09%	5.90%	252.3	0.052
61	0.95	4	12,105	240.9	242.2	50	2.03%	12.25%	3.76%	5.17%	251.7	0.057
62	0.95	4	9,079	240.9	242.2	50	1.81%	12.15%	4.37%	5.56%	252.0	0.052
63	0.95	4	6,053	240.8	242.2	50	1.55%	12.03%	5.17%	6.08%	252.2	0.052
64	0.95	3	12,105	240.8	242.2	50	2.39%	15.73%	3.70%	5.29%	251.5	0.057
65	0.95	3	9,079	240.9	242.2	50	2.16%	15.60%	4.30%	5.64%	252.0	0.052
66	0.95	3	6,053	240.7	242.2	50	1.85%	15.54%	5.16%	6.17%	252.1	0.052
67	0.95	2	12,105	240.9	242.2	50	2.89%	20.70%	3.56%	5.34%	251.2	0.057
68	0.95	2	9,079	240.9	242.2	50	2.66%	20.84%	4.15%	5.71%	251.6	0.052
69	0.9	8	12,105	241.6	242.2	65	0.81%	4.99%	5.58%	5.55%	257.7	0.052
70	0.9	8	9,079	241.7	242.4	65	0.80%	4.93%	5.55%	5.58%	257.8	0.052
71	0.9	7	12,105	241.5	242.3	65	1.10%	6.25%	5.06%	5.28%	255.9	0.055

Pt. No.	Feed composition			Reactor conditions			Product composition				Hot spot	
	COR	SN	GHSV	TI01	TI02	p	y <sub>CO</sub>	y <sub>CO2</sub>	y <sub>MeOH</sub>	y <sub>H2O</sub>	T <sub>hs</sub>	z <sub>hs</sub>
[-]	[-]	[-]	[h <sup>-1</sup> ]	[°C]	[°C]	[bar]	[mol-%]	[mol-%]	[mol-%]	[mol-%]	[°C]	[m]
72	0.9	7	9,079	241.4	242.3	65	0.91%	5.91%	5.72%	5.74%	257.7	0.052
73	0.9	7	6,053	241.7	242.2	65	0.77%	5.67%	6.33%	5.85%	259.6	0.052
74	0.9	6	12,105	241.3	242.3	65	1.27%	7.42%	5.14%	5.42%	255.8	0.055
75	0.9	6	9,079	241.5	242.2	65	1.06%	7.19%	5.89%	5.91%	257.8	0.052
76	0.9	6	6,053	241.7	242.3	65	0.88%	6.92%	6.60%	6.09%	259.7	0.052
77	0.9	5	12,105	241.3	242.2	65	1.50%	9.11%	5.21%	5.53%	256.0	0.052
78	0.9	5	9,079	241.5	242.2	65	1.26%	8.91%	6.04%	6.10%	257.9	0.055
79	0.9	5	6,053	241.6	242.2	65	1.03%	8.62%	6.91%	6.38%	259.7	0.052
80	0.9	4	12,105	241.3	242.2	65	1.79%	11.49%	5.24%	5.60%	256.0	0.052
81	0.9	4	6,053	241.5	242.2	65	1.25%	11.14%	7.10%	6.35%	259.6	0.052
82	0.9	3	12,105	241.4	242.2	65	2.24%	15.12%	5.21%	5.62%	256.0	0.055
83	0.9	3	9,079	241.4	242.2	65	1.90%	15.02%	6.16%	6.17%	257.6	0.055
84	0.9	3	6,053	241.6	242.2	65	1.53%	14.49%	7.43%	6.92%	259.2	0.052
85	0.9	2	12,105	241.2	242.2	65	2.87%	20.22%	5.06%	5.50%	255.4	0.055
86	0.9	2	9,079	241.4	242.2	65	2.46%	20.35%	6.03%	6.00%	257.2	0.052
87	0.8	8	12,105	241.3	242.2	65	1.01%	4.82%	5.50%	4.65%	257.1	0.055
88	0.8	8	6,053	241.6	242.2	65	0.71%	4.30%	6.64%	5.41%	264.7	0.099
89	0.8	7	12,105	241.3	242.2	65	1.16%	5.73%	5.71%	4.73%	257.3	0.125
90	0.8	7	9,079	241.5	242.2	65	0.95%	5.47%	6.40%	5.19%	260.9	0.125
91	0.8	7	6,053	241.6	242.2	65	0.80%	5.20%	6.96%	5.40%	265.9	0.099
92	0.8	6	12,105	241.2	242.2	65	1.38%	6.97%	5.92%	4.80%	257.5	0.127
93	0.8	6	9,079	241.5	242.2	65	1.12%	6.71%	6.68%	5.31%	261.1	0.125
94	0.8	5	9,079	241.4	242.2	65	1.34%	8.32%	6.97%	5.37%	261.2	0.125
95	0.8	4	12,105	241.3	242.2	65	2.04%	10.99%	6.23%	4.90%	257.7	0.091
96	0.8	4	9,079	241.4	242.2	65	1.66%	10.79%	7.26%	5.45%	261.3	0.125
97	0.8	4	6,053	241.8	242.2	65	1.34%	10.54%	8.24%	5.67%	267.3	0.122
98	0.8	3	12,105	241.2	242.2	65	2.65%	14.19%	6.35%	4.78%	257.7	0.091
99	0.8	3	6,053	241.7	242.2	65	1.70%	14.02%	8.63%	5.57%	268.4	0.122
100	0.8	2	12,105	241.1	242.2	65	3.62%	19.59%	6.37%	4.56%	257.3	0.091
101	0.8	2	9,079	241.3	242.2	65	2.92%	19.73%	7.68%	4.97%	260.8	0.125
102	0.8	2	6,053	241.6	242.2	65	2.30%	19.78%	9.03%	5.48%	268.4	0.125
103	0.7	8	12,105	241.2	242.2	65	1.02%	4.34%	6.22%	4.22%	262.1	0.125
104	0.7	8	9,079	241.4	242.2	65	0.84%	4.12%	6.78%	4.50%	268.6	0.125
105	0.7	8	6,053	241.7	242.2	65	0.73%	3.95%	7.21%	4.80%	272.8	0.099
106	0.7	7	12,105	241.0	242.2	65	1.19%	5.21%	6.54%	4.25%	262.9	0.127
107	0.7	7	6,053	241.5	242.2	65	0.84%	4.78%	7.74%	4.85%	274.4	0.099
108	0.7	6	12,105	241.1	242.2	65	1.41%	6.38%	6.87%	4.33%	263.5	0.187
109	0.7	6	9,079	241.4	242.2	65	1.16%	6.11%	7.65%	4.67%	270.9	0.125

Pt. No.	Feed composition			Reactor conditions			Product composition				Hot spot	
	COR	SN	GHSV	TI01	TI02	p	y <sub>CO</sub>	y <sub>CO2</sub>	y <sub>MeOH</sub>	y <sub>H2O</sub>	T <sub>hs</sub>	z <sub>hs</sub>
[-]	[-]	[-]	[h <sup>-1</sup> ]	[°C]	[°C]	[bar]	[mol-%]	[mol-%]	[mol-%]	[mol-%]	[°C]	[m]
110	0.7	6	6,053	241.7	242.2	65	0.98%	5.88%	8.25%	5.00%	276.0	0.099
111	0.7	5	12,105	241.2	242.2	65	1.71%	7.85%	7.27%	4.30%	264.0	0.195
112	0.7	5	9,079	241.4	242.2	65	1.41%	7.71%	8.14%	4.69%	271.6	0.125
113	0.7	5	6,053	241.7	242.2	65	1.16%	7.49%	8.86%	5.15%	277.4	0.099
114	0.7	4	9,079	241.4	242.2	65	1.75%	10.00%	8.70%	4.79%	272.4	0.125
115	0.7	3	12,105	241.3	242.2	65	2.89%	13.46%	8.14%	4.10%	266.2	0.195
116	0.7	3	9,079	241.6	242.2	65	2.31%	13.35%	9.31%	4.60%	273.9	0.125
117	0.7	3	6,053	241.9	242.2	65	1.87%	13.21%	10.29%	4.97%	281.0	0.101
118	0.7	2	12,105	241.3	242.2	65	4.18%	18.74%	8.57%	3.78%	266.3	0.195
119	0.7	2	9,079	241.8	242.2	65	3.32%	18.95%	9.93%	4.18%	274.2	0.127
120	0.7	2	6,053	241.9	242.2	65	2.68%	19.12%	11.07%	4.54%	282.6	0.125
121	0.95	8	12,105	240.7	242.2	65	0.94%	5.44%	4.66%	5.36%	254.5	0.052
122	0.95	8	9,079	240.9	242.2	65	0.80%	5.17%	5.23%	5.79%	255.8	0.052
123	0.95	8	6,053	241.0	242.2	65	0.68%	4.91%	5.81%	5.98%	256.6	0.049
124	0.95	7	12,105	240.6	242.2	65	1.08%	6.43%	4.69%	5.54%	254.3	0.055
125	0.95	7	9,079	240.9	242.2	65	0.91%	6.19%	5.34%	5.96%	255.8	0.052
126	0.95	7	6,053	241.0	242.2	65	0.77%	5.90%	6.00%	6.13%	256.5	0.049
127	0.95	6	9,079	240.8	242.2	65	1.08%	7.58%	5.48%	6.17%	255.7	0.052
128	0.95	5	12,105	240.7	242.2	65	1.45%	9.56%	4.78%	5.82%	254.8	0.052
129	0.95	5	9,079	240.9	242.2	65	1.23%	9.20%	5.54%	6.37%	256.0	0.052
130	0.95	5	6,053	241.0	242.2	65	1.02%	8.85%	6.43%	6.68%	256.5	0.049
131	0.95	4	12,105	240.7	242.2	65	1.71%	11.86%	4.76%	5.93%	254.7	0.052
132	0.95	4	6,053	241.0	242.2	65	1.22%	11.43%	6.57%	6.91%	256.4	0.049
133	0.95	3	12,105	240.6	242.2	65	2.07%	15.35%	4.69%	6.01%	254.4	0.055
134	0.95	3	9,079	240.7	242.2	65	1.80%	15.20%	5.50%	6.46%	255.6	0.052
135	0.95	3	6,053	241.0	242.2	65	1.49%	15.12%	6.58%	6.89%	256.0	0.049
136	0.95	2	12,105	240.6	242.2	65	2.57%	20.52%	4.49%	6.03%	254.1	0.055
137	0.95	2	9,079	240.9	242.2	65	2.25%	20.46%	5.30%	6.53%	255.0	0.052
138	0.9	8	12,105	240.8	242.2	80	0.75%	4.76%	5.91%	5.90%	258.9	0.055
139	0.9	8	9,079	240.9	242.2	80	0.63%	4.41%	6.55%	6.32%	261.1	0.094
140	0.9	8	6,053	240.8	242.2	80	0.53%	4.12%	7.00%	6.25%	264.8	0.094
141	0.9	7	12,105	240.8	242.2	80	0.87%	5.65%	6.05%	6.09%	258.8	0.055
142	0.9	7	9,079	240.9	242.2	80	0.72%	5.33%	6.83%	6.72%	261.0	0.055
143	0.9	7	6,053	240.7	242.2	80	0.61%	4.94%	7.54%	6.94%	264.7	0.094
144	0.9	6	12,105	240.9	242.2	80	1.02%	7.01%	6.18%	6.25%	259.0	0.055
145	0.9	6	9,079	240.9	242.2	80	0.85%	6.62%	6.93%	6.49%	261.1	0.055
146	0.9	6	6,053	240.8	242.2	80	0.70%	6.23%	7.56%	6.48%	264.2	0.094
147	0.9	5	12,105	241.0	242.2	80	1.23%	8.66%	6.23%	6.44%	259.1	0.055

Pt. No.	Feed composition			Reactor conditions			Product composition				Hot spot	
	COR	SN	GHSV	TI01	TI02	p	y <sub>CO</sub>	y <sub>CO2</sub>	y <sub>MeOH</sub>	y <sub>H2O</sub>	T <sub>hs</sub>	z <sub>hs</sub>
[-]	[-]	[-]	[h <sup>-1</sup> ]	[°C]	[°C]	[bar]	[mol-%]	[mol-%]	[mol-%]	[mol-%]	[°C]	[m]
148	0.9	5	9,079	241.0	242.2	80	1.01%	8.22%	7.17%	7.06%	261.1	0.055
149	0.9	5	6,053	240.9	242.2	80	0.84%	7.99%	7.93%	6.58%	264.0	0.094
150	0.9	4	12,105	240.8	242.3	80	1.50%	11.07%	6.27%	6.44%	259.1	0.055
151	0.9	4	9,079	241.1	242.3	80	1.23%	10.80%	7.30%	7.03%	261.2	0.055
152	0.9	4	6,053	240.9	242.3	80	1.01%	10.30%	8.53%	7.77%	263.8	0.055
153	0.9	3	12,105	240.8	242.3	80	1.91%	14.50%	6.26%	6.37%	259.1	0.055
154	0.9	3	9,079	241.0	242.3	80	1.56%	14.24%	7.37%	6.84%	261.1	0.055
155	0.9	3	6,053	240.9	242.2	80	1.26%	14.01%	8.53%	7.32%	263.3	0.055
156	0.9	2	12,105	240.7	242.2	80	2.49%	19.97%	6.04%	6.21%	258.6	0.055
157	0.9	2	9,079	240.9	242.2	80	2.08%	19.96%	7.21%	6.82%	260.5	0.055
158	0.9	2	6,053	241.0	242.2	80	1.67%	19.93%	8.56%	7.14%	262.0	0.055
159	0.8	8	12,105	241.3	242.2	80	0.77%	4.30%	6.46%	5.38%	262.5	0.099
160	0.8	8	6,053	241.2	242.2	80	0.54%	3.74%	7.52%	5.77%	273.7	0.094
161	0.8	7	12,105	241.4	242.2	80	0.89%	5.18%	6.73%	5.50%	263.3	0.094
162	0.8	7	9,079	241.3	242.2	80	0.74%	4.87%	7.48%	5.85%	268.5	0.099
163	0.8	7	6,053	241.2	242.2	80	0.62%	4.60%	7.99%	5.99%	275.1	0.094
164	0.8	6	12,105	241.5	242.2	80	1.06%	6.46%	7.02%	5.66%	263.7	0.094
165	0.8	6	9,079	241.5	242.2	80	0.86%	6.06%	7.85%	6.05%	269.3	0.127
166	0.8	6	6,053	241.3	242.2	80	0.71%	5.68%	8.51%	6.46%	276.0	0.094
167	0.8	5	9,079	241.5	242.2	80	1.05%	7.74%	8.22%	6.18%	269.6	0.127
168	0.8	5	6,053	241.5	242.2	80	0.87%	7.41%	8.95%	6.26%	277.5	0.094
169	0.8	4	12,105	241.4	242.2	80	1.60%	10.44%	7.55%	5.76%	263.8	0.094
170	0.8	4	9,079	241.5	242.2	80	1.29%	10.10%	8.66%	6.33%	269.7	0.127
171	0.8	4	6,053	241.5	242.2	80	1.07%	9.77%	9.54%	6.77%	278.3	0.094
172	0.8	3	12,105	241.4	242.2	80	2.09%	13.68%	7.73%	5.61%	263.8	0.094
173	0.8	3	6,053	241.5	242.2	80	1.35%	13.31%	10.42%	7.13%	278.8	0.094
174	0.8	2	12,105	241.4	242.2	80	2.94%	19.30%	7.76%	5.19%	263.3	0.094
175	0.8	2	9,079	241.5	242.2	80	2.32%	19.34%	9.18%	5.85%	268.9	0.127
176	0.8	2	6,053	241.5	242.2	80	1.83%	19.06%	10.92%	7.19%	278.6	0.099
177	0.7	8	12,105	241.6	242.2	80	0.74%	3.81%	7.21%	4.93%	270.9	0.153
178	0.7	7	12,105	241.6	242.2	80	0.87%	4.65%	7.64%	4.98%	272.8	0.153
179	0.7	7	6,053	241.4	242.2	80	0.64%	4.12%	8.72%	5.52%	285.3	0.094
180	0.7	6	12,105	241.8	242.2	80	1.04%	5.77%	8.12%	5.08%	274.4	0.153
181	0.7	6	9,079	241.7	242.2	80	0.87%	5.52%	8.83%	5.49%	281.7	0.127
182	0.7	6	6,053	241.5	242.2	80	0.74%	5.19%	9.27%	5.58%	287.1	0.094
183	0.7	5	12,105	241.7	242.2	80	1.29%	7.31%	8.63%	5.20%	275.7	0.153
184	0.7	5	9,079	241.8	242.2	80	1.06%	7.07%	9.44%	5.65%	283.6	0.127
185	0.7	5	6,053	241.7	242.2	80	0.90%	6.72%	10.27%	6.17%	289.7	0.094

Pt. No.	Feed composition			Reactor conditions			Product composition				Hot spot	
	COR	SN	GHSV	TI01	TI02	p	y <sub>CO</sub>	y <sub>CO2</sub>	y <sub>MeOH</sub>	y <sub>H2O</sub>	T <sub>hs</sub>	z <sub>hs</sub>
[-]	[-]	[-]	[h <sup>-1</sup> ]	[°C]	[°C]	[bar]	[mol-%]	[mol-%]	[mol-%]	[mol-%]	[°C]	[m]
186	0.7	4	9,079	241.8	242.2	80	1.33%	9.23%	10.08%	5.67%	285.7	0.127
187	0.7	3	12,105	241.7	242.2	80	2.18%	12.95%	9.81%	5.04%	278.1	0.153
188	0.7	3	9,079	242.0	242.2	80	1.77%	12.84%	10.87%	5.58%	287.4	0.127
189	0.7	2	12,105	241.5	242.2	80	3.15%	18.55%	10.41%	4.57%	278.2	0.198
190	0.95	8	12,105	241.0	242.2	80	0.79%	5.01%	5.39%	5.97%	257.3	0.055
191	0.95	8	9,079	240.6	242.2	80	0.65%	4.68%	6.09%	6.51%	258.1	0.052
192	0.95	8	6,053	241.0	242.2	80	0.55%	4.31%	6.77%	6.84%	259.5	0.055
193	0.95	7	12,105	240.9	242.2	80	0.91%	6.07%	5.46%	6.20%	257.1	0.055
194	0.95	7	9,079	240.6	242.2	80	0.75%	5.64%	6.21%	6.51%	258.0	0.052
195	0.95	7	6,053	240.8	242.2	80	0.62%	5.24%	6.87%	6.48%	259.3	0.055
196	0.95	6	9,079	240.8	242.2	80	0.88%	6.95%	6.38%	6.98%	258.0	0.052
197	0.95	5	12,105	240.7	242.2	80	1.25%	9.01%	5.56%	6.49%	257.4	0.055
198	0.95	5	9,079	240.6	242.2	80	1.05%	8.72%	6.45%	6.95%	258.2	0.052
199	0.95	5	6,053	240.8	242.2	80	0.84%	8.23%	7.49%	7.45%	259.1	0.052
200	0.95	4	12,105	240.7	242.2	80	1.51%	11.51%	5.54%	6.61%	257.3	0.055
201	0.95	4	6,053	240.5	242.2	80	1.01%	10.72%	7.83%	8.01%	258.8	0.036
202	0.95	3	12,105	240.6	242.2	80	1.85%	15.10%	5.45%	6.72%	257.1	0.055
203	0.95	3	9,079	240.5	242.2	80	1.57%	14.71%	6.42%	7.07%	257.8	0.052
204	0.95	3	6,053	240.6	242.2	80	1.27%	14.40%	7.71%	7.62%	258.3	0.036
205	0.95	2	12,105	240.5	242.2	80	2.34%	20.18%	5.19%	6.55%	256.6	0.055
206	0.95	2	9,079	240.3	242.2	80	2.00%	20.20%	6.18%	7.12%	257.3	0.055
207	0.98	8	12,105	240.3	242.2	50	1.24%	6.21%	3.27%	4.63%	250.7	0.055
208	0.98	8	9,079	240.2	242.2	50	1.10%	6.08%	3.75%	4.92%	250.9	0.052
209	0.98	8	6,053	240.2	242.2	50	0.92%	5.70%	4.33%	5.36%	251.5	0.036
210	0.98	7	12,105	240.1	242.2	50	1.40%	7.20%	3.28%	4.77%	250.5	0.055
211	0.98	7	9,079	240.2	242.2	50	1.23%	7.02%	3.77%	5.10%	250.9	0.052
212	0.98	7	6,053	240.3	242.2	50	1.03%	6.71%	4.42%	5.55%	251.7	0.036
213	0.98	6	9,079	240.2	242.2	50	1.39%	8.32%	3.80%	5.24%	250.8	0.052
214	0.98	5	12,105	240.1	242.2	50	1.76%	10.19%	3.30%	5.08%	250.5	0.055
215	0.98	5	9,079	240.2	242.2	50	1.58%	10.10%	3.83%	5.40%	251.0	0.052
216	0.98	5	6,053	240.2	242.2	50	1.34%	9.88%	4.58%	5.95%	251.8	0.034
217	0.98	4	12,105	240.0	242.2	50	2.01%	12.59%	3.28%	5.25%	250.5	0.052
218	0.98	4	6,053	240.2	242.2	50	1.56%	12.14%	4.61%	6.12%	251.8	0.034
219	0.98	3	12,105	240.0	242.2	50	2.32%	15.97%	3.21%	5.42%	250.4	0.055
220	0.98	3	9,079	240.2	242.2	50	2.13%	15.90%	3.74%	5.74%	250.8	0.052
221	0.98	3	6,053	240.1	242.2	50	1.86%	15.80%	4.55%	6.29%	251.4	0.034
222	0.98	2	12,105	240.0	242.2	50	2.70%	21.04%	3.09%	5.53%	250.1	0.055
223	0.98	2	9,079	240.1	242.2	50	2.56%	20.97%	3.57%	5.88%	250.3	0.052

Pt. No.	Feed composition			Reactor conditions			Product composition				Hot spot	
	COR	SN	GHSV	TI01	TI02	p	y <sub>CO</sub>	y <sub>CO2</sub>	y <sub>MeOH</sub>	y <sub>H2O</sub>	T <sub>hs</sub>	z <sub>hs</sub>
[-]	[-]	[-]	[h <sup>-1</sup> ]	[°C]	[°C]	[bar]	[mol-%]	[mol-%]	[mol-%]	[mol-%]	[°C]	[m]
224	0.98	8	12,105	240.3	242.2	65	1.03%	5.75%	4.14%	5.26%	253.3	0.052
225	0.98	8	9,079	240.3	242.2	65	0.87%	5.51%	4.76%	5.73%	253.9	0.052
226	0.98	8	6,053	240.4	242.3	65	0.71%	5.12%	5.50%	6.33%	254.8	0.036
227	0.98	7	12,105	240.3	242.3	65	1.15%	6.83%	4.17%	5.41%	253.3	0.052
228	0.98	7	9,079	240.3	242.3	65	0.98%	6.53%	4.83%	5.90%	253.9	0.052
229	0.98	7	6,053	240.3	242.2	65	0.80%	6.15%	5.66%	6.54%	254.9	0.036
230	0.98	6	9,079	240.4	242.3	65	1.11%	7.77%	4.89%	6.07%	253.9	0.052
231	0.98	5	12,105	240.3	242.2	65	1.50%	9.89%	4.21%	5.75%	253.5	0.052
232	0.98	5	9,079	240.4	242.2	65	1.28%	9.46%	4.94%	6.26%	254.3	0.052
233	0.98	5	6,053	240.4	242.2	65	1.06%	9.09%	5.93%	7.01%	255.0	0.036
234	0.98	4	12,105	240.3	242.2	65	1.74%	12.10%	4.18%	5.90%	253.4	0.052
235	0.98	4	6,053	240.3	242.2	65	1.24%	11.62%	6.00%	7.19%	254.9	0.034
236	0.98	3	12,105	240.2	242.2	65	2.05%	15.62%	4.10%	6.07%	253.3	0.052
237	0.98	3	9,079	240.5	242.2	65	1.81%	15.45%	4.85%	6.57%	254.1	0.052
238	0.98	3	6,053	240.4	242.2	65	1.53%	15.23%	5.95%	7.32%	254.8	0.034
239	0.98	2	12,105	240.2	242.2	65	2.45%	20.42%	3.92%	6.16%	253.0	0.052
240	0.98	2	9,079	240.4	242.2	65	2.23%	20.73%	4.62%	6.65%	253.3	0.052
241	0.98	8	12,105	240.5	242.2	80	0.80%	5.18%	4.95%	6.05%	255.8	0.055
242	0.98	8	9,079	240.7	242.2	80	0.67%	4.86%	5.78%	6.57%	257.2	0.055
243	0.98	8	6,053	240.6	242.2	80	0.55%	4.44%	6.53%	6.86%	257.9	0.036
244	0.98	7	12,105	240.6	242.2	80	0.93%	6.25%	5.10%	6.15%	256.1	0.055
245	0.98	7	9,079	240.7	242.2	80	0.77%	5.86%	5.91%	6.76%	257.2	0.055
246	0.98	7	6,053	240.7	242.2	80	0.62%	5.41%	6.72%	6.84%	258.0	0.036
247	0.98	6	9,079	240.7	242.2	80	0.89%	7.11%	6.01%	6.99%	257.1	0.055
248	0.98	5	12,105	240.6	242.2	80	1.26%	9.29%	5.18%	6.52%	256.6	0.055
249	0.98	5	9,079	240.7	242.2	80	1.05%	8.96%	6.08%	7.07%	257.4	0.055
250	0.98	5	6,053	240.6	242.2	80	0.85%	8.44%	7.19%	7.63%	258.0	0.036
251	0.98	4	12,105	240.5	242.2	80	1.49%	11.67%	5.15%	6.66%	256.5	0.055
252	0.98	4	6,053	240.7	242.2	80	1.01%	10.96%	7.31%	7.82%	258.0	0.036
253	0.98	3	12,105	240.5	242.2	80	1.80%	15.20%	5.03%	6.79%	256.3	0.055
254	0.98	3	9,079	240.5	242.2	80	1.55%	14.85%	5.98%	7.40%	256.9	0.052
255	0.98	2	12,105	240.3	242.2	80	2.23%	20.59%	4.78%	6.82%	255.6	0.052
256	0.98	2	9,079	240.6	242.2	80	1.93%	20.40%	5.69%	7.46%	256.1	0.052
257	0.9	8	12,105	220.2	222.2	50	1.53%	6.75%	2.24%	2.99%	228.6	0.057
258	0.9	8	9,079	220.3	222.2	50	1.42%	6.53%	2.68%	3.31%	229.8	0.055
259	0.9	8	6,053	220.2	222.2	50	1.15%	6.19%	3.44%	3.82%	230.4	0.052
260	0.9	7	12,105	220.2	222.2	50	1.69%	7.81%	2.25%	3.06%	228.6	0.057
261	0.9	7	9,079	220.1	222.2	50	1.57%	7.49%	2.68%	3.39%	229.6	0.055

Pt. No.	Feed composition			Reactor conditions			Product composition				Hot spot	
	COR	SN	GHSV	TI01	TI02	p	y <sub>CO</sub>	y <sub>CO2</sub>	y <sub>MeOH</sub>	y <sub>H2O</sub>	T <sub>hs</sub>	z <sub>hs</sub>
[-]	[-]	[-]	[h <sup>-1</sup> ]	[°C]	[°C]	[bar]	[mol-%]	[mol-%]	[mol-%]	[mol-%]	[°C]	[m]
262	0.9	7	6,053	220.3	222.2	50	1.30%	7.31%	3.49%	3.90%	230.8	0.052
263	0.9	6	12,105	220.3	222.2	50	1.87%	9.07%	2.26%	3.10%	229.1	0.057
264	0.9	6	9,079	220.2	222.2	50	1.79%	8.86%	2.72%	3.47%	229.9	0.057
265	0.9	6	6,053	220.1	222.2	50	1.47%	8.47%	3.52%	3.96%	231.0	0.057
266	0.9	5	12,105	220.1	222.2	50	2.09%	10.78%	2.28%	3.15%	229.1	0.057
267	0.9	5	9,079	220.3	222.2	50	2.02%	10.54%	2.73%	3.52%	230.1	0.055
268	0.9	5	6,053	220.3	222.2	50	1.71%	10.35%	3.55%	4.04%	231.7	0.057
269	0.9	4	12,105	220.2	222.2	50	2.39%	13.00%	2.28%	3.19%	229.3	0.073
270	0.9	4	9,079	220.3	222.2	50	2.31%	12.74%	2.74%	3.56%	230.2	0.057
271	0.9	4	6,053	220.2	222.2	50	2.01%	12.55%	3.57%	4.09%	231.8	0.057
272	0.9	3	12,105	220.2	222.2	50	2.81%	16.44%	2.26%	3.22%	229.5	0.075
273	0.9	3	9,079	220.1	222.1	50	2.73%	16.32%	2.72%	3.60%	230.1	0.060
274	0.9	3	6,053	220.1	222.2	50	2.43%	16.13%	3.54%	4.09%	232.0	0.057
275	0.9	2	12,105	220.0	222.2	50	3.41%	21.28%	2.20%	3.20%	229.3	0.075
276	0.9	2	9,079	220.2	222.1	50	3.33%	21.36%	2.65%	3.56%	230.2	0.057
277	0.9	2	6,053	220.3	222.2	50	3.06%	21.47%	3.47%	4.06%	232.1	0.057
278	0.8	8	12,105	220.1	222.1	50	2.14%	6.29%	2.29%	2.54%	228.3	0.057
279	0.8	8	6,053	220.3	222.2	50	1.38%	5.81%	3.80%	3.26%	230.8	0.057
280	0.8	7	12,105	220.1	222.1	50	2.39%	7.19%	2.32%	2.59%	228.4	0.057
281	0.8	7	9,079	220.2	222.1	50	2.10%	7.03%	2.86%	2.84%	229.6	0.055
282	0.8	7	6,053	220.3	222.1	50	1.58%	6.79%	3.87%	3.30%	231.2	0.057
283	0.8	6	12,105	220.1	222.1	50	2.75%	8.44%	2.34%	2.59%	228.5	0.057
284	0.8	6	9,079	220.3	222.1	50	2.42%	8.17%	2.90%	2.86%	229.7	0.060
285	0.8	6	6,053	220.3	222.2	50	1.85%	8.00%	3.93%	3.32%	231.7	0.057
286	0.8	5	9,079	220.3	222.2	50	2.82%	9.85%	2.92%	2.89%	229.9	0.055
287	0.8	4	12,105	220.2	222.1	50	3.69%	12.12%	2.34%	2.63%	229.0	0.075
288	0.8	4	9,079	220.2	222.1	50	3.38%	11.94%	2.92%	2.88%	230.0	0.060
289	0.8	4	6,053	220.3	222.2	50	2.73%	11.95%	4.03%	3.31%	232.1	0.055
290	0.8	3	12,105	220.0	222.1	50	4.51%	15.30%	2.31%	2.60%	229.0	0.075
291	0.8	3	6,053	220.3	222.2	50	3.43%	15.25%	4.04%	3.23%	232.3	0.055
292	0.8	2	12,105	220.1	222.2	50	5.74%	19.79%	2.24%	2.47%	229.0	0.075
293	0.8	2	9,079	220.1	222.2	50	5.41%	20.05%	2.81%	2.73%	229.8	0.060
294	0.8	2	6,053	220.3	222.1	50	4.59%	20.18%	3.96%	3.08%	232.2	0.055
295	0.7	8	12,105	220.2	222.1	50	2.78%	5.74%	2.39%	2.14%	227.8	0.057
296	0.7	8	9,079	220.2	222.1	50	2.33%	5.47%	3.06%	2.37%	229.2	0.055
297	0.7	7	12,105	220.2	222.1	50	3.17%	6.57%	2.42%	2.16%	228.0	0.057
298	0.7	7	6,053	220.3	222.1	50	1.87%	6.23%	4.39%	2.83%	231.4	0.057
299	0.7	6	12,105	220.1	222.2	50	3.64%	7.51%	2.43%	2.16%	228.1	0.057

Pt. No.	Feed composition			Reactor conditions			Product composition				Hot spot	
	COR [-]	SN [-]	GHSV [h <sup>-1</sup> ]	TI01 [°C]	TI02 [°C]	p [bar]	y <sub>CO</sub> [mol-%]	y <sub>CO2</sub> [mol-%]	y <sub>MeOH</sub> [mol-%]	y <sub>H2O</sub> [mol-%]	T <sub>hs</sub> [°C]	z <sub>hs</sub> [m]
300	0.7	6	9,079	220.4	222.1	50	3.19%	7.48%	3.13%	2.35%	229.5	0.055
301	0.7	6	6,053	220.3	222.1	50	2.27%	7.41%	4.51%	2.80%	231.6	0.057
302	0.7	5	12,105	220.1	222.1	50	4.32%	8.97%	2.43%	2.17%	228.2	0.057
303	0.7	5	9,079	220.3	222.1	50	3.77%	8.94%	3.14%	2.33%	229.6	0.060
304	0.7	5	6,053	220.4	222.1	50	2.77%	8.92%	4.60%	2.76%	231.9	0.057
305	0.7	4	9,079	220.3	222.2	50	4.68%	11.00%	3.13%	2.33%	229.6	0.060
306	0.7	3	12,105	220.1	222.1	50	6.56%	13.70%	2.37%	2.09%	228.5	0.075
307	0.7	2	12,105	220.2	222.1	50	8.66%	18.26%	2.27%	1.98%	228.6	0.078
308	0.95	8	12,105	220.1	222.1	50	1.29%	7.01%	2.22%	3.28%	228.9	0.060
309	0.95	8	9,079	220.3	222.1	50	1.24%	6.81%	2.62%	3.64%	229.7	0.055
310	0.95	8	6,053	220.2	222.2	50	1.07%	6.48%	3.32%	4.15%	230.5	0.055
311	0.95	7	12,105	220.2	222.2	50	1.40%	8.05%	2.22%	3.33%	229.0	0.057
312	0.95	7	9,079	220.2	222.1	50	1.36%	7.77%	2.62%	3.72%	229.7	0.055
313	0.95	7	6,053	220.1	222.1	50	1.18%	7.41%	3.33%	4.24%	230.8	0.057
314	0.95	6	9,079	220.2	222.2	50	1.50%	9.09%	2.63%	3.80%	229.8	0.055
315	0.95	5	12,105	220.1	222.1	50	1.65%	11.14%	2.25%	3.47%	229.1	0.057
316	0.95	5	9,079	220.2	222.1	50	1.66%	10.86%	2.66%	3.89%	230.0	0.057
317	0.95	5	6,053	220.1	222.1	50	1.50%	10.57%	3.38%	4.45%	231.5	0.055
318	0.95	4	12,105	220.1	222.1	50	1.84%	13.43%	2.25%	3.53%	229.2	0.055
319	0.95	4	6,053	220.3	222.1	50	1.73%	12.95%	3.38%	4.56%	231.8	0.055
320	0.95	3	12,105	220.2	222.1	50	2.05%	16.88%	2.23%	3.58%	229.3	0.055
321	0.95	3	9,079	220.2	222.1	50	2.14%	16.56%	2.63%	4.04%	230.4	0.057
322	0.95	3	6,053	220.1	222.1	50	2.01%	16.46%	3.34%	4.63%	231.8	0.055
323	0.95	2	12,105	220.0	222.1	50	2.41%	22.07%	2.18%	3.57%	229.2	0.055
324	0.95	2	9,079	220.2	222.1	50	2.50%	21.77%	2.57%	4.04%	230.2	0.057

## A.14 Mass balances of the miniplant experiments

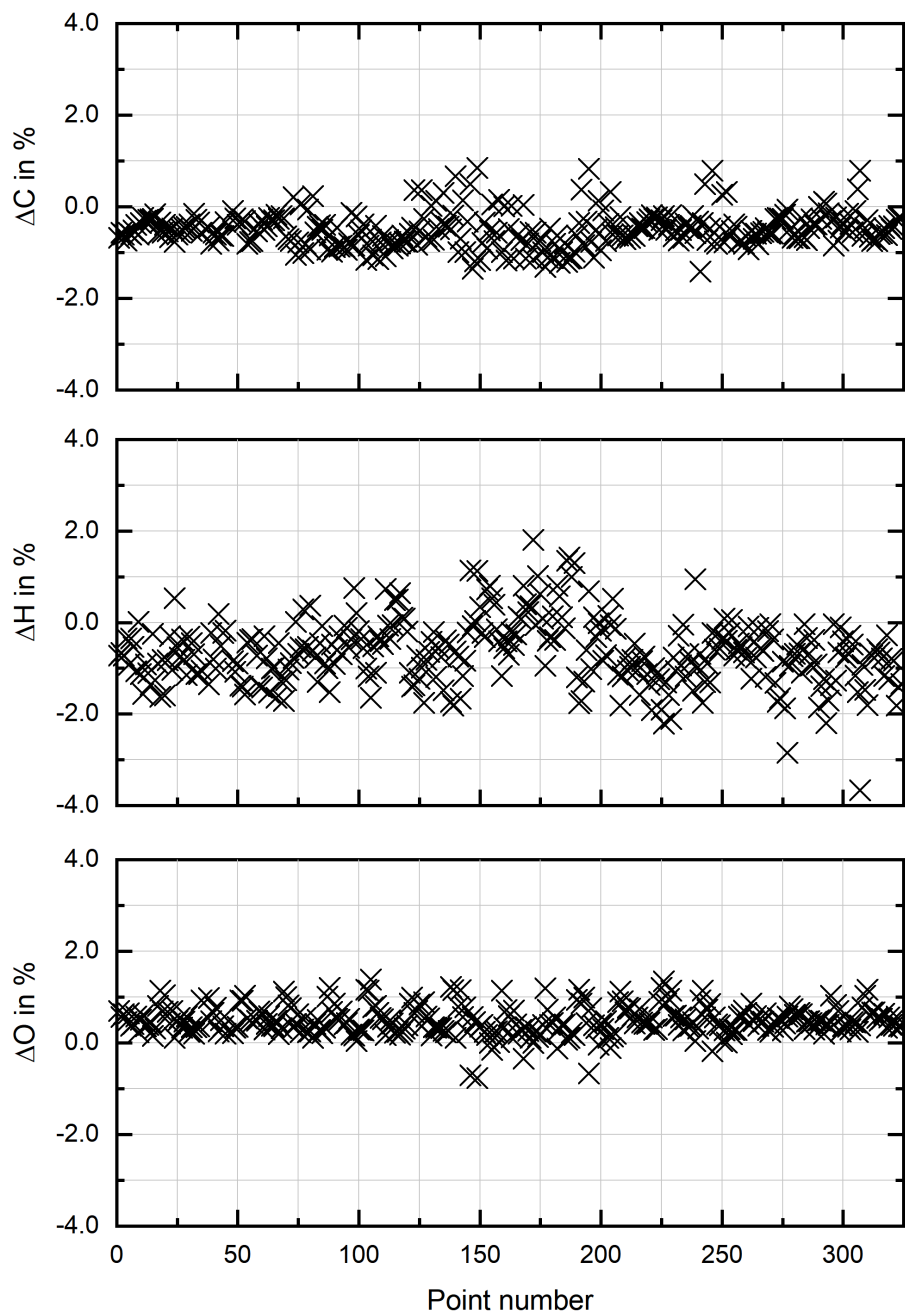


Figure A.11: C-/H-/O- balance of the miniplant experimental points used within this study.

## A.15 Axial deactivation

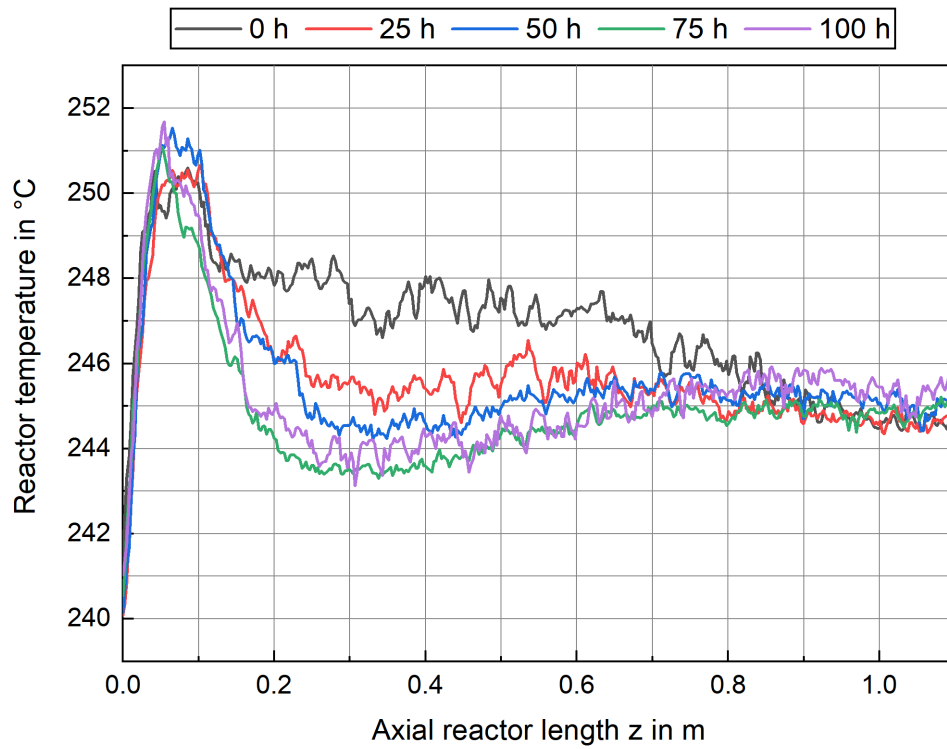


Figure A.12: Temperature profile at benchmark point ( $COR = 0.9$ ;  $SN = 4.0$ ;  $GHSV = 12,000 \text{ h}^{-1}$ ;  $p = 50 \text{ bar}$ ;  $T_{cool} = 240 \text{ °C}$ ) at beginning of the experimental campaign, after 25 h, 50 h, 75 h as well as 100 h.

## A.16 NMR liquid phase measurement

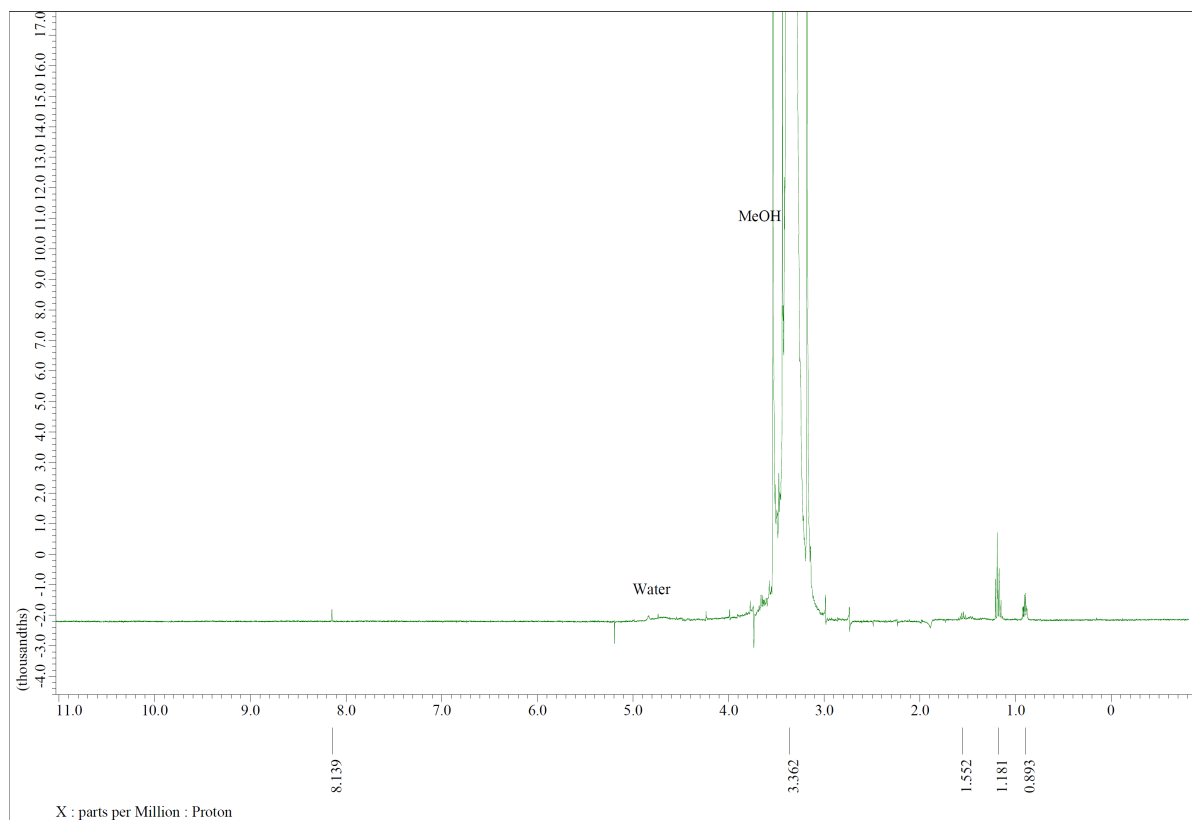


Figure A.13: NMR measurement of a liquid product sample;  $^1\text{H}$  NMR (400 MHz,  $\text{D}_2\text{O}$ ):  $\delta$ /ppm = 8,139 (s,  $\text{HCOOH}$ , traces), 4,8 (s,  $\text{H}_2\text{O}$ ), 3,362 (s,  $\text{CH}_3\text{OH}$ ;  $\text{CH}_3\text{CH}_2\text{OH}$  and  $\text{CH}_3\text{CH}_2\text{CH}_2\text{OH}$  is covered by  $\text{CH}_3\text{OH}$ ), 1,552 (m,  $\text{CH}_3\text{CH}_2\text{CH}_2\text{OH}$ ), 1,181 (t,  $\text{CH}_3\text{CH}_2\text{OH}$ ), 0,893 (t,  $\text{CH}_3\text{CH}_2\text{CH}_2\text{OH}$ ).

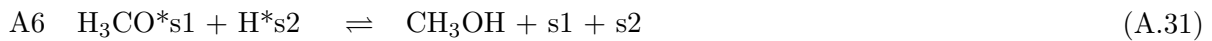
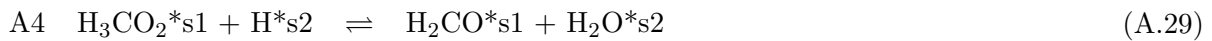
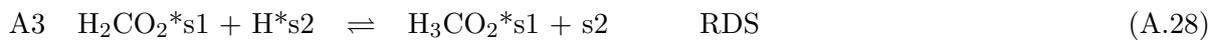
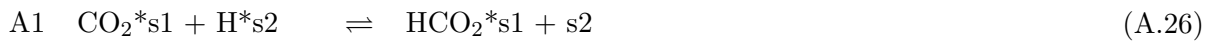
## A.17 Kinetic model by Graaf

Reaction mechanism proposed by Graaf[192]:

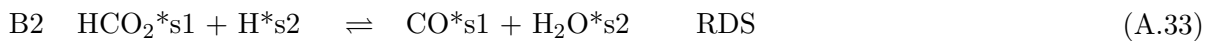
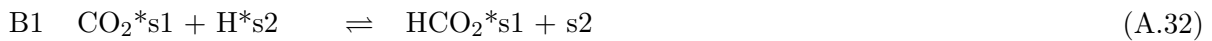
Adsorption of educts



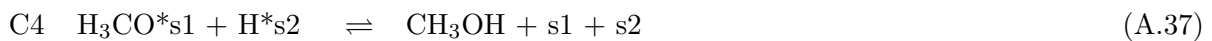
CO<sub>2</sub>-hydrogenation



rWGS



CO-hydrogenation



Rate equations proposed by Graaf[192]:

$$r_{\text{CO}_2} = \frac{k_1 \cdot K_2 \cdot EQ_1}{(1 + K_1 \cdot f_{\text{CO}} + K_2 \cdot f_{\text{CO}_2}) (f_{\text{H}_2}^{0.5} + K_3 \cdot f_{\text{H}_2\text{O}})} \quad (\text{A.38})$$

$$r_{r\text{WGS}} = \frac{k_2 \cdot K_2 \cdot EQ_2}{(1 + K_1 \cdot f_{\text{CO}} + K_2 \cdot f_{\text{CO}_2}) (f_{\text{H}_2}^{0.5} + K_3 \cdot f_{\text{H}_2\text{O}})} \quad (\text{A.39})$$

$$r_{\text{CO}} = \frac{k_3 \cdot K_1 \cdot EQ_3}{(1 + K_1 \cdot f_{\text{CO}} + K_2 \cdot f_{\text{CO}_2}) (f_{\text{H}_2}^{0.5} + K_3 \cdot f_{\text{H}_2\text{O}})} \quad (\text{A.40})$$

Table A.6: Original kinetic parameters proposed by Graaf et al. [193].

	Unit	Parameters
$k_1$	$mol \cdot kg^{-1} \cdot s^{-1} \cdot bar^{-1}$	$1.09 \cdot 10^5 \cdot \exp\left(\frac{-87,500}{R \cdot T}\right)$
$k_2$	$mol \cdot kg^{-1} \cdot s^{-1} \cdot bar^{-0.5}$	$9.64 \cdot 10^{11} \cdot \exp\left(\frac{-152,900}{R \cdot T}\right)$
$k_3$	$mol \cdot kg^{-1} \cdot s^{-1} \cdot bar^{-1}$	$4.89 \cdot 10^7 \cdot \exp\left(\frac{-113,000}{R \cdot T}\right)$
$K_1$	$bar^{-1}$	$2.16 \cdot 10^{-5} \cdot \exp\left(\frac{46,800}{R \cdot T}\right)$
$K_2$	$bar^{-1}$	$7.05 \cdot 10^{-7} \cdot \exp\left(\frac{61,700}{R \cdot T}\right)$
$K_3$	$bar^{-0.5}$	$6.37 \cdot 10^{-9} \cdot \exp\left(\frac{84,000}{R \cdot T}\right)$

Table A.7: Kinetic parameters for the Graaf<sub>fit</sub> model obtained with the miniplant setup.

	Unit	Parameters
$k_1$	$mol \cdot kg^{-1} \cdot s^{-1} \cdot bar^{-1}$	$5.861 \cdot 10^4 \cdot \exp\left(\frac{-62,403}{R \cdot T}\right)$
$k_2$	$mol \cdot kg^{-1} \cdot s^{-1} \cdot bar^{-0.5}$	$3.027 \cdot 10^{11} \cdot \exp\left(\frac{-123,083}{R \cdot T}\right)$
$k_3$	$mol \cdot kg^{-1} \cdot s^{-1} \cdot bar^{-1}$	$-1.459 \cdot 10^8 \cdot \exp\left(\frac{-159,919}{R \cdot T}\right)$
$K_1$	$bar^{-1}$	$6.830 \cdot 10^{-5} \cdot \exp\left(\frac{37,420}{R \cdot T}\right)$
$K_2$	$bar^{-1}$	$8.014 \cdot 10^{-8} \cdot \exp\left(\frac{68,624}{R \cdot T}\right)$
$K_3$	$bar^{-0.5}$	$1.181 \cdot 10^{-8} \cdot \exp\left(\frac{105,009}{R \cdot T}\right)$

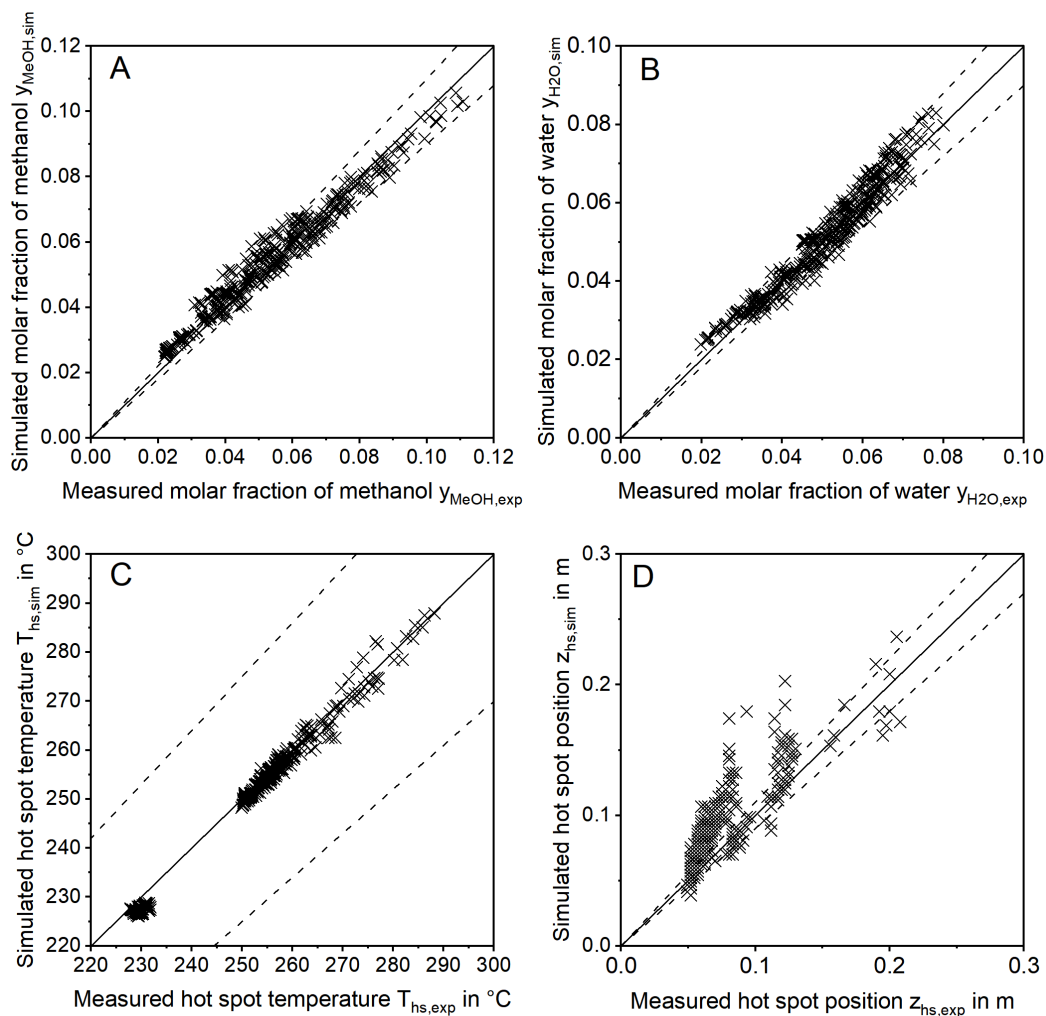


Figure A.14: Parity plots of the refitted model "Graaf<sub>fit</sub>" for outlet molar fractions of methanol (A) and water (B) as well as hot spot temperature (C) and axial hot spot position (D) including error lines for 0% (solid line) and for 10% (dashed line); Experiments were carried out with the miniplant setup.

## A.18 Kinetic model by Bussche

Reaction mechanism proposed by Bussche and Froment [145]:

Adsorption of educts



CO<sub>2</sub>-hydrogenation



rWGS



Rate equations proposed by Bussche [145]:

$$r_{\text{CO}_2} = \frac{k_1 \cdot f_{\text{CO}_2} \cdot f_{\text{H}_2} \cdot EQ_1}{\left(1 + K_1 \cdot \left(\frac{f_{\text{H}_2\text{O}}}{f_{\text{H}_2}}\right) + K_2 \cdot f_{\text{H}_2}^{0,5} + K_3 \cdot f_{\text{H}_2\text{O}}\right)^3} \quad (\text{A.53})$$

$$r_{\text{rWGS}} = \frac{k_2 \cdot f_{\text{CO}_2} \cdot EQ_2}{\left(1 + K_1 \cdot \left(\frac{f_{\text{H}_2\text{O}}}{f_{\text{H}_2}}\right) + K_2 \cdot f_{\text{H}_2}^{0,5} + K_3 \cdot f_{\text{H}_2\text{O}}\right)} \quad (\text{A.54})$$

Table A.8: Original kinetic parameters proposed by Bussche et al. [145].

	Unit	Parameters
$k_1$	$\text{mol} \cdot \text{kg}^{-1} \cdot \text{s}^{-1} \cdot \text{bar}^{-2}$	$1.07 \cdot \exp\left(\frac{36,696}{R \cdot T}\right)$
$k_2$	$\text{mol} \cdot \text{kg}^{-1} \cdot \text{s}^{-1} \cdot \text{bar}^{-1}$	$1.22 \cdot 10^{10} \cdot \exp\left(\frac{-94,765}{R \cdot T}\right)$
$K_1$	—	3,453.38
$K_2$	$\text{bar}^{-0.5}$	$0.499 \cdot \exp\left(\frac{17,197}{R \cdot T}\right)$
$K_3$	$\text{bar}^{-1}$	$6.62 \cdot 10^{-11} \cdot \exp\left(\frac{124,119}{R \cdot T}\right)$

Table A.9: Kinetic parameters for the Bussche<sub>fit</sub> model obtained with the miniplant setup.

	Unit	Parameters
$k_1$	$mol \cdot kg^{-1} \cdot s^{-1} \cdot bar^{-2}$	$0.020 \cdot \exp\left(\frac{-29,122}{R \cdot T}\right)$
$k_2$	$mol \cdot kg^{-1} \cdot s^{-1} \cdot bar^{-1}$	$1.989 \cdot 10^9 \cdot \exp\left(\frac{-119,461}{R \cdot T}\right)$
$K_1$	–	$0.337 \cdot \exp\left(\frac{-2}{R \cdot T}\right)$
$K_2$	$bar^{-0.5}$	$-1.438 \cdot 10^{-3} \cdot \exp\left(\frac{17,263}{R \cdot T}\right)$
$K_3$	$bar^{-1}$	$1.972 \cdot 10^{-10} \cdot \exp\left(\frac{90,516}{R \cdot T}\right)$

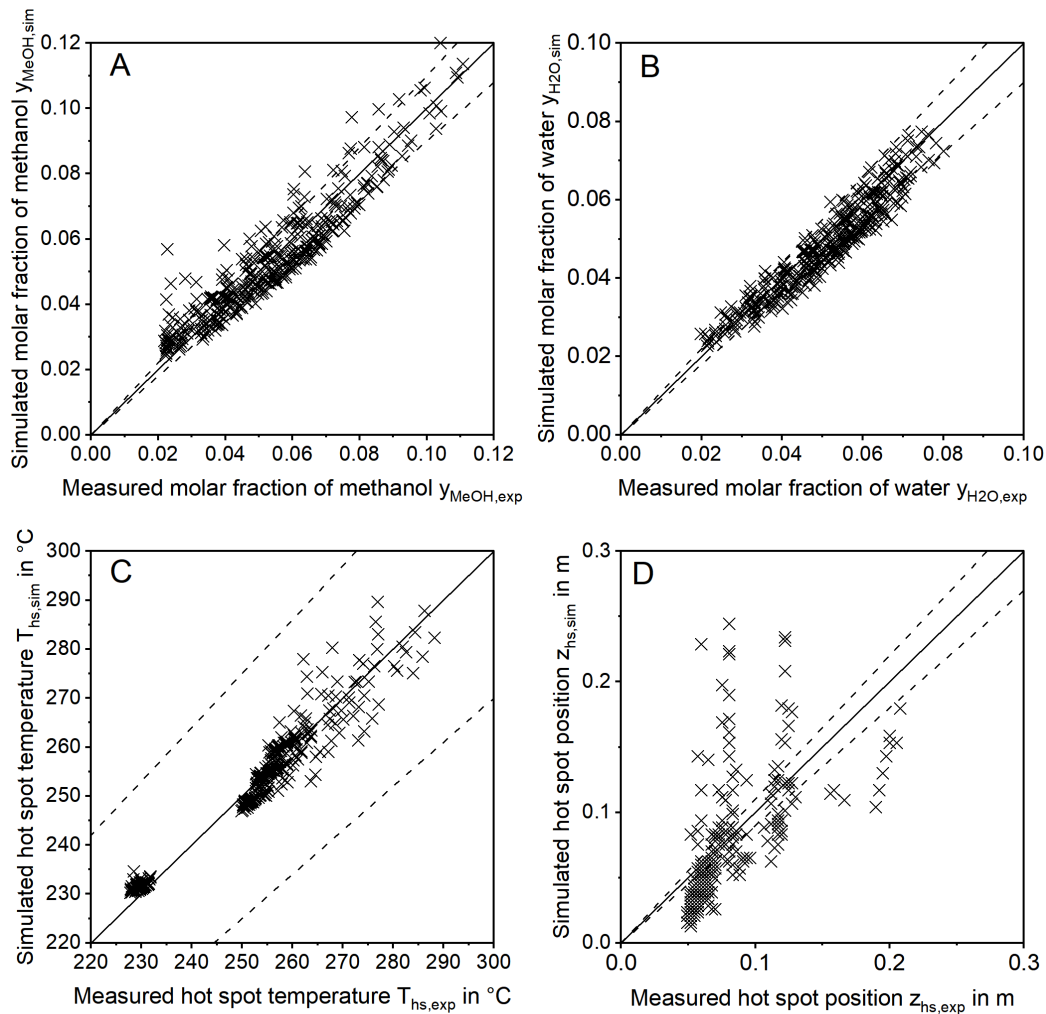
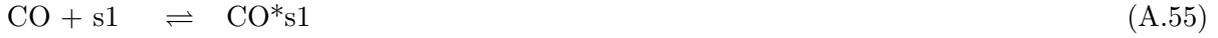


Figure A.15: Parity plots of the refitted model "Bussche<sub>fit</sub>" for outlet molar fractions of methanol (A) and water (B) as well as hot spot temperature (C) and axial hot spot position (D) including error lines for 0% (solid line) and for 10% (dashed line); Experiments were carried out with the miniplant setup.

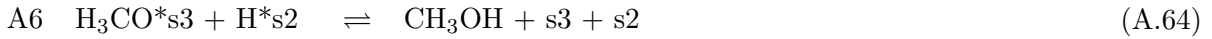
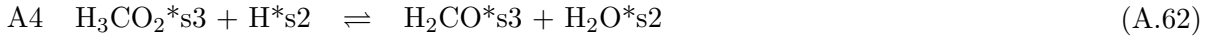
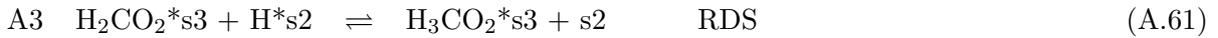
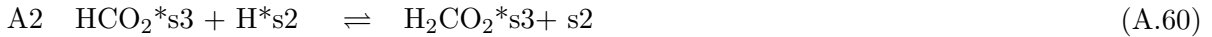
## A.19 Kinetic model by Park

Reaction mechanism proposed by Park et al. [203]:

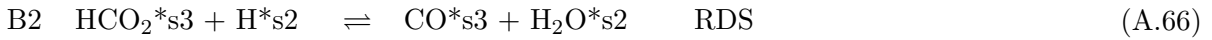
Adsorption of educts



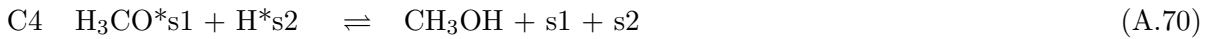
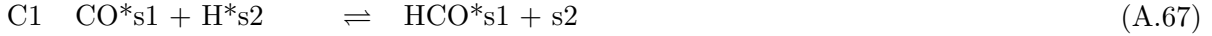
CO<sub>2</sub>-hydrogenation



rWGS



CO-hydrogenation



Rate equations proposed by Park et al. [203]:

$$r_{\text{CO}_2} = \frac{k'_C \cdot K_{\text{CO}_2} \cdot \left[ f_{\text{CO}_2} \cdot f_{\text{H}_2}^{1,5} - f_{\text{H}_2\text{O}} \cdot f_{\text{MeOH}} / (K_{\text{eq},1} \cdot f_{\text{H}_2}^{1,5}) \right]}{\left( 1 + K_{\text{CO}_2} \cdot f_{\text{CO}_2} \right) \cdot \left( 1 + K_{\text{H}_2}^{0,5} \cdot f_{\text{H}_2}^{0,5} + K_{\text{H}_2\text{O}} \cdot f_{\text{H}_2\text{O}} \right)} \quad (\text{A.71})$$

$$r_{\text{WGS}} = - \frac{k'_B \cdot K_{\text{CO}_2} \cdot \left[ f_{\text{CO}_2} \cdot f_{\text{H}_2} - f_{\text{CO}} \cdot f_{\text{H}_2\text{O}} / K_{\text{eq},2} \right]}{\left( 1 + K_{\text{CO}_2} \cdot f_{\text{CO}_2} \right) \cdot \left( 1 + K_{\text{H}_2}^{0,5} \cdot f_{\text{H}_2}^{0,5} + K_{\text{H}_2\text{O}} \cdot f_{\text{H}_2\text{O}} \right)} \quad (\text{A.72})$$

$$r_{\text{CO}} = \frac{k'_A \cdot K_{\text{CO}} \cdot \left[ f_{\text{CO}} \cdot f_{\text{H}_2}^{1,5} - f_{\text{MeOH}} / (K_{\text{eq},3} \cdot f_{\text{H}_2}^{0,5}) \right]}{\left( 1 + K_{\text{CO}} \cdot f_{\text{CO}} \right) \cdot \left( 1 + K_{\text{H}_2}^{0,5} \cdot f_{\text{H}_2}^{0,5} + K_{\text{H}_2\text{O}} \cdot f_{\text{H}_2\text{O}} \right)} \quad (\text{A.73})$$

$$r_{\text{DME}} = \frac{k'_{\text{DME}} \cdot K_{\text{MeOH}}^2 \cdot \left[ c_{\text{MeOH}}^2 - c_{\text{H}_2\text{O}} \cdot c_{\text{DME}} / K_{p,\text{DME}} \right]}{\left( 1 + 2\sqrt{K_{\text{MeOH}} \cdot c_{\text{MeOH}}} + K_{\text{H}_2\text{O},\text{DME}} \cdot c_{\text{H}_2\text{O}} \right)^4} \quad (\text{A.74})$$

Table A.10: Kinetic parameters proposed by Park et al. [203, 261].

	Unit	Parameters
$k'_A$	$mol \cdot kg^{-1} \cdot s^{-1} \cdot bar^{-1.5}$	$1.88 \cdot 10^8 \cdot exp\left(\frac{-133,711}{R.T}\right)$
$k'_B$	$mol \cdot kg^{-1} \cdot s^{-1} \cdot bar^{-1}$	$1.16 \cdot 10^{10} \cdot exp\left(\frac{-126,573}{R.T}\right)$
$k'_C$	$mol \cdot kg^{-1} \cdot s^{-1} \cdot bar^{-1.5}$	$7.08 \cdot 10^4 \cdot exp\left(\frac{-68,252}{R.T}\right)$
$K_{CO}^*$	$bar^{-1}$	$8.00 \cdot 10^{-7} \cdot exp\left(\frac{58,015}{R.T}\right)$
$K_{CO_2}^*$	$bar^{-1}$	$1.02 \cdot 10^{-7} \cdot exp\left(\frac{67,439}{R.T}\right)$
$K_{H_2}^*$	$bar^{-1}$	$27.08 \cdot exp\left(\frac{-6,291}{R.T}\right)$
$K_{H_2O}$	$bar^{-1}$	$3.80 \cdot 10^{-10} \cdot exp\frac{80,876}{R.T}$
$k'_{DME}$	$mol \cdot kg^{-1} \cdot s^{-1}$	$8.54 \cdot 10^9 \cdot exp\left(\frac{-123,779}{R.T}\right)$
$K_{MeOH}$	$m^3 \cdot mol^{-1}$	$7.9 \cdot 10^{-4} \cdot exp\left(\frac{70,500}{R.T}\right)$
$K_{H_2O,DME}$	$m^3 \cdot mol^{-1}$	$0.84 \cdot 10^{-1} \cdot exp\left(\frac{41,100}{R.T}\right)$
$K_{p,DME}$	—	$0.106 \cdot exp\left(\frac{2.1858 \cdot 10^4}{R.T}\right)$

\* these parameters were published by the group subsequently to their original publication [262]

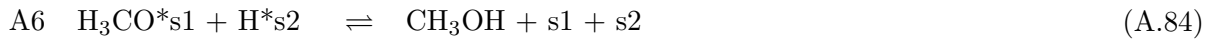
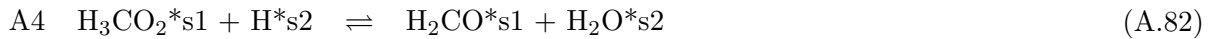
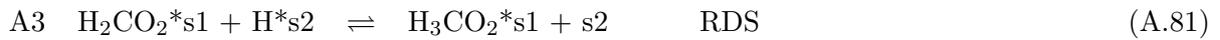
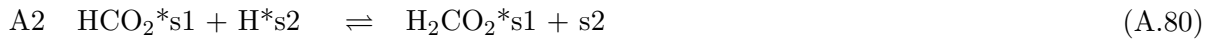
## A.20 Kinetic model by Henkel

Reaction mechanism proposed by Henkel [202]:

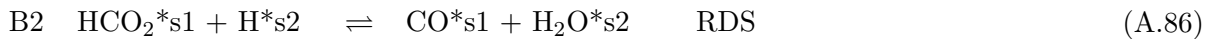
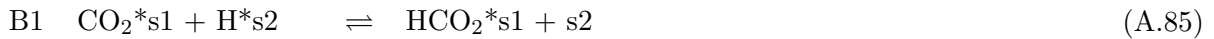
Adsorption



CO<sub>2</sub>-hydrogenation



rWGS



Rate equations proposed by Henkel [202]:

$$r_{\text{CO}_2} = \frac{k_1 \cdot K_2 \cdot f_{\text{CO}_2} \cdot f_{\text{H}_2}^{1.5} \cdot EQ_1}{(1 + K_1 \cdot f_{\text{CO}} + K_2 \cdot f_{\text{CO}_2}) (f_{\text{H}_2}^{0.5} + K_3 \cdot f_{\text{H}_2\text{O}})} \quad (\text{A.87})$$

$$r_{r\text{WGS}} = \frac{k_2 \cdot K_2 \cdot f_{\text{CO}_2} \cdot f_{\text{H}_2} \cdot EQ_2}{(1 + K_1 \cdot f_{\text{CO}} + K_2 \cdot f_{\text{CO}_2}) (f_{\text{H}_2}^{0.5} + K_3 \cdot f_{\text{H}_2\text{O}})} \quad (\text{A.88})$$

Table A.11: Kinetic parameters fitted by Henkel for the Berty reactor and the micro fixed bed reactor [202].

Unit	Berty	Micro fixed bed
$k_1 \quad \text{mol} \cdot \text{kg}^{-1} \cdot \text{s}^{-1} \cdot \text{Pa}^{-1}$	$4.629 \cdot 10^{-4} \cdot \exp\left(\frac{-47,472}{R \cdot T}\right)$	$3.172 \cdot 10^{-4} \cdot \exp\left(\frac{-45,893}{R \cdot T}\right)$
$k_2 \quad \text{mol} \cdot \text{kg}^{-1} \cdot \text{s}^{-1} \cdot \text{Pa}^{-0.5}$	$12.975 \cdot \exp\left(\frac{-60,609}{R \cdot T}\right)$	$2.021 \cdot 10^6 \cdot \exp\left(\frac{-112,322}{R \cdot T}\right)$
$K_1 \quad \text{Pa}^{-1}$	$2.743 \cdot 10^{-17} \cdot \exp\left(\frac{108,082}{R \cdot T}\right)$	$2.420 \cdot 10^{-14} \cdot \exp\left(\frac{81,976}{R \cdot T}\right)$
$K_2 \quad \text{Pa}^{-1}$	$1.935 \cdot 10^{-4}$	$1.000 \cdot 10^{-4}$
$K_3 \quad \text{Pa}^{-0.5}$	$5.797 \cdot 10^{-14} \cdot \exp\left(\frac{112,322}{R \cdot T}\right)$	$1.040 \cdot 10^{-8} \cdot \exp\left(\frac{61,856}{R \cdot T}\right)$

Table A.12: Fitted parameters for the Nestler<sub>integ</sub> kinetic model obtained from the measured data by Park et al. [203] in Sec. 4.1.

	Unit	Nestler <sub>integ</sub> kinetic parameters
$k_1$	$\text{mol} \cdot \text{kg}^{-1} \cdot \text{s}^{-1} \cdot \text{Pa}^{-1}$	$5.411 \cdot 10^{-4} \cdot \exp\left(\frac{-45,458}{R \cdot T}\right)$
$k_2$	$\text{mol} \cdot \text{kg}^{-1} \cdot \text{s}^{-1} \cdot \text{Pa}^{-0.5}$	$4.701 \cdot \exp\left(\frac{-54,970}{R \cdot T}\right)$
$K_1$	$\text{Pa}^{-1}$	$3.321 \cdot 10^{-18} \cdot \exp\left(\frac{109,959}{R \cdot T}\right)$
$K_2$	$\text{Pa}^{-1}$	$8.262 \cdot 10^{-6}$
$K_3$	$\text{Pa}^{-0.5}$	$6.430 \cdot 10^{-14} \cdot \exp\left(\frac{119,570}{R \cdot T}\right)$

Table A.13: Fitted parameters for the Nestler<sub>diff</sub> kinetic model obtained from the miniplant data in Sec. 4.2.3.

	Unit	Proposed kinetic parameters
$k_1$	$\text{mol kg}^{-1} \text{ s}^{-1} \text{ Pa}^{-1}$	$2.385 \cdot 10^{-5} \cdot \exp\left(\frac{-14,709}{R \cdot T}\right)$
$k_2$	$\text{mol kg}^{-1} \text{ s}^{-1} \text{ Pa}^{-0.5}$	$244.433 \cdot \exp\left(\frac{-53,741}{R \cdot T}\right)$
$K_1$	$\text{Pa}^{-1}$	$1.440 \cdot 10^{-17} \cdot \exp\left(\frac{-570}{R \cdot T}\right)$
$K_2$	$\text{Pa}^{-1}$	$4.223 \cdot 10^{-6}$
$K_3$	$\text{Pa}^{-0.5}$	$6.407 \cdot 10^{-13} \cdot \exp\left(\frac{126,843}{R \cdot T}\right)$

## A.21 Alternative kinetic approaches

As the set of rate equations proposed by Henkel [202] is based a assumption regarding the rate determining step in the suggested mechanism (see Eq. A.75 until Eq. A.86), the question arises whether this combination led to the lowest possible deviation between experimental and simulation data. In order to clarify this question, rate equations were derived for all possible combinations of RDS in rWGS and CO<sub>2</sub>-hydrogenation:

A1

$$r_{A1} = \frac{k_{A1} \cdot K_{CO_2} \cdot \sqrt{K_{H_2}} \cdot f_{CO_2} \cdot \sqrt{f_{H_2}} \cdot EQ_1}{(1 + K_{CO} \cdot f_{CO} + K_{CO_2} \cdot f_{CO_2}) \cdot (1 + K_{H_2O} \cdot f_{H_2O} + \sqrt{K_{H_2} \cdot f_{H_2}})} \quad (A.89)$$

A2

$$r_{A2} = \frac{k_{A2} \cdot K_{CO_2} \cdot K_{H_2} \cdot f_{CO_2} \cdot f_{H_2} \cdot EQ_1}{(1 + K_{CO} \cdot f_{CO} + K_{CO_2} \cdot f_{CO_2}) \cdot (1 + K_{H_2O} \cdot f_{H_2O} + \sqrt{K_{H_2} \cdot f_{H_2}})} \quad (A.90)$$

A3

$$r_{A3} = \frac{k_{A3} \cdot K_{CO_2} \cdot K_{H_2}^{1.5} \cdot f_{H_2}^{1.5} \cdot f_{CO_2} \cdot EQ_1}{(1 + K_{CO} \cdot f_{CO} + K_{CO_2} \cdot f_{CO_2}) \cdot (1 + K_{H_2O} \cdot f_{H_2O} + \sqrt{K_{H_2} \cdot f_{H_2}})} \quad (A.91)$$

A4

$$r_{A4} = \frac{k_{A4} \cdot K_{CO_2} \cdot K_{H_2}^2 \cdot f_{CO_2} \cdot f_{H_2}^2 \cdot EQ_1}{(1 + K_{CO} \cdot f_{CO} + K_{CO_2} \cdot f_{CO_2}) \cdot (1 + K_{H_2O} \cdot f_{H_2O} + \sqrt{K_{H_2} \cdot f_{H_2}})} \quad (A.92)$$

A5

$$r_{A5} = \frac{k_{A5} \cdot K_{CO_2} \cdot K_{H_2}^{2.5} \cdot K_{H_2O}^{-1} \cdot \frac{f_{CO_2} \cdot f_{H_2}^{2.5}}{f_{H_2O}} \cdot EQ_1}{(1 + K_{CO} \cdot f_{CO} + K_{CO_2} \cdot f_{CO_2}) \cdot (1 + K_{H_2O} \cdot f_{H_2O} + \sqrt{K_{H_2} \cdot f_{H_2}})} \quad (A.93)$$

A6

$$r_{A6} = \frac{\frac{k_{A6} \cdot K_{H_2}^3 \cdot K_{CO_2}}{K_{H_2O}} \cdot \frac{f_{H_2}^3 \cdot f_{CO_2}}{f_{H_2O}} \cdot EQ_1}{(1 + K_{CO} \cdot f_{CO} + K_{CO_2} \cdot f_{CO_2}) \cdot (1 + K_{H_2O} \cdot f_{H_2O} + \sqrt{K_{H_2} \cdot f_{H_2}})} \quad (A.94)$$

B1

$$r_{B1} = \frac{k_{B1} \cdot K_{CO_2} \cdot \sqrt{K_{H_2}} \cdot f_{CO_2} \cdot \sqrt{f_{H_2}} \cdot EQ_2}{(1 + K_{CO} \cdot f_{CO} + K_{CO_2} \cdot f_{CO_2}) \cdot (1 + K_{H_2O} \cdot f_{H_2O} + \sqrt{K_{H_2} \cdot f_{H_2}})} \quad (A.95)$$

B2

$$r_{B2} = \frac{k_{B2} \cdot K_{CO_2} \cdot K_{H_2} \cdot f_{CO_2} \cdot f_{H_2} \cdot EQ_2}{(1 + K_{CO} \cdot f_{CO} + K_{CO_2} \cdot f_{CO_2}) \cdot (1 + K_{H_2O} \cdot f_{H_2O} + \sqrt{K_{H_2} \cdot f_{H_2}})} \quad (A.96)$$

All possible combinations of rate equations were then subjected to the parameter fitting described in Sec. 3.5.2.2. The remaining errors depicted in Fig. A.16 show that the best parameter estimation was obtained with the combinations of RDS proposed by Henkel (A3B2). The fact that other combinations led to higher deviations underlines the ability of the miniplant setup to discriminate between different mechanistic assumptions.

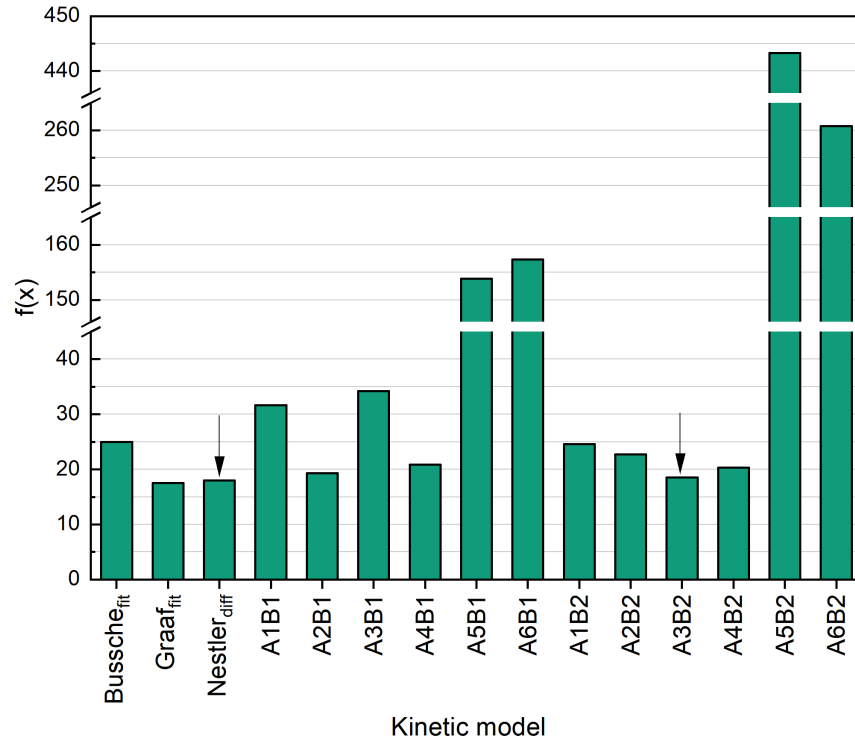


Figure A.16: Remaining objective function with respect to Eq. 3.79 obtained for the kinetic models Bussche<sub>fit</sub>, Graaf<sub>fit</sub> and Nestler<sub>diff</sub> as well as for all possible combinations of Eq. A.89 until Eq. A.96; Arrows indicate the same combination of RDS, however in case of A3B2 without the simplification  $1 \ll K_{\text{H}_2\text{O}} \cdot f_{\text{H}_2\text{O}} + \sqrt{K_{\text{H}_2} \cdot f_{\text{H}_2}}$  proposed by Graaf [192].

## A.22 Single versus global data fitting

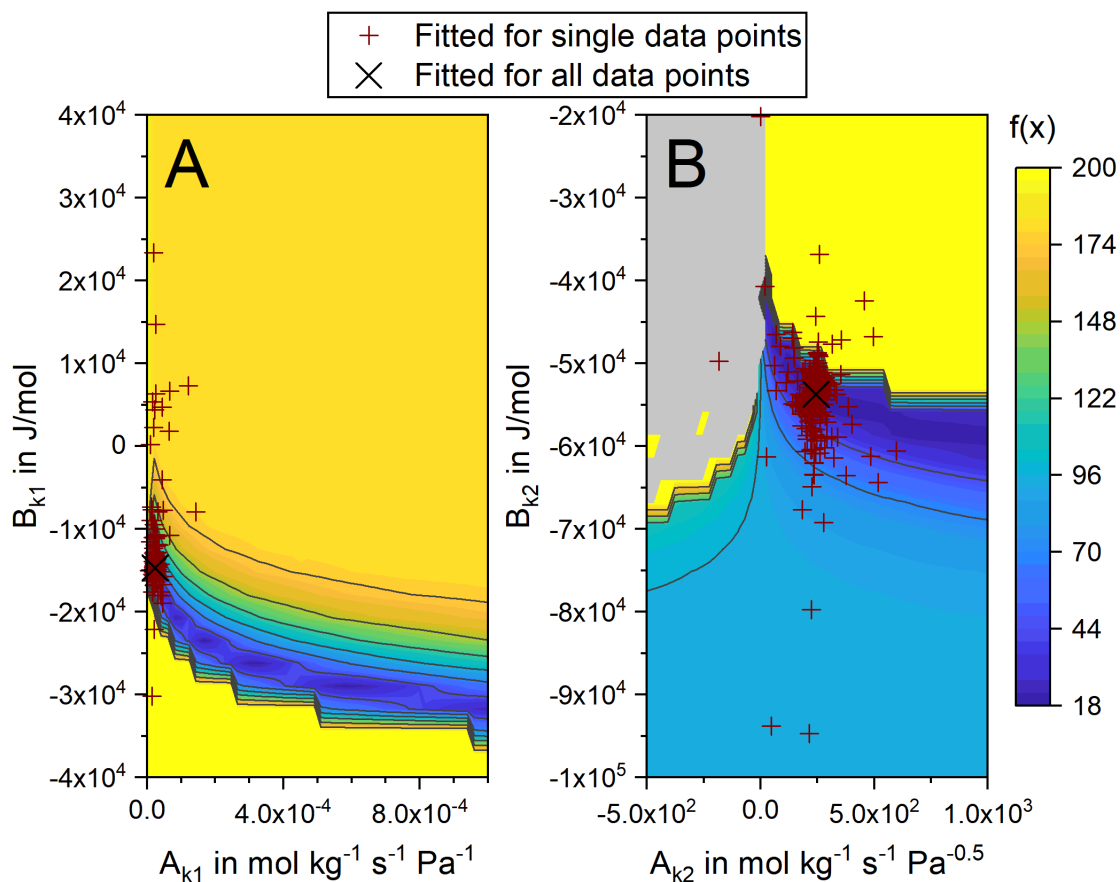


Figure A.17: Sensitivity analysis of the objective function defined in Eq. 3.79 on the kinetic parameters  $A_{k1}$  and  $B_{k1}$  (A) as well as  $A_{k2}$  and  $B_{k2}$  (B) simulated for all experimental data points with the kinetic model  $\text{Nestler}_{\text{fit}}$ ; Color of the heat map symbolizes the value of the objective function; The gray area could not be calculated due to divergence of the kinetic model; The final data set fitted for all experimental data points in Sec.4.2.3 is marked by (x); The values fitted for each individual data point are marked by (+).

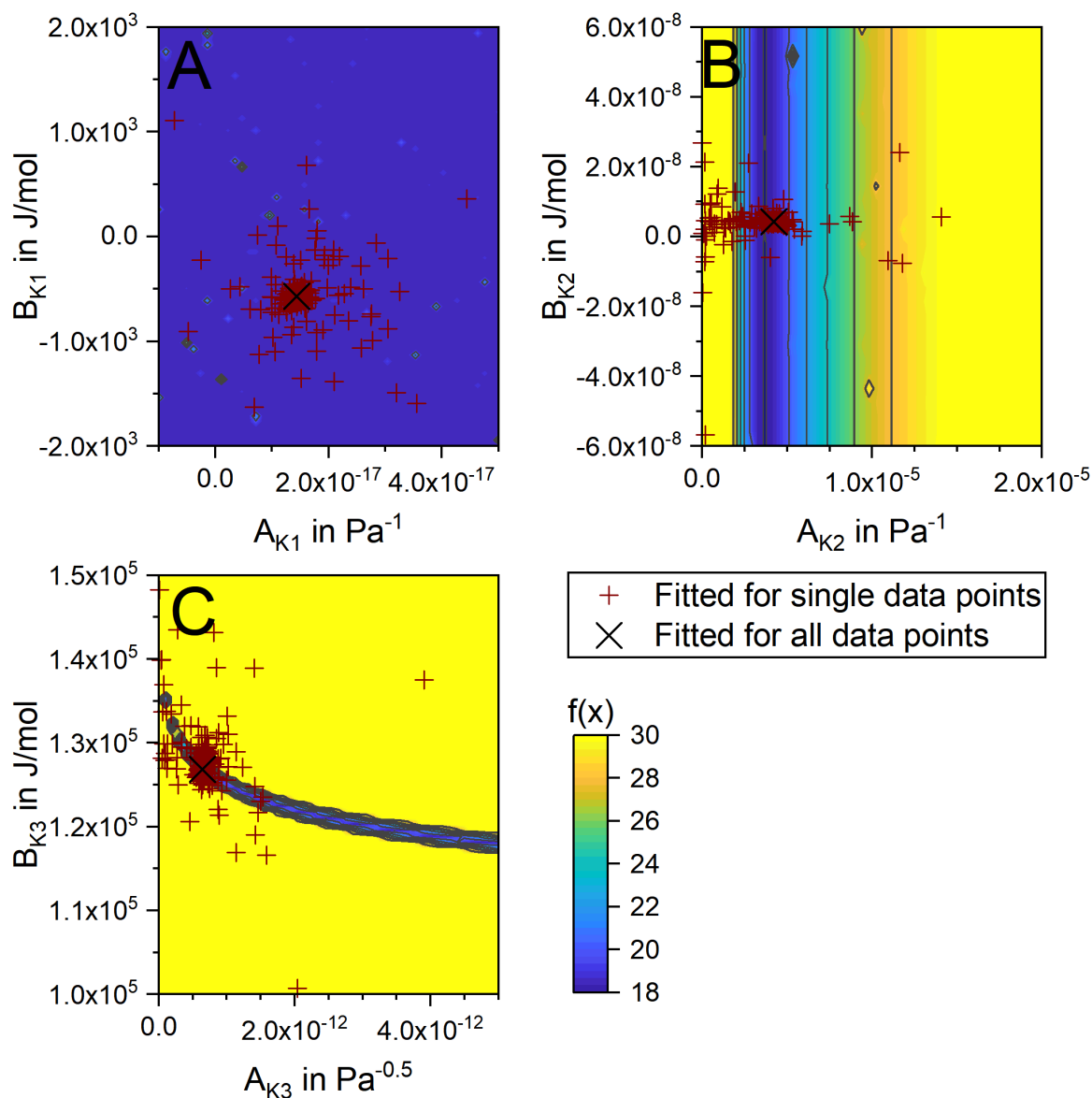


Figure A.18: Sensitivity analysis of the objective function defined in Eq. 3.79 on the adsorption parameters  $A_{K1}$  and  $B_{K1}$  (A),  $A_{K2}$  and  $B_{K2}$  (B) as well as  $A_{K3}$  and  $B_{K3}$  (C) simulated for all experimental data points with the kinetic model Nestler<sub>fit</sub>; Color of the heat map symbolizes the value of the objective function; The final data set fitted for all experimental data points in Sec.4.2.3 is marked by (x); The values fitted for each individual data point are marked by (+).

## A.23 Comparison of experimental and simulated gas phase composition data

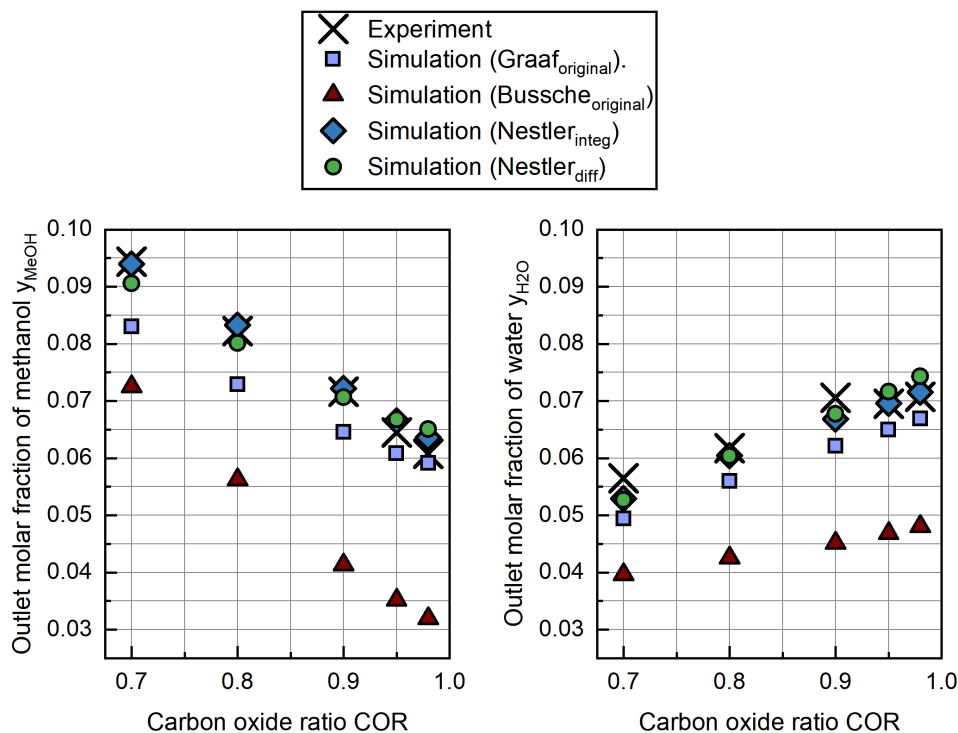


Figure A.19: Gas phase compositions obtained from the miniplant experiments and simulated using the kinetic models by Graaf [192] (A), Bussche [145] (B) as well as the kinetic model Nestler<sub>integ</sub> (compare Sec. 4.1, C) and Nestler<sub>diff</sub> (compare Sec. 4.2, D) at  $p = 80$  bar;  $T_{\text{cool}} = 240$  °C;  $\text{SN} = 5.0$  and  $\text{GHSV} = 9,000$  h<sup>-1</sup> for COR = 0.7, 0.8, 0.9, 0.95 and 0.98.

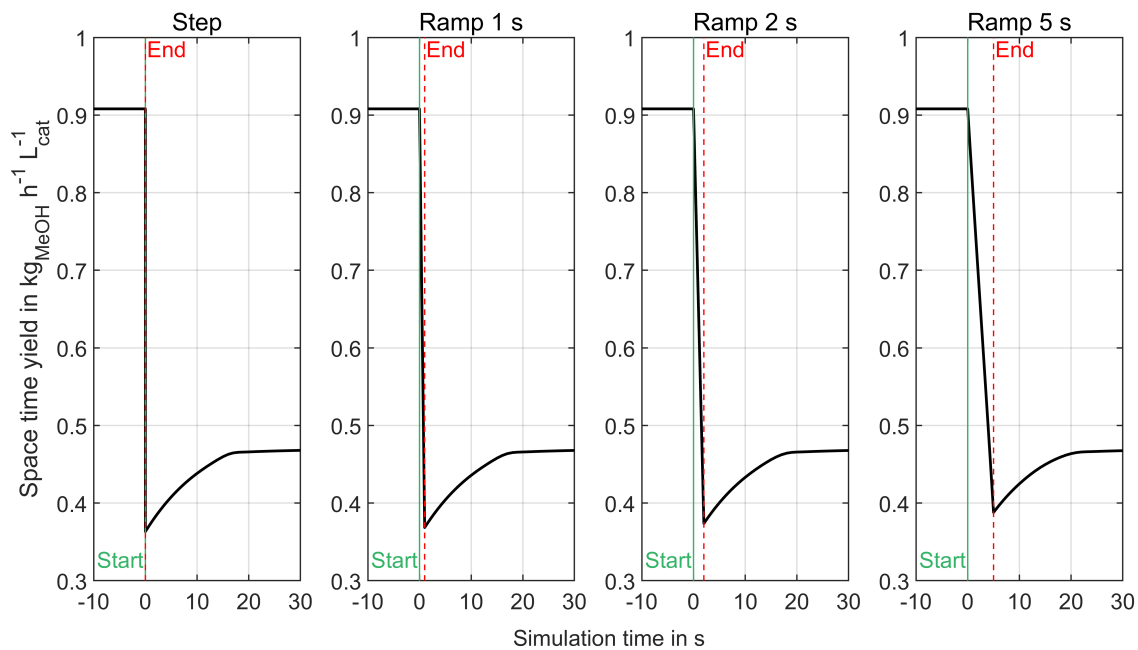
## A.24 Dynamic simulation study

In order to discuss the behavior of a steam cooled tubular reactor under transient conditions and account for possible issues arising for reactor design, a dynamic simulation campaign was performed applying the Nestler<sub>diff</sub> kinetic model and the dynamic reactor model presented in Sec. 3.1.5. The reactor dimensions were considered with regard to Tab. 3.5. To keep the simulation parameters in the validated data range of the kinetic model, a base case of  $COR = 0.85$ ,  $SN = 3.0$  and  $GHSV = 10,000 \text{ h}^{-1}$  was defined for the three pressure levels of 50 bar, 65 bar and 80 bar at a cooling temperature of  $240^\circ\text{C}$ . The load changes in the simulation campaign were applied separately for COR, SN and GHSV from the base case and executed as step (transition time 0 s) and ramps of 1 s, 2 s as well as 5 s. COR was varied to 0.7 and 1.0, SN to 2.0 and 4.0 and GHSV to  $4,000 \text{ h}^{-1}$  and  $16,000 \text{ h}^{-1}$ . The diffusion limitation (compare Sec. 3.5.2) was neglected in this simulation campaign to decrease computation time.

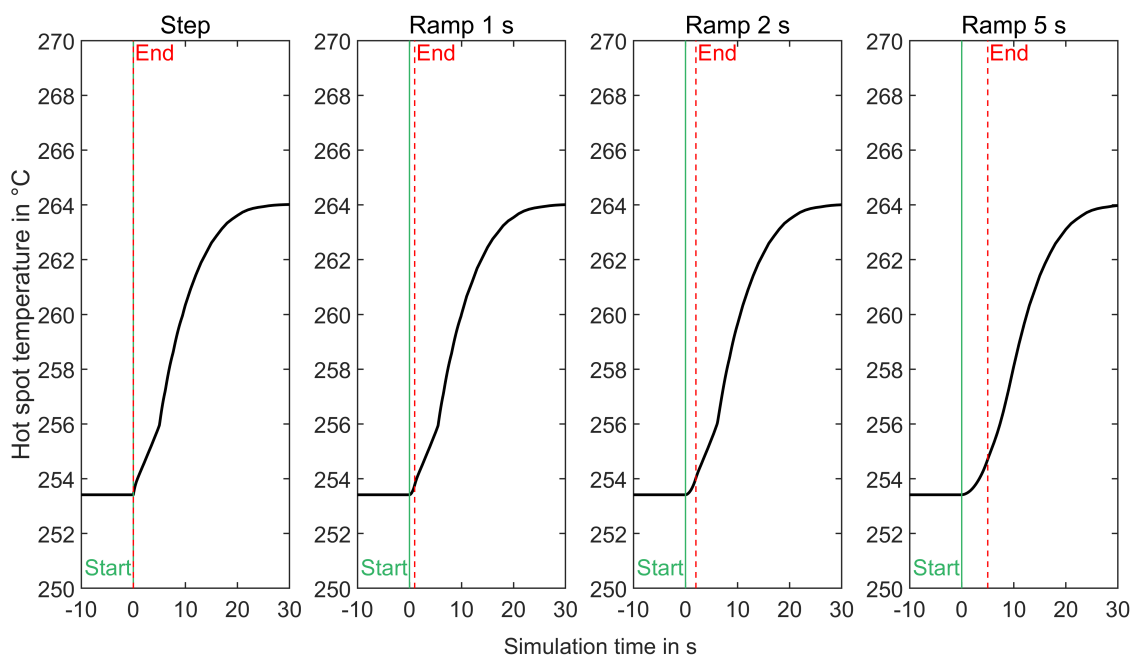
The goal of this simulation campaign was the determination of possible critical load gradients, e.g. due to a temperature overshoot during the load change. However, it is to be denoted that the load changes applied in the simulation campaign would be very unlikely to proceed in a state-of-the-art methanol synthesis process as the dead volume of the process equipment in the recycle loop would decrease the gradient. In case of an uncritical behavior of the reactor during the load changes considered here, it can therefore be assumed that the reactor can be operated dynamically when it is integrated into the methanol synthesis loop process.

In Fig. A.20, the development of the reactor's STY (a) (compare Eq. 2.9) and hot spot temperature is shown during the reduction of the GHSV from  $10,000 \text{ h}^{-1}$  to  $4,000 \text{ h}^{-1}$  for the four load gradients. Fig. A.20 (a) indicated a sharp decrease in STY during the time of the load transition with a subsequent slight increase and a stabilization at the new steady state. The initial decrease in STY can be explained by the reduced reactor output due to the lower flow rate, however, with an output composition related to the shorter residence time in the reactor before the load change ( $GHSV = 10,000 \text{ h}^{-1}$ ). The slight increase of STY after the load change can be explained by the longer residence time of the gas in the reactor after the load change and the consequently higher conversion. Except of the change in transition time, no fundamental differences in the STY calculated for the four load gradients considered can be observed.

In Fig. A.20 (b) the increase in hot spot temperature over time as a consequence of the decreased GHSV can be observed. For the load transition performed as step, within 1 s as well as within 2 s, a change in the slope of the temperature increase after the load change can be observed. As shown in Fig A.21 (a) this effect is the consequence of a new hot spot forming upstream the original hot spot position. This effect is not observed at the load change performed within 5 s, as the new hot spot is in this case superimposed by the load hot spot moving upstream (compare Fig. A.21 (b)).

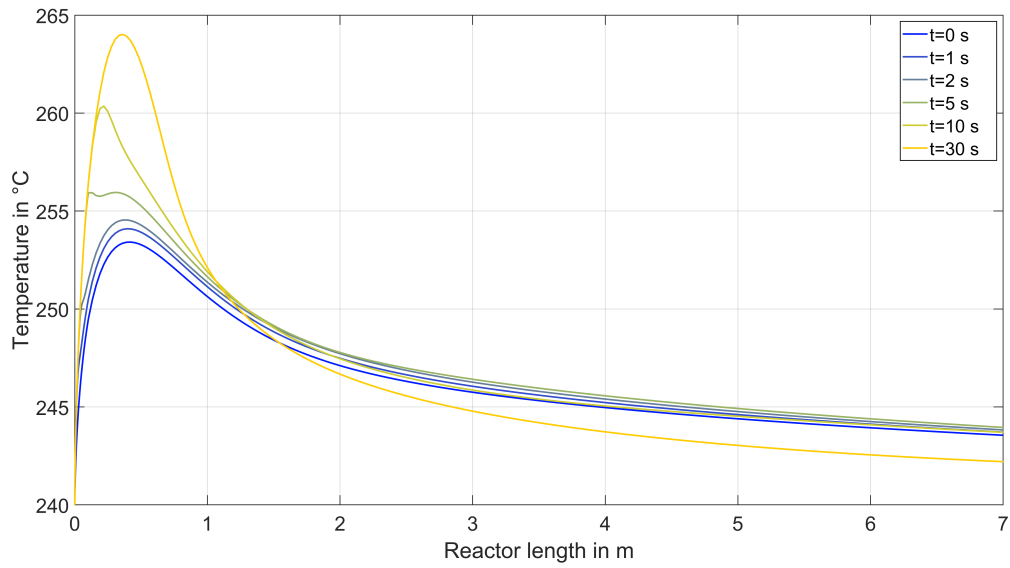


a) Space time yield.

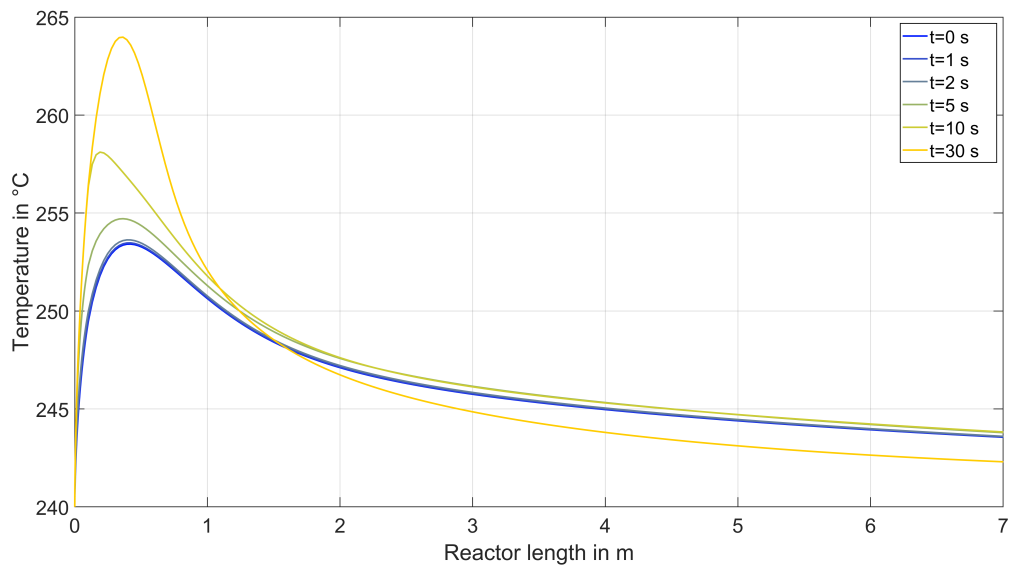


b) Hot spot temperature.

Figure A.20: Development of the reactor's space time yield (a) and hot spot temperature (b) during a load reduction from  $\text{GHSV} = 10,000 \text{ h}^{-1}$  to  $\text{GHSV} = 4,000 \text{ h}^{-1}$  at  $\text{COR} = 0.85$ ,  $\text{SN} = 3.0$ ,  $T_{\text{cool}} = 240 \text{ }^{\circ}\text{C}$  and  $p = 80 \text{ bar}$ ; Load change performed as a step as well as ramp of 1 s, 2 s and 5 s (from left to right).



a) Load transition performed as step.



b) Load transition performed as ramp of 5 s.

Figure A.21: Development of the reactor's temperature profile during a load reduction from  $GHSV = 10,000 \text{ h}^{-1}$  to  $GHSV = 4,000 \text{ h}^{-1}$  at  $COR = 0.85$ ,  $SN = 3.0$ ,  $T_{cool} = 240 \text{ °C}$  and  $p = 80 \text{ bar}$ ; Load change performed as a step (a) as well as ramp of 5 s (b).

In Fig. A.22 the dynamic load changes described in Sec. 3.1.5 are discussed with regard to their impact on hot spot temperature. Marked were the hot spot temperatures before the load transition (green triangle), after the load transition was performed (red triangle) as well as the maximum temperature inside the reactor during the total time of the load change (blank circle). In order to discuss the influence of transition time, the load changes were performed as step as well as ramps of 1 s, 2 s and 5 s (per section from left to right).

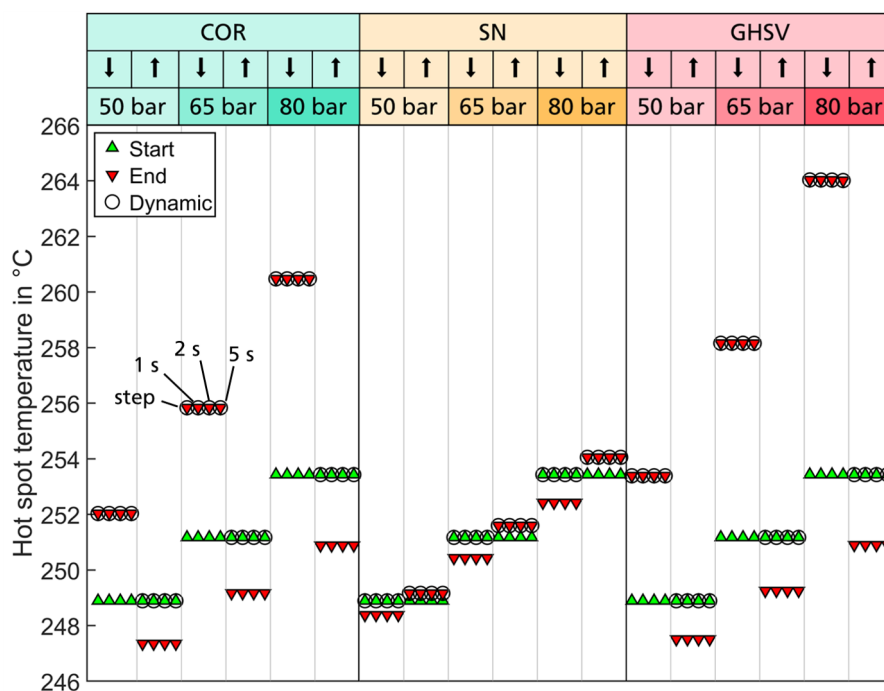


Figure A.22: Dynamic simulation campaign applying load changes from the base case  $COR = 0.85$ ,  $SN = 3.0$ ,  $GHSV = 10,000 \text{ h}^{-1}$ ,  $T_{\text{cool}} = 240 \text{ }^\circ\text{C}$  at 50 bar, 65 bar and 80 bar towards  $COR = 0.7$  ( $\downarrow$ ),  $COR = 1.0$  ( $\uparrow$ ),  $SN = 2.0$  ( $\downarrow$ ),  $SN = 4.0$  ( $\uparrow$ ),  $GHSV = 4,000 \text{ h}^{-1}$  ( $\downarrow$ ) and  $GHSV = 16,000 \text{ h}^{-1}$  ( $\uparrow$ ) as a step as well as a ramp within 1 s, 2 s and 5 s (symbols per section from left to right).

Fig. A.22 shows that both, a decrease of COR as well as a reduction of GHSV lead to higher hot spot temperatures. In case of COR this can be explained by the higher exothermic heat of CO-hydrogenation in comparison to CO<sub>2</sub>-hydrogenation. In case of GHSV the lower gas velocity inside the reactor leads to a higher heat production per reactor volume. As this heat cannot instantly be removed, temperature rises until the  $\Delta T$  between reactor inside and steam cooling is sufficient for the removal of the exothermic heat. Vice versa, lower hot spot temperatures are obtained when COR and GHSV are increased. Smaller effects on hot spot temperature are obtained by a variation of SN. While a decline to  $SN = 2.0$  decreases hot spot temperature, an increase to  $SN = 4.0$  leads towards slightly higher temperatures. This effect is obtained, as excess of H<sub>2</sub> moves equilibrium to the side of the products and consequently increases the reactions driving force (compare Fig. 2.4). Moreover, higher H<sub>2</sub> contents in the syngas decrease the partial pressure of water and therefore increase reaction kinetics.

Overall, load changes towards higher CO contents and lower GHSVs could be problematic from

a thermal point of view. However, even though hot spot temperature decreases in case of an increase of the CO<sub>2</sub>, this load point could be problematic regarding to catalyst stability as a result of the higher water contents in the reaction product. An appropriate deactivation model would be necessary to determine the critical water content with regard to catalyst stability.

In terms of the dynamic behavior of the hot spot temperature, none of the cases considered here resulted in the formation of an intermediate hot spot exceeding that of the steady states before or after the load change, respectively. Similar results were obtained in a comparable analysis with higher CO contents, i.e. working points with a higher exothermic heat and consequently increased hot spot temperatures. Therefore, according to the simulation results obtained for the load changes considered here the steady state model could be applied to identify critical hot spot temperatures in the reactor instead of the dynamic model for the benefit of a reduced model complexity and faster computation time. This finding stresses the necessity of an accurate steady-state reactor model for dynamically operated PtM processes.